



187(4), 2021



COMBUSTION ENGINES



Join us in person in 2022!

Powertrains, Fuels & Lubricants Conference & Exhibition

September 7-9, 2022
Krakow, Poland

SPONSORS:

BOSMAL



Call for Papers/Presentations

Share your innovative research by submitting an abstract for consideration as part of our 2022 technical program. It only takes 250 words to get started!

Deadline for submissions: March 9, 2022

Contact: Dr. Piotr Bielaczyc, FSAE – Chair of the SAE 22 PF&L Organizing Committee
email: piotr.bielaczyc@bosmal.com.pl
phone: +48 33 8130598

Exhibit Space & Sponsorships Available

Contact Megan McCoy for information on exhibiting or sponsoring in Krakow.

o: +1.724.772.4037

e: megan.mccoy@sae.org

sae.org/pfl

PTNSS Supporting Members Członkowie wspierający PTNSS

BOSMAL Automotive Research and Development Institute Ltd

Instytut Badań i Rozwoju
Motoryzacji BOSMAL Sp. z o.o

Motor Transport Institute

Instytut Transportu Samochodowego

Institute of Aviation

Sieć Badawcza Łukasiewicz
– Instytut Lotnictwa

Automotive Industry Institute

Sieć Badawcza Łukasiewicz
– Przemysłowy Instytut Motoryzacji

The Rail Vehicles Institute TABOR

Sieć Badawcza Łukasiewicz
– Instytut Pojazdów Szynowych TABOR

Industrial Institute of Agricultural Engineering

Sieć Badawcza Łukasiewicz
– Przemysłowy Instytut Maszyn Rolniczych

AVL List GmbH

Solaris Bus & Coach S.A.

Air Force Institute of Technology

Instytut Techniczny Wojsk Lotniczych

Military Institute of Armoured & Automotive Technology

Wojskowy Instytut Techniki Panczernej
i Samochodowej

Toyota Motor Poland Ltd. Sp. z o.o.

RADWAG Balances and Scales

RADWAG Wagi Elektroniczne

MS Mechatronic Solutions Group



COMBUSTION ENGINES

A Scientific Magazine

2021, 187(4)

Year LX

PL ISSN 2300-9896

PL eISSN 2658-1442

Publisher:

Polish Scientific Society of Combustion Engines

60-965 Poznan, pl. M. Skłodowskiej-Curie 5, Poland

tel.: +48 61 6475966, fax: +48 61 6652204

E-mail: sekretariat@ptnss.pl

WebSite: <http://www.ptnss.pl>

Papers available on-line: <http://combustion-engines.eu>

Scientific Board:

- Krzysztof Wisłocki – chairman, Poland (*Poznan University of Technology*)
- Yuzo Aoyagi – Japan (*Okayama University*)
- Ewa Bardasz – USA (*National Academy of Engineering*)
- Piotr Bielaczyc – Poland (*BOSMAL Automotive Research and Development Institute Ltd.*)
- Zdzisław Chłopek – Poland (*Warsaw University of Technology*)
- Tadeu Cordeiro de Melo – Brazil (*Petrobras*)
- Jan Czerwinski – Switzerland (*CJ Consulting*)
- Friedrich Dinkelacker – Germany (*Leibniz Universität Hannover*)
- Hubert Friedl – Austria (*AVL*)
- Barouch Giechaskiel – Italy (*European Commission, JRC Italy*)
- Leslie Hill – UK (*Horiba*)
- Timothy Johnson – USA (*Corning Inc.*)
- Kazimierz Lejda – Poland (*Rzeszow University of Technology*)
- Hans Peter Lenz – Austria (*TU Wien*)
- Helmut List – Austria (*AVL*)
- Toni Kinnunen – Finland (*Proventia*)
- David Kittelson – USA (*University of Minnesota*)
- Christopher Kolodziej – USA (*Delphi Automotive Systems*)
- Hu Li – UK (*University of Leeds*)
- Federico Millo – Italy (*Politecnico Torino*)
- Jeffrey D. Naber – USA (*Michigan Technological University*)
- Andrzej Niewczas – Poland (*Motor Transport Institute*)
- Marek Orkisz – Poland (*Rzeszow University of Technology*)
- Dieter Peitsch – Germany (*TU Berlin*)
- Stefan Pischinger – Germany (*FEV Germany*)
- Andrzej Sobiesiak – Canada (*University of Windsor*)
- Stanisław Szwaja – Poland (*Częstochowa University of Technology*)
- Piotr Szymański – Netherlands (*European Commission, JRC*)
- Leonid Tartakovsky – Israel (*Technion – Israel Institute of Technology*)
- Andrzej Teodorczyk – Poland (*Warsaw University of Technology*)
- Xin Wang – China (*Beijing Institute of Technology*)
- Thomas Wallner – USA (*Argonne National Laboratory*)
- Michael P. Walsh – USA (*International Council on Clean Transportation*)
- Mirosław Wendeker – Poland (*Lublin University of Technology*)
- Piotr Wolański – Poland (*Warsaw University of Technology*)
- Mirosław Wyszynski – UK (*University of Birmingham*)

Contents

Biały M., Grabowski L., Skórzyński B., Barański G., Majczak A. Analyzing mechanical vibrations of an aircraft opposed piston engine 3

Krakowski R. Research on the effect of the effective microorganisms, silver solution and colloidal nanosilver addition on the engine oil base number (TBN) 8

Kaźmierski B., Górka K., Kapusta Ł.J. A conceptual design and numerical analysis of the mixerless urea-SCR system 12

Fafara J.-M., Modliński N. Numerical investigation of the internal flue gas recirculation system applied to methane powered gas microturbine combustor 21

Żmudka Z., Postrzednik S. Improving the effective efficiency of a spark ignition engine through the use of a fully independent valve control system 30

Szymlet N., Kamińska M., Lijewski P., Rymaniak Ł., Tutak P. Use of toxicity indicators related to CO₂ emissions in the ecological assessment of an two-wheel vehicle 36

Kalwara M., Kuźniar M., Orkisz M. A rotating piston engine with electric generator in serial hybrid propulsion system for use in light aircraft 42

Andrzejewski M., Nowak M., Woch A., Stefańska N. Analysis of pollutant emissions and fuel consumption for the use of a multistorey carpark 46

Walentynowicz J. The aircraft engines in the land vehicles 52

Chmielewski Z. Cylinder liner wear as a function of selected physicochemical indicators of engine oil 60

Szramowiat M., Szalek A. Analysis of the operation of the hybrid drive system in the light of the proposed Euro7 standard 65

Wolczyński Z., Żak M. SI engine fuel mixture type indicator and an assessment of its suitability of an economic driving style 69

Kaźmierczak A., Tkaczyk M. Team durability test of a 1.3 MW locomotive diesel engine with prototype piston rings 77

Czarnigowski J., Rękas D., Ścisłowski K., Trendak M., Skiba K. Analysis of operating parameters of the aircraft piston engine in real operating conditions 83

Bogdanowicz A., Kniaziewicz T., Zadrąg R. The emission of harmful compounds from the marine diesel engine fueled by a blend of n-butanol and marine fuel 90

Urbański B., Przybyła G. Hybrid drivetrain systems 48 V in rally cars 96

Laskowski P., Zimakowska-Laskowska M., Zasina D., Wiatrak M. Comparative analysis of the emissions of carbon dioxide and toxic substances emitted by vehicles with ICE compared to the equivalent emissions of BEV 102

Wolczyński Z. Examples of the use of the embedded systems for the long-term collection of slowly-changing parameters in the traction of a car 106

Editorial:

Institute of Combustion Engines and Powertrains
 Poznan University of Technology
 60-965 Poznan, Piotrowo 3 Street
 tel.: +48 61 2244505, +48 61 2244502
 E-mail: papers@ptnss.pl

Prof. Jerzy Merkisz, DSc., DEng. (Editor-in-chief)
 Miłosław Kozak, DSc., DEng.
 Prof. Jacek Pielecha, DSc., DEng. (Editorial Secretary for Science)
 Prof. Ireneusz Pielecha, DSc., DEng.
 Wojciech Cieślak, DEng. (Technical Editors)
 Joseph Woodburn, MScI (Proofreading Editor)
 Wojciech Serdecki, DSc., DEng. (Statistical Editor)
 and Associate Editors

Publisher:

Polish Scientific Society of Combustion Engines
 60-965 Poznan, pl. M. Skłodowskiej-Curie 5, Poland
 tel.: +48 61 6475966, fax: +48 61 6652204
 E-mail: sekretariat@ptnss.pl
 WebSite: <http://www.ptnss.pl>

The Publisher of this magazine does not endorse the products or services advertised herein. The published materials do not necessarily reflect the views and opinions of the Publisher.

© Copyright by
Polish Scientific Society of Combustion Engines
 All rights reserved.

No part of this publication may be reproduced, stored in a retrieval system or transmitted, photocopied or otherwise without prior consent of the copyright holder.

Subscriptions

Send subscription requests to the Publisher's address.
 Cost of a single issue PLN 40.

Preparation for print

ARS NOVA Publishing House
 60-782 Poznan, ul. Grunwaldzka 17/10A

Circulation: 100 copies

Printing and binding

Zakład Poligraficzny Moś i Łuczak, sp. j.,
 Poznań, ul. Piwna 1

The journal is registered and listed in the Polish and international database



Papers published in the

Combustion Engines

quarterly receive 20 points as stated by the Notification of the Minister of Science and Higher Education dated 31 July 2019.

Declaration of the original version

The original version of the Combustion Engines journal is the printed version.

Cover

I – DEUTZ TCG 7.8 H2 + KEYOU Technology (*foto. keyou.de*);
 background (Abstract colorful of night star – *pexels.com*)

IV – Land Cruiser 3.3 dm³ V6 diesel twin turbo engine
 (*foto. www.opposite-lock.com*)

Analyzing mechanical vibrations of an aircraft opposed piston engine

ARTICLE INFO

Received: 15 July 2021
 Revised: 3 August 2021
 Accepted: 11 August 2021
 Available online: 23 August 2021

The paper presents the results of the bench tests to measure mechanical vibrations of a new aircraft opposed piston engine with reciprocating pistons. The PLZ-100 engine is a three-cylinder, six-piston, two-shaft drive unit with a two-stroke diesel cycle. This type of engine is dedicated for powering light aircraft, e.g. autogyros. The tests were carried out on a test bench at the Lublin University of Technology. The engine was loaded with constant torque, for several fixed values of rotational speed of a crankshaft. The angle of the start of diesel injection was changed for each of the rotational speeds. The mechanical vibrations that accompanied the operation of this drive unit were recorded with three measurement transducers and a National Instruments conditioning system. Each of the transducers was mounted on a different axis of the engine. The signals were analyzed from their diagrams with the DIAdem software. The results were the diagrams of effective speed and vibration acceleration to conduct a vibration-acoustic evaluation of the PLZ-100, detect and prevent various types of defects or failures.

Key words: DIAdem, mechanical vibrations, opposed pistons, PZL-100, vibroacoustics

This is an open access article under the CC BY license (<http://creativecommons.org/licenses/by/4.0/>)

1. Introduction

Air transport is the transfer of people or goods by air. The main means of transport are aircraft in the categories of aeroplanes and helicopters. However, for individual transport, gyroplane are increasingly used [4, 5].

In contrast, internal combustion engines are commonly used to power aircraft, especially gyroplanes. The largest group includes piston aircraft engines. Compared to turbine engines, these engines are significantly cheaper and require less maintenance. Since their first use, aircraft engines have been continuously developed and modified. [3]. In addition, some manufacturers are attempting to use compression ignition engines or engines with reciprocating pistons to power aircraft [7, 8, 15].

Two-stroke engines with opposed pistons have been known since 1890. They are used to drive road vehicles, marine vessels and even aircraft. [9, 15]. Engines of this type made a comeback after Achatés Powers presented a three-cylinder engine with a capacity of 2.7 dm³. Originally, the power unit was dedicated to drive vans. The engine was first unveiled at the 2015 international exhibition in Detroit. Series production, on the other hand, is expected to start as early as 2024 [1].

The opposed piston engine has a number of advantages and disadvantages in comparison with turbine engines. The advantages include, for example, the lack of a cylinder head – the combustion chamber is limited by two moving piston bottoms (with reciprocating motion). In addition, there is no need for a valve drive, which limits the loss of mechanical power.

The main disadvantage of the classical piston engine, as compared to turbine engines, is the mechanical vibrations generated due to the cyclic working process and the design of the piston-crank system. The engine with its heat generation process is a direct source of such oscillations. As well as a drop in the generated power, the vibrations

may be transmitted to the structure of an aircraft or a vehicle, generating a high level of discomfort for the persons travelling in it [6, 9]. Compression-ignition engines generate a high compression ratio, which translates into the generation of variable torque at the crankshaft. The high level of torsional vibration results in changes in torque transmitted not only to the drivetrain but also to the engine mounting. Therefore, opposed cylinder arrangements and a two-stroke operating process are used to reduce mechanical vibrations [2]. Engines of this type have two opposing pistons always moving in the opposite direction (in one cylinder). These pistons are mechanically connected to their crankshafts, which are also mechanically connected. Therefore, relatively small loads are transferred to the engine block, which mitigates vibrations of the entire engine. Engines with reciprocating pistons are considered self-balancing, without the need for additional mechanisms [10, 11, 13].



Fig. 1. Model of crank-piston system of PZL-100 engine in CAD environment

This paper presents the results of bench testing for measuring the mechanical vibrations of an engine with opposed pistons. This is a two-stroke, three-cylinder aircraft engine called PZL-100. The engine has two crankshafts and six pistons, which move against each other, but the rotation

of the shafts is shifted in phase by 14 (Fig. 1). Understanding the level of vibration generated by the engine is essential for its correct installation and the selection of vibration isolators. Vibration analysis provides information about the technical condition of the engine during operation.

2. Research object and test stand

The object of the research was a prototype aircraft engine design with opposed pistons. The unit implements a two-stroke diesel cycle. The engine will be dedicated to propel gyroplanes. The PZL-100 engine has three cylinders and two opposed pistons in each of the cylinders. The engine generates 100 kW of mechanical power from a capacity of 1.5 dm³. The propulsion unit was developed as part of the Diesel Engine for Aircraft Propulsion project carried out at the Lublin University of Technology.

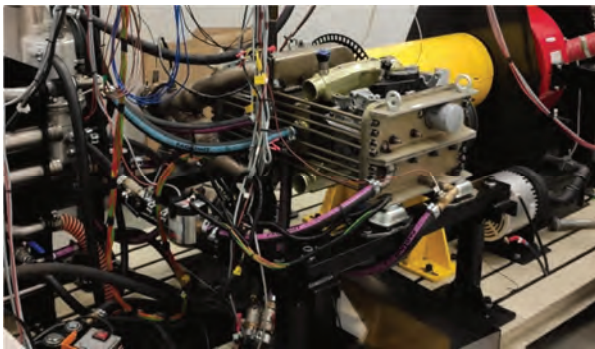


Fig. 2. PZL-100 engine on the test stand

A PZL 100 research engine installed on a brake stand in the Lublin University of Technology laboratory was tested within the scope of the research work (Fig. 2). This test stand was equipped with control and measurement systems allowing testing of the power unit under various operating conditions (load and crankshaft rotational speed). PCB sensors were used to record the vibration level – engine acceleration values (Table 1). Three sensors, for each engine axis, were installed on the engine block, as shown in Fig. 3.

Table 1. Features of the PCB352C03 sensor [14]

Parameter	Unit	Value
Sensitivity	mV/g	10 mV/g
Measurement range	g pk	±500
Broadband resolution	g rms	0.0005
Frequency range	Hz	0.5 to 10000
Sensing element	–	Ceramic



The measurement signals were collected and conditioned using a module from National Instruments. It is a system control and real-time data archiving device for advanced applications. The platform used has a built-in network interface, which enables remote download of data recorded by the device.

The tests were carried out for a constant torque load of 25 Nm on the drive unit. The engine drive shaft speed and injection start angle were changed during the tests. Figure 4

shows the location of all measurement points. In addition, for each accelerometer, individual signals for each of the three axes were recorded in real time.

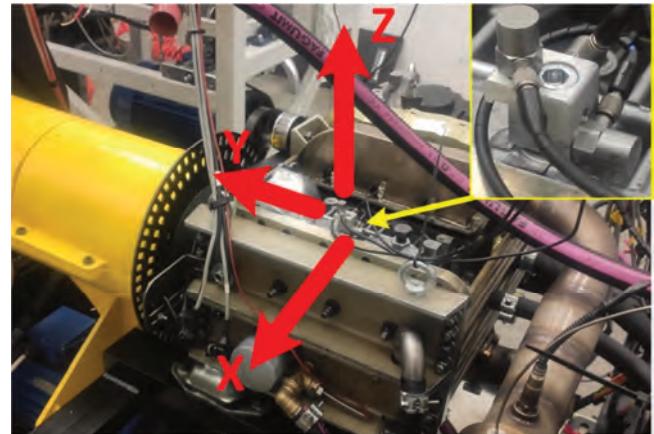


Fig. 3. Location of accelerometers on the test unit block (X-axis of cylinders, Y-axis of crankshaft, Y-vertical axis)

The conditioned signals were then archived and processed using DIAdem National Instruments software. In this software, the values of the signals from the vibration sensors were filtered, converted into units of velocity and acceleration, and the RMS values and RMS mean values were calculated. In addition, for a rotational speed of 3600 rpm, tests were carried out for torque values of: 50 and 75 Nm. This speed is the cruising speed of the PZL 100 aircraft engine.

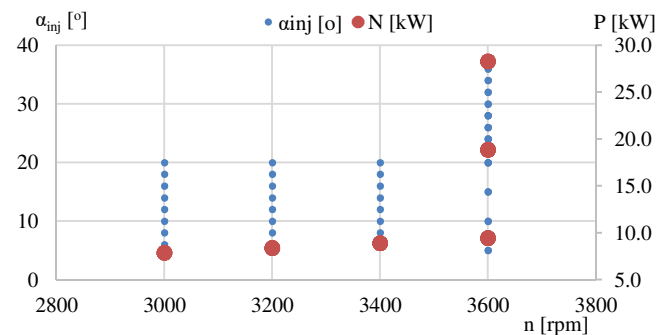


Fig. 4. Location of vibration test points on the PLZ-100 engine

3. Results of bench tests

For all measurement points during the vibration test of the PZL 100 engine, signals from accelerometers installed in three axes were recorded (Fig. 3):

- "X" – in the axis parallel to the axis of the cylinders (horizontal axis),
- "Y" – in the axis parallel to the crankshaft axis (horizontal axis, normal to the "X" axis),
- "Z" – in the vertical axis, normal to the "X" and "Y" axes".

Using DIAdem software from National Instruments, they were analysed. As a result of the analysis, the waveforms of the engine block vibration velocity, RMS velocity, acceleration and RMS acceleration were prepared. Example results were compiled for the engine crankshaft rotational speed corresponding to the cruising speed, n = 3600 rpm,

and the injection start angle $\alpha_{inj} = 5^\circ$ (load $M = 75 \text{ Nm}$) – Figs 9–13.

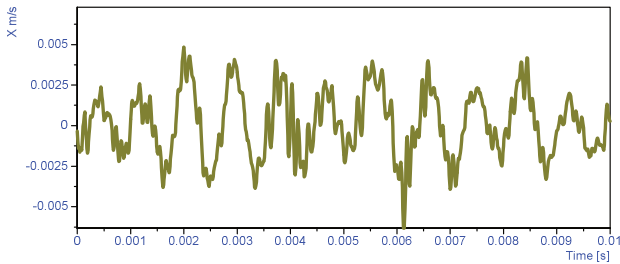


Fig. 5. The diagram of the vibration velocity in the X axis; $n = 3600 \text{ rpm}$, $M = 75 \text{ Nm}$, $\alpha_{wtr} = 5^\circ$

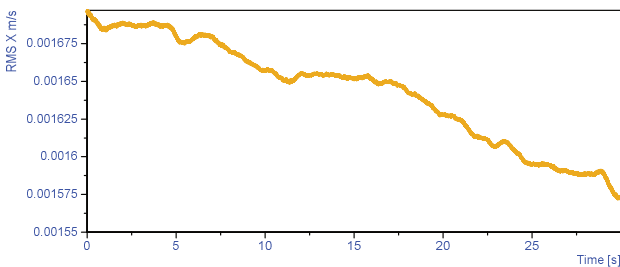


Fig. 6. The diagram of the effective RMS velocity of vibrations along the X axis; $n = 3600 \text{ rpm}$, $M = 75 \text{ Nm}$, $\alpha_{wtr} = 5^\circ$

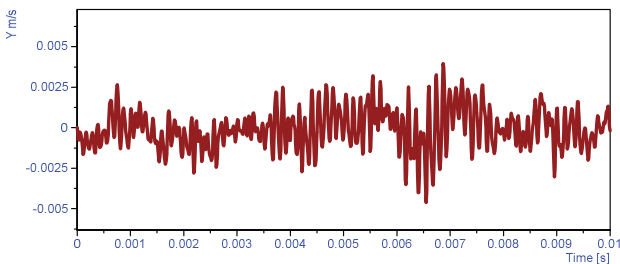


Fig. 7. The diagram of the vibration velocity in the Y axis; $n = 3600 \text{ rpm}$, $M = 75 \text{ Nm}$, $\alpha_{wtr} = 5^\circ$

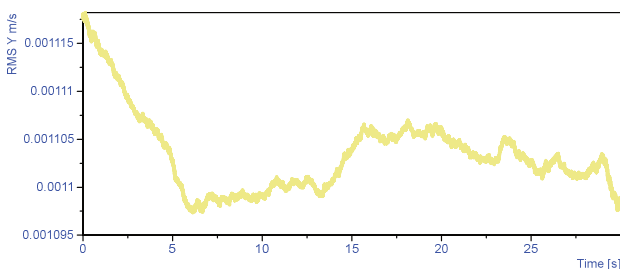


Fig. 8. The diagram of the effective RMS velocity of vibrations along the Y axis; $n = 3600 \text{ rpm}$, $M = 75 \text{ Nm}$, $\alpha_{wtr} = 5^\circ$

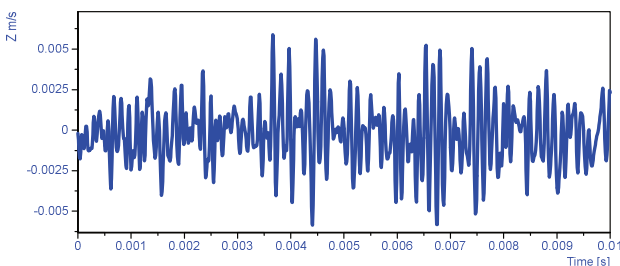


Fig. 9. The diagram of the vibration velocity in the Z axis; $n = 3600 \text{ rpm}$, $M = 75 \text{ Nm}$, $\alpha_{wtr} = 5^\circ$

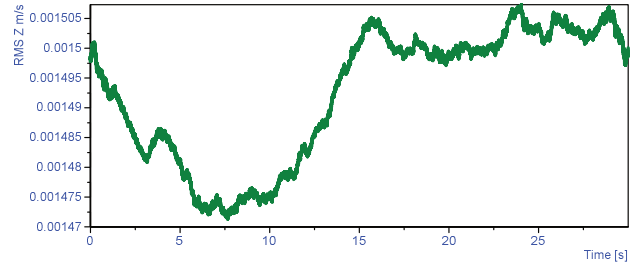


Fig. 10. The diagram of the effective RMS velocity of vibrations along the Z axis; $n = 3600 \text{ rpm}$, $M = 75 \text{ Nm}$, $\alpha_{wtr} = 5^\circ$

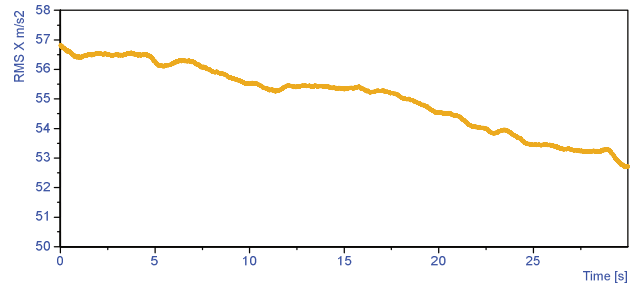


Fig. 11. The diagram of the effective RMS acceleration of vibrations along the X axis; $n = 3600 \text{ rpm}$, $M = 75 \text{ Nm}$, $\alpha_{wtr} = 5^\circ$

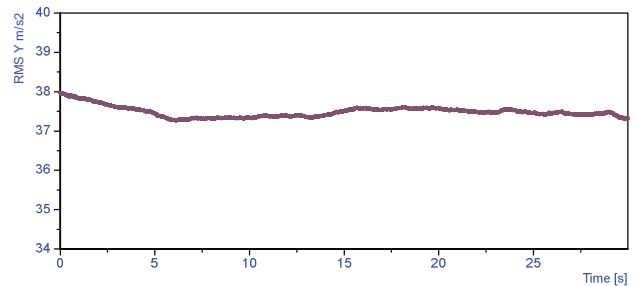


Fig. 12. The diagram of the effective RMS acceleration of vibrations along the Y axis; $n = 3600 \text{ rpm}$, $M = 75 \text{ Nm}$, $\alpha_{wtr} = 5^\circ$

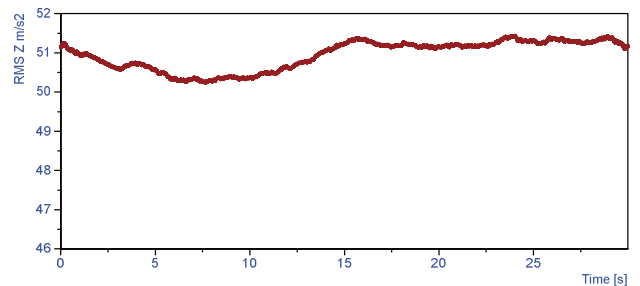


Fig. 13. The diagram of the effective RMS acceleration of vibrations along the Z axis; $n = 3600 \text{ rpm}$, $M = 75 \text{ Nm}$, $\alpha_{wtr} = 5^\circ$

4. Summary

As a result of the research work carried out and the analysis of their results, the diagrams of mechanical vibrations of the PLZ-100 engine were prepared. The engine was conditioned by bench tests for a constant load of the crankshafts with a torque of 25, 50 and 75 Nm (for power: 7.8, 8.4, 8.9, 9.5, 18.9 and 28.7 kW). The rotational speed of the engine crankshafts was changed during the tests. For each speed the fuel injection start angle was changed and mechanical vibrations were recorded in three engine axes (Fig. 3) – in the axis along the crankshafts, cylinders and in the vertical axis.

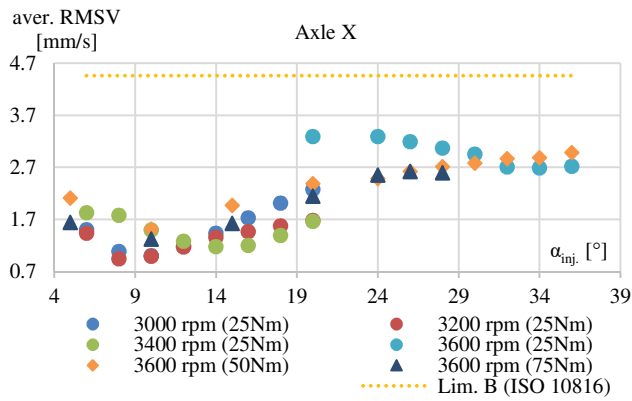


Fig. 14. Average RMS value of the vibration velocity depending on the injection angle for the X axis (25, 50 and 75 Nm)

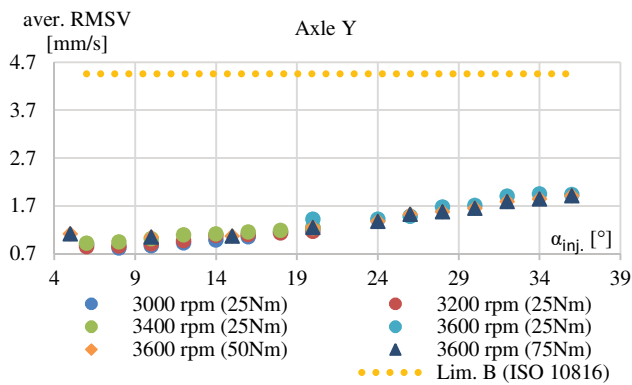


Fig. 15. Average RMS value of the vibration velocity depending on the injection angle for the Y axis (25, 50 and 75 Nm)

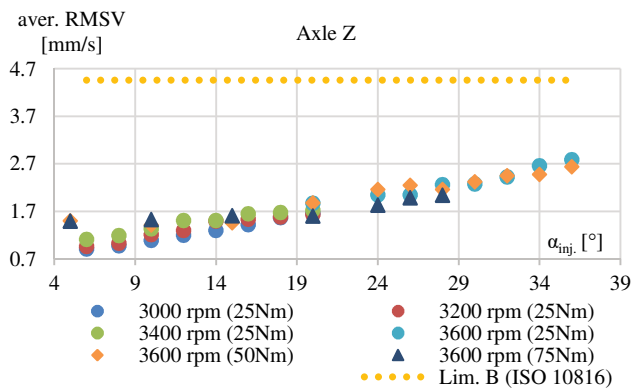


Fig. 16. Average RMS value of the vibration velocity depending on the injection angle for the Z axis (25, 50 and 75 Nm)

The measurement signals from the accelerometers were then processed using DIAdem software. In this software, the signals were subjected to, among others, de-noising (filtering) and integration. As a result of this analysis, the waveforms of velocity and acceleration values of mechanical vibrations and average RMS values for all measuring points of the research engine were obtained (Figs 14–16).

Nomenclature

CAD Computer Aided Design
 RMS Root Mean Square

The results obtained in this way were compared with the legal regulations concerning the measurement of mechanical vibrations in technical machines. The representative of such legal act is the In of machine *ISO 10816-6 – Mechanical vibration – Evaluation vibration by measurements on non-rotating parts*. The presented research engine PZL-100 falls under *Part 6: Reciprocating machines with power ratings above 100 kW*. Figure 17 shows the range of acceptable values of mechanical vibrations for reciprocating engines according to ISO 10816-6. Furthermore, this standard specifies general conditions and procedures for the measurement and evaluation of vibrations, using measurements performed on non-rotating and non-reversing parts of reciprocating machines. It applies to rigidly or resiliently mounted reciprocating machinery with a rated power exceeding 100 kW. The general assessment criteria presented apply to both in-service monitoring and acceptance testing. They are also used to ensure that the vibrations of the machine do not have a negative effect on equipment directly mounted on the machine. The standard divides reciprocating machinery into 7 classes, depending on engine power, displacement, design or crankshaft speed (Fig. 17). According to the standard, the priority for piston engines is the average RMS value for the displacement speed of the engine block, while internal combustion piston engines are placed between class 5 and 7.

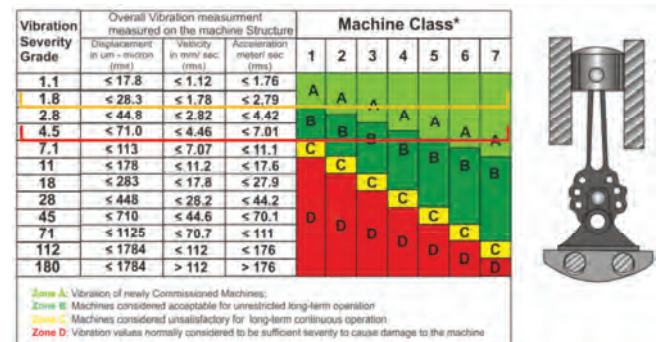


Fig. 17. Range of mechanical vibration values for internal combustion engines depending on engine class – ISO 10816-6 [12]

With reference to ISO 10816 standard, the PZL-100 engine can be qualified to A/B class (Fig. 17), that is the machine suitable for unlimited long-term exploitation – none of the measurement points of vibration velocity in different dynamic states of the engine has exceeded the value of 4.46 mm/s.

Acknowledgements

This work has been realized in cooperation with The Construction Office of WSK "PZL-KALISZ" S.A. and is part of Grant Agreement No. POIR.01.02.00-00-0002/15 financed by the Polish National Centre for Research and Development.

Bibliography

- [1] BROOKE, L. Advancing the OP engine on three fronts. *SAE International*. 2021. www.sae.org
- [2] CHANGMING, H., SICHUAN, X. The investigation of self-balanced property and vibration on the particular crankshaft system for an opposed piston engine. *SAE Technical Paper* 2016-01-1768. 2016. <https://doi.org/10.4271/2016-01-1768>
- [3] CZARNIGOWSKI, J., WENDEKER, M., JAKLIŃSKI, P. et al. Model of injection system for SI radial aircraft engine. *SAE Technical Paper* 2007-01-1903. 2007. <https://doi.org/10.4271/2007-01-1903>
- [4] CZYŻ, Z., KARPIŃSKI, P., SKIBA, K. CFD investigation of the aerodynamic characteristics of the autogyro with a double tail stabilizer. *Journal of Physics: Conference Series*. 2021, **1736**, 1-8. <https://doi.org/10.1088/1742-6596/1736/1/012045>
- [5] CZYŻ, Z., WENDEKER, M., RACZYŃSKI, R. Koncepcja hybrydowego statku powietrznego z napędem wielowirnikowym. *Logistyka*. 2014, **6**, 2936-2945.
- [6] GĘCA, M., WENDEKER, M., LITAK, G. Combustion variability and uniqueness in cylinders of a large power radial engine. *Journal of Vibroengineering*. 2012, **14**(2), 582-590.
- [7] GRABOWSKI, Ł., PIETRYKOWSKI, K., KARPIŃSKI, P. Energetic analysis of the aircraft diesel engine. *MATEC Web of Conferences*. 2019, **252**, 1-6. <https://doi.org/10.1051/mateconf/201925205012>
- [8] GRABOWSKI, Ł., SOCHACZEWSKI, R., BARAŃSKI, G. et al. Research into a fuel supply system in the aircraft diesel opposed engine. *2020 IEEE 7th International Workshop on Metrology for AeroSpace (MetroAeroSpace)*. 2020, 620-624. <https://doi.org/10.1109/MetroAeroSpace48742.2020.9160096>
- [9] HOFBAUER, P. Opposed piston opposed cylinder (OPOC) engine for military ground vehicles. *SAE Technical Paper* 2005-01-1548. 2005. <https://doi.org/10.4271/2005-01-1548>
- [10] HUO, P.W., QIU, J.S. Analysis of self-balance characteristics of OPOC engine. *Advanced Materials Research*. 2011, **211-212**, 93-96. <https://doi.org/10.4028/www.scientific.net/AMR.211-212.93>
- [11] MAGRYTA, P., GĘCA, M. FEM analysis of piston for aircraft two stroke diesel engine. *MATEC Web of Conferences*. 2019, **252**, 1-6. <https://doi.org/10.1051/mateconf/201925207004>
- [12] Mechanical vibration ISO 10816. *Online Browsing Platform* <http://www.iso.org>. 2021.
- [13] MIKALSEN, R., ROSKILLY, A.P. A computational study of free-piston diesel engine combustion. *Applied Energy*. 2009, **86**(7-8), 1136-1143. <https://doi.org/10.1016/j.apenergy.2008.08.004>
- [14] PCB, PiezoElectronics. Model 352C03 2021. <http://www.pcb.com>. 2021.
- [15] PIRAULT, J.P., FLINT, M. Opposed piston engines evolution, use and future applications. *Publisher SAE International*. 2010.

Michał Biały, MEng. – Faculty of Technical Sciences, Pope John Paul II State School of Higher Education in Biała Podlaska.

e-mail: m.bialy@dydaktyka.pswbp.pl



Łukasz Grabowski, DEng. – Faculty of Mechanical Engineering at the Lublin University of Technology.

e-mail: l.grabowski@pollub.pl



Bartłomiej Skórzyński, MEng. – general designer in WSK „PZL-KALISZ” S.A.

e-mail: bartlomiej.skorzynski@wsk.kalisz.pl



Grzegorz Barański, DEng. – Faculty of Mechanical Engineering at the Lublin University of Technology.

e-mail: g.barański@pollub.pl



Adam Majczak, MEng. – Faculty of Mechanical Engineering at the Lublin University of Technology.

e-mail: a.majczak@pollub.pl



Research on the effect of the effective microorganisms, silver solution and colloidal nanosilver addition on the engine oil base number (TBN)

ARTICLE INFO

Received: 26 June 2021

Revised: 5 July 2021

Accepted: 9 July 2021

Available online: 26 July 2021

In the article, base number as a parameter characterizing the washing and dispersing abilities of engine oil were characterized. Next, the influence of additives enriching engine oils on the natural environment was described. In the further part of the article, the research methodology, applied oil samples with additives of effective microorganisms and silver solution, both for fresh oil and used oil were presented. In addition, the measuring test stand with instrumentation and measuring device was shown. In the main part of the article base number value for fresh and used oil compared to oils with the addition of microorganisms and a solution of silver and colloidal silver were described. Next the analysis of the influence of these additives on the base number value was made. The article was completed conclusions.

Key words: petroleum products, base number value, ennobling additives, effective microorganisms, silver solution

This is an open access article under the CC BY license (<http://creativecommons.org/licenses/by/4.0/>)

1. Introduction

Crude oil, or rock oil, is the most important hydrocarbon raw material for the production of valuable industrial products, such as gasoline, diesel oils, lubricating oils, paraffin. Among hydrocarbon products, lubricating oil, diesel and biodiesel (blends of fatty acid methyl esters with diesel fuel) that are used in diesel engines are the most susceptible to microbial degradation. Such a decomposition occurs even in the case of properly operated engines. The condition for the growth and development of numerous - bacteria and fungi in these products is the presence of organic carbon compounds and water [3, 6]. Hydrocarbon products are characterized by the ease of adsorption of water particles at the interface, hence it is a common pollutant. Many species of bacteria and fungi have the ability to grow in petroleum products that are a source of carbon and energy. Therefore, the life activity of microorganisms causes the decomposition of hydrocarbons and refining additives and the release of water, sulphur compounds, surface-active substances to the fuel. The result is changes in the chemical composition of the fuel and the value of some physical parameters, such as boiling point, base number or viscosity.

In this study the impact of the effective microorganisms, silver solution and colloidal nanosilvers addition on the fresh and used engine oil base number was analyzed [4].

2. The base number as a parameter characterizing the washing and dispersing abilities of engine oil

Modern engine oils are technologically advanced products that meet stringent requirements in terms of physico-chemical properties and actual performance.

The parameters characterizing lubricating oils include, among others, viscosity, volatility describing the tendency of an oil to evaporate at high temperatures. Then it is the Total Base Number (TBN) of the so-called reserve of alkalinity in the oil (TBN is the ability of the oil to neutralize the acid products of combustion). The alkalinity buffer is used to neutralize the acids formed as a result of oxidation processes, especially fuel combustion, especially in the case

of using low-quality fuel with high sulfur content and oil oxidation. The amount of acid in the oil is described by another number known as the Total Acid Number (TAN), measured according to ASTM D 664. As the oil ages, the TBN value gradually decreases as the TAN increases. At some point, these values become the same, which is known as TBN/TAN point crossover (Fig. 1). In this situation, the protection of the engine against corrosion deteriorates significantly and an oil change is necessary. Unless poor quality fuel is used and oil change intervals are adhered to, it is unlikely that there will be a TBN/TAN break-off point. In most cases, particle contamination, not acidity, is the main cause of an oil change [2, 10].

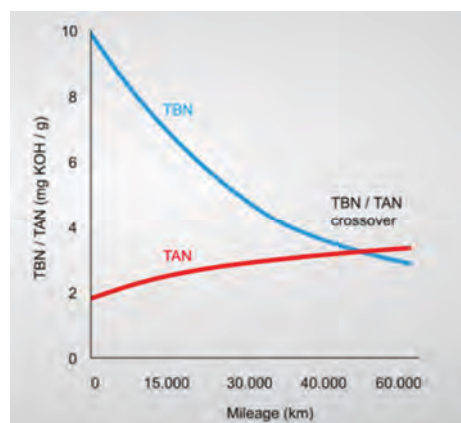


Fig. 1. Change in the value of TBN and TAN depending on the oil mileage [1]

3. The impact of additives enriching engine oils on the natural environment

The preparation of high-quality engine oil is no longer possible just by using advanced base oils. Contemporary lubricating oils consist of two basic groups: base oils and a package of enriching additives.

The use of an oil base and refining additives of petroleum origin in the content of lubricants is associated with a negative impact on health and the environment [5].

Lubricating oils with additives cause serious damage to soils, due to the multistep physicochemical processes leading to a change in the forms and distribution of organic matter, in the range of carbon, water, nitrogen, and phosphorus. As soil is an environment for a variety of microorganisms and higher living organisms, its contamination with petroleum-based lubricants becomes hazardous and a detrimental effect on biological life may occur. The proper functioning of the ecosystem may be disturbed. Mineral oil can clog pores in the soil, resulting in reduced aeration and water infiltration. The presence of petroleum compounds may reduce or limit the permeability of soils, and, consequently, cause the degradation of soils due to oxygen deficit [1, 7].

One of the additives are biocides, which are pesticides used, inter alia, to combat or limit the growth of microorganisms in petroleum products. They should have a broad spectrum of activity on various groups of microorganisms, dissolve in the aqueous and organic phase, be effective at low concentrations and efficient in use. It is very important to dose the biocides correctly. Too small amounts may result in the immunization of microorganisms and, consequently, the use of ever higher doses to ensure the expected effectiveness. It is not without its impact on the natural environment, because most biocides also destroy beneficial organisms and cause unfavorable changes in the composition of microorganisms. Despite the number of benefits resulting from the use of biocides, there are currently strong tendencies to limit their use [6]. They are caused by the fear of the harmful effects of these highly concentrated substances on the environment [8, 9].

One way of combating microorganisms with regard to environmental aspects can be effective microorganisms (EM), that is, a complex of cultures of beneficial naturally occurring microorganisms, genetically unmodified, remaining in a state of equilibrium, not only harmless to humans, animals and the environment, but even necessary for their proper functioning.

Another environmentally friendly compound is nanosilver, i.e. microscopic particles. Thanks to the fragmentation of silver into nanoparticles with a size of 1 to 5 nm, the effectiveness of using the bactericidal, fungicidal and virucidal properties of silver has increased incomparably. Crushed silver to nanoparticles has a disproportionately larger active surface, and thus a previously unattainable biocidal potential. The effectiveness of nanosilver includes the elimination of over 99.99% of bacteria, fungi, viruses and mold. Nanosilver is able to attach to bacterial cell membranes and block their production of enzymes necessary for reproduction and growth.

Therefore, as part of research work with the use of the effective microorganisms and silver compounds, their influence on, among others, the base number of lubricating oil was investigated.

4. The research methodology

In the conducted tests, the base number of engine oil was measured. For this purpose the Titrator TitroMatic 2S has been used (Fig. 2).

TitroMatic 2S titrators are equipped with two exchangeable burettes. Additionally, the titrator used for the tests is equipped with a peristaltic pump for automatic dosing of

reagents, mediating in the analysis process and automatic determination of the sample volume before titration.

In this titrator, the movement of the piston of the digital glass burette (piston) is provided by a precise stepping motor with a resolution of 1/40000 steps. For a 10 ml burette, the maximum dispensing resolution is 0.00025 ml and ensures a real minimum dispensing accuracy of 1 μ l (0.001 ml). The dosing precision of the titrator is compared with the accuracy of the analytical balance [11].

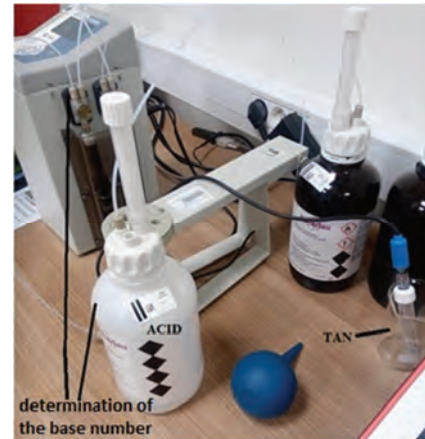


Fig. 2. Titrator TitroMatic 2S device prepared to determine the base number

The tests were carried out using samples of the 5W30 fresh and used motor oil according to the ASTM D 2896 standard. Each sample was tested three times and the final result is the mean of these measurements.

One of the additives which improve the properties of oil are effective microorganisms. They are specially selected the smallest organisms on Earth. It is a composition of 81 different strains of aerobic and anaerobic microorganisms, incl. lactic acid bacteria, yeast, photosynthetic bacteria and actinomycetes. This technology was developed by Teruo Higa, Professor of Horticulture at the Agricultural Academy of Ryukyus University in Okinawa, Japan. In trade, effective microorganisms exist in liquid form and as ceramic tubes. EM ceramic tubes are clay fermented with effective microorganisms and then fired under special anaerobic conditions. Effective microorganisms preserved in a ceramic form are characterized by the fact that they are resistant to high temperatures and maintain their beneficial properties for a long time. Effective microorganisms have a pH of 3.5.

The second addition was non-ionic and ionic silver. Non-ionic silver, i.e. colloidal silver (research studies used silver with a concentration of 25 ppm and pH 6–8). Colloidal silver is 80% of silver particles, while the remaining 20% are silver ions. It has a yellow color because the silver particles that are dispersed in the water block the light passing through them. Ionic silver is silver solution (research studies used silver with a concentration of 37 ppm and pH 6–8). Ionic silver is as transparent as water. Ionic silver contains 90% silver ions and only about 10% silver particles. As 90% of the particles are silver ions, a more appropriate name is "silver solution".

Samples have the addition of the effective microorganisms in liquid form in the amount of 2.5 ml and 5 ml and

ceramic tubes in the amount of 3 pieces and 6 pieces. In addition, silver solution and colloidal nanosilver in the amount of 2.5 ml and 5 ml to fresh and used oil were added. In addition, fresh oil and used oil without any additives were also tested to compare the base number obtained.

In order to measure the base number, the device was first calibrated by recognizing buffer solutions with known pH values. After calibrating the device, a titration was made. First, a blank test was made, pouring 100 ml of solvent Mixture T.A.N. After this test, 20 ml of oil of known weight was poured in. After these activities, electrometric titration with hydrochloric acid solution HCl was carried out. After the end of the titration, the weight of the tested oil was entered and then the base number in mg/KOH was obtained, which was determined to be equivalent in terms of acid neutralization ability to the alkaline additives contained in 1 g of improved lubricating oil.

5. Results and analysis of tests

In order to analyse oil base number changes for each samples, the test results are presented in the form of graphs in Figs 3–6. These graphs show different values of the base number after adding to fresh and used oil effective microorganisms in liquid form (2.5 ml and 5 ml per 100 ml of oil) and in the form of ceramic tubes (3 pieces and 6 pieces with a diameter of 9 mm and a height of 11 mm for 100 ml of oil). In addition, silver solution and colloidal nanosilver were added to fresh and used oil in the same proportions as for effective microorganisms (2.5 ml and 5 ml per 100 ml of oil).

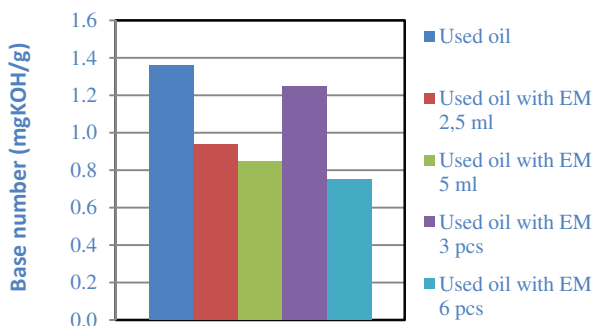


Fig. 3. Base number of used oil and used oil with EM in liquid form and ceramic tubes

Analysing the above results, it can be seen in Fig. 3, that for used oil the base number is 1.358 mgKOH/g, while the addition of the effective microorganisms to the oil in the amount of 2.5 ml and 5 ml causes the base number to drop to 0.937 mgKOH/g and 0.844 mgKOH/g, respectively, which means more greater deterioration of oil properties. On the other hand, adding microorganisms to the oil in the form of ceramic tubes in the amount of 6 pieces also reduces the base number to the value of 0.749 mgKOH/g, which is not favorable for the oil, but for the amount of 3 pieces of these tubes, the smallest decrease occurs, to 1.250 mgKOH/g. In general, the addition of any amount of the effective microorganisms to the used oil deteriorates the properties of the oil, reducing the already low base number.

In the case of adding 2.5 ml of colloidal nanosilver to the oil, a slight decrease in the base number to 1.350

mgKOH/g can be observed (Fig. 4), i.e. it can be concluded that this amount of silver addition neither improved nor deteriorated the properties of the oil. It looks different when adding 5 ml of colloidal nanosilver, because in this case there was a slight increase in this number to 1.402 mgKOH/g. As for silver solution, this additive significantly reduced the base number, both with the addition of 2.5 ml and 5 ml, to 1.037 mgKOH/g and 1.199 mgKOH/g, respectively, which means that it adversely affected the properties of the oil. From this it follows that adding any additives to the used oil does not improve the properties of the oil, and even makes them worse. The oil behaves as if it were the higher mileage than it actually is.

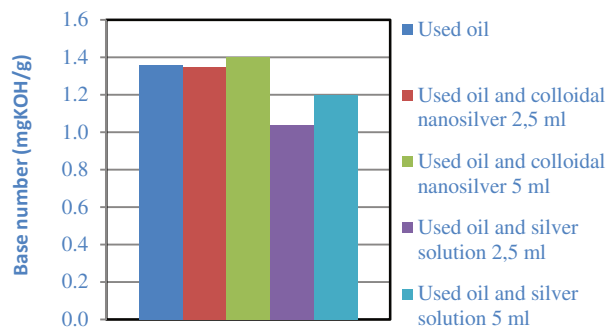


Fig. 4. Basenumber of usedoil and usedoil with colloidalnanosilver and silversolution

The base number for fresh oil (Fig. 5) is 3.907 mgKOH/g, while the addition of 2.5 ml and 5 ml of the effective microorganisms in liquid form reduces the base number to 3.606 mgKOH/g and 3.444 mgKOH/g, respectively. As a result, such oil will require earlier replacement with a new one, as its degradation will occur faster. The higher the amount of this supplement, the more the acid value is reduced.

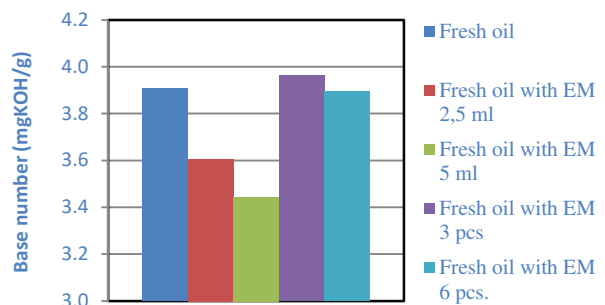


Fig. 5. Base number of fresh oil and fresh oil with EM in liquid form and ceramic tubes

The addition of EM to fresh oil in the form of ceramic tubes causes an increase of the base number to the value of 3.962 mgKOH/g with the addition of 3 pieces of ceramic tubes, while 6 pieces basically does not change the value of the base number. In general, it is worth adding EM ceramic tubes to the fresh oil and see how it reduces this number during the operation of the combustion engine.

The addition of fresh colloidal nanosilver in the amount of 2.5 ml and 5 ml to the oil resulted in a significant reduction of the base number to the value of 3.604 mgKOH/g

and 3.7551 mgKOH/g, respectively, while the addition of silver solution in the same amount as colloidal nanosilver also reduces the base number, thus together to a value of 3.479 mgKOH/g and 3.731 mgKOH/g.

In this case, it should be noted that for both silver solution and colloidal nanosilver additions, a greater decrease in the base number occurs with a smaller amount of this additive, a greater amount caused a smaller decrease in the base number. Therefore, it is worth checking the addition of silver ions to fresh oil with even more added to the oil than in previous studies.

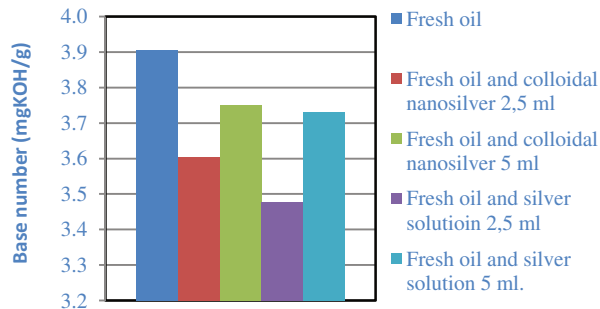


Fig. 6. Base number of fresh oil and fresh oil with colloidal nanosilver and silver solution

6. Conclusion

The aim of the research was to test the effect of the addition of the effective microorganisms and silver solution and colloidal silver on the base number of used and fresh oil. Adding any amount of EM to the used oil worsens the properties of the oil, reducing the already low base number,

although for three pieces of ceramic tubes the smallest decrease occurs.

The addition of colloidal nanosilver and silver solution to the oil also does not favorably affect the value of the base number. Only the addition of colloidal silver in the amount of 5 ml causes a slight increase in the base number, but it is not significant enough to improve the properties of the oil. In general, adding any additives to the used oil does not improve the properties of the oil, and even causes them to deteriorate. The oil has parameters as if it were the higher mileage than it actually is.

The situation is different in the case of adding EM and silver to fresh oil, because the addition of effective microorganisms in the form of a liquid reduces the base number, which will cause such oil to require an earlier replacement with a new one because its degradation will occur faster.

The greater the amount of this addition, the number of base lowers more. On the other hand, adding EM to fresh oil in the form of ceramic tubes increases the base number of fresh oil, which may have an impact on the reduction of this number during the operation of the engine. Too many tubes does not have a positive effect on the value of this number.

Moreover, for the addition of silver solution and colloidal nanosilver to the fresh oil, a greater decrease in the base number occurs with a smaller amount of this additive, a greater amount resulted in a smaller decrease in the base number. Therefore, it is worth checking the addition of silver ions to fresh oil with even more added to the oil than in previous studies.

Nomenclature

TBN total base number
TAN total acid number
EM effective microorganisms

HCl hydrochloric acid
KOH potassium hydroxide

Bibliography

- [1] ABOSEDE, E.E. Effect of crude oil pollution on some soil physical properties. *IOSR Journal of Agriculture and Veterinary Science*. 2013, **6**, 14-17. <https://doi.org/10.9790/2380-0631417>
- [2] DENYER, S.P. Mechanisms of action of biocides. *International Biodeterioration*. 1990, **26**, 89-100. [https://doi.org/10.1016/0265-3036\(90\)90050-H](https://doi.org/10.1016/0265-3036(90)90050-H)
- [3] GAYLARDE, C.C., BENTO, F., KELLEY, J. Microbial contamination of stored hydrocarbon fuels and its control. *Revista de Microbiologia*. 1999, **30**, 1-10. <https://doi.org/10.1590/S0001-37141999000100001>
- [4] KLOFUTAR, B., GOLOB, J. Microorganisms in diesel and in biodiesel fuels. *Acta Chimica Slovenica*. 2007, **54**, 744-748.
- [5] MARKOWSKI, J. Dodatki uszlachetniające do olejów napędowych. *Nafta-Gaz*. 2017, **3(73)**, 208-213. <https://doi.org/10.18668/NG.2017.03.09>
- [6] PTAK, S., JAKÓBIEC, J. Ropa naftowa jako główny surowiec energetyczno-przemysłowy. *Nafta-Gaz*. 2016, **6(72)**, 451-460. <https://doi.org/10.18668/NG.2016.06.09>
- [7] RAMADAN, K.M.A., ABDEL AZEIZ, A.Z., HASSANIEN, S.E. et al. Biodegradation of used lubricating and diesel oils by a new yeast strain *Candida viswanathii* KA-2011. *African Journal of Biotechnology*. 2012, **11**, 14166-14174. <https://doi.org/10.5897/AJB12.1339>
- [8] ŻÓŁTY, M. Wpływ biocydu wchodzącego w skład pakietów dodatków uszlachetniających do olejów napędowych na kompatybilność z olejami silnikowymi. *Nafta-Gaz*, 2015, **4(71)**, 242-249.
- [9] AMSOIL, www.amsoil.com/newsstand/articles/what-is-total-base-number/
- [10] BIZOL, www.bizol.com/fr/produits/recherche-developpement/detail-view/news/tbn-whats-in-it-for-me
- [11] Labindex, www.labindex.pl/titraty/titraty_potencjometryczne/titraty_titromatic_s.html

Rafał Krakowski, DEng. – Faculty of Marine Engineering, Gdynia Maritime University.
e-mail: krakowski.r@interia.pl



A conceptual design and numerical analysis of the mixerless urea-SCR system

ARTICLE INFO

Received: 14 July 2021
Revised: 26 July 2021
Accepted: 26 July 2021
Available online: 18 August 2021

In the present study, an innovative design of a urea-selective catalytic reduction (SCR) system without conventional mixing elements was developed. The aim was to obtain a high degree of urea decomposition, and uniform ammonia distribution at the inlet to the catalyst, while minimising the liquid film deposition and keeping the compact design. The concept of the design was based on creating high turbulence and elongating the flow paths of the droplets. The design was verified through a series of numerical simulations based on the Reynolds-averaged Navier-Stokes (RANS) approach and a discrete droplet model (DDM) spray representation. The analysis included various operating conditions as well as subcooled and superheated sprays. A uniform ammonia distribution was achieved regardless of the operating points and spray properties. Additionally, in the case of a flash-boiling injection, a further reduction of the wall film was observed.

Key words: NO_x , SCR, selective catalytic reduction, wall film, CFD

This is an open access article under the CC BY license (<http://creativecommons.org/licenses/by/4.0/>)

1. Introduction

Current-day emission standards for vehicles impose strict limits of exhaust gas pollutants, inter alia, nitrogen oxides. Selective catalytic reduction is one of the most efficient methods of NO_x reduction. A urea-water solution (UWS) is sprayed into the flow of the exhaust gases, and then the urea is decomposed to ammonia (NH_3), required for further NO_x conversion. Furthermore, diesel engines' exhaust systems occupy a relatively large space and therefore, the maximum reduction of the size is highly desirable [13, 15]. Modern design concepts comprise close-coupled layouts that due to the minimised distance from the engine enable a higher temperature to be attained in an aftertreatment system, and thus, an increased efficiency of the catalytic conversion. These systems combine diesel oxidation catalysts (DOC), UWS dosing and mixing devices, and selective catalytic reduction coated on particulate filters (SCRoF). However, a reduction in size causes shortening of the UWS droplets' flow paths and residence time, which adversely affects ammonia generation [3, 15, 17]. Efficiency of SCR is highly dependent on the uniformity of the ammonia distribution at the inlet to the catalyst [10, 21]. Static mixing devices are commonly applied to enhance UWS mixing and decomposition, and subsequently to provide a more uniform distribution of ammonia. Nonetheless, significant compression of a system and a presence of mixing elements favour liquid film deposition by spray-wall interactions. Low temperature in the system walls may decrease the UWS temperature below that required for urea crystallisation and make the liquid film turn into solid deposits [20, 26, 27]. The occurrence of deposits is highly undesirable as it leads to a gradual blockage of the SCR, as well as adversely influences the mixing process [29]. On the other hand, the interactions of the droplets with the walls may have a positive effect via the occurrence of additional droplet breakup [23]; consequently leading to a re-

duced droplet size, improved dispersion and urea decomposition as well as enhanced mixing [26, 28].

Another challenge for SCR systems is adaptability to diverse exhaust conditions [21] and spray properties. As shown in [11], one of the methods to significantly improve SCR performance is to superheat the UWS prior to the injection and hence, obtain different spray parameters. This phenomenon, also known as flash boiling, reduces the size of the droplets, increases the spray angle, improves the droplets' dispersion and lowers the particles' velocity [3, 30]. Consequently, water evaporation from the UWS is intensified and the rate of urea decomposition is increased. Therefore, the generation of ammonia and its uniformity are improved, and the liquid film formation is reduced [11].

Numerical and experimental analyses of urea-mixing devices have been presented in multiple studies, most of which were aimed at enhancing ammonia generation and its distribution in compact-sized systems, as well as mitigating the risk of solid deposit formation. Park et al. [24] numerically determined the advantage of turbulent and swirling flow in the mixing process of water spray instead of UWS. The swirl-type mixers enabled the creation of large-scale vortices and therefore, more uniform water distribution than in the case of the small-scale vortex mixer. The authors pointed out the importance of the distance available for the droplets to ensure proper UWS mixing in view of the favourable effect of large-scale vortices. Tan et al. [28] numerically investigated the impact of static mixers on turbulent mixing, interactions of UWS droplets with the walls, and water evaporation. The analysis showed a significant acceleration of urea decomposition due to turbulence and swirling motion, as well as to droplet breakup caused by their collisions with mixing elements. The latter led to a reduction of droplet size and hence the time required for water to evaporate. Kapusta et al. [11] examined the influence of the injection of subcooled and superheated UWS sprays on ammonia uniformity and liquid film deposition in

an SCR system by numerical analysis. The subcooled spray injection was characterised by droplet breakup due to spray impingement on the mixer blades. The injection angle played a significant role since the superheated UWS spray was strongly deflected when the gas mass flow rate was relatively high, and hence the droplets interacted intensively with the system's wall. Nonetheless, according to their results, even when increased interactions occurred, a lower film deposition was achieved as a consequence of flash boiling. The aforementioned spray blowing caused deterioration of the ammonia distribution. Modification of the injection angle prevented the superheated spray from intensive contact with the system's wall and improved the uniformity of the ammonia distribution. However, this process deteriorated the NH_3 distribution when the subcooled spray was deployed again. Thus, the authors concluded that the injector location and inclination may require careful adjustment depending on operating conditions. The application of a superheated spray along with an appropriate injection angle led to an increased uniformity of ammonia distribution and a significant reduction of liquid film, which minimises the risk of solid deposit development. The importance of the injector's location and its inclination in the aftertreatment system with regard to a solid deposit formation was pointed out by Li et al. [19]. Those parameters were particularly meaningful in the cases of relatively low flow temperatures. Otherwise, the general mixer design was of primary importance. A numerical analysis from Zhang et al. [29], partly validated by experiments, proved that certain implementation of swirling and turbulent flow enables high levels of both ammonia uniformity and velocity uniformity right after the SCR inlet. This required the application of complex mixing elements that were aimed to provide flow changes and droplet breakup through splashing. Sadashiva Prabhu et al. [25] indicated the importance of the mixing zone length and location of the injector, which if properly defined, may provide a higher amount of NH_3 at the catalyst inlet. Their numerical analysis pointed out the advantages of an increased spray angle, namely enhanced evaporation of water and a rise in ammonia concentration. Additionally, according to the authors, an optimal angle may lead to a reduction of liquid film deposition; while in general, wider spray plumes result in increased film formation. It is to be noted that increased spray angles are one of the consequences of flash-boiling injections. Numerical and experimental analysis conducted by Cho et al. [5] comprised multiple mixer layouts and decomposition pipes in order to determine the uniformity of the ammonia distribution and the efficiency of the NO_x conversion in the urea-SCR system. The results proved that the application of static mixers composed of blades significantly enhances ammonia distribution and UWS decomposition due to turbulent vortices. The turbulent flow was particularly advantageous in terms of SCR performance if it occurred close to the inlet of the catalyst. Moreover, the length of the mixing system (decomposition pipe) played a crucial role. A relatively short length impaired the UWS decomposition and mixing, while an excessively long decomposition pipe was exposed to heat loss and reduced the efficiency of the NO_x conversion in the SCR catalyst. A rise in the flow velocity

resulted in lower NO_x conversion efficiency. However, the system characterised by a higher uniformity of ammonia distribution was less sensitive to changes in gas mass flow rates. Lee [18] performed a numerical analysis of a marine SCR system for various operating conditions and experimentally validated the uniformity of the ammonia distribution. The working principle of that mixing device was based on a partly reversed flow in the mixing zone to enhance the mixing process and increase the residence time of the UWS droplets. In another study, Michelin et al. [22] presented an innovative design for a mixing device for close-coupled applications, based on a spiral gas flow along with tangential UWS injection. The available distance for the UWS decomposition was thereby increased while the compact size was maintained. Their approach showed that the application of blade-based or perforated mixers is not the only way to achieve highly uniform ammonia distribution within a limited space. The design was free from deposit formation. The high-level performance was achieved for both relatively low and large angles of spray plumes. Huang et al. [10] analysed the liquid film and solid deposit formation in a urea-SCR system by numerical simulations. They optimised the mixing device for improved uniformity of ammonia and velocity at the inlet to the SCR, as well as for lower pressure drops. They achieved an improvement in all considered criteria. Moreover, the design led to a reduced liquid film deposition. One of the conclusions was that a rise in the number of mixing vanes can result in higher uniformity of ammonia distribution. Nonetheless, this improvement was advantageous to a certain extent. Lecompte et al. [17] presented a multistage experiment, where the impact of additives in a UWS on deposit formation and ammonia generation was evaluated in a close-coupled system from a passenger car. Relatively low gas mass flow rate and gas temperature caused an increase in the mass of the solid deposits. The ammonia generation was enhanced when the temperature increased.

According to the above studies, much emphasis has been placed on increasing the exhaust system's performance while reducing its size to the maximum extent. However, solid deposit formation in exhaust systems posed a serious concern in most cases. None of those studies proposed and evaluated a design based on the application of a highly turbulent flow field without mixing elements and complex geometry.

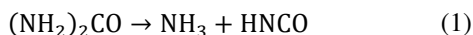
The aim of the present work is numerical verification of the innovative mixerless urea-SCR system, to solve the issue of low mixing space availability, minimise deposit formation and provide uniform ammonia distribution for a wide range of operating conditions and injection properties.

2. Methods

The performance of the mixing device was evaluated by numerical simulations performed using AVL Fire™. The main concept of the mixerless SCR system was the development of a highly turbulent flow and large-scale vortices, increasing the flow paths. Nonetheless, the flow was presumed to be adaptable for the Reynolds-averaged Navier-Stokes (RANS) approach.

The numerical modelling of the spray was based on a discrete droplet model (DDM) [6], in which droplets

characterised by corresponding properties are grouped into parcels. Each parcel is treated as a single droplet, while droplets within a parcel are randomly dispersed. Groups are then resolved by the Lagrangian approach; while the gas flow field is treated according to the Eulerian approach. This provides a significant reduction of computational time, however it may lead to convergence issues if the mesh resolution is excessively large [7]. The decomposition of the UWS was modelled through Birkhold's approach [2], according to which the water evaporates first. Once the water mass fraction is less than 5%, thermolysis occurs according to Eq. (1):



The system was numerically tested for conventional (subcooled) and superheated UWS sprays. A flash-boiling effect was simulated by an analogy to a subcooled spray, which was based on the SCR-thermolysis evaporation model. Instead of modelling flash boiling, its implications in the form of the changed spray properties were derived from the experiments [12] and posed input data. According to [11], where such an approach is presented, it results in high compliance with the experiments. The same experimental data was used [11] in the present study. Droplet-wall interactions were characterised by the approach of Kuhnke [16], which identifies four specific regimes. If the wall temperature is higher than approximately 110% of the droplet saturation temperature, a rebound or a thermal breakup occurs. The latter regime is reached if the impingement velocity is high enough. This regime is particularly desired as it does not contribute to liquid film deposition. Moreover, it provides a droplet breakup, which consequently enhances the droplets' surface area leading to faster urea decomposition and improvement of the mixing process [26]. The size of the entrained droplets was characterised by the model of Kataoka et al. [14].

To properly determine the liquid film deposition in the test system, a wall film module implemented in AVL Fire™ was applied [1]. The general rule was to determine the film's thickness based on its velocity, which in turn was derived from the film's shear force distribution. The approach proposed by Kuhnke [16] was used to determine any splashing effects, some of which could result in film occurrence. Water evaporation and urea decomposition within the liquid film were evaluated according to Birkhold's approach [2].

Catalytic converters were defined as porous zones, where exclusively a longitudinal flow occurred. Any pressure drop was specified by Forchheimer's formula [8]. The pressure drop coefficients were calculated based on the geometrical data with a reference to physical conditions.

2.1. Mixerless urea-SCR system

The present geometry was a close-coupled SCR system, which consisted of a DOC, spray (middle) cone and a SCRoF. The layout of the exhaust system is depicted in Fig. 1. The spray cone was of particular interest since in that part mixing of UWS droplets and products of UWS decomposition with the gas flow occurred.

The main working principle of the proposed design was the development of a highly turbulent and swirled flow in the mixing chamber without any additional static mixing

elements. The injector was mounted behind the inlet to the middle cone and it was inclined to extend a droplet path to the impingement plate. The purpose of the impingement plate was twofold. Firstly, it was aimed at providing secondary droplet breakup through the intense impingement. Secondly, it allowed the minimisation of the temperature reductions caused by spray-wall contact, which normally leads to liquid film deposition, as reported in [20] and [26]. The impingement plate was made of a thin metal sheet and was washed around the upper and the bottom side by exhaust gas. Thus, fast temperature recovery between the injections was expected. The section view of the spray cone and its characteristic regions is presented in Fig. 2.

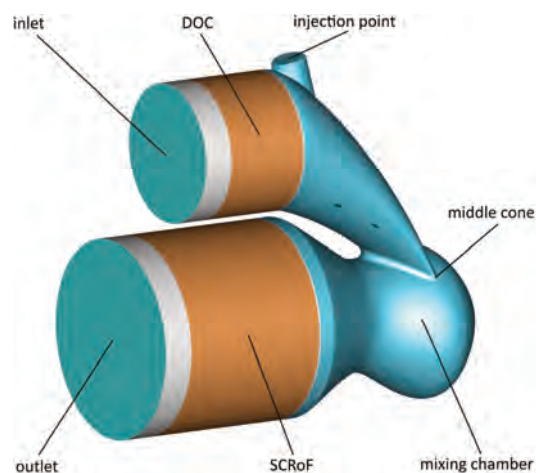


Fig. 1. Geometrical model of the considered close-coupled SCR system

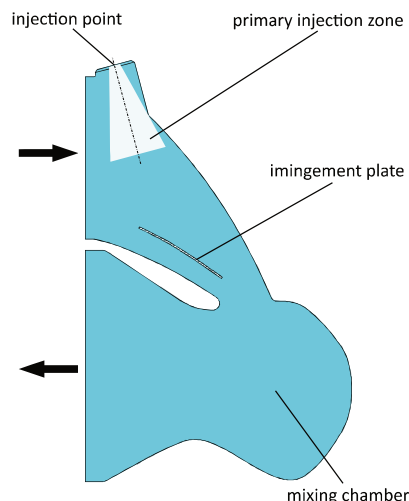


Fig. 2. Section view of the middle cone

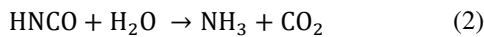
2.2. Numerical cases

To evaluate the performance of the mixerless urea-SCR system, two operating points were considered. The mass flow rates corresponded to low and high engine loads, namely 100 kg/h and 300 kg/h. The flow temperature was specified to 250°C in all cases. The relatively low temperature allowed the investigation of the liquid film deposition risk as according to the studies of Grout et al. [9] and Shahariar et al. [26] the lower the temperature of the gas flow, the more film is developed. The exhaust gas was composed of air and NO_x, with the concentration specified at 150 ppm.

Table 1. Considered cases and corresponding physical conditions

Case	Gas mass flow	Gas temperature	NO _x	ΔT	UWS mass per injection	Injection time	Number of injections
1	100 kg/h	250°C	150 ppm	-20°C	3.33 mg	7.6 ms	4
2				+40°C			
3	-20°C			9.99 mg	22.8 ms		
4	+40°C						

The injection frequency was 4 Hz and the simulated injection corresponded to the spray formed by a commercial UWS injector (Bosch 0444025030). Therefore, the amount of injected UWS and injection duration were determined in accordance with the previous measurements [11, 12] and the molar ratio from the equations of thermolysis (Eq. (1)) and hydrolysis (Eq. (2)):



All the cases were tested for UWS temperatures corresponding to degrees of superheat of -20°C and +40°C. The degree of superheat ΔT was defined as the difference between the actual temperature of the UWS (T_{UWS}) and its saturation temperature (T_{S UWS}), according to Eq. (3). The UWS saturation temperature under standard conditions is 103°C [4], and this value was used to calculate the degree of superheat.

$$\Delta T = T_{\text{UWS}} - T_{\text{S UWS}} \quad (3)$$

According to the simulations' results, large-scale eddies were observed, and an entirely steady flow was unreach-able. Therefore, the results were presumed to depend on the starting point of the injection (namely on the flow conditions when the injection starts), and only a few injections were considered. Simulation of multiple UWS injections would result in lower time dependence, however, this approach was rejected due to the substantial computational time. Instead, a series of four injections were simulated at three different starting points. The offset between the following starting points was specified to 0.5 s, and it was presumed in order to avoid the results' correlation with the large-scale-vortex fluctuations. All the considered cases are presented in Table 1.

The mesh for the numerical analysis was generated in AVL FIRE™ M software and consisted of polyhedral and prism elements. The basic cell size was specified at 6 mm. The primary injection zone, where the highest number density of spray droplets occurred, was meshed with 5 mm-sized cells. The surface cell size on the impingement plate was reduced to 3 mm as the accuracy of wall film modeling greatly depends on the mesh resolution in the impingement zone and the adjacent wetting regions.

3. Results and discussion

The performance of the mixerless SCR system was evaluated by numerical methods. In order to confirm the versatility of the design, two operating points were considered, each of them characterised by the two diverse types of UWS injections: conventional (subcooled) and superheated. The exhaust gas flow was characterised by periodic break-downs despite the constant mass flow rate.

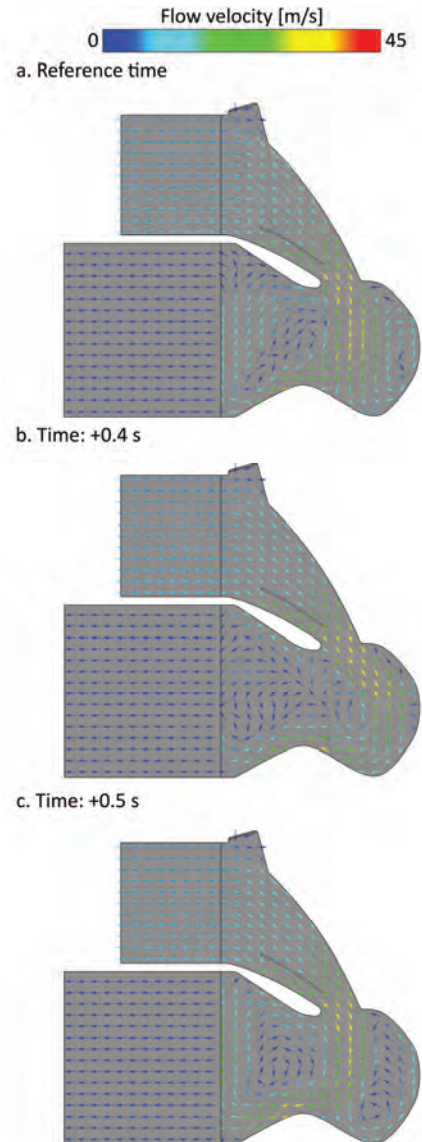


Fig. 3. Velocity fluctuations presented by flow velocity vectors – three particular layouts, mass flow rate: 300 kg/h

The flow was accelerated in the constriction, then expanded in the mixing zone where it was decelerated, and the streamlines were curled due to geometrical constraints. Throughout most of the simulation time, the flow was split into two main swirl zones: one in the back, and the other located upstream of the SCR inlet (Fig. 3a). However, the flow entering the mixing chamber was gradually deflected backwards, and the frontal swirl motion was diminished (Fig. 3b), until a breakdown occurred (Fig. 3c). Then, the flow was rapidly deflected forwards and returned to the initial state, demonstrating strong fluctuations. This indicated that the LES approach would be more appropriate to

fully recognise these effects. However, at this point, due to computational limitations and the need for initial evaluation of the concept, the studies were continued with the RANS method.

The application of the mixing chamber and the related swirling nature of the flow were intended to result in some strong turbulence. The turbulence kinetic energy in the mixing chamber at three particular simulation times (Fig. 4), corresponding to the velocity fields presented in Fig. 3, confirmed the occurrence of large-scale vorticity. In reference to the order of magnitude of the flow velocity (10^1 m/s), the turbulence kinetic energy was substantial, which enabled the prediction of the high-level mixing efficiency of the presented design.

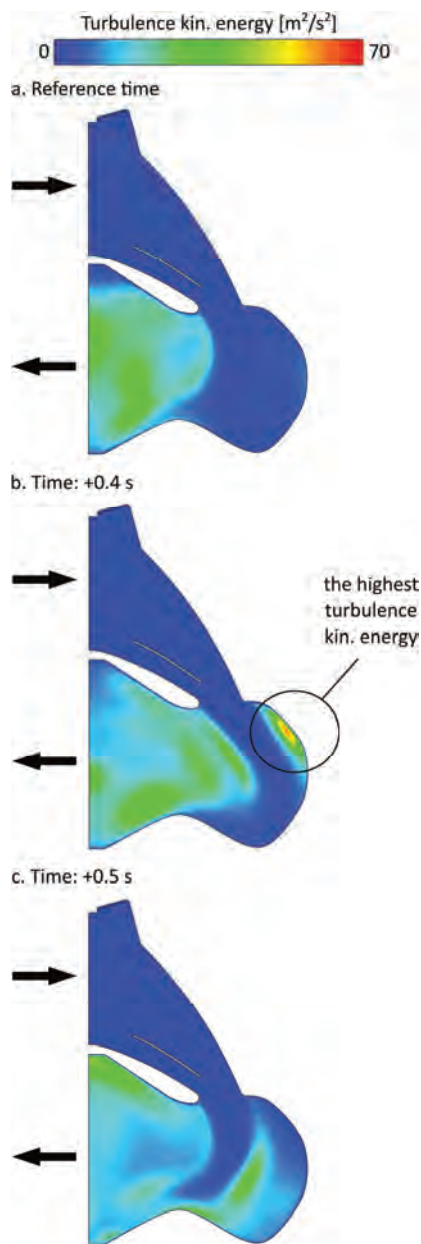


Fig. 4. Turbulence kinetic energy, mass flow rate: 300 kg/h; a. prevailing layout, b. flow breakdown, c. flow recovery

Since the flow field was subjected to fluctuations, each of the cases was evaluated thrice. Namely, with different

delays until the first injections were considered; each of them was characterised by a 0.5 s offset.

One of the key factors influencing the performance of SCR systems is liquid film occurrence. It leads to a solid deposit formation and may substantially lower NO_x conversion efficiency. Therefore, one of the evaluated quantities was the total mass of liquid film developed inside the whole system. The individual results for all the subcases of the 100 kg/h and 300 kg/h cases are presented in Fig. 5 and Fig. 6, as follows.

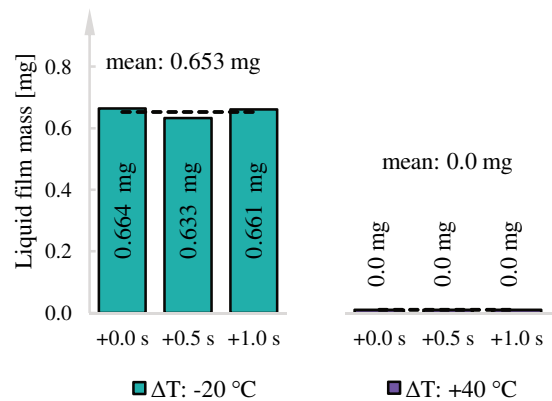


Fig. 5. Total liquid film mass at a gas mass flow rate of 100 kg/h, all subcases listed

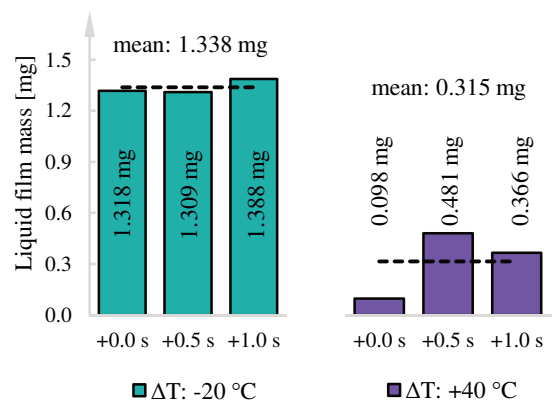


Fig. 6. Total liquid film mass at a gas mass flow rate of 300 kg/h, all subcases listed

The resulting values indicated a relatively low liquid film mass inside the system. An increased gas mass flow rate led to a rise in film mass, which resulted from increased injection time and hence a longer time when the droplet-wall collisions occurred. The liquid film was observed mostly on the plate due to intense local cooling caused by liquid impingement. It particularly concerned the subcooled injection characterised by a narrower spray plume and higher impingement velocity. The constriction above the mixing chamber caused intensified droplet-wall contacts. However, no film was formed there because of the high droplet dispersion and low degree of local cooling. Trace amounts of the film were deposited in the mixing chamber and near the injector. The latter resulted directly

from the design's features. The close distance from the nozzle to the wall led to some interactions of the smallest droplets and additionally, the low flow velocity in this region intensified the deposition. Those trace amounts of wall film prevailed in the case of flash-boiling injection and high gas mass flow rate, where no film occurred on the plate. The lowest observed temperature in the vicinity of the upper surface of the impingement plate after the start of the injection (ASOI) for various UWS conditions and the highest gas mass flow rate is presented in Fig. 7. The decline of the local temperature in the case of the subcooled injection was much higher than for the superheated injection. The superheated spray was characterised by a reduced droplet size and increased spray angle. The smaller droplets were then shifted farther downstream and were more dispersed, which influenced the lower temperature drops. It is to be noted that droplet-plate collisions started later in the case of the flash-boiling injection as the droplet velocity was lower. Therefore, the maximum temperature drop in the case of the superheated-liquid injection occurred approximately 29 ms ASOI, compared to 10 ms ASOI for the conventional injection. The distribution of the temperature corresponded to the locations of the droplet-wall collisions and wetting regions, as well as to the liquid film deposition, which is consistent with the analysis of Li et al. [19]. Consequently, the application of the flash-boiling injection resulted in a total reduction of the liquid film in low-mass-flow rated conditions and a substantial reduction for the higher mass flow rate (Figs 5–6).

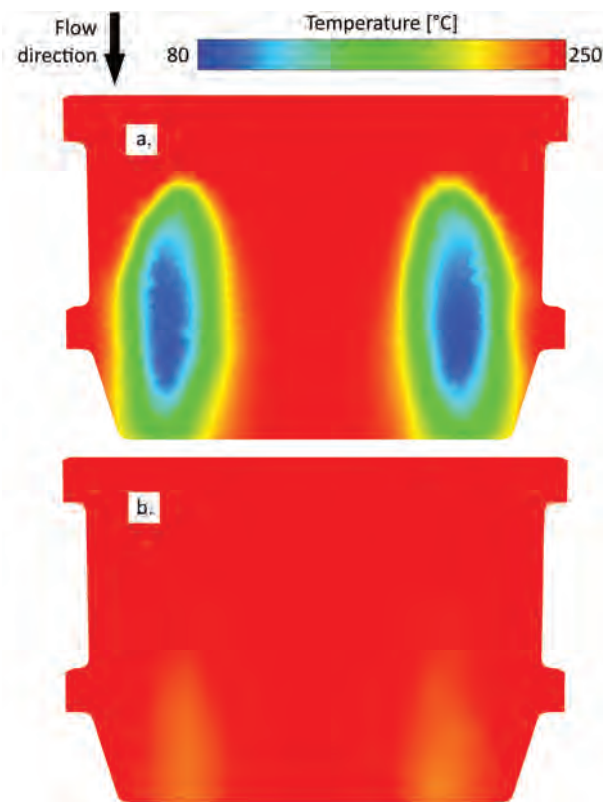


Fig. 7. The local temperature in the vicinity of the impingement plate mapped on its surface at the time of the maximum temperature drop, mass flow rate: 300 kg/h; a. subcooled spray, 10 ms ASOI; b. superheated spray, 29 ms ASOI

Since ammonia is a reducing agent for NO_x compounds in SCR systems and its uniform distribution is crucial for the high performance of those systems, the quality of mixing was assessed based on the dispersion of NH₃ approximately 10 mm from the SCR's inlet (inside the porous medium). The uniformity was described by the uniformity index of ammonia distribution UI_{NH₃} according to Eq. (4):

$$UI_{NH_3} = 1 - \frac{\sum |c_{iNH_3} - c_{NH_3}| \cdot A_i}{2 \cdot c_{NH_3} \cdot \sum A_i} \quad (4)$$

where: A_i was a surface of a given mesh element; c_{NH₃} was the mean NH₃ concentration; and c_{iNH₃} was the concentration of NH₃ in the corresponding mesh element.

The resulting values of the ammonia uniformity index are presented in Fig. 8 and Fig. 9 for the cases of 100 kg/h and 300 kg/h gas mass flow rates.

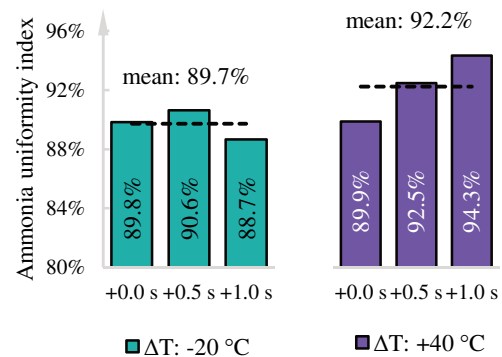


Fig. 8. Ammonia uniformity index at a gas mass flow rate of 100 kg/h, all subcases listed

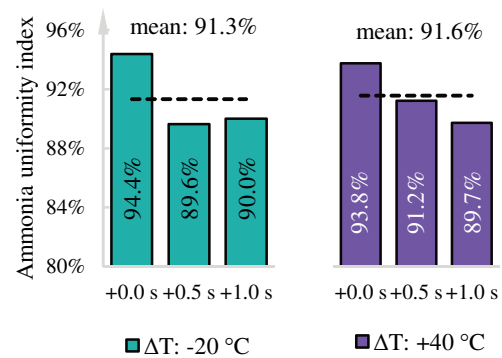


Fig. 9. Ammonia uniformity index at a gas mass flow rate of 300 kg/h, all subcases listed

Despite the lack of mixing elements, the uniformity of the ammonia distribution reached an excellent and comparable level regardless of the gas mass flow rate. Firstly, the flow in the mixing chamber was subjected to intense turbulence and streamline deflections according to the predictions. Streamlines of the exhaust gas flow are presented in Fig. 10.

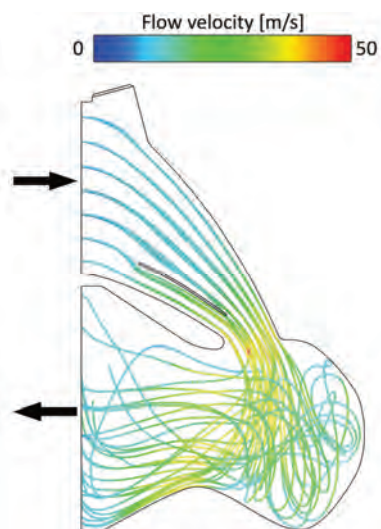


Fig. 10. Velocity streamlines inside the middle cone at a gas mass flow rate of 300 kg/h

Secondly, the inclination of the injector and the swirl motion in the mixing chamber significantly increased the length of the droplets' paths to reach the impingement plate and the porous medium, respectively. Since the UWS residence time was increased, water could evaporate to a higher extent and the urea conversion efficiency was increased. Another reason for high ammonia uniformity at the inlet to the SCR was a substantial reduction in droplet size caused by impingement on the top surface of the plate (Fig. 11). Location of the plate and local gas velocity favoured a relatively high impingement velocity. Consequently, the spray-wall interaction regimes corresponded to splash and thermal breakup for the subcooled spray, while rebound and thermal breakup for the superheated spray followed Kuhnke's description [16], which allowed for droplet breakups. Smaller droplets led to improved water evaporation and urea decomposition. Thus, the ammonia generation and mixing were enhanced.

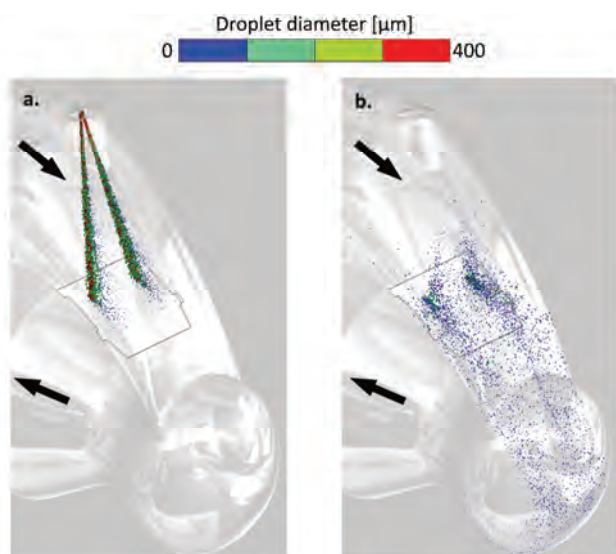


Fig. 11. Spray impingement, subcooled injection; a. 10 ms ASOI, droplet size scale: 10; b. 29 ms ASOI, droplet size scale: 15

Ammonia dispersion was improved by flash boiling, particularly in the case of a low gas mass flow rate. When the gas mass flow rate was increased, improvement of the ammonia uniformity by flash boiling was marginal. It resulted from strong spray interactions with the gas, and thus the droplets were transferred onto the walls. Since the size of the droplets was reduced, the surface-to-volume ratio was increased making the droplets more sensitive to the aerodynamic drag. The droplets quickly exchanged momentum with the exhaust gases and changed their trajectories. However, the size reduction also shortened the time required for the UWS to decompose and finally, the ammonia uniformity after the SCR's inlet remained at a similar level.

Actually, the presented mixing device was characterised by a high performance in the case of both conventional and flash boiling UWS injections. The latter was particularly advantageous for low engine-load conditions. Nevertheless, the system was universal, and provided high mixing regardless of the UWS temperature.

4. Conclusions

The results obtained during the numerical simulations showed that the system was characterised by the large-scale vortices in the turbulent flow. To fully recognise these unsteady changes and verify the results obtained with the RANS approach, the LES (large eddy simulations) method should be applied. Thus, the results presented here should be considered as an initial evaluation of the newly presented concept.

The simulations performed suggested that it is possible to reach high uniformity of ammonia concentration before the inlet to the SCR catalyst at a significantly limited distance, without implementing static mixing elements into the middle cone. High mixing efficiency has been achieved by generating a very turbulent flow in the mixing zone. The developed flow field also allowed only a very low liquid film deposition, despite the relatively low temperature of the exhaust gas. This was caused by the initial flow acceleration, which favoured the transport of the injected or splashed droplets into the mixing chamber, and subsequent turbulent mixing. Moreover, numerical simulations showed a significant reduction of the total wall film in the case of increased temperature of the injected UWS causing the flash-boiling phenomenon. The system operating under such conditions was characterised by a significant reduction of the risk of the deposits' formation. In the case of both subcooled and superheated liquids, it was possible to reduce the cooling of the system walls caused by the spray-wall interactions, as well as to enhance the consequent temperature recovery of the wetted walls. This effect was achieved by implementing a thin impingement plate (resulting in relatively low volume and large surface), which was located so that the hot gases washed it from both sides.

The CFD calculations suggested that the tested system is able to work effectively at a wide range of operating points. For both mass flow rates of 100 and 300 kg/h, high uniformity of ammonia after the inlet to the SCR catalyst was achieved due to intensive turbulent mixing and secondary breakup caused by droplet-plate collisions. It was found that the device ensures excellent operation under the condi-

tions of a subcooled-liquid injection and when the flash-boiling phenomenon occurs.

The prototype mixing system has compact dimensions, thanks to which it is possible to mount DOC and SCR catalysts close to each other in accordance with the trend of close-coupled systems. Moreover, the internal structure is considerably simplified compared to most of the systems which implement static mixing devices.

The presented concept of the mixing device in the SCR system has features that offer potential improvements to the currently used systems. However, to obtain a complete picture of the functioning of the device, further research using the LES approach and the creation of an actual proto-

type, which would enable experimental tests and the verification of the system's performance, are necessary.

Acknowledgements

The project leading to this application has received funding from the National Centre for Research and Development (NCBiR), grant no. MAZOWSZE/0101/19-00, programme Ścieżka dla Mazowsza, project budget: 9 880 490.25 PLN.

Numerical simulations were performed using AVL FIRE™ software under AVL University Partnership Program.

Nomenclature

A_i	surface of a given (i-th) mesh element	NO_x	nitrogen oxides
ASOI	after start of the injection	RANS	Reynolds-averaged Navier-Stokes
C_{NH_3}	mean NH_3 concentration	SCR	selective catalytic reduction
$C_{i \text{ NH}_3}$	mean NH_3 concentration of a given (i-th) mesh element	SCRoF	selective catalytic reduction on particulate filter
CFD	computational fluid dynamics	T_{UWS}	temperature of UWS
DDM	discrete droplet model	$T_{\text{S UWS}}$	saturation temperature of UWS
DOC	diesel oxidation catalyst	$U_{\text{I NH}_3}$	ammonia uniformity index
LES	large eddy simulations	UWS	urea-water solution
NH_3	ammonia	ΔT	degree of superheat

Bibliography

- [1] AVL LIST GmbH FIRE™ 2019.2 Wall Film Module User Guide. *Wall Film Module*. 2019
- [2] BIRKHOFF, F. Selektive katalytische Reduktion von Stickoxiden in Kraftfahrzeugen: Untersuchung der Einspritzung von Harnstoffwasserlösung. 2007, **15**(6), 893-900.
- [3] BRIZI, G., POSTRIOTI, L. Experimental analysis of SCR spray evolution and sizing in high-temperature and flash boiling conditions. *SAE International Journal of Fuels and Lubricants*. 2019, **12**(2), 87-107. <https://doi.org/10.4271/04-12-02-0006>
- [4] BROCKLEY GROUP LTD. Safety data sheet BlueCat AdBlue. 2014
- [5] CHO, Y.S., LEE, S.W., CHOI, W.C. et al. Urea-SCR system optimization with various combinations of mixer types and decomposition pipe lengths. *International Journal of Automotive Technology*. 2014, **15**(5), 723-731. <https://doi.org/10.1007/s12239-014-0075-x>
- [6] DUKOWICZ, J.K. A particle-fluid numerical model for liquid sprays. *Journal of Computational Physics*. 1980, **35**(2), 229-253. [https://doi.org/10.1016/0021-9991\(80\)90087-X](https://doi.org/10.1016/0021-9991(80)90087-X)
- [7] EDELBAUER, W. Coupling of 3D Eulerian and Lagrangian spray approaches in industrial combustion engine simulations. *Journal of Energy and Power Engineering*. 2014, **8**(1). <https://doi.org/10.17265/1934-8975/2014.01.022>
- [8] FORCHHEIMER, P. Wasserbewegung durch boden. *Zeitschrift des Vereins deutscher Ingenieure*, 45th edition. 1901.
- [9] GROUT, S., BLAISOT, J.-B., PAJOT, K. et al. Experimental investigation on the injection of an urea-water solution in hot air stream for the SCR application: Evaporation and spray/wall interaction. *Fuel*. 2013, **106**, 166-177. <https://doi.org/10.1016/j.fuel.2012.09.022>
- [10] HUANG, H., CHEN, Y., LI, Z. et al. Analysis of deposit formation mechanism and structure optimization in urea-SCR system of diesel engine. *Fuel*. 2020, **265**, 116941. <https://doi.org/10.1016/j.fuel.2019.116941>
- [11] KAPUSTA, Ł.J., ROGOZ, R., BACHANEK, J. Experimental and numerical study to evaluate the effect of flash boiling on urea-water solution sprays and SCR system performance. *Atomization and Sprays*. 2021, **31**(5), 89-117. <https://doi.org/10.1615/AtomizSpr.2021035461>
- [12] KAPUSTA, Ł.J., ROGOZ, R., BACHANEK, J. et al. Low-pressure injection of water and urea-water solution in flash-boiling conditions. *SAE International Journal of Advances and Current Practices in Mobility*. 2020, **3**(1), 365-377. <https://doi.org/10.4271/2020-01-2110>
- [13] KAŠPAR, J., FORNASIERO, P., HICKEY, N. Automotive catalytic converters: current status and some perspectives. *Catalysis Today*. 2003, **77**(4), 419-449. [https://doi.org/10.1016/S0920-5861\(02\)00384-X](https://doi.org/10.1016/S0920-5861(02)00384-X)
- [14] KATAOKA, I., ISHII, M., MISHIMA, K. Generation and size distribution of droplet in annular two-phase flow. *Journal of Fluids Engineering*. 1983, **105**(2), 230-238. <https://doi.org/10.1115/1.3240969>
- [15] KOEBEL, M., ELSENER, M., KLEEMANN, M. Urea-SCR: a promising technique to reduce NO_x emissions from automotive diesel engines. *Catalysis Today*. 2000, **59**(3), 335-345. [https://doi.org/10.1016/S0920-5861\(00\)00299-6](https://doi.org/10.1016/S0920-5861(00)00299-6)
- [16] KUHNKE, D. Spray/wall-interaction modelling by dimensionless data analysis. 2004.
- [17] LECOMPTE, M., OBIOLS, J., CHEREL, J. et al. The benefits of diesel exhaust fluid (DEF) additivation on urea-derived deposits formation in a close-coupled diesel SCR on filter exhaust line. *SAE International Journal of Fuels and Lubricants*. 2017, **10**(3), 864-877. <https://doi.org/10.4271/2017-01-2370>

- [18] LEE, C. Numerical and experimental investigation of evaporation and mixture uniformity of urea–water solution in selective catalytic reduction system. *Transportation Research Part D: Transport and Environment*. 2018, **60**, 210-224. <https://doi.org/10.1016/j.trd.2017.04.015>
- [19] LI, M., ZHANG, Y., LIU, X. et al. Numerical investigation on the urea deposit formation process in a selective catalytic reduction system of a diesel engine based on a fluid–solid coupling method. *ACS Omega*. 2021, **6**(8), 5921-5932. <https://doi.org/10.1021/acsomega.1c00021>
- [20] LIAO, Y., DIMOPOULOS EGGENSCHWILER, P., RENTSCH, D. et al. Characterization of the urea-water spray impingement in diesel selective catalytic reduction systems. *Applied Energy*. 2017, **205**, 964-975. <https://doi.org/10.1016/j.apenergy.2017.08.088>
- [21] MAIZAK, D., WILBERFORCE, T., OLABI, A.G. DeNOx removal techniques for automotive applications – a review. *Environmental Advances*. 2020, **2**, 100021. <https://doi.org/10.1016/j.envadv.2020.100021>
- [22] MICHELIN, J., GUILBAUD, F., GUIL, A. et al. Advanced compact SCR mixer: BlueBox. *SAE Technical Paper* 2014-01-1531. 2014. <https://doi.org/10.4271/2014-01-1531>
- [23] NISHAD, K., STEIN, M., RIES, F. et al. Thermal decomposition of a single AdBlue® droplet including wall–film formation in turbulent cross-flow in an SCR system. *Energies*. 2019, **12**(13), <https://doi.org/10.3390/en12132600>
- [24] PARK, T., SUNG, Y., KIM, T. et al. Effect of static mixer geometry on flow mixing and pressure drop in marine SCR applications. *International Journal of Naval Architecture and Ocean Engineering*. 2014, **6**(1), 27-38. <https://doi.org/10.2478/IJNAOE-2013-0161>
- [25] PRABHU, S.S., NATESAN, K., SHIVAPPA NAYAK, N. Effect of UWS spray angle and positioning of injector on ammonia concentration in urea-SCR system. *Materials Today: Proceedings*. 2021, <https://doi.org/10.1016/j.matpr.2021.03.026>
- [26] SHAHARIAR, G.M.H., LIM, O.T. A study on urea-water solution spray-wall impingement process and solid deposit formation in urea-SCR de-NOx system. *Energies*. 2019, **12**(1), 1-18. <https://doi.org/10.3390/en12010125>
- [27] SMITH, H., LAUER, T., SCHIMIK, V. et al. Evaluation and prediction of deposit severity in SCR systems. *SAE International Journal of Engines*. 2016, **9**(3), 1735-1750. <https://doi.org/10.4271/2016-01-0970>
- [28] TAN, L., FENG, P., YANG, S. et al. CFD studies on effects of SCR mixers on the performance of urea conversion and mixing of the reducing agent. *Chemical Engineering and Processing: Process Intensification*. 2018, **123**, 82-88. <https://doi.org/10.1016/j.ccep.2017.11.003>
- [29] ZHANG, C., SUN, C., WU, M. et al. Optimisation design of SCR mixer for improving deposit performance at low temperatures. *Fuel*. 2019, **237**, 465-474. <https://doi.org/10.1016/j.fuel.2018.10.025>
- [30] ZUO, B., GOMES, A.M., RUTLAND, C.J. Modelling superheated fuel sprays and vaporization. *International Journal of Engine Research*. 2000, **1**(4), 321-336. <https://doi.org/10.1243/1468087001545218>

Bartosz Kaźmierski, BEng. – Faculty of Power and Aeronautical Engineering, Warsaw University of Technology, Poland.

e-mail: bartosz.kazmierski@gmail.com



Łukasz Jan Kapusta, DEng. – Faculty of Power and Aeronautical Engineering, Warsaw University of Technology, Poland.

e-mail: lukasz.kapusta@pw.edu.pl



Krzysztof Górka, BEng. – Faculty of Power and Aeronautical Engineering, Warsaw University of Technology, Poland.

e-mail: krzysztof.gorka21@gmail.com



Numerical investigation of the internal flue gas recirculation system applied to methane powered gas microturbine combustor

ARTICLE INFO

The gas microturbines gain significance in various industry sectors. One of their most crucial advantages is the capability of utilizing variety of fuels. At the same time, the emissions regulations become increasingly strict. This is why there is a need to look for a new technological solution to limit the emissions of selected substances, like carbon monoxide (CO) and nitrogen oxides (NO_x). The internal recirculation of the flue gases is well known to limit the temperature peak and for the homogenization of the temperature field gradient in different combustion chambers. This paper presents a numerical investigation of a novel internal flue gas recirculation system applied to gas microturbine combustors. The ability to perform an internal exhaust gases recirculation by adding a combustor internal pipe system was verified numerically. This paper exposed the numerical investigation methods and obtained results. The study presents the concept and results performed on three cases of internal exhaust gases recirculation systems applied to a reference combustor. The work permitted to demonstrate numerically that it is possible to perform an autonomous exhaust gases recirculation inside gas microturbine combustor at a maximum global rate of 0.51%, and that the recirculation system has an impact on the combustion processes without specially modifying the combustor work parameters.

Received: 29 June 2021

Revised: 2 August 2021

Accepted: 25 August 2021

Available online: 26 August 2021

Key words: gas microturbine, exhaust gases recirculation, combustion chamber, CO emission, NO_x emission

This is an open access article under the CC BY license (<http://creativecommons.org/licenses/by/4.0/>)

1. Introduction

Gas microturbines are engines used to convert fuel energy into mechanical and/or thermal energy. These devices are used in locations where waste fuel is generated (described by Chitrarth Lav and Raj Kumar Singh [1]), as emergency electricity generators for hospitals, as a power drive for drones and even cars (Jaguar C-X75 or Pininfarina H600), etc. In the near future, it is expected that gas microturbines applicability will grow substantially. This expectation is related to the multiple advantages of microturbines. It has a compact design, high power to mass ratio, limited number of rotating parts, low noise pollution level, low vibration level, high potential for the use of various fuel, etc. [1].

Since few decades, more restrictive environmental regulations are being enforced and gas turbine producers are forced to maintain the agreement between efficient and clean combustion. The major pollutants are the nitrogen oxides (NO_x) and carbon monoxide (CO). The main engineering objective of this work is to elaborate a new type of combustor solution that could be adopted to energy devices.

The use of the gas microturbine considering emission regulations leads to the development of new types of combustor for gas microturbines. This paper investigates a novel concept of combustor for gas microturbine equipped with an internal exhaust gas recirculation system. The exhaust gas recirculation system is often applied to piston combustion engines and to power industry gas turbines. The recirculation system may be realized by adding a pipe system permitting to transfer a part of the exhaust gases into the inlet of the power device. This solution is often called the External Flue Gas Recirculation (EFGR). Another recirculation system may be based on transferring part of the exhaust gases from the end of the combustion zone, in power device combustor, to the combustion zone. This is

called Internal Flue Gas Recirculation (IFGR). The role of recirculating exhaust gases is to reduce the temperature peaks and its gradients, which have a direct impact on the reduction of thermal NO_x. In this paper, a gas microturbine combustor equipped with a novel IFGR system is investigated numerically. The current paper describes the numerical investigation of the above-mentioned design solution.

Numerical methods are often used in order to verify and optimize design solutions. The works of Sarlej et al., Chen and Liu, Liu et al., Kim et al. and Huang et al. were oriented on the combustion investigation of the burner and were performed using numerical tools [2]. In the work [3] the influence of the heat supplied into the combustor of the gas microturbine GTM-120 on the aerodynamics of the flow through the combustor was numerically investigated. The work presented a cold flow analysis and the combustion was not simulated in the combustor. The authors underline that the applied RANS k-epsilon model gives accurate results.

The work [4] describes a numerical simulation of the combustion chamber of the gas microturbine GTM-140. The authors used the RANS k-epsilon turbulence model, the non-premixed combustion model and the Discrete Ordinates radiation model. The obtained flow and combustion parameters were compared with the experimental data. It permitted to validate the mathematical models used to perform the simulation.

The work [5] presented a numerical investigation of the influence of the reference area on the velocity profile, temperature field, mixing process and the flame behaviour, in a gas microturbine combustor. The authors used the Shear Stress Transfer turbulence model, the P-1 radiation model and the Eddy Dissipation model for the combustion. The results were compared with the calculation methodology presented by Lefebvre and performed in GateCycle pro-

gram. The results from the simulation and from the Lefebvre calculation methodology were similar. This work shows that the use of various methods (simulation and calculation methodology) permitted to investigate phenomena without using real devices.

In the work [6] a flow with combustion processes occurring in gas turbine was investigated. The numerical results were compared with experimental results, and many of the performed simulations were accurate. The work presented many combustion models (Eddy dissipation model, Finite-rate chemistry model, Flamelet model, Burning velocity model, Extended coherent flame model, Monotone integrated LES, and Linear eddy mixing model). In this work, the Flamelet model appears to be an interesting solution to simulate the combustion processes in gas turbine. This model permits to get an accurate temperature and species field using a detailed chemistry, while having shorter calculation time than other more complex combustion models.

In the work [7] the KJ66 gas microturbine combustor was simulated. In this work, the steady flamelet model with a reduced mechanism of 63 species and 167 reactions (kerosene fuel) was used. In terms of the combustion modelling, the temperature field at the outlet of the combustor was in agreement with the experimental results.

Novelty of the current paper is based on introduction of a totally new concept of recirculating exhaust gases by adding an autonomous pipe system directly inside the combustor. In previous research the recirculation process was realized by the vortex generation but not by adding a pipe system.

This study aims to perform a numerical investigation in order to assess the ability to obtain an autonomous exhaust gases recirculation and analyze its impact on the combustion processes and work parameters of the gas microturbine combustor.

2. Case study combustor and operating conditions

A referential combustor was designed to be suitable for microturbine application. It has a nominal power of around 40 kW and it is fired with methane. The designed combustor calculated work parameters are listed in the table 1, while the characteristic cross sections of the gas microturbine are shown in Fig. 1. The scheme of the referential combustor is presented in Fig. 2.

Table 1 The referential gas microturbine and combustor work parameters

Parameters	H	1	2	3	4
p^* [Pa]	101325	99298	324992	311992	-
p [Pa]	101325	90918	306584	301133	101325
T^* [K]	288	288	433	1185	-
T [K]	288	280	426	1175	-
c [m/s]	0	120	120	155	-80
$c_s = 4.874 \cdot 10^{-3} \frac{kg}{s}$; $\dot{m} = 0.251 \frac{kg}{s}$					

The main objective of this investigation is to check the possibility to design an autonomous IFGR system applied to gas microturbine combustor. The main technical issue is that the exhaust gases are transferred to a combustor region

representing higher pressure. The proposed novel combustor design takes this fact into account.

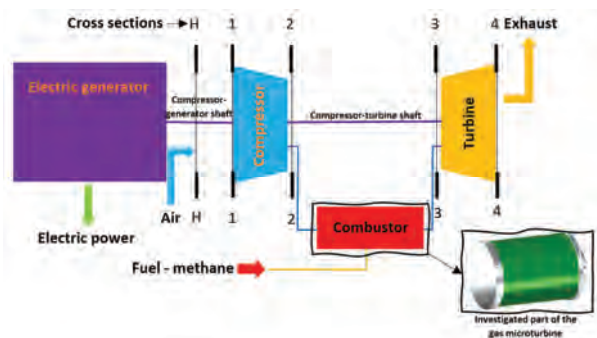


Fig. 1. The cross sections available for the analysed gas microturbine

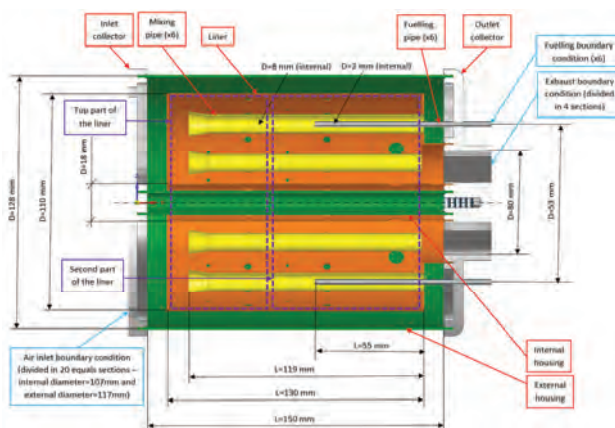


Fig. 2. The scheme of the referential combustor in 3D model

Investigation of the IFGR system applied to the gas microturbine was divided into three major concepts of the modified referential combustor.

The first modified combustor (Case A) is presented in Fig. 3 with this IFGR system concept. Additional IFGR pipes are connected to the existing mixing tubes in the vicinity of their outlets. The idea behind this concept is to redirect part of the exhaust gases into the fresh air-fuel mixture.

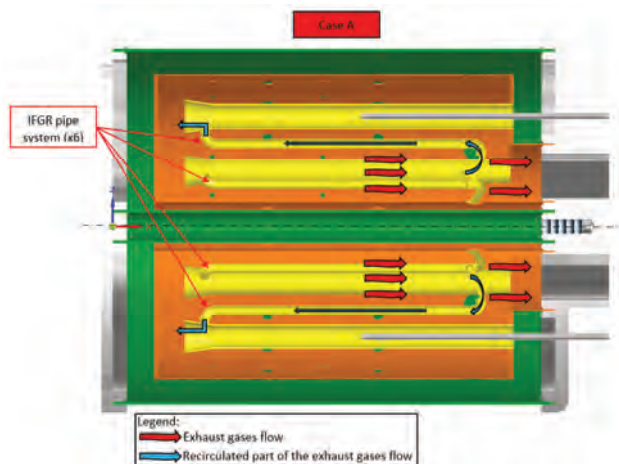


Fig. 3. Modified combustor (Case A)

The second concept of modified combustor (Case B) is presented in Fig. 4. In this IFGR case, additional pipes are installed outside of the liner which permits to transfer a portion of exhaust gases from the outlet of the combustor into the combustion zone, located at the beginning of the liner. The third combustor concept (Case C) is presented in Fig. 5. This IFRG solution consists of adding a pipe connected to the base of the mixing tube. The internal channel of the mixing pipe is shaped as a venturi tube, which permits to generate sufficient under pressure acting as a driving force able to direct the exhaust gases and mix them with air in the mixing pipe.

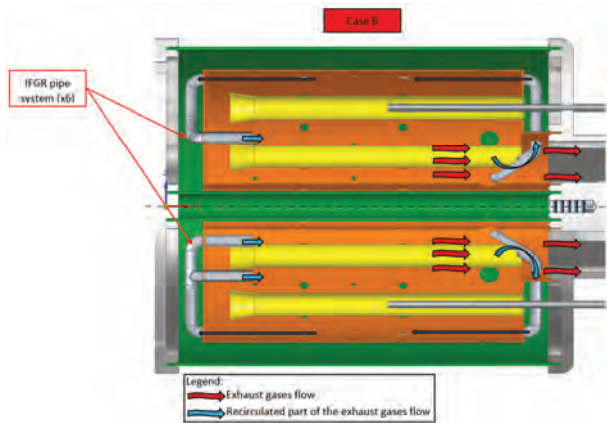


Fig. 4. Modified combustor (Case B)

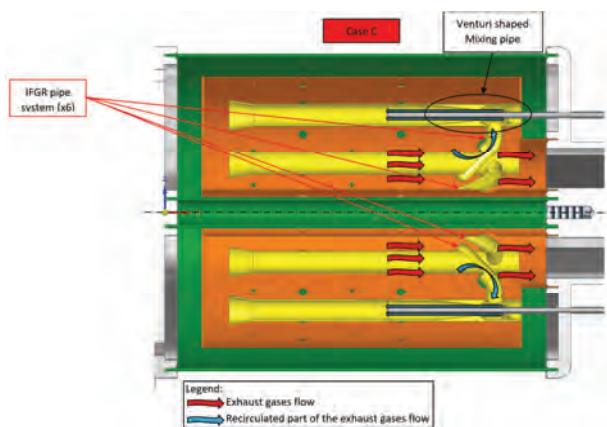


Fig. 5. Modified combustor (Case C)

3. Numerical methods

3.1. Computational domain grid system

The three-dimensional geometry was created using Solid Edge and Ansys preprocessor [8]. Computational domain is shown in Fig. 6. Mesh is one of the most important factors in the simulation of the combustion chamber. To resolve the major flow properties, the tetrahedral cell system is often created. It was previously proven that this meshing solution is successful in case of gas microturbines combustors [3–7]. This kind of element permits to fill a complex geometry, while keeping correct values of quality parameters (skewness, orthogonality and aspect ratio). Recently, the polyhedral cell mesh was intensively developed and then analyzed. This kind of cells are considered to give relatively good results, similarly to the tetrahedral elements,

while obtaining elements with better quality parameters [9–11]. Finally, the polyhedral mesh with a maximum cell length of 0.8 mm was selected for this study. The volume mesh was improved by selecting the value of 0.45 for the cell quality limit (desired orthogonal quality). Additionally, boundary layers were generated in order to not exceed the Y^+ value of 300. Table 2 shows the quality parameters of the obtained mesh system.

Table 2. Quality parameters of the meshes

Case	Number of cells [millions]	Maximum aspect ratio	Maximum skewness	Minimum orthogonal quality
Reference	5.8	38.3	0.895	0.435
Case A	6.3	93.2	0.899	0.420
Case B	7.0	35.8	0.900	0.432
Case C	6.4	62.0	0.895	0.200

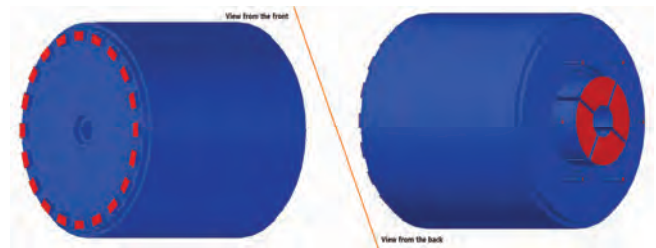


Fig. 6. External view of the computational domain (the external view is similar in all cases)

3.2. Mathematical model

The mathematical model used here is based on the commercial CFD code Ansys FLUENT [12]. Simulation of the following processes occurs in the combustor: turbulent flow, gas phase combustion and radiative transport.

Realizable $k-\epsilon$ model [13, 14] was used as a closure of the turbulent Reynolds equations. The realizable $k-\epsilon$ model is relatively widely used for engineering applications and provides better performance in many industrial turbulent flows than the standard $k-\epsilon$ model. The enhanced wall treatment was enabled. This model permits to resolve the flow when the value of Y^+ is less or equal to 1, or to apply the enhanced wall function if the value of Y^+ is greater than 1. This wall treatment is a good compromise in the case when the phenomena arising at the wall do not have a crucial impact on the general flow properties, like in our case.

In case of combustion in furnace problem, radiation is not only the dominant energy transport mechanism but also one of the most complex problems. A Discrete Ordinates method [4, 14] was used to evaluate the radiative heat transfer. In a typical combustion chamber, H_2O and CO_2 are the main gaseous absorbers and emitters of radiant energy. The total emissivity of gas is calculated by a number of gray gases using polynomial correlations for weighing factors and absorption coefficient according to Weighted Sum of Grey Gases method [14]. Widely employed coefficients for emissivity [15], fitted from the benchmark exponential wide-band model, have been used in this work. The WSGGM represents the entire spectrum with three gray gases having uniform absorption coefficients. The total gas phase absorption coefficient is calculated from the total

emissivity with the mean path length calculated from the characteristic cell size. The wall emissivity was set to unity, which is a typical recommendation in gas microturbine combustor simulations [16].

The non-premixed steady diffusion flamelet model [17] was used as a general concept for treating the interaction between turbulence and chemistry in flames. The assumption is that turbulent diffusion combustion processes can be described as an ensemble of discrete, steady laminar flames, called flamelets. These flamelets are similar to opposite laminar diffusion flames and can be calculated using detailed chemical mechanism, which means that kinetic effects play an important role here. This formulation also takes into account local turbulence effects via strain rates. Thus, with flamelets, the results are not only dependent on the local mixture of fuel and oxidizer and enthalpy levels, but also on the local turbulence. Based on the flamelet, a look-up pdf table is generated

The flamelets were created on the base of the detailed GRI-MECH 3.0 mechanism [18]. This is a 53 species mechanism with 325 reactions created to model the combustion process of methane. Firstly, the Grimech 3.0 mechanism and thermodynamic files were downloaded from the Berkeley website [18]. These files were introduced into the Fluent software using the non-premixed steady diffusion flamelet model first dialog window. Then, the fuel was modelled as pure methane and the air was simplified to 23% mass fraction of oxygen (O₂) and 77% mass fraction of nitrogen (N₂) (these parameters were selected in the second dialog window). Finally, based on these files and fuel/oxidizer parameters, the flamelet and the pdf look-up table were generated, according to the Fluent software pre-defined parameters (in the next dialog windows). The use of the pdf look-up table is an interesting method for combustion modeling, because the physical and chemical properties (such as density, temperature and species mass fraction) of the flow are determined based on this table and some parameters, such as local mean mixture fraction and its variance, the scalar dissipation and the mean enthalpy, which are calculated. Once this process is achieved, the turbulent combustion model is ready to perform calculations in the fluent software.

Boundary conditions are discussed below. Inlet: experimental data at the entry are used. Outlet: it is assumed that in case of the exit plane normal to the x-direction, the gradients of all variables except pressure are zero. Values of x-velocity at the exit are initially assumed to be the same as those immediately upstream of the exit plane and subsequently scaled appropriately to satisfy the overall mass conservation. Hence, at the exit plane it may be written as $(\partial\phi/\partial x)_{\text{exit}} = 0$. Wall: at the wall, no slip condition is applied and the values of velocity components are set to zero. The flow near the wall is influenced by molecular viscosity rather than by turbulence. The wall function method of [19] uses algebraic formulations to link quantities at the wall to those further away. The boundary conditions were implemented as described in the next Table 3.

The spatial discretization was of the second order [4], with a pressure-velocity coupled method and the pseudo-transient approach [20]. The pressure based solver was used.

Table 3. Implemented boundary conditions

Designation of the boundary condition	Type	Parameters
Air inlet	Mass Flow Inlet	Mass flow = 0.251 kg/s Turbulent Intensity = 15 % Turbulent Viscosity Ratio = 10 Total Temperature = 433.834 K Mean Mixture Fraction = 0 Mixture Fraction Variance = 0
Fuel inlet	Mass Flow Inlet	Mass flow = 0.004874 kg/s Turbulent Intensity = 15 % Turbulent Viscosity Ratio = 10 Total Temperature = 300 K Mean Mixture Fraction = 1 Mixture Fraction Variance = 0
Exhaust	Pressure Outlet	Static Pressure = 0 Pa Turbulent Intensity = 15 % Turbulent Viscosity Ratio = 10 Backflow Total Temperature = 300 K Mean Mixture Fraction = 0 Mixture Fraction Variance = 0
Wall	Wall	Stationary Wall No Slip No Heat Exchange Internal Emissivity = 1 Opaque Wall Diffuse Fraction of Radiation = 1
Operating conditions	-	Operating pressure = 301133.803 Pa Gravity off

4. Results and discussion

The combustors can be characterized using various parameters. In this study, the ability to perform the autonomous exhaust recirculation was analysed. The impact of this IFGR system implementation on the pressure drop was assessed and the influence on combustion processes will be evaluated by the analysis of temperature fields and evolution of CO and NO_x emissions.

4.1. Ability to recirculate exhaust gases

In this section the numerical simulation results of the three cases are discussed. Numerical simulations prove that it is possible to perform an autonomous exhaust gases recirculation inside gas microturbine combustor at a maximum global rate of 0.51% and that the recirculation system has an impact on the combustion processes without significantly modifying the combustor work parameters. Figure 7 shows the calculated air mass flows and recirculated exhaust gases across the mixing pipes for different cases.

Based on the performed simulations, the recirculated exhaust gases mass flows in each combustor case were performed. IFGR ratios were calculated following the definitions given by equations 1 and 2. The parameter IFGR% refers to the ratio of the recirculated exhaust gases mass flow to the air mass flow passing across the mixing pipe, while the parameter IFGR%* refers to the ratio of the recirculated exhaust gases mass flow to the exhaust gases mass flow leaving the combustor. The table 4 represents the calculated ratios.

$$\text{IFGR}\% = \frac{\text{Recirculated exhaust gases mass flow [kg/s]} \cdot 100}{\text{Air mass flow passing across the mixing pipe [kg/s]}} \quad (1)$$

$$\text{IFGR}\%^* = \frac{\text{Recirculated exhaust gases mass flow [kg/s]} \cdot 100}{\text{Exhaust gases mass flow leaving the combustor [kg/s]}} \quad (2)$$

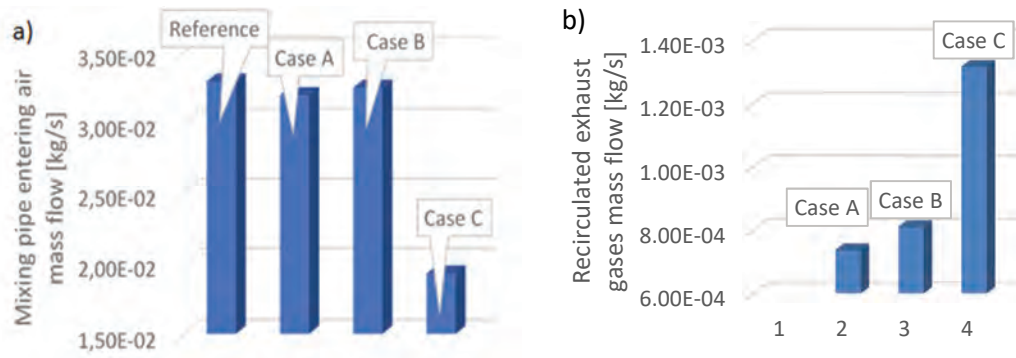


Fig. 7. a) Air mass flow across the mixing pipes, b) Recirculated exhaust gases

Table 4. The IFGR ratio

Case	IFGR%	IFGR%*
Reference	0	0
Case A	2.31	0.29
Case B	2.50	0.32
Case C	6.85	0.51

The IFGR ratio is the most significant in case C (Table 4) with the value of 0.51% for IFGR* and around 6.85% for IFGR. In cases A and B the IFGR ratios are comparable having values of around 0.29% and 0.32% respectively and 2.31% and 2.5% for IFGR*. The difference between each case is due to design differences. In the cases A and B, the recirculation of the exhaust gases is accomplished by creating a pressure difference between the collection and injection locations. The difference between the total pressure (in the location where the exhaust gases are collected) and static pressure (in the location where the exhaust gases are released) is utilized.

In the last case (C), the recirculation of exhaust gases was driven not only by the total-static pressure difference but also by an additional pressure difference generated by the venturi implemented into the mixing pipe (Fig. 5). On the other hand, due to the fact that the recirculating pipe in the case C has a higher diameter (6 mm) than in the cases A (3 mm) and B (4 mm), the axial velocity of the recirculated exhaust gases (10 m/s) is smaller than in the others cases A (22.95 m/s) and B (16.13 m/s). Each of the three IFGR cases was designed in a way to obtain the greater mass flow of the recirculated exhaust gases.

In the case A, the recirculation velocity is the highest and this is a desired phenomenon because the recirculated part of the exhaust gases permits to cool the IFGR pipe passing across the combustion zone. In the case B, the recirculating velocity in the IFGR pipe is not as important as in the case A, because this pipe is located in the cool part of the combustor; the pipes are located between the liner and the external housing of the combustor. In the last IFGR case (C), as in the case B, the recirculated exhaust gases velocity is not of crucial importance, because the IFGR pipe is connected to the mixing pipe inside of the liner, a location which is out of the major combustion zone.

Summarizing the IFGR system solution cases, one must notice the fact that case C procures the higher IFGR ratio

while having the lowest recirculation velocity in the IFGR pipe. The case A presents the totally inverted parameter compared to the case C. The case B is an intermediate case in terms of mass flow and velocity of recirculated exhaust gases. The design of the IFGR systems in the cases B and C permits them to have lower recirculating exhaust gases velocity without exposing the IFGR pipe to overheat. Taking into account the mass flow and the design safety (in terms of overheat), the designs presented in the cases B and C seem to be the most appropriate.

4.2. Impact of the IFGR system on the pressure drop

Another parameter taken into account during the analysis of the IFGR concept is the total pressure drop in the combustor. Table 5 presents the total pressure drop in each case, calculated with equation 3.

$$\Delta p^* = \frac{p_2^* - p_3^*}{p_2^*} \cdot 100 \quad (3)$$

Table 5. The total pressure drop in the combustor

Case	Δp^* [%]
Reference	10.00
Case A	10.12
Case B	10.49
Case C	10.78

It was observed that the smallest total pressure drop is ensured in the referential combustor (10%). This fact is not surprising, because in the IFGR cases were introduced extra IFGR pipe systems, sources of additional flow resistance. The case A has a total pressure drop equal to 10.12%, in the case B it is equal to 10.49% and in the case C it is equal to 10.78%. Being strict in terms of the values, the most advantageous IFGR case is the case A. Taking into consideration the fact that the total pressure drop rises just around 0.78% and the fact that the cases B and C ensure the higher mass flow of the recirculated exhaust gases, it may be considered that the best cases to be taken into consideration are still the cases B and C.

4.3. Impact of the IFGR system on the temperature field

The static temperature homogeneity in the combustor was described in the first part of this section. Differences in the temperature field in the studied cross section were visi-

ble in each case (Fig. 8). In the referential case, a hot-spot near the outlet of the mixing pipes and near the liner internal perimetrical wall can be observed.

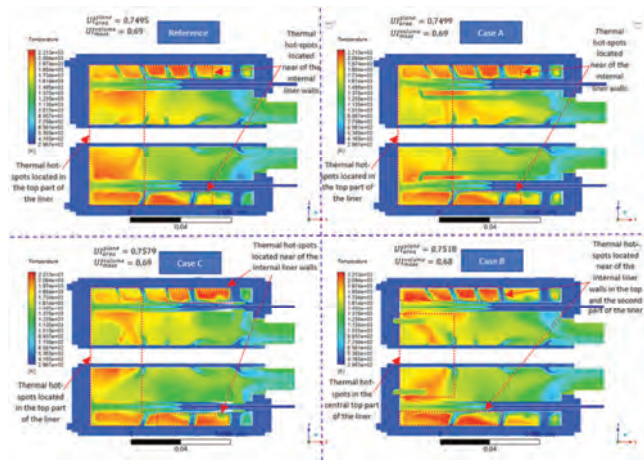


Fig. 8. Static temperature [K] field comparison

In the case A, the temperature field with a more homogeneous gradient around the mixing pipe outlet can be noticed and the hot-spots are still present near the liner internal perimetrical walls (Fig. 8). This least hot-spot is even larger than in the referential case. Observations prove that the presence of the exhaust gases in the combustion zone affects the combustion process and thus the temperature field.

In case B, the recirculation system permits to inject a stream of exhaust gases in the top central part of the liner. This enhances a more homogenous temperature gradient in the vicinity of the mixing pipes outlets, but just in the central part of the liner. In the top internal wall close to the liner an important hot spot can be noticed. The presence of this hot spot is comprehensive in terms of the recirculated part of exhaust gases entering the central location of the liner and not in the perimetrical location of the liner. Near the liner internal perimetrical wall in the second part of the liner, as in the previous case (referential and A), there is a hot-spot. These observations are presented in Fig. 8.

In the last studied case (C), the part of the recirculated exhaust gases is moved into the combustion zone by the mixing pipe, like in the case A, but with the highest mass flow of exhaust gases. This phenomenon affects the combustion zone in the top part of the liner. The temperature gradient is the most homogeneous compared to the others cases. This is the most advantageous effect in terms of the temperature field gradient in the top location of the liner. This effect is less intensive in the second part of the liner. Near the internal perimetrical walls the hot spot is present, as in the others cases, but it is smaller. This description permits to remark that the case C presents the best particularities in terms of the temperature field gradient. The described case C is presented on Fig. 8.

Summarizing the above analysis, the case C has the strongest impact on the temperature field. Cases A and B are less affected by the recirculated exhaust gases. This is linked to the mass flow of the recirculated gases and its injection location. According to the descriptions performed

above, the temperature field gradient is more homogeneous in the locations where the recirculated gases are injected.

It was shown that each of the obtained mass flow of the recirculated exhaust gases is sufficient to affect the combustion processes. The fact that the temperature field is more homogeneous isn't necessarily equivalent to the reduction of the peak temperature. It may happen that the average temperature in the combustion zone may rise. Even with a higher temperature peak it may result in more homogeneous combustion (lower temperature gradient).

According to the performed visual analysis, the most homogenous temperature field is in the case C. The temperature field homogeneity increases from the reference case to the case C. This visual analysis is supported by the value of the static temperature uniformity index related to the area (equation 4). In the reference case the static temperature uniformity index related to the area is 0.7495, for the case A it is 0.7499, for the case B it is 0.7518 and for the case C it is 0.7579. The static temperature uniformity index is similar in all cases and is around 0.75. This analysis is performed just on one selected plane. While computing the static temperature uniformity index related to the mass (equation 5) in the whole 3-D computational domain, all cases have a value of 0.69. Exception is the case B, for which the value is 0.68. This exception is linked to the fact that the IFGR system consists of a set of six pipes located between the liner and the external housing. It indicates that the IFGR system doesn't effectively impact the global static temperature homogeneity in the combustor.

$$UI_{\text{area}}^{\text{plane}} = 1 - \frac{\sum_{i=1}^N [(T_{\text{face}_i} - T_{\text{average}}) \cdot A_i]}{2 \cdot T_{\text{average}} \cdot \sum_{i=1}^N [A_i]} \quad (4)$$

$$UI_{\text{mass}}^{\text{volume}} = 1 - \frac{\sum_{i=1}^N [(T_{\text{cell}_i} - T_{\text{average}_{\text{mass}}}) \cdot (V_i \cdot \rho_i)]}{2 \cdot T_{\text{average}_{\text{mass}}} \cdot \sum_{i=1}^N [V_i \cdot \rho_i]} \quad (5)$$

The above study dedicated to the static temperature homogeneity permits to remark that the implementation of the IFGR system has a local impact on the combustion processes and temperature homogeneity, but the global effect, inside of the whole combustor, is less visible.

In the second part of this section, the evolution of the maximum static temperature in the combustor will be discussed.

Figure 9 shows that the maximum static temperature in the combustor increases from the reference case to the case C. This phenomenon originates from two facts. The first fact is that the IFGR system impacts the equivalence ratio in the combustion processes. This equivalence ratio modification may provoke the apparition of a combustion zone which is near to the stoichiometric conditions. This might result in the increase of the local combustion temperature. The second fact is that the exhaust gases replace a part of the fresh air in the top of the liner. The exhaust gases have higher temperature than the air coming from the compressor, which can increase the combustion peak temperature in the top part of the liner.

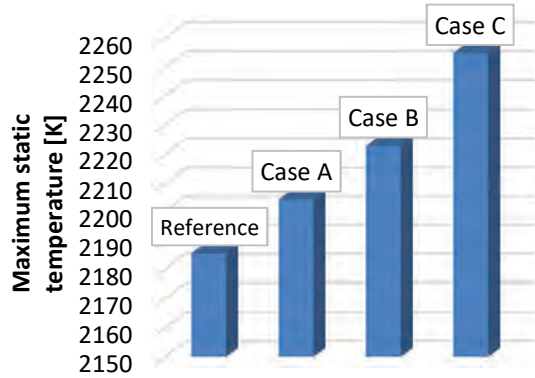


Fig. 9. Maximum static temperature in the combustors

The total exhaust temperature evolution in the combustor was analysed in the third part of this section and presented in Fig. 10. The maximum mass averaged total temperature at the outlet of the combustor is noticed in the case A (1230 K), and the lowest in the case C (1228 K). The difference is just about 2 K, which is a negligible value. It shows that the implementation of the IFGR system doesn't affect the total exhaust temperature.

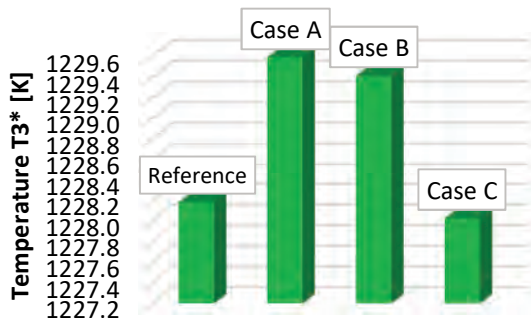


Fig. 10. Total exhaust gases temperature

4.4. Impact of the IFGR system on the CO and NO_x emissions

The CO dry emissions are presented in Fig. 11. The CO emissions meet a decreasing evolution from the referential to the C case combustor. For all IFGR cases, the CO emissions are under the value of 10 ppm. The decreasing values of the CO emissions are corresponding to the increase of the maximum combustion temperature and the recirculated part of the exhaust gases mass flow. This CO emission reduction may be linked with two facts. The first is that the combustion temperature from the referential case to the C case increases, and it is the factor that makes this emission decreases. The second fact is that a part of CO present in the exhaust gases is recirculated into the combustion zone, and the CO of this part of the exhaust gases is reburnt, causing the CO emission reduction in the IFGR cases.

The NO_x dry emissions are presented in Fig. 12. In terms of NO_x emissions, there is an augmentation from the referential to case C combustor. In the case of the referential combustor the NO_x emission is around 127 ppm, while for the last case (C), the NO_x emission is around 140 ppm. In this kind of power devices, the NO_x emission is strongly linked to the thermal NO mechanism. As the maximum

combustion temperature increases from the referential to the case C combustor, the NO_x emission also increases from the referential case to the case C. These results are coherent with the CO emissions and the maximum combustion temperature evolutions.

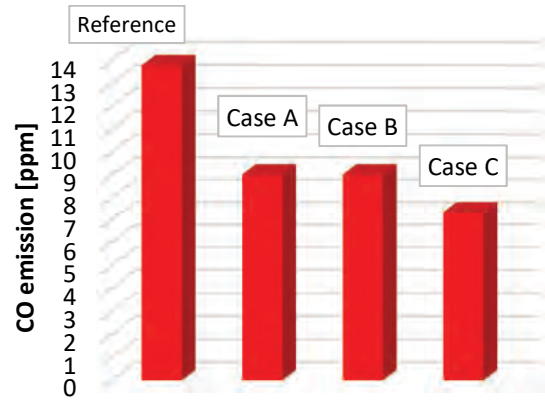
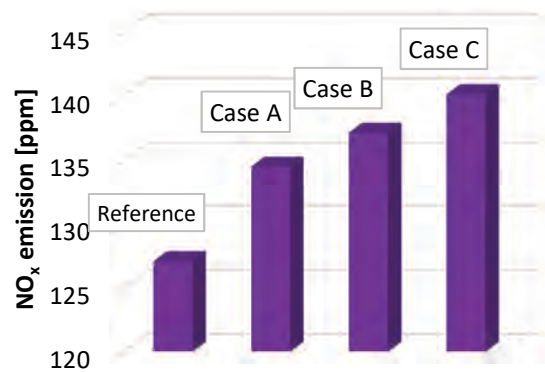


Fig. 11. The CO emissions

Fig. 12. The NO_x emissions

To sum up the emissions consideration of the IFGR concept, it must be underlined that the IFGR case C is the most advantageous in the context of CO emissions, while being the worst in terms of the NO_x emissions. In the context of the NO_x emissions, the referential case is the most advantageous, while being the worst in terms of the CO production. This may be explained by the augmentation of the maximum combustion temperature (hot-spots) from the case A to the case C. This first study permits to demonstrate that the IFGR concept adopted for the gas microturbine combustors permits to reduce the CO emissions, while provoking the NO_x augmentation.

5. Conclusion

This study exposes the IFGR concept adapted to the gas microturbine combustor as well as the numerical investigation of the referential and three IFGR combustors. The results were examined and brought several conclusions listed below:

- by applying the adequate pipe system into the referential combustor, it is possible to achieve the recirculation of a part of the exhaust gases,

- the IFGR combustor case C permits to obtain the maximum mass flow of the recirculated exhaust gases. In addition to the total-static pressure difference, a Venturi shaped channel was added in the mixing pipe,
- the introduction of the IFGR pipe system into the referential model of the combustor provoked a negligible augmentation of the total pressure drop between the inlet and outlet of the combustor (the increase of the total pressure drop has a maximum value of 0.8% – case C),
- the introduction of the exhaust gases into the combustion permitted to softly homogenize the temperature field on the analysed plane, especially in the case C,
- the introduction of the exhaust gases into the combustion doesn't significantly affect the temperature homogeneity in the whole combustor,
- the maximum combustion temperature increases successively from the referential to the C case combustor. It is a consequence of modifying the equivalence ratio in the combustion zone of the liner, introducing hot exhaust gases into the fresh air entering inside of the mixing pipe and reburning the CO present in the exhaust gases,
- the implementation of the IFGR system doesn't impact the exhaust total temperature,
- the application of the IFGR system in the combustor permits to reduce the emission of the CO species, especially in the case C combustor. It is the consequence of

- reburning part of CO present in the exhaust gases and increasing the maximum combustion temperature,
- the implementation of the IFGR system into the combustor provokes the increase of NO_x emissions, which is linked with the increase of the maximum combustion temperature (explained above), and the maximum emission is obtained in the case C while the minimum in the referential case.

The concept of the IFGR applied in the gas micro-turbine combustor was investigated numerically and it permitted to demonstrate that an autonomous internal flue gas recirculation is possible and that it has a visible effect on the combustion process. Taking into consideration the mass flow efficiency of the recirculated exhaust gases, the cases B and C (especially C) are the most desirable. At the same time, it was shown that the implementation of the IFGR system doesn't strongly affect the total pressure drop and the exhaust total temperature, which is a positive observation. Taking into account the reduction of the CO emission, the C case is the most interesting. Taking into consideration the lowest emission of the NO_x emissions, the referential combustor is better than the IFGR combustor cases. The IFGR system applied to gas microturbines permits to reduce the CO emissions. The study permitted also to demonstrate that the IFGR system provokes an increase of the NO_x emissions. Further investigations will be performed in order to analyse the impact of this IFGR concept in the context of emissions.

Nomenclature

A_i	surface of the i facet defining the analysed surface [m ²]	$T_{cell\ i}$	static temperature in the i cell defining the computational domain [K]
c	velocity [m/s]	$T_{face\ i}$	static temperature on the facet i defining the analysed surface [K]
c_s	fuel mass flow [kg/s]	U_{area}^{plane}	plane area weighted static temperature uniformity index [-]
CO	carbon monoxide	U_{mass}^{volume}	volume mass weighted static temperature uniformity index [-]
IFGR	Internal Flue Gas Recirculation	V_i	volume of the cell i defining the computational domain [m ³]
\dot{m}	air mass flow [kg/s]	ρ_i	density of the cell i defining the computational domain [kg/m ³]
NO _x	nitrogen oxides	1, 2, 3, 4	gas microturbine cross section designation
p	pressure [Pa]	*index	total value of a parameter
T	temperature [K]		
$T_{average}$	average static temperature in the analysed cross-section plane [K]		
$T_{average\ mass}$	average static temperature in the analysed computational domain [K]		

Bibliography

- [1] LAV, C., KAUL, C., SINGH, R. et al. (2013). Potential of micro turbines for small scale power generation. *International Journal of Advanced Information Science and Technology*. 2013, **2**(5), 35-39. <https://doi.org/10.15693/ijaist/2013.v2i5.77-81>
- [2] KWON, M., NGUYEN, B.H., KIM, S. et al. Numerical investigation of buoyancy and thermal radiation effects on a mid-/large-sized low NO_x combustion system with flue-gas internal recirculation. *Advances in Mechanical Engineering*. 2018, **10**(4), 1-17. <https://doi.org/10.1177/1687814018769139>
- [3] GIERAS, M., STANKOWSKI, T. Computational study of an aerodynamic flow through a micro turbine engine combustor. *Journal of Power Technologies*. 2012, **92**(2), 68-79.
- [4] SUCHOCKI, T., LAMPART, P., KLONOWICZ, P. Numerical investigation of a GTM 140 turbojet engine. *Open Engineering*, 2015, **5**, 478-484. <https://doi.org/10.1515/eng-2015-0053>
- [5] DIAS, F.L.G., NASCIMENTO, M.A.R., RODRIGUES, L.O. Reference area investigation in a gas turbine combustion chamber using CFD. *Journal of Mechanical Engineering and Automation*. 2014, **4**(2), 73-82. <https://doi.org/10.5923/j.jmea.20140402.04>

- [6] VILAG, V., VILAG, J., CARLANESCU, R. et al. CFD application for gas turbine combustion simulations. In: JI, G., ZHU, J. (Ed.). Computational fluid dynamics simulations. *IntechOpen*. 2019. <https://doi.org/10.5772/intechopen.89759>
- [7] GONZALEZ, C., WONG, K.C., ARMFIELD, S. Computational study of a micro turbine engine combustor using Large Eddy Simulation and Reynolds Averaged turbulence models. *ANZIAM Journal*. 2007, **49**, 407-422. <https://doi.org/10.21914/anziamj.v49i0.338>
- [8] ANSYS, Inc. Retrieved from <https://www.ansys.com/>
- [9] SOSNOWSKI, M., KRZYWANSKI, J., GNATOWSKA, R. Polyhedral meshing as an innovative approach to computational domain discretization of a cyclone in a fluidized bed CLC unit. *E3S Web of Conferences*, 2017, **14**(01027). <https://doi.org/10.1051/e3sconf/20171401027>
- [10] ZAHID, Q., CHAN, A. A study of the effect of element types on flow and turbulence characteristics around an isolated high-rise building. *Eleventh International Conference on CFD in the Minerals and Process Industries, CSIRO*. Melbourne 2015.
- [11] MATYUSHENKO, A., STABNIKOV, A., GARBARUK, A. Criteria of computational grid generation for turbulence models taking into account laminar-turbulent transition. *Journal of Physics: Conference Series*, 2019, **1400**(7). <https://doi.org/10.1088/1742-6596/1400/7/077047>
- [12] ANSYS, Inc. Ansys Fluent Theory Guide – Release 15.0. 2013.
- [13] SUCHOCKI, T., LAMPART, P., SURWIŁO, J. Designation of operating characteristics for micro-jet engine and CFD validation. *Mechanik*. 2015, **7**, 813-820. <https://doi.org/10.17814/mechanik.2015.7.301>
- [14] GIERAS, M. Miniaturowe silniki turboodrutowe (Micro-turbojet engine). *Publishing House of the Warsaw University of Technology*, Warsaw 2016.
- [15] SMITH, T., SHEN, Z., FRIEDMAN, J. Evaluation of coefficients for the weighted sum of gray gases model. *Journal of Heat Transfer*. 1982, **104**(4), 602-608. <https://doi.org/10.1115/1.3245174>
- [16] FUCHS, F., MEIDINGER, V., NEUBURGER, N. et al. Challenges in designing very small jet engines fuel distribution and atomization. *International Symposium on Transport Phenomena and Dynamics of Rotating Machinery*, Honolulu 2016.
- [17] PETERS, N. Turbulent Combustion. *Cambridge University Press*. Cambridge 2000.
- [18] SMITH, G.P., GOLDEN, D.M., FRENKLACH, M. et al. Grimech 3.0. Retrieved from http://www.me.berkeley.edu/gri_mech/
- [19] LAUNDER, B.E., SPALDING, D.B. The numerical computation of turbulent flows. *Computer Methods in Applied Mechanics and Engineering*. 1974, **3**(2), 269-289. [https://doi.org/10.1016/0045-7825\(74\)90029-2](https://doi.org/10.1016/0045-7825(74)90029-2)
- [20] ANSYS, Inc. Ansys Fluent Tutorial Guide – Release 18.0. 2017.

Jean-Marc Fafara, MEng. – Faculty of Mechanical and Power Engineering, Wrocław University of Science and Technology.

e-mail: jean-marc.fafara@pwr.edu.pl



Norbert Modliński, DSc., DEng. – Faculty of Mechanical and Power Engineering, Wrocław University of Science and Technology.

e-mail: norbert.modlinski@pwr.edu.pl



Improving the effective efficiency of a spark ignition engine through the use of a fully independent valve control system

ARTICLE INFO

The article presents theoretical research of the proposed system of fully independent valve control (FIVC) of the SI engine. The analysis included controlling the movement of the intake valves, which results in adjusting the mass of the fresh charge to the current engine load, as well as the movement of the exhaust valves, where the main aim is to keep the rest of the exhaust gas in the cylinder, i.e. implementation of internal EGR. The open theoretical Seiliger-Sabathe cycle with the classic throttle regulation of load is the reference cycle for assessment of benefits and study of the effectiveness of obtaining work as a result of application of the FIVC system. A comparative analysis of the effectiveness of application of the proposed system was carried out based on the selected quantities: fuel dose, cycle work, relative work of charge exchange and cycle efficiency. The use of the FIVC to regulate the SI engine load makes it possible to eliminate the throttle and thus reduce the charge exchange work, especially in the partial load range. And this then leads to an increase in internal and effective work, which in turn results in an increase in the effective energy efficiency of an engine operation.

Received: 26 July 2021
Revised: 16 August 2021
Accepted: 23 August 2021
Available online: 30 August 2021

Key words: SI engine, theoretical cycle, charge exchange, engine efficiency, independent valve control

This is an open access article under the CC BY license (<http://creativecommons.org/licenses/by/4.0/>)

1. Introduction – the importance of the charge exchange process in an ICE

The energy conversion process taking place in an internal combustion engine can be characterized by the effective energy efficiency η_e , defined as:

$$\eta_e = \frac{N_e}{\dot{m}_p H_u} \quad (1)$$

where \dot{m}_p – mass flux of consumed fuel, H_u – calorific value of fuel.

The theoretical cycle of the ICE consists of physical processes that reflect the idealized course of the real engine processes. The ratio of the theoretical cycle power N_o to the fuel chemical energy flux expresses the energy efficiency of the theoretical cycle:

$$\eta_o = \frac{N_o}{\dot{m}_p H_u} \quad (2)$$

Based on the real cycle of the engine, the internal power N_i is determined and then the internal efficiency, defined as:

$$\eta_i = \frac{N_i}{\dot{m}_p H_u} \quad (3)$$

The perfection of the implementation of thermodynamic processes in an ICE is assessed by the rate of internal excellence ξ_i , which expresses the ratio of the internal power N_i of the engine to the power N_o of the theoretical cycle:

$$\xi_i = \frac{N_i}{N_o} \quad (4)$$

The mechanical friction losses and the power necessary to drive the engine auxiliary mechanisms are characterized by the rate of mechanical excellence ξ_m , defined as the ratio of the effective power N_e to the internal power N_i :

$$\xi_m = \frac{N_e}{N_i} \quad (5)$$

The effective energy efficiency η_e of an internal combustion engine can therefore be expressed as the product of the theoretical cycle efficiency η_o and the rates of excellence:

$$\eta_e = \eta_o \xi_i \xi_m \quad (6)$$

Formula (6) shows that due to changes in the theoretical cycle, leading to an increase in the value of its energy efficiency η_o , it is possible to obtain an increase in the value of the effective energy efficiency η_e of the engine.

The operation of the car engine at the optimal point, due to the maximum, effective efficiency η_e , occurs relatively rarely. For a spark ignition engine, this point of optimal operation is situated close to the external characteristic. In operation range far away from the optimal point, i.e. for partial loads, the effective energy efficiency η_e of the internal combustion engine is significantly lower than the maximum value.

Among the many reasons for the reduction of efficiency in the area of partial loads, two should be mentioned as significant:

- an increase in the work of charge exchange leading to a decrease in the rate ξ_i of internal excellence,
- an increase in the relative work of friction, related to the internal work, resulting in a decrease in the rate ξ_m of mechanical excellence.

Greater potential for improving the situation is associated with the reduction of losses in the process of charge exchange, which in turn will result in an increase in the rate of internal excellence, mainly in the field of partial loads. A significant reduction in charge exchange work in the SI engine can be achieved by eliminating the throttle by introducing independent valve control.

Independent valves control (IVC) is one of the most promising technical solutions to solve the pumping losses problem in SI engines due to its potential in eliminating the throttle. In recent years, various kind of IVC systems have been developed, but only few has been successfully brought into the market, such as the Valvetronic, Valvematic and MultiAir (UniAir) [5, 16, 19]. A considerable improvement in engine performance and fuel economy at partial load has been reported by using these systems [3, 13].

Many engine concerns are working on design solutions of valve trains in which the valve movement control will be completely independent. The most advanced works are on mechanisms in which the opening and closing of valves is performed using electromagnetic systems [4, 9, 10, 15].

Camless valve trains, in which the valve motion is completely independent of the piston motion, can improve the fuel economy by 20% or higher with no pumping loss for SI engines [17]. Optimizing the valve timing at all operating conditions results in a nearly flat torque characteristic with 10% increase in maximum torque and up to 50% at low torque [17].

Initial tests of a passenger car, according to the Japanese driving cycle (type 10-15), with an SI engine equipped with an electromagnetic valve actuator showed the possibility of reducing fuel consumption by approximately 7% compared to an engine with a conventional timing system [14]. These tests also showed an increase in torque by 20% in the range of low and medium engine loads. On the other hand, tests of the car, carried out according to the NEDC, with the SI engine also equipped with an electromagnetic valve control system, showed a reduction in fuel consumption of up to 19% [12]. An increase in torque of up to 20% in the low engine load range was also found.

Camless timing systems in internal combustion engines are also developed on the basis of an electrohydraulic drive [11, 20]. The first car, produced in series since September 2009, to use an SI engine with the UniAir system characterized by full variable valve timing is the Alfa Romeo MiTo [8]. The drive unit used in this car is a turbocharged SI engine with a maximum power of 100 kW. This engine uses an electrohydraulic system for independent control, but only the intake valves. The exhaust valves are controlled conventionally by means of a camshaft. The benefits of using the UniAir system are as follows [1, 7]:

- reduction of fuel consumption up to 10%,
- power increase up to 10%,
- increase of the torque up to 15% in the range of lower engine loads.

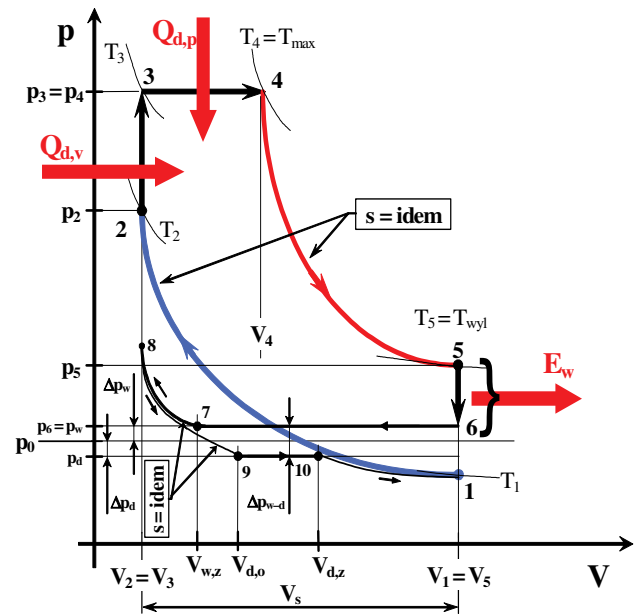
However, with the electro-hydraulic UniAir system, the maximum valve lift is reduced when the inlet valve is earlier closed. Electromagnetic motor valve drives do not have this disadvantage [2, 18].

A novelty in the presented solutions, which are the subject of the research, is the development and analysis of a system of fully independent control of valves, both inlet and exhaust. The task of the inlet valves will be to adjust the mass of the charge load to the required engine load. On the other hand, the independent movement of the exhaust valves will enable the controlled retention of the rest of the exhaust gas in the cylinder, i.e. the implementation of inter-

nal exhaust gas recirculation. Thus, the aim of using fully independent valve control (FIVC) is to eliminate the throttle, the regulatory function of which is taken over by the valves, while maintaining quantitative control of the engine load.

2. Basic features of the cycle

A fully independent valve control (FIVC) system is achieved by combining the early inlet valve closing (EIVC) system [6, 21] with the early exhaust valve closing (EEVC) system [20]. The FIVC system enables the implementation of internal exhaust gas recirculation and full adjustment of the fuel dose. The theoretical open cycle of a piston internal combustion engine for a fully independent valve control system is shown in Fig. 1.



p_d – pressure in the intake system p_w – pressure in the exhaust system
 p_0 – ambient pressure s – entropy
 V_s – cylinder displacement

Fig. 1. Open, ideal cycle for the system of fully independent valve control (FIVC)

The engine load regulation in the FIVC system is made using two independent control parameters:

- compression ratio of the recirculated exhaust gas $\epsilon_{w,z}$:

$$\epsilon_{w,z} = \frac{V_{w,z}}{V_2}, \quad (7)$$

which is a parameter that regulates the mass of the recirculated exhaust gas m_{sr} ,

- relative cylinder volume $\epsilon_{d,z}$ at which the intake valve closes:

$$\epsilon_{d,z} = \frac{V_{d,z}}{V_2}, \quad (8)$$

which is a parameter that regulates the mass of fresh charge fed to the cylinder.

The values of the control parameters in relative terms, depending on the cycle work L_o , are shown in Fig. 2. The cycle work L_o is related to the maximum work $L_{o,max}$ of the

Seiliger-Sabathe open cycle. The dependence of the cycle work on the control parameters is linear, which is advantageous for regulatory reasons.

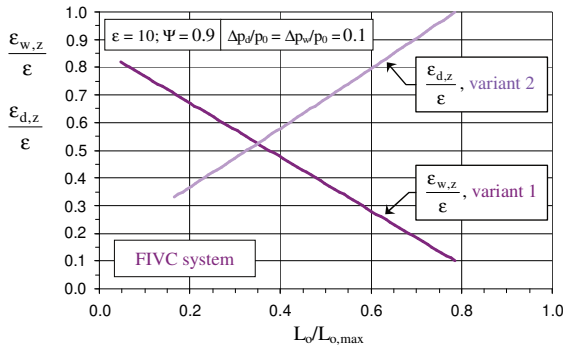


Fig. 2. Control parameters for the FIVC system versus cycle work for two boundary variants

The characteristics in Fig. 2 and in all other figures are presented for two limit variants of the analysed system:

- **variant 1:** for $\epsilon_{d,z} = \epsilon = \text{idem}$, then the control parameter is $\epsilon_{w,z} = \text{var}$,
- **variant 2:** for $\epsilon_{w,z} = 1 = \text{idem}$, then the control parameter is $\epsilon_{d,z} = \text{var}$.

3. Fuel dose

The basic parameters deciding about the amount of fuel dose are (Fig. 1): $V_{w,z}$ – cylinder volume when closing the exhaust valve, $V_{d,o}$ – cylinder volume corresponding to the beginning of the inlet valve opening, $V_{d,z}$ – cylinder volume when closing the inlet valve, Δp_w – exhaust gas pressure drop in the exhaust system, Δp_d – air pressure drop in the intake system, λ – excess air ratio.

Assuming that $\lambda = \text{idem}$, the fuel dose can be expressed as follows [20]:

$$m_p = m_{p,0} \frac{p_d}{p_0} \frac{V_{d,z} - V_{d,o}}{V_1 - V_2}, \quad (9)$$

where $m_{p,0}$ – base amount of fuel dose, corresponding to the maximum mass of fresh charge delivered to the cylinder, p_d – intake manifold pressure.

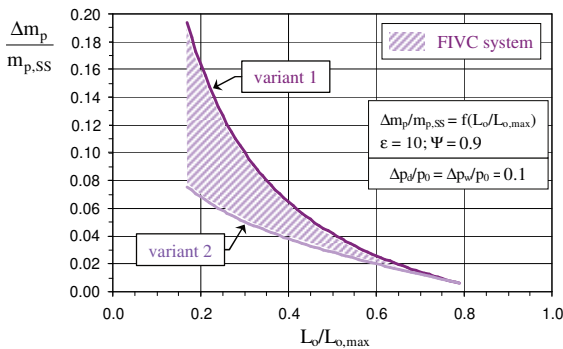


Fig. 3. Relative reduction of the fuel dose $\Delta m_p/m_{p,SS}$ for the FIVC system compared with the classic throttle governing system, versus cycle work

The relative reduction of the fuel dose $\Delta m_p/m_{p,SS}$ for the FIVC, compared to the system with classic throttle control, is shown in Fig. 3. The hatched area covers the full range of value changes of two independent engine load control pa-

rameters $\epsilon_{w,z}$ and $\epsilon_{d,z}$. A reduction of the fuel dose in relation to the classical throttle control was found in the whole load range, and particularly significant (reaching up to 18%) in the low load area.

4. Charge exchange work

The work of charge exchange L_w for the FIVC can be written as the sum of the components of the useful works:

$$L_w = L_{u,6-7} + L_{u,7-8} + L_{u,8-9} + L_{u,9-10} \quad (10)$$

The index μ of the relative charge exchange work is defined as the ratio of the charge exchange work L_w (10) to the cycle work L_o :

$$\mu = \frac{|L_w|}{L_o} \quad (11)$$

The work of charge exchange L_w for the FIVC system is shown in Fig. 4. In this figure, for comparison, the work for the Seiliger-Sabathe open cycle is also presented. The course of the charge exchange work for the FIVC system is the opposite in terms of quality, compared to the system with classic throttle control (open Seiliger-Sabathe cycle). In the FIVC system, the absolute value of the charge exchange work decreases as the engine load is reduced, which is a significant advantage. As a result, the relative work of the charge exchange μ does not reach significant values in the range of low loads (Fig. 5).

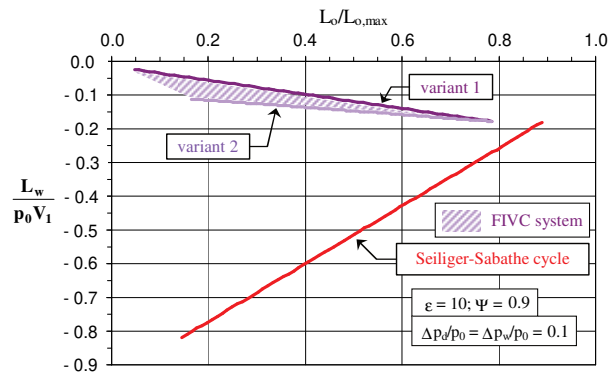


Fig. 4. Comparison of the charge exchange works $L_w/(p_0 V_1)$ for the FIVC system and Seiliger-Sabathe cycle

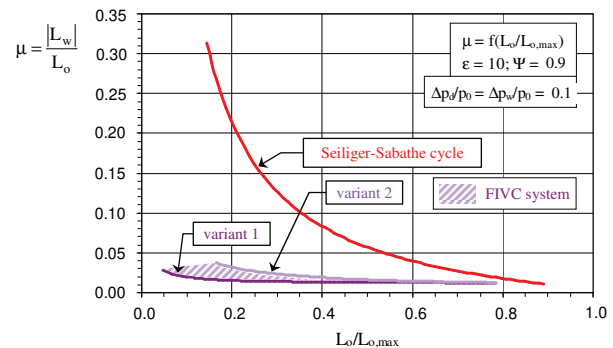


Fig. 5. Comparison of the relative charge exchange works μ for the FIVC system and Seiliger-Sabathe cycle

For the FIVC system, the index μ does not exceed 4%. Such low values of the relative work of charge exchange

are the result of the elimination of the throttle from the intake system.

5. Cycle efficiency

In the energy aspect, an important parameter is the cycle efficiency η_o . The efficiency of the theoretical cycle expresses the ratio of the work of the cycle L_o to the total energy Q_d fed into the cycle:

$$\eta_o = \frac{L_o}{Q_d} \quad (12)$$

The efficiencies η_o of the FIVC cycle and Seiliger-Sabathe cycle are shown in Fig. 6.

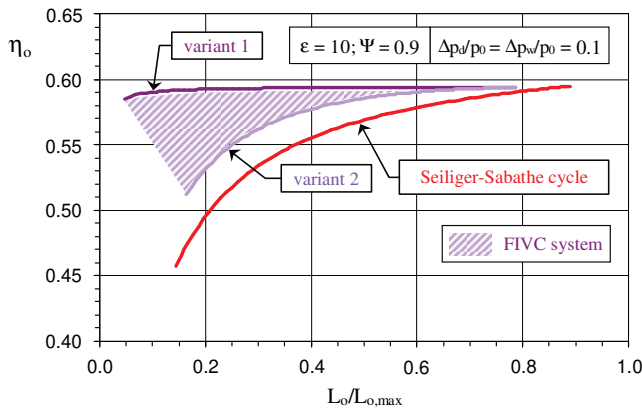


Fig. 6. Comparison of efficiencies η_o of the cycles for the FIVC system and Seiliger-Sabathe cycle

The efficiencies η_o of the cycles for the FIVC are higher than the efficiency of the open theoretical Seiliger-Sabathe cycle. By increasing the value of the cycle efficiency η_o , it is possible to increase the value of the effective energy efficiency η_e of an engine. The highest efficiency is achieved by the cycle for the limit variant 1. In the range of low loads, the cycle efficiency of the variant 1 is about 0.1 greater than the efficiency of the cycle with classic throttle control. Characteristic and advantageous for variant 1 is the flat course of the cycle efficiency over the entire range of the cycle work. Thus, this variant is most suitable for load regulation of a spark-ignition engine. The only limitation in this respect may be too high values of the exhaust gas recirculation rate, but only at the lowest values of the cycle work (Fig. 7).

6. Parameters of the internal exhaust gas recirculation process

The main parameters characterizing the process of internal exhaust gas recirculation are:

– exhaust gas recirculation rate α_r :

$$\alpha_r = \frac{m_{sr}}{m_1}, \quad 0 \leq \alpha_r < 1 \quad (13)$$

where m_{sr} – mass of the recirculated exhaust gas (retained in the cylinder), m_1 – total charge mass (charge mass at point 1 of the cycle);

– multiplicity of exhaust gas recirculation α_k :

$$\alpha_k = \frac{m_{sr}}{m_m}, \quad \alpha_k > 0 \quad (14)$$

where m_m – mass of the fresh charge (mixture) fed into the cylinder.

Taking into account the relationships connecting the masses appearing in definitions (13) and (14) and additionally that $m_1 = m_{10}$, the above definitions can be written in the form:

$$\alpha_r = \frac{m_{sr}}{m_m + m_{sr}}, \quad \alpha_k = \frac{m_{sr}}{m_1 - m_{sr}} \quad (15)$$

and indicate the interdependence between the parameters α_r and α_k :

$$\alpha_r = \frac{\alpha_k}{1 + \alpha_k}, \quad \alpha_k = \frac{\alpha_r}{1 - \alpha_r} \quad (16)$$

The exhaust gas recirculation rate α_r can also be expressed by the cycle parameters. Taking into account the dependencies between the relevant cycle parameters, the following is achieved [20]:

$$\alpha_r = \frac{1 + \frac{\Delta p_w}{p_0}}{1 - \frac{\Delta p_d}{p_0}} \frac{\epsilon_{w,z}}{\epsilon_{d,z}} \left(\frac{\epsilon}{\epsilon_{d,z}} \right)^{(\kappa-1)} \frac{\phi^{-\kappa} M_{sr}}{\gamma M_1} \quad (17)$$

Similarly, if formulas expressing the mass m_{sr} of recirculated exhaust gas and the mass m_m of the fresh mixture supplied are substituted in the definition (14) of the exhaust gas recirculation multiplicity α_k , and the relationships between the relevant cycle parameters are taken into account, it is obtained [20]:

$$\alpha_k = \frac{1 + \frac{\Delta p_w}{p_0}}{1 - \frac{\Delta p_d}{p_0}} \frac{\epsilon_{w,z}}{\epsilon_{d,z} - \epsilon_{d,o}} \frac{\phi^{-\kappa} \left(\frac{\epsilon}{\epsilon_{d,z}} \right)^{(\kappa-1)}}{1 + \frac{p_w}{p_1} \frac{\epsilon_{w,z}}{(\epsilon_{d,z} - \epsilon_{d,o})} \left[\left(\frac{\epsilon_{w,z}}{\epsilon_{d,o}} \right)^{(\kappa-1)} - \left(\frac{\epsilon}{\epsilon_{d,z}} \right)^{(\kappa-1)} \frac{\phi^{-\kappa}}{\gamma} \right]} \frac{M_{sr}}{M_m} \quad (18)$$

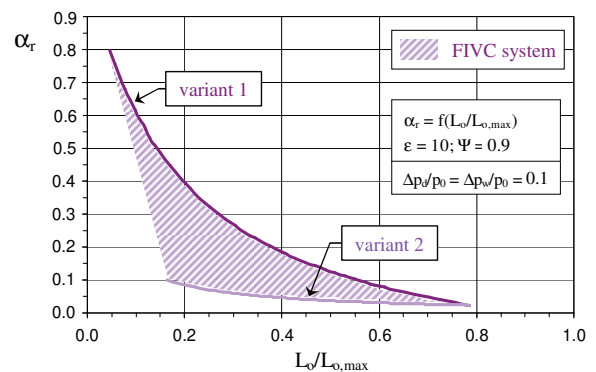


Fig. 7. Exhaust gas recirculation rate α_r for the FIVC system versus cycle work

The exhaust gas recirculation rate α_r and multiplicity the exhaust gas recirculation α_k for the FIVC system, depending on the cycle work, are shown in Figs 7 and 8, respectively.

In the range of low loads, for the limit variant 1 of the load control, high values of the recirculation rate α_r (up to 80%) are achieved, and the recirculation multiplicity α_k reaches 4. These values may turn out to be too high due to

the certainty of ignition, as well as the correctness of the fuel combustion process. Then, when using the FIVC system to regulate the load in the engine, the FIVC system in this area of the engine operation will not be available. The acceptable values of the recirculation rate and the exhaust gas recirculation multiplicity may be determined only through experimental tests.

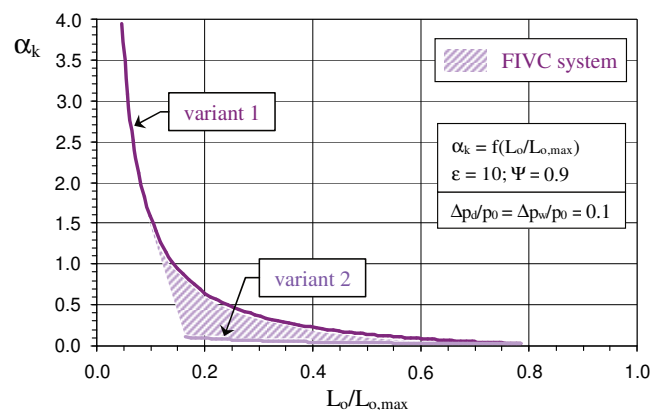


Fig. 8. Multiplicity of exhaust gas recirculation α_k for the FIVC system versus cycle work

The ecological aspect of the application of the FIVC system should also be emphasized. Thanks to exhaust gas recirculation, the maximum combustion temperature is lowered, thereby reducing nitrogen oxide emissions. More-

over, the heat flux (heat loss) to the cylinder walls is reduced.

7. Conclusion

The observed beneficial effects of the use of the fully independent valve control system are, first of all, the result of elimination of the throttle as an actuator for regulating the SI engine load, while maintaining quantitative load regulation. In the scope of regulation of filling and engine load, in the proposed system the valves take over the function of the throttle. It has been confirmed that one of the significant ways to improve the efficiency of SI engines, especially in terms of partial loads, is to reduce the work of charge exchange. The work of charge exchange for the analysed FIVC system is much smaller than the work of charge exchange for the classic throttle control (Seiliger-Sabathe cycle). For the FIVC system, the value of the relative charge exchange work does not exceed 4% over the entire load range. As a result, in the low load range, the efficiency of the FIVC cycle is increased by more than 10 percentage points compared to the Seiliger-Sabathe cycle.

For ecological reasons, it may also be beneficial to combine the proposed independent valve control system with other primary and secondary measures aimed at reducing emission of harmful substances.

Acknowledgements

This scientific work was supported by Faculty of Power and Environmental Engineering of the Silesian University of Technology within the statutory research.

Nomenclature

EIVC	early inlet valve closing
EEVC	early exhaust valve closing
FIVC	fully independent valve control
ICE	internal combustion engine
IVC	independent valve control
L	work
m	mass
M	molar mass
N	power
NEDC	New European Driving Cycle
p	pressure

Q	heat
SI	spark ignition
T	temperature
V	volume
α_k	multiplicity of exhaust gas recirculation
α_r	exhaust gas recirculation rate
ϵ	compression ratio
λ	excess air ratio
η	energy efficiency
μ	relative charge exchange work
Ψ	heat distribution number

Bibliography

- BERNARD, L., FERRARI, A., MICELLI, D. et al. Electrohydraulic valve control with "MultiAir" technology. *MTZ – Motortechnische Zeitschrift*. 2009, **70**, 4-10. <https://doi.org/10.1007/BF03226988>
- CHANG, S.C. Stability analysis, routes to chaos, and quenching chaos in electromechanical valve actuators. *Mathematics and Computers in Simulation*. 2020, **177**, 140-151. <https://doi.org/10.1016/j.matcom.2020.04.021>
- COPE, D., WRIGHT, A., CORCORAN, C. et al. Fully flexible electromagnetic valve actuator: design, modelling and measurements. *SAE Technical Paper* 2008-01-1350. 2008. <https://doi.org/10.4271/2008-01-1350>
- DIMITROVA, D., TARI, M., LANUSSE, P. et al. Robust control for an electromagnetic actuator for a camless engine. *Mechatronics*. 2019, **57**, 109-128. <https://doi.org/10.1016/j.mechatronics.2018.12.004>
- FLIERL, R., GOLLASCH, D., KNECHT, A. et al. Improvements to a four-cylinder gasoline engine through the fully variable valve lift and timing system UniValve. *SAE Technical Paper* 2006-01-0223, 2006. <https://doi.org/10.4271/2006-01-0223>
- FRANCA, O.M. Impact of the Miller cycle in the efficiency of an FVVT engine during part load operation. *SAE Technical Paper* 2009-36-0081. 2009. <https://doi.org/10.4271/2009-36-0081>
- HAAS, M. UniAir – the first fully variable, electrohydraulic valve control system. *9th Schaeffler Symposium Book*, 2010.
- HAAS, M., RAUCH, M. Electrohydraulic fully variable valve train system. *MTZ – Motortechnische Zeitschrift worldwide*. 2010, **71**, 16-21. <https://doi.org/10.1007/BF03227946>

- [9] JIAYULU, J., CHANG, S. Precise motion control of an electromagnetic valve actuator with adaptive robust compensation of combustion force. *Journal of the Franklin Institute*. 2019, **356**(4), 1750-1770. <https://doi.org/10.1016/j.jfranklin.2018.12.010>
- [10] MIANZO, L., NEWTON, S., POPOVIC, Z. Integrated control and power electronics for an electromechanical valve actuation system. *Proceedings of the IEEE/ASME*. 2005, 485-491. <https://doi.org/10.1109/AIM.2005.1511029>
- [11] MITIANIEC, W., BAC, G. Camless hydraulic valve timing system in combustion engines. *Combustion Engines*. 2011, **146**(3), 28-37. <https://doi.org/10.19206/CE-117089>
- [12] PICRON, V., POSTEL, Y., NICOT, E. et al. Electromagnetic valve actuation system: first steps toward mass production. *SAE Technical Paper* 2008-01-1360. 2008. <https://doi.org/10.4271/2008-01-1360>
- [13] REINHOLZ, B.A., REINHOLZ, L., SEETHALER, R.J. Optimal trajectory operation of a cogging torque assisted motor driven valve actuator for internal combustion engines. *Mechatronics*. 2018, 51, 1-7. <https://doi.org/10.1016/j.mechatronics.2018.02.011>
- [14] SUGIMOTO, C., SAKAI, H., UMEMOTO, A. et al. Study on variable valve timing system using electromagnetic mechanism. *SAE Technical Paper* 2004-01-1869. 2004. <https://doi.org/10.4271/2004-01-1869>
- [15] SCHRÖDER, C. Ein neues elektromechanisches Ventiltriebssystem von Valeo. *MTZ – Motortechnische Zeitschrift*. 2007, **68**, 196-197. <https://doi.org/10.1007/BF03227391>
- [16] SICZEK, K. The analysis of operating conditions for valves actuated by camless coupled drive. *Combustion Engines*. 2009, **137**(2), 93-108. <https://doi.org/10.19206/CE-117186>
- [17] SICZEK, K.J. Tribological processes in the valve train systems with lightweight valves. New research and modelling. Chapter 10 – Future valve train systems. *Butterworth-Heinemann*, 2016, 205-219. <https://doi.org/10.1016/B978-0-08-100956-7.00020-5>
- [18] YANG, X., LIANG, K. Measurement and modelling of a linear electromagnetic actuator driven camless valve train for spark ignition IC engines under full load condition. *Mechatronics*. 2021, **77**, 102604. <https://doi.org/10.1016/j.mechatronics.2021.102604>
- [19] ZHOU, X., CHEN, Z., ZOU, P. et al. Combustion and energy balance analysis of an unthrottled gasoline engine equipped with innovative variable valvetrain. *Applied Energy*. 2020, **268**, 115051. <https://doi.org/10.1016/j.apenergy.2020.115051>
- [20] ŻMUDKA, Z. Energetyczne i ekologiczne aspekty doskonalenia procesu wymiany ładunku w silniku spalinowym. *Wydawnictwo Politechniki Śląskiej, Gliwice* 2010.
- [21] ŻMUDKA, Z., POSTRZENIK, S., PRZYBYŁA, G. Throttleless control of SI engine load by fully flexible inlet valve actuation system. *Combustion Engines*. 2016, **164**(1). <https://doi.org/10.19206/CE-116488>

Prof. Zbigniew Żmudka, DSc., DEng. – Faculty of Energy and Environmental Engineering, Silesian University of Technology.
e-mail: zbigniew.zmudka@polsl.pl



Prof. Stefan Postrzednik, DSc., DEng. – Faculty of Energy and Environmental Engineering, Silesian University of Technology.
e-mail: stefan.postrzednik@polsl.pl



Use of toxicity indicators related to CO₂ emissions in the ecological assessment of an two-wheel vehicle

ARTICLE INFO

Received: 8 July 2021
Revised: 18 August 2021
Accepted: 20 August 2021
Available online: 30 August 2021

The subject of the article is proposed proprietary *M* toxicity indicator, which is based on the assumption that CO₂ emissions are a measure of the correctness of the combustion process. For this purpose, gaseous exhaust compounds such as hydrocarbons, nitrogen oxides, carbon monoxide and carbon dioxide were measured and analyzed. The test object was a motorcycle, equipped with an gasoline engine with a displacement of 0.7 dm³ and a maximum power of 55 kW. The tests were carried out using the PEMS (Portable Emissions Measurement System) AxionR/S+. The exhaust emissions measurement was done in line with the WMTC (World Motorcycles Test Cycle) certification test, dedicated to vehicles in this category. The test consists of three parts, each of them lasts 600 s and has a different maximum speed value. The test was performed on a single-roller chassis dynamometer, designed for testing two-wheeled vehicles. The toxicity indicators and rotation speed results were presented as a function of time.

Key words: motorcycles, toxicity indicator, laboratory conditions, WMTC test, PEMS

This is an open access article under the CC BY license (<http://creativecommons.org/licenses/by/4.0/>)

1. Introduction

For several years, the leading direction of vehicle type-approval tests has been testing them in real operating conditions, i.e. when using the vehicle on public roads. Many scientific papers [2, 3, 5, 8, 11, 12] have shown that adopted type approval tests, such as WMTC do not fully reproduce the real operating conditions of two-wheeled vehicles, and thus also their emissions. This solution enables finding the real energy consumption and exhaust emission of the tested vehicle. In 1992, the Earth Summit was held in Brazil in Rio De Janeiro, during which 172 participating countries have agreed on their commitment, among other things, to reducing CO₂ emissions by 50 percent by 2050, compared to 1987 [13]. The largest reduction was to apply to highly developed and highly industrialized countries – including Poland. The automotive industry is one of the main sources of carbon dioxide formation. For this reason, alternative drive solutions for automotive vehicles are being developed. China, for example, has completely barred its drivers from driving taxis and buses with internal combustion engines in the centers of some cities, replacing them with those equipped with electric motors [4].

Another of the ideas to reduce emissivity is the use of an electric engine and an internal combustion engine cooperating with each other in larger vehicles. Such a hybrid system is currently widely promoted by most of the major automotive OEMs. Many manufacturers also see a niche in the European automotive market, which is two-wheeled vehicles.

Legislation in Poland allows driving two-wheeled vehicles with a category B driving license up to vehicles with an engine displacement of 125 cm³, which also facilitates exposure of more people to ecological two-wheeled vehicles. Two-wheeled vehicles help to avoid urban congestion, consume less fuel, save time spent commuting to and from

work. In addition, many cities offer free parking spaces for two-wheelers and enable bus lanes [1].

From 2017, with the entry into force of the Euro 4 limits, all newly-manufactured two-wheeled vehicles must be additionally equipped with several safety enhancing elements (braking system equipped with ABS) and a signaling device on economic driving clocks. For people requiring low fuel consumption from two-wheelers, while maintaining very good movement dynamics and having a category A driving license, motorcycles of medium engine displacement, small dimensions and compact design are provided.

2. Methodology

2.1. Test vehicle

The tests during vehicle operation were performed on a motorcycle of one of the leading Japanese manufacturers. The technical data provided in Table 1 accurately describe its specification. From the data presented in the table 1, it can be concluded that the tested vehicle has a naturally aspirated engine. The compression ratio of 11.5:1 is indeed high in relation to the classification of gasoline internal combustion engines in passenger cars, but motorcycles often have a compression ratios of even 13:1 and higher. The engine of the tested vehicle is supplied by injectors located indirectly in the inlet (one for each cylinder).

Table 1. Test motorcycle operating parameters

Engine type	2 cylinders, liquid-cooled 4-stroke, DOHC, 4-valve
Displacement	0.7 dm ³
Minimum power	55 kW/9000 rpm
Maximum torque	68 Nm/6500 rpm
Cylinder diameter/piston stroke	80.0 mm × 68.6 mm
Compression ratio	11.5:1
Lubrication system	wet oil sump

DENSO 32-bit controller communicating with other vehicle controllers (ABS module, clock display) via CAN bus was responsible for controlling the proper fuel dosage and combustion process. It had at its disposal a number of sensors monitoring the external conditions in which the vehicle is moving (external temperature, atmospheric pressure) as well as those reading the parameters of the engine itself. The engine unit, after warming up to its operating temperature, works in a closed loop using a narrowband lambda probe, correcting the fuel dose with its readings and ignition maps saved in the controller so as to keep the mixture close to stoichiometric. Only when switching to maximum throttle opening the controller enters the open loop and uses rigid saved maps without the need for corrections with data from the probe. This is a solution often used in road-class vehicles. Figure 1 shows the test object at the chassis dynamometer.



Fig. 1. Picture of the tested motorcycle along with the measuring apparatus on the designated dynamometer

The design of the entire engine is among the simpler designs – it has no variable timing phases, four valves per cylinder in the head are controlled by two camshafts driven by a chain directly from the crankshaft. The power supply system is also one of the less complex of those found on the motorcycle market. There are no dynamically changed lengths of the intake system, no valves or flaps in the exhaust system, one 4-hole injector per cylinder. The only important element that distinguishes this engine from the competition is the crankpins rearrangement by 270 degrees, unlike the classic 360 degrees. Despite its simplicity, the vehicle met the applicable emission standards and was approved for the European market.

2.2. Measuring equipment

In order to perform the intended tests, the device of the American company Global MRV – AxionR/S+ was used to analyze the exhaust gases. The device allows to measure emissions of harmful and toxic compounds, both gaseous: hydrocarbons (HC), carbon monoxide (CO), carbon dioxide (CO₂), nitrous oxide (NO) as well as solid particles. NO_x emission was estimated on the basis of the producer's assumption and own experience that NO constitutes 95% share in the total NO_x emission. Technical data of the apparatus is presented in Table 2, while the test object with the

measuring setup on the dynamometer stand is shown in Fig. 2. Electrochemical analyzers are used to determine NO and O₂. The concentration of the first three of these compounds is measured by an NDIR (Nondispersive Infrared Sensor) analyzer. The PM measurement method uses a Laser Scatter based method [14].

In addition, the manufacturer equipped the device with a meteorological station, a GPS and a module enabling registration of data from the on-board vehicle diagnostic system (OBD). Measurement and data acquisition was done at a frequency of 1 Hz. Corrections are made to the obtained results from the recorded data, and then the road/unit emissions of the tested exhaust gases are calculated. Moreover the AxionR/S+ allows measurement and recording of vehicle and engine data: vehicle speed, acceleration, engine speed, intake air temperature, manifold air pressure.



Fig. 2. The view of AxionR/S+

Table 2. AxionR/S+ device technical data [14]

Gas	Measurement range	Accuracy	Resolution	Type of measurement
HC	0–4000 ppm	±8 ppm abs. or ±3% rel.	1 ppm	NDIR
CO	0–10%	±0.02% abs. or ±3% rel.	0.001 vol. %	NDIR
CO ₂	0–16%	±0.3% abs. or ±4% rel.	0.01 vol. %	NDIR
NO	0–4000 ppm	±25 ppm abs. or ±3% rel.	1 ppm	E-chem
O ₂	0–25%	±0.1% ppm abs. or ±3% rel.	0.01 vol. %	E-chem
PM	0 mg/m ³ to 300 mg/m ³	±2%	0.01 mg/m ³	Laser Scatter

2.3. Chassis dynamometer

The test was carried out on a motorcycle chassis dynamometer, INERTIAL 70, manufactured by SOFT-ENGINE. It made it possible to read the instantaneous power and torque on the wheel of the vehicle, as well as acceleration, speed and distance traveled. When preparing the test stand, data on temperature and ambient pressure, humidity as well as correction factor were input into the software. The final parameter is individual for a given motorcycle model. A large number of introduced environmental parameters has a positive effect on the measurement accuracy. The dynamometer technical data were presented in Table 3.

Table 3. Technical specifications of the dynamometer station [15]

Dynamometer	Inertial
Maximum received power	59 kW (80 HP)
Maximum received velocity	180 km/h
Dimensions: length/width/height	1900/800/4200 mm
Own weight	450 kg
Software	INERTIAL 3.0

2.4. WMTC test

The World Motorcycle Test Cycle (WMTC) is a driving cycles used to measure fuel consumption and emissions in motorcycles. The methods of WMTC cycle are set up as part of the Global Technical Regulation established under the United Nations’ World Forum for Harmonization of Vehicle Regulations. The speed curve was a reflection of the speed characteristic of the harmonized WMTC type approval test, consisting of three phases (Fig. 3). Each of them lasted 600 seconds and was characterized by a different maximum value of the speed.

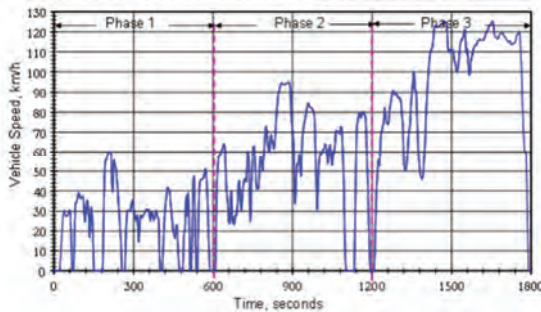


Fig. 3. WMTC test [10]

2.4. Phases of the test

After setting up the test vehicle on the stand, a number of sensors and probes had to be mounted on the vehicle. To the stub pipe, before the throttle, a cable was routed that passed information about the engine vacuum to the vacuum transducer. The transducer converts the pressure values into the corresponding DC voltage in the range from 0.5–5.5 V (Fig. 4). Next, a temperature probe was placed in the intake system) connected to the measuring device.

To read the rotational speed of the crankshaft, it was necessary to use a sensor fastened with a high-voltage cable behind the ignition coil attached by the PEMS manufacturer to the measuring equipment kit. Figure 5 shows the speed sensor after mounting it on an adapted high voltage cable.

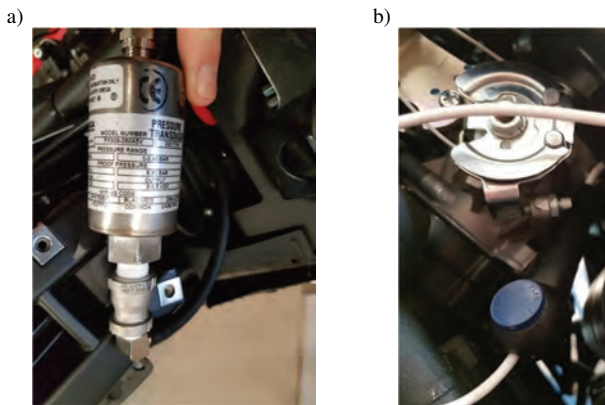


Fig. 4. Tooling for the intake manifold: a) vacuum transducer, b) temperature probe



Fig. 5. Speed sensor mounted on the high voltage cable

After preparation of the vehicle, it was necessary to calibrate the AxionR/S+ measuring device using technical gases in gas bottles located at the test stand. After a successful calibration process, the probe was mounted on the end of the motorcycle exhaust system introduced to a depth of about 20 cm. With the coordinated cooperation of the recording equipment operator and the motorcycle operator, the measurement process was started so that the values of speed, duration it is maintained, distance traveled and accelerations corresponded as closely as possible to the WMTC test procedure.

2.5. Definition of motorcycle toxicity indicators in relation to CO₂

Based on the basic combustion equations, a new toxicity factor M was proposed, which is the ratio of CO₂ to other toxic exhaust gas compounds. It was assumed that the toxicity index plays the role of a measure of the correctness of the combustion process. The values to be substituted for the formula structure formulated by the authors must be expressed in the same units, which will allow for its dimensionlessness, as a result of which a comparative analysis of vehicles of different categories and intended use is possible. The toxicity index thus defined makes it possible to efficiently compare different heat engines with each other with exhaust aftertreatment systems. The dimensionless quantitative toxicity index M is defined by the quotient:

$$M_j = b \cdot \frac{e_{real,j}}{e_{CO_2}} \tag{1}$$

where: M – dimensionless toxicity indicator [–]; j – toxic exhaust component for which the emission indicator was determined; b – universal constant (for CO, THC and NO_x = 10³, for PM = 10⁵); e_{real,j} – specific emission, road emission or mass of toxic compound j determined during the measurements in the emission test [g/(kW·h); g/(km); g]; e_{CO₂} – specific emission, road emission or mass of CO₂ determined during the measurements in the emission test (having the same unit as e_{real,j}) [g/(kW·h); g/(km); g].

The presence of the constant b allows to increase the readability of the results, because the number of decimal places is limited. This has been confirmed on other vehicles that meet various emission standards [6, 7, 9]. Therefore, it is possible to ecologically assess the L-category vehicles and vehicles of other categories based on the proposed M factor in terms of emission tests obtained both in laboratory tests and in real operating conditions.

3. Results

On the basis of the measurement data recorded during the tests, the second emission of individual toxic compounds (HC, CO, NO_x) was determined, which was then compared to the second emission value of CO₂. When analyzing the results obtained during the test, some dependencies of CO₂ emissions and toxicity indicators on the instantaneous test conditions can be observed.

Due to the direct relationship of the amount of CO₂ with the amount of fuel consumed, it was found that when the demand for fuel is high (driving at higher speed, sudden accelerations) the amount of carbon dioxide increases in direct proportion (Fig. 6). The average rate of CO₂ emissions in the test was 1.69 g/s.

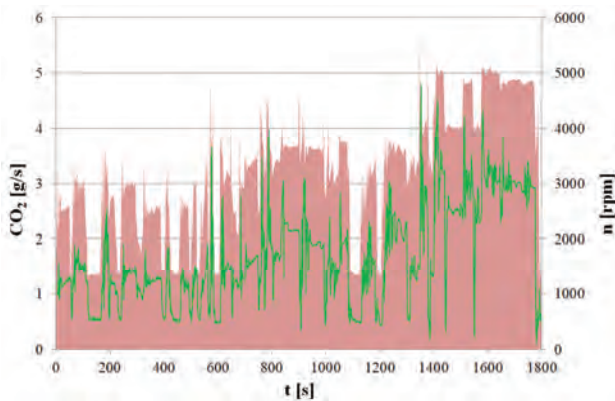


Fig. 6. The course of the engine torque and the CO₂ emission intensity recorded during the tests in the WMTC test

The observed relationship is the significantly increasing value of carbon monoxide toxicity during engine braking, where the local maximum M_CO of the engine operation near idling and CO₂ emission close to zero at these points was recorded (Fig. 7). This is, among others, due to insufficient heating of the combustion chamber and low temperature of the exhaust system (idling). This enriched the mixture to the $\lambda < 1$ range, which is one of the main causes of carbon monoxide formation.

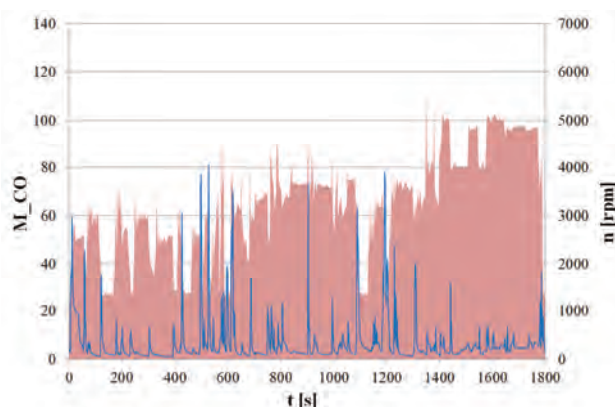


Fig. 7. The course of the engine torque and the M index for CO recorded during the tests in the WMTC test

In addition to the negative phenomena in the engine cylinders, a significant impact on the significant value of the dimensionless M index is also caused by the incorrect oper-

ation of the exhaust gas treatment system – a three-way catalytic converter. Significant values of M_CO (~ 60) were obtained in the first minute of the research test, i.e. for idling, where the aftertreatment systems had not yet worked, and the combustion temperature was low.

Most of the factors contributing to the formation of an excessive amount of carbon monoxide in the exhaust gas (flame extinction, incomplete combustion) also cause an excessive content of hydrocarbons, hence the highest toxicity values of both compounds were recorded at the same points of the test (engine braking), where CO₂ emission was close to zero (Fig. 8). The local maximum (55) was recorded in the third phase of the test during sudden braking. The mean value of the toxicity index for the entire trip was 2.7.

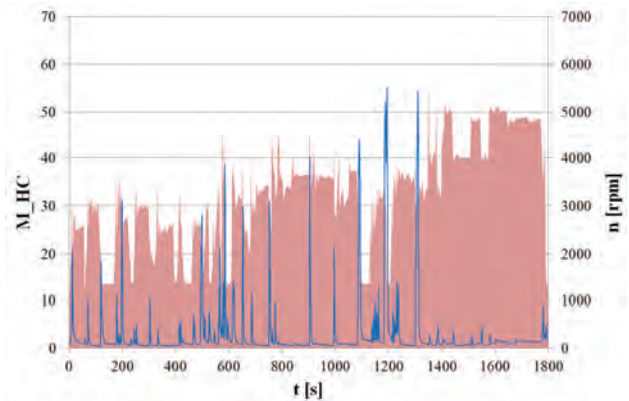


Fig. 8. The course of the engine torque and the M index for HC recorded during the tests in the WMTC test

The analyzed index M in the cases considered so far is characterized by a strong dependence in the points of the engine operation where the reduction of the engine torque occurs. Otherwise, it is the opposite in relation to NO_x (Fig. 9).

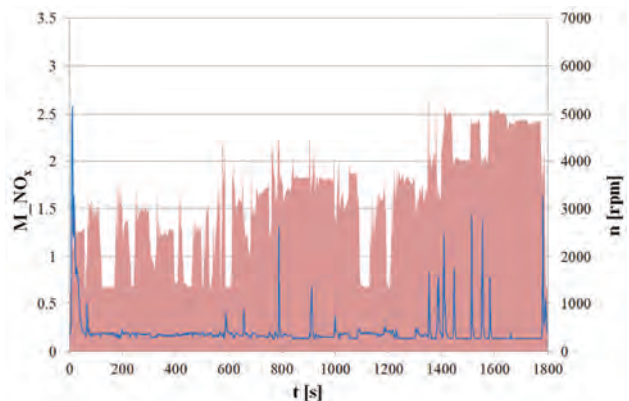


Fig. 9. The course of the engine torque and the M index for NO_x recorded during the tests in the WMTC test

The maxima of the considered parameter occur during the rapid increase of the rotational speed. When accelerating the vehicle, when the power train requires a lot of energy, more fuel is transferred to the cylinders. This has a direct impact on obtaining significant temperatures (over 2300 K) in the front of the flame during combustion. According to Zeldowicz's theorem, these are very favorable conditions for NO_x formation. The sudden and strong emis-

sion intensity of the compound under consideration is so significant in comparison to CO₂ that it causes the extremes (above 1) in the analyzed test.

The tests were carried out with the utmost care to reproduce the conditions of actual type approval tests as accurately as possible. The test was carried out on a chassis dynamometer, in a ventilated room, but with an ambient temperature lower than recommended in the legislation. In addition, to avoid the stage of heating the vehicle to operating temperature during the test, the vehicle has previously been warmed up. This in turn caused that during the final stages of measurements, the cooling that was to be provided by the electric fan ceased to be sufficient and the temperature of the coolant began to rise above normal operating conditions (78–95°C – operating temperature) and reached 110°C. This temperature was still below the maximum allowable temperature (this was set by the manufacturer at 115°C). Based on the determined masses of individual gaseous compounds, a comparison of their M toxicity indices was made (Fig. 10). Due to the dimensionlessness of the M index, it is possible to compare not only terms of the same category, but also objects belonging to different groups. Therefore, the obtained results from the motorcycle were compared to the results of a vehicle of another category. In the work of the authors [7], considerations were made in the aspect of the use of the toxicity index for conventional, hybrid and alternative fuel city buses. The measurements were made in accordance with the SORT 2 drive test procedure and on the test route in the Poznań agglomeration. The comparison of the results of both studies shows that the two-wheel vehicle achieves the most similar values of the M index for each of the considered toxic compounds with the values recorded for a bus powered by compressed natural gas (M_CO = 6.5; M_HC = 1.65; M_NO_x = 0.51).

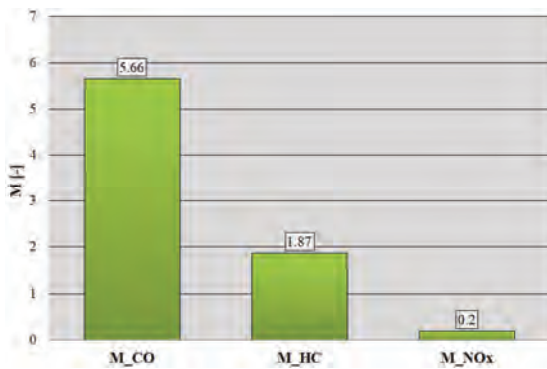


Fig. 10. Summary of M toxicity indicators for CO, HC, and NO_x when tested in the WMTC test

4. Conclusions

At present, concepts such as ecology, environmental protection and global climate change are not just points of

discourse but a real challenge for vehicle manufacturers. Therefore, actions are taken that have a direct impact on the development of modern drive systems. Referring to the European policy of Sustainable Development, it can be said that the direction in which the further development of technology will be directed will have a key impact on the future, which will be experienced not only by us, but above all by future generations. Until 1997, two-wheelers were not subject to any Euro emission limits. Only from this moment manufacturers began to use three-way catalytic converters. Considering the progress in reducing emissions of passenger cars and trucks, it is clear that the two-wheeler market is still just waiting for the challenges posed by Euro norms.

The paper presents exhaust emission tests of a vehicle meeting the Euro 4 norm, in which tests were carried out on a chassis dynamometer in accordance with the currently applicable type approval regulations. The test vehicle has been prepared and instrumented in such a way that it was possible to determine its ecological indicators. A new proprietary M toxicity index has been proposed, which is based on the use of carbon dioxide measurements (e.g. the emission intensity of this compound). The values substituted into its structure must be expressed in the same units, which will allow for its dimensionlessness and comparative analysis of vehicles of different categories.

In order to meet the requirements of the Euro 4 norm in motorcycles, there was no need to seek advanced control of the fuel supply system, or relying on direct injection. It was also not necessary to use electronically controlled throttles. From January 1, 2020, a new emission norm – Euro 5 for newly manufactured motorcycles will come into force. Given its guide-lines, it is expected that manufacturers in the near future will be forced to apply the solutions currently commonly used by car manufacturers. Probably the future will mostly rely on turbocharged engines, with direct injection and variable valve timing. Taking into account the construction of the test vehicle and the results of the research, it can be stated that:

- Using an electronically controlled throttle would be beneficial. This would reduce HC emissions primarily by compensating for rapid throttle openings.
- Striving for the fastest and most frequent engine operation in steady state mode would contribute to reducing CO and NO_x emissions. One way to achieve this could be to use a coolant pump that is disconnected during cold start. To do this simply, the pump should be electrically driven and controlled by a separate program in the engine control unit. This would increase the speed of warming up the engine to its operating temperature, which would reduce the time operating on rigid maps and allow faster work in closed loop mode.

Bibliography

- [1] DZIENNIK USTAW. Ustawa Dz.U.2017.1260, Prawo o ruchu drogowym. 20 czerwca 1997.
- [2] KHAN, T., FREY, T.C. Comparison of real-world and certification emission rates for light duty gasoline vehicles. *Science of The Total Environment*. 2018, **622**, 790-800. <https://doi.org/10.1016/j.scitotenv.2017.10.286>
- [3] KUMAR PATHAK, S., SOOD, V., SINGH, Y., et al. Real world vehicle emissions: their correlation with driving parameters. *Transportation Research Part D: Transport and Environment*. 2016, **44**, 157-176. <https://doi.org/10.1016/j.trd.2016.02.001>

- [4] LAMBERT, F. Shenzhen shows the world how it's done, electrifies all public transit with massive fleet of 16,000+ electric buses. <https://electrek.co/2017/12/28/shenzhen-electrifies-entire-public-transit-fleet-electric-buses> (accessed on 28.06.2021).
- [5] MERKISZ, J., PIELECHA, J., BIELACZYK, P. et al. Analysis of emission factors in RDE tests as well as in NEDC and WLTC chassis dynamometer tests. *SAE Technical Paper* 2016-01-0980. 2016. <https://doi.org/10.4271/2016-01-0980>
- [6] MERKISZ, J., RYMANIAK, Ł. Determining the environmental indicators for vehicles of different categories in relation to CO₂ emission based on road tests. *Combustion Engines*. 2017, **170**(3), 66-72. <https://doi.org/10.19206/CE-2017-310>
- [7] MERKISZ, J., RYMANIAK, Ł. The assessment of vehicle exhaust emissions referred to CO₂ based on the investigations of city buses under actual conditions of operation. *Eksplatacja i Niezawodność – Maintenance and Reliability*. 2017, **19**(4), 522-529. <https://doi.org/10.17531/ein.2017.4.5>
- [8] O'DRISCOLL, R., STETTLER, M.E.J., MOLDEN, N. et al. Real world CO₂ and NO_x emissions from 149 Euro 5 and 6 diesel, gasoline and hybrid passenger cars. *Transportation Research Part D: Transport and Environment*. 2018, **62**1, 282-290. <https://doi.org/10.1016/j.scitotenv.2017.11.271>
- [9] RYMANIAK, Ł., MERKISZ, J., SZYMLET, N. et al. Use of emission indicators related to CO₂ emissions in the ecological assessment of an agricultural tractor. *Eksplatacja i Niezawodność – Maintenance and Reliability*. 2021, **4**(23), 605-611. <https://doi.org/10.17531/ein.2021.4.2>
- [10] THE EUROPEAN COMMISSION. Commission delegated regulation (EU) No 134/2014 of 16 December 2013 supplementing Regulation (EU) No 168/2013 of the European Parliament and of the Council with regard to environmental and propulsion unit performance requirements and amending Annex V thereof. 2013.
- [11] THOMAS, D., LI, H., WANG, X. et al. A comparison of tailpipe gaseous emissions for RDE and WLTC using SI passenger cars. *SAE Technical Paper* 2017-01-2391. 2017. <https://doi.org/10.4271/2017-01-2391>
- [12] TSAI, J.H., CHIANG, H.L., HSU, Y.C. et al. Development of a local real world driving cycle for motorcycles for emission factor measurements. *Atmospheric Environment*. 2005, **39**, 6631-64 <https://doi.org/10.1016/j.atmosenv.2005.07.040>
- [13] UNITED NATIONS CONFERENCE ON ENVIRONMENT. Preamble to the Declaration of the United Nations Conference on Environment and Development: Rio de Janeiro, 3-14 June 1992. (1992: Rio de Janeiro, Brazil).
- [14] Global MRV. www.global.mrv (accessed on 28.06.2021)
- [15] Soft-Engine. www.soft-engine.org (accessed on 28.06.2021)

Natalia Szymlet, MEng. – Faculty of Civil and Transport Engineering, Poznan University of Technology.
e-mail: natalia.r.szymlet@doctorate.put.poznan.pl



Przemysław Tutak, BEng. – Faculty of Civil and Transport Engineering, Poznan University of Technology.
e-mail: p.tutak86@gmail.com



Prof. Piotr Lijewski, DSc., DEng. – Faculty of Civil and Transport Engineering, Poznan University of Technology.
e-mail: piotr.lijewski@put.poznan.pl



Michalina Kamińska, MEng. – Faculty of Civil and Transport Engineering, Poznan University of Technology.
e-mail: michalina.kaminska@put.poznan.pl



Prof. Łukasz Rymaniak, DSc., DEng. – Faculty of Civil and Transport Engineering, Poznan University of Technology.
e-mail: lukasz.rymaniak@put.poznan.pl



A rotating piston engine with electric generator in serial hybrid propulsion system for use in light aircraft

ARTICLE INFO

Received: 15 July 2021
 Revised: 27 July 2021
 Accepted: 17 August 2021
 Available online: 1 September 2021

Analysis of the possibility of using a rotary engine based electric generator to propel a powered sailplane. The paper presents analysis of utilising Wankel type engine as a power input for an electric generator in the motor glider propulsion system. This generator would be a part of the propulsion system of a hybrid motor glider using the AOS 71 motor glider airframe. In the research, the rotational characteristics of the LCR 407ti wankel engine were determined experimentally. Driving torque run, power and fuel consumption were determined as a function of engine speed. The obtained results are presented in diagrams. The conceptual diagram of the hybrid drive is presented. The electric generator was selected and its effectiveness, as well as the effectiveness of entire propulsion system was assessed from the motor glider's performance point of view. Basing on the research conducted, conclusions were drawn and there were indicated the objectives and directions of further research on hybrid propulsion with specific aerodynamic and mass limitations of the aircraft.

Key words: hybrid, combustion engines, motor glider, rotary engine, Wankel engine, hybrid propulsion

This is an open access article under the CC BY license (<http://creativecommons.org/licenses/by/4.0/>)

1. Introduction

Aviation designs, especially in relation to light aircraft, are increasingly often equipped with electric propulsion [1, 2]. The electric motors drive the propellers to generate thrust. The use of electric motors brings a number of advantages such as [15]: a) low level of vibrations generated by the drive unit, b) high unit power (power to weight ratio of the electric motor), c) flat torque waveform available from low engine speed, thanks to which the propeller can cooperate with the engine at high efficiency. The energy needed to run these motors can be obtained from batteries. This is the easiest way to configure such a power unit. Unfortunately, the still large mass of batteries and their low energy density limit the payload carried on board the plane and the range of the aircraft [5–10]. To overcome these disadvantages a hybrid propulsion can be considered – a propulsion in which an additional source of energy, especially an internal combustion engine, will be installed on board. The application where the electric motor driving the propeller draws energy from a set of batteries and a generator driven by an internal combustion engine is called a series hybrid [7]. The diagram of the series hybrid drive system is shown in Fig. 1 [8].

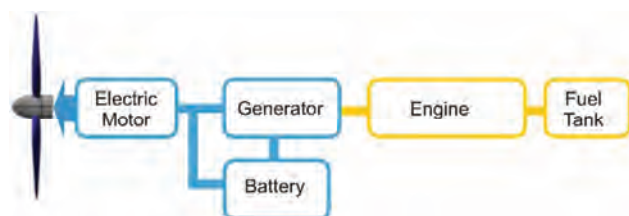


Fig. 1. Series hybrid system

In systems with a high degree of hybridization, the combustion unit and the electric generator are used to recharge the battery and maintain its capacity, thus increasing the range and duration of the flight. The system of an internal combustion engine and an electric engine cooperating

as an electric energy generator is called a range extender in the English literature. The article will describe the method of selecting such a propulsion for a light aircraft.

2. Description of the research object

The research object used to carry out the research is the AOS H2 motor glider airframe, developed by the consortium of Rzeszów University of Technology, Warsaw University of Technology, AGH University of Science and Technology and Zakład Szybowcowy Jeżów Henryk Mynarski. It is in use at the Department of Aerospace Engineering of Rzeszów University of Technology as a research object. It is built in the arrangement of a cantilever high-wing with classic empennage. The materials used for its construction were mostly carbon fibre reinforced epoxy composites, with some parts made of glass and aramid fibers. The powered sailplane has a single-spar wing with an auxiliary rear spar. The fuselage with the tailplane is a single-piece semi-monocoque structure. The aircraft has a hybrid propulsion, where the energy needed for take-off and flight comes from both the Li-Poly battery pack, located in the front part of the fuselage, and the hydrogen fuel cell, located behind the pilot's cabin in the fuselage. The power unit consists of the EMRAX 268 engine located on a fixed mast in the rear part of the fuselage and a two-bladed wooden propeller. The view of the powered sailplane is shown in Fig. 2.



Fig. 2. The AOS H2 motor glider

Table 1 shows the basic data of the airframe, while Fig. 3 present the values of power required for the flight for this airframe depending on the flight speed.

Table 1. Basic data of the AOS H2 motor glider [13, 14]

Wing area	S [m ²]	15.8
Wing span	R [m]	16.4
Aspect ratio	Λ	17
Maximum take-off mass	M _{max} [kg]	660
Minimum motor glider mass	M _{min} [kg]	500

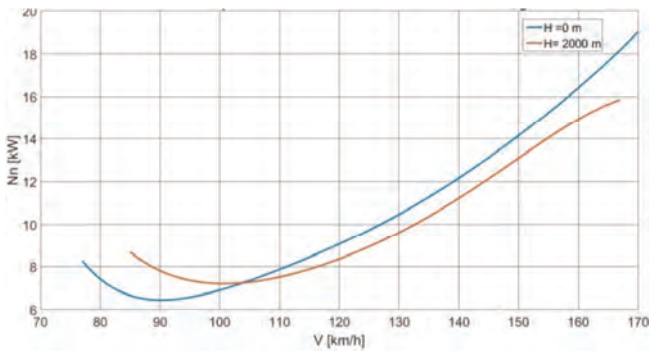


Fig. 3. Power required for flight in the function of flight speed – for the AOS H2 motor glider; M_{max} = 660 kg [13, 14]

In the analyzed case, the hydrogen fuel cell was replaced with an internal combustion engine cooperating with an electric generator. The diagram of this drive is shown in Fig. 4.

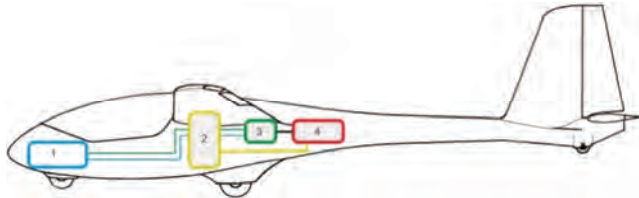


Fig. 4. Diagram of the hybrid propulsion system with an internal combustion engine for the AOS motor glider: 1 – battery, 2 – fuel tank, 3 – Emrax 188 engine working in generator mode, 4 – Wankel AG 407 TG engine

3. Cooperation of a rotary engine and an electric generator

In the serial hybrid system adopted for analysis, the generator should meet the following assumptions:

- high unit power,
- low level of vibrations generated by the drive unit,
- easy-to-use,
- high level of reliability [15].

In the analysis, the Wankel AG 407TG rotating piston engine was selected to drive the electric generator. This choice was dictated by the advantages of rotary piston engines, such as low engine weight, low vibration levels and high drive torque compared to reciprocating piston engines. The engine runs on a mixture of gas and two-stroke oil in the ratio of 100:1 – which significantly simplifies its design and weight (no lubricating oil system needed).

Table 2 presents a comparison of selected data of several internal combustion engines with a similar power range used in general aviation.

Table 2. Technical data of internal combustion engines[15, 16]

Engine		407TG	Rotax 125	Rotax 28 Max
Maximum engine power	N _{max} [kW]	31.5	25	28
Maximum torque	M _{max} [Nm]	51	22	–
Engine mass	m _s [kg]	20	29	58
Revolutions for M _{max}	n _{Mmax} [rev/min]	4000	10,500	–

Table 2 shows that the Wankel engine has a relatively high unit power indicator (power related to the dry engine mass) among the remaining engines. In addition, it has a much higher torque than the 1-cylinder Rotax engine, which is available at low rotational speed. An additional advantage of using this type of engine will be less vibrations generated by a rotary engine than a traditional high-speed single-cylinder unit, which will favourably affect the fatigue strength of the engine and airframe structure.

In order to determine the scope of cooperation, it was necessary to determine the rotational characteristics of the combustion engine. Figure 5 shows the view of the test stand with an electro-swirl brake.



Fig. 5. Stand for testing engine characteristics

The determined rotational characteristic, presented in Fig. 6.

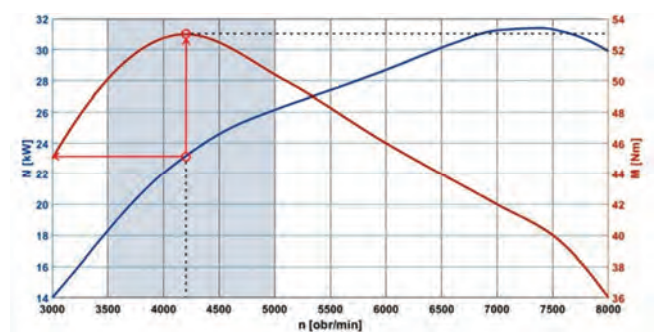


Fig. 6. Rotational characteristics of the 407tgi

The characteristics presented in Fig. 6 show that the highest torque values of the Wankel engine (above 28 Nm) range between 3500 rpm and 5000 rpm, while the maximum torque (53 Nm) corresponds to the power of about 22.5–23 kW. In these ranges the engine achieves its best thermal efficiency, which means the ratio of the power delivered to power consumed is highest with the highest

torque parameters that the engine can achieve. At the same time, the engine manual [17] provides the value of the minimum unit fuel consumption (0.3 kg/kWh) for the rotational speed of 4000 rpm, which corresponds to the power developed by the engine at the level of 22 kW. This range of combustion engine operation was adopted as the most favorable for regenerative operation.

For the cooperation of the internal combustion engine and the electric motor, the operating range of the electric motor should be selected so that – the characteristics of the electric motor (in particular, the ratio of power to the obtained revolutions) matched the characteristics of the internal combustion engine in the range close to the rotational speeds of the piston engine shaft corresponding to the ranges of maximum torque and the lowest specific fuel consumption – this is to ensure high efficiency of generating electricity – in the event of an emergency, when it is necessary to increase electricity production (beyond the range of steady operation), the electric motor should develop a maximum power greater than the maximum power of the internal combustion engine – this is to avoid damage to the electric motor [12]. Emrax 188 engine was chosen as the generatig unit with the following technical data (given in Table 4).

Table 4. Technical data of the Emrax 188 engine [16]

Engine	Emrax 188	–
Continuous power	N_{const} [kW]	32
Peak power	N_{max} [kW]	50
Continuous torque	M_{const} [Nm]	60
Engine mass	m_s [kg]	6.8

Together with the factory-dedicated control system [16], this engine is able to operate in generator mode with the efficiency of 98%.

As can be seen from Table 4, the choice of this engine was dictated by similar values of the obtained maximum continuous power. Moreover, the Emrax 188 and Emrax 268 powering the propeller, belong to the same group of engines. Hence completing the entire propulsion and integration of the electrical system will be easier based on previous experience

Figure 7 presents the characteristics of the Emrax 188 and Wankel 407TGi engines. The characteristics of the Emrax engine were obtained from the manufacturer's manual [16].

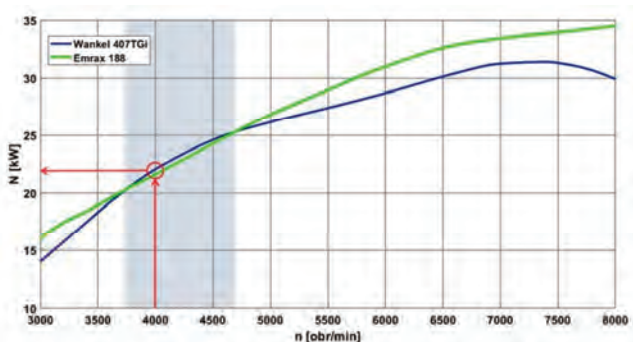


Fig. 7. Rotational characteristics of the 407tgi

On the basis of the characteristics of the engines, it can be concluded that the most favorable operating range of the generator set will be the range from 3700 rpm corresponding to 20 kW of power, to 4700 rpm corresponding to 25 kW of power. At these points, the characteristics of the motors intersect, and between these points the characteristics nearly overlap, differing of up to about 0.5 kW.

Due to the fact that the engine with a rotating piston achieves the lowest specific fuel consumption at 22 kW of developed power at 4000 rpm of the engine rotational speed, this operating point was adopted for the generator operation. The fuel mass assumed to run the generator is 7 kg. The total weight of the fuel, fuel system, internal combustion engine, electric engine and their accessories was approximately estimated on the basis of the technical parameters of the elements of the proposed modification. A mass balance of the energy source was made in order to relate it to the take-off mass of the aircraft. The analysis is summarized in Table 5.

Table 5. Specifications of the hybrid battery set

System	Mass [kg]
Fuel tank+fuel sstem	15
Engine inverter	7
High-current wiring	7,3
Battery set	60
Battery inverter	8
Generator inwrtter	10
Wankel 407 tgi ice	25
Fuel	7
Generator (Emrax 188)	7
Generator control unit	30
Complete system	176.3

In relation to the take-off weight of 660 kg, the weight of the drive unit is 26% of the take-off weight. The selected generator system works with a set of batteries of the parameters given in Table 6.

Table 6. Specifications of the hybrid battery set

Battery type	Li-Poly	–
Capacity	C [Ah]	16
Voltage	U_{bat} [V]	355

After determining the appropriate range of cooperation between the internal combustion engine and the electric engine, it is possible to determine the energy stored on board the aircraft using the following formula [1]:

$$E = I \cdot 3600 [s] \cdot U_{bat} + \eta_{gen} \cdot (N_s \cdot t_s) \quad (1)$$

were t_s – generator working time

$$t_s = \frac{m_{pal}}{SFC \cdot N_s} \quad (2)$$

where: SFC – specific fuel consumption, N_s – engine power during generator operation mode.

The energy stored on board the powered sailplane is sufficient for 2 hours and 40 minutes of flight at a speed of 100 km per hour after take-off at an altitude of 500 m.

The presented range value was calculated by dividing the energy stored on board by the power necessary to main-

tain level flight under the selected flight conditions, related to the efficiency of the engine:

$$t = \frac{E_{POZ}}{\frac{NN}{\eta_S}} \quad (3)$$

The methodology of determining energy parameters for the AOS H2 motor glider was presented in the doctoral dissertation [12].

For comparison, the AOS 71 powered sailplane with electric drive for the same flight conditions will be able to use the energy stored in the batteries only for about 40 minutes.

4. Results of research conducted and conclusions

Based on the presented research, it can be concluded that in the application of a series hybrid, the rotating piston engine provides sufficient performance. Compared to other piston engines of similar power, it has a lower weight, and due to its design, it generates a lower level of vibrations.

This is extremely important in relation to aircraft construction. In addition, a Wankel engine operating at a fixed rotational speed of the engine shaft should maintain high reliability and durability (which will be subject to further research by the authors of the article). With regard to purely electric propulsion, the use of serial hybrid propulsion, assuming unchanged take-off weight, allowed for a significant increase in the duration of the unit's operation, which will translate into an increase in the endurance and range of the flight.

The presented research shows the achievements of the authors to date in the use of a rotating piston engine as a drive for an electric generator. Currently, detailed studies of the performance characteristics of the internal combustion engine are being carried out (in cooperation with Bosmal). The next step will be the integration of the combustion and electric units.

Bibliography

- [1] AYAR, M., GULEREN, K.M., KARAKOC, T. Motor selection process with AHP on mini electric UAV. *International Symposium on Electric Aviation and Autonomous Systems ISEAS*, Kiev 2018.
- [2] BREJLE, B., MARTINS, J. Electric, hybrid, and turboelectric fixed-wing aircraft: a review of concepts, models, and design approaches. *Progress in Aerospace Sciences*. 2019, **104**, 1-19. <https://doi.org/10.1016/j.paerosci.2018.06.004>
- [3] DE VRIES, R. HOOGREEFF, M., VOS R. Preliminary sizing of a hybrid-electric passenger aircraft featuring over-the-wing distributed-propulsion. *American Institute of Aeronautics and Astronautics*. 2019. <https://doi.org/10.2514/6.2019-1811>
- [4] DONATEO, T., SPEDICANTO, L. Fuel economy of hybrid electric flight. *Applied Energy*. 2017, **206**, 723-738. <https://doi.org/10.1016/j.apenergy.2017.08.229>
- [5] FEFERMANN, Y., MAURY, C., CLELIA, C. et al. Hybrid-electric motive power systems for commuter transport applications. *30th Congress of the International Council of the Aeronautical Sciences*. Daejeon 2016.
- [6] FILLIPPONE, A. Flight performance of fixed and rotary wing aircraft. *Butteorth-Heinemann* 2006, USA.
- [7] FINGER, F.D., BRAUN, C., BIL, C. A review of configuration design for distributed propulsion transitioning VTOL aircraft. *2017 Asia-Pacific International Symposium on Aerospace Technology*. Seoul 2017.
- [8] FINGER, D.F., GÖTTEN, F., BRAUN, C. et al. On aircraft design under the consideration of hybrid-electric propulsion systems. ZHANG X. (ed.) *The Proceedings of the 2018 Asia-Pacific International Symposium on Aerospace Technology* (APISAT 2018). *Lecture Notes in Electrical Engineering*. 2019, **459**. Springer. Singapore. https://doi.org/10.1007/978-981-13-3305-7_99
- [9] FINGER, F.D., BRAUN, C., BIL, C. Case studies in initial sizing for hybrid-electric general aviation aircraft. *2018 AIAA/IEEE Electric Aircraft Technologies Symposium*. 2018. <https://doi.org/10.2514/6.2018-5005>
- [10] FINGER, F.D., BRAUN, C., BIL, C. Impact of engine failure constraints on the initial sizing of hybrid-electric GA aircraft. *AIAA Scitech 2019 Forum*, San Diego. <https://doi.org/10.2514/6.2019-1812>
- [11] FINGER, D.F., BRAUN, C., BIL, C. Impact of electric propulsion technology and mission requirements on the performance of VTOL UAVs. *CEAS Aeronautical Journal*. 2019, **10**, 827-843. <https://doi.org/10.1007/s13272-018-0352-x>
- [12] KUŹNIAR, M. Wielokryterialna ocena doboru napędów lotniczych nowej generacji z wykorzystaniem metod energetycznych – *PhD Thesis*. Rzeszów 2021.
- [13] MARIANOWSKI, J., FRĄCZEK, W., CZARNOCKI, F. Założenia podstawowe dla projektu motoszybowca AOS-H2. (*not publish*)
- [14] MARIANOWSKI, J., TOMASIEWICZ, J., CZARNOCKI, F. Analiza masowa motoszybowca AOS-H2. (*not publish*)
- [15] ORKISZ, M., KUŹNIAR, M. 3E – a new paradigm for the development of civil aviation. *Combustion Engines*. 2020, **181**(2), 3-10. <https://doi.org/10.19206/CE-2020-201>
- [16] EMRAX d.o.o. <https://emrax.com/>
- [17] Wankel aircraft-engine. WANKEL AG. <http://wankel-ag.de>

Maciej Kalwara, MEng. – Faculty of Mechanical Engineering and Aeronautics, Rzeszow University of Technology.

e-mail: kalmac@prz.edu.pl



Michał Kuźniar, DEng. – Faculty of Mechanical Engineering and Aeronautics, Rzeszow University of Technology.

e-mail: mkuzniar@prz.edu.pl



Prof. Marek Orkisz, DSc., DEng. – Faculty of Mechanical Engineering and Aeronautics, Rzeszow University of Technology.

e-mail: mareko@prz.edu.pl



Analysis of pollutant emissions and fuel consumption for the use of a multi-storey carpark

ARTICLE INFO

Received: 27 July 2021
 Revised: 30 July 2021
 Accepted: 30 August 2021
 Available online: 1 September 2021

In Poland, the number of vehicles owned per capita is systematically increasing. There is also a noticeable increase in traffic in large urban agglomerations. This creates a number of problems, such as difficulties in finding a parking spot. Then it becomes necessary to search for a long time to stop, which is correlated with higher emission of harmful substances and energy consumption. The aim of the work is a multi-criteria analysis of the selection of a parking spot at a shopping center focused on travel times, pollutant emissions and fuel consumption. In addition, consideration was given to the selection of the optimal parking spot. The tests were carried out in Real Driving Conditions similar to Real Driving Emissions testing. The procedure, currently used as an extension of the type-approval tests, reflects the actual exhaust emissions from vehicles more accurately than tests under laboratory conditions. Specialized PEMS (Portable Emissions Measurement System) apparatus was used for the measurements.

Key words: *real driving emissions, exhaust emissions, fuel consumption, energy consumption, parking*

This is an open access article under the CC BY license (<http://creativecommons.org/licenses/by/4.0/>)

1. Introduction

Transport has a significant impact on the natural environment through the emission of harmful substances. The consequence of its negative impact include climate changes, which leads to, among others, melting glaciers, shrinking Arctic sea ice sheets, rising sea levels, changing the structure of precipitation and intensification of extreme weather events [1]. To reduce emissions, the European Union has set a climate and energy plan that covers the period up to 2050. One idea is to reduce transport emissions by 60% compared to 1990. As passenger vehicles account for 61% of all CO₂ emissions from road transport, steps have been taken to reduce their environmental impact (Fig. 1). More and more restrictive requirements are introduced, and manufacturers, in order to obtain approval, must meet the conditions provided for in the emission standards [2]. In addition, the new regulations include tests under real driving conditions, which better reflect pollutant emissions and complement laboratory tests [3].

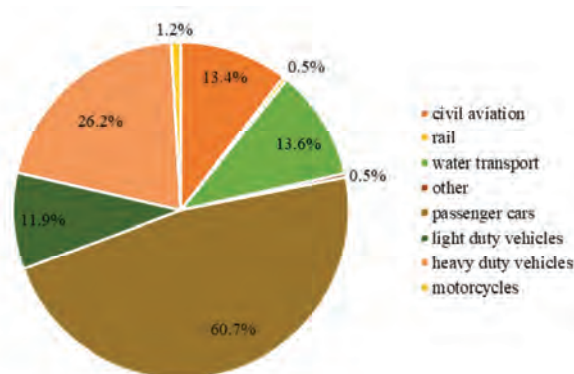


Fig. 1. Share of CO₂ emission of each transport type [3]

Poland is one of the most motorized countries in Europe. There are 617 passenger vehicles per 1,000 people (as

of 2018) [4], which is associated with an increase in traffic, especially in larger cities such as Poznań (Table 1). According to the results presented by TomTom International BV, the volume of traffic in Poznań is systematically increasing. In 2019, a 5% increase in traffic was recorded as compared to the previous year [5]. This creates a number of problems, incl. difficulty in finding a parking space. Having a large number of vehicles makes it very difficult to park near your destination. This mainly applies to places visited by a large number of people, such as shopping malls or the city center.

Table 1. Countries in the European Union with the highest number of passenger vehicles per 1,000 inhabitants [4]

Country	Number of passenger cars per 1000 inhabitants in 2018
Luxembourg	676
Italy	646
Cyprus	629
Finland	629
Poland	617
Malta	608
Germany	567
Estonia	563
Austria	562
Slovenia	549

Areas around parking lots are considered a source of harmful substances from exhaust emissions. Pollutants are emitted by vehicles entering and leaving, as well as when the engine is idling or warming up, which is more typical for the winter period [6]. In addition, parking lot users are exposed to the harmful effects of toxic compounds due to the proximity of the source. It is especially important in closed car parks. The increase in exhaust emissions in closed spaces, such as multi-storey car parks, which are not adequately ventilated, has negative effects on human health [7]. Diseases caused by inhaling car exhaust fumes include: asthma, chronic lung diseases, inflammation of the respiratory tract, cancer, as well as heart and nervous system dis-

eases. The negative impact of passenger vehicles on the environment makes it important to be limiting the traffic volume, such as by selecting the optimal route [8]. The solutions associated with Intelligent Transport Systems [9–11] may facilitate the process of parking a vehicle.

The aim of the presented work is to perform a multi-criteria analysis of the parking space selection at a shopping mall, focusing on reducing, among others, travel time, pollutant emissions and fuel consumption. In addition, consideration was given to finding the optimal parking space in the process.

2. Method

The road tests were performed at a multi-storey car park located at one of the shopping malls in Poznań. The aim of the measurements was to analyze exhaust emissions during trips in individual zones of the building. The research was divided into stages. Each part corresponded to a particular zone of the car park in which the drive test was performed reflecting the regular use of the car park, i.e. ground floor, 1st floor, 2nd floor, exit (Table 2). As the infrastructure of multi-storey car parks is usually quite extensive, and in the analyzed case the entrance to the car park was located in a different place than the exit, the point at the nearest intersection was assumed as the beginning of the measurements including the entrance and the end of emission measurement during the exit from the car park.

Table 2. Description of the conducted test drives

Test stage	Performed tests
Ground level	Entering the ground floor of the car park and searching for a parking space on this level
Level 1	Immediately after entering the parking lot, the vehicle was directed to the first floor and went on to search for a parking space on that floor
Level 2	Immediately after entering the parking lot, the vehicle was directed to the second floor and went on to search for a parking space on that floor
Exit	Leaving the parking space, leaving the second floor and leaving the parking lot

PEMS equipment was used in the tests for measuring exhaust emissions in real operating conditions. A mobile Semtech-DS unit (Fig. 2) was used, which allows to measure and record the concentrations of several gaseous exhaust compounds. The device includes analyzers with which it is possible to measure individual compounds in the exhaust gas. The exhaust gases at a temperature of 191°C from the exhaust system first go to the Flame Ionization Detector (FID), which is responsible for measuring the THC concentration. Then the exhaust gas passes through the cooler, where it is cooled to a temperature of 4°C, and after being cooled, it is directed to the NDUV analyzer where the NO_x concentration is measured. Then the NDIR analyzer using infrared is responsible for measuring the concentrations of CO and CO₂. The emission rate of individual compounds is obtained through calculations based on data from an exhaust gas flow meter recording the mass flow rate. Additionally, it is possible to connect data from the OBD and the GPS on-board diagnostic system to the results.

The test runs were made in real road traffic conditions with the use of a Skoda PC (Passenger Car) (Fig. 3), powered by a turbocharged spark ignition engine. The test vehicle met the Euro 6 emission standard, which was achieved, among others, by using a dual injection system using direct injection into the cylinder along with a multi-point injection into the intake manifold. The vehicle was equipped with a TWC (Three Way Catalyst) catalytic converter. Table 3 presents the test vehicle’s technical parameters.



Fig. 2. The SEMTECH-DS exhaust measurement device

Table 3. Basic technical data of the test vehicle

Parameter	Unit	Value
Ignition type	–	spark
Engine type	–	4 cylinders/in-line, 4 valves/cylinder
Displacement	dm ³	1.8
Nominal power	kW/rpm	132/5100–6200
Nominal torque	N·m/rpm	250 /1250–5000
Equipment	–	turbocharger, fuel supply system – direct gasoline injection TSI, TWC
Emission norm	–	Euro 6



Fig. 3. The test vehicle Skoda Octavia III

3. Test results

During the tests carried out in real operating conditions, the operating parameters of the vehicle as well as its location and movement were recorded using the GPS and the vehicle's on-board diagnostic system. Thus the distance

traveled (Fig. 4) and the average speed of the vehicle (Fig. 5) were determined. The routes of individual test drives differed in length. The longest measuring section was recorded for the route marked as the ground floor, and its length was 327.2 m. The remaining routes were noticeably shorter (the passage through level 1 was the shortest). The differences in relation to the longest tested drive section, and the other test routes, were at the level of about 30% to 60% and resulted mainly from the building internal layout as well as the time spent searching for a parking space. The mean speed values for the individual routes were very similar to each other and were in the range of approx. 5.4 km/h – 10.7 km/h. The smallest value was recorded during the drive in the ground floor zone, where the speed was about 5.4 km/h. The reason for the lowest speed values measured in this zone was the high volume of vehicle and pedestrian traffic. This level is the only one meant for entering and exiting the building. The shorter distance and higher mean speeds characterizing the drives along the remaining routes were mainly due to the shorter duration of searching for a parking space on higher storeys of the car park. The drive defined as an exit was characterized only by leaving the parking lot without looking for a parking space, and this was the reason for obtaining the highest mean speed value (at the level of 10.7 km/h).

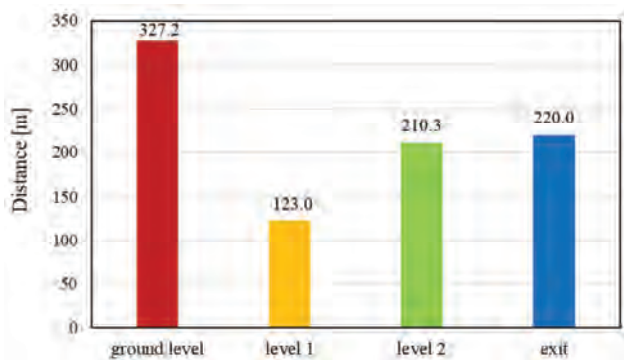


Fig. 4. Comparison of the distance travelled for each test stage

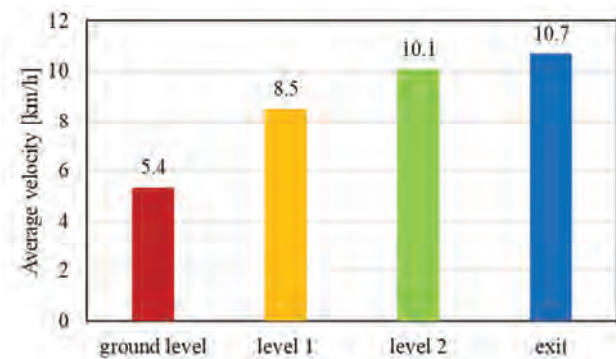


Fig. 5. Comparison of the mean vehicle travel speed for each test stage

The vehicle speed and the emission intensity of the analyzed exhaust components during the trip on the ground floor were shown in Figure 6. During vehicle acceleration the emission intensity of all measured exhaust components increased. This was due to the fact that the individual acceleration maneuvers were all very short-lived – the engine

was still operating in transient states while performing them. In addition, the acceleration of the vehicle increases the engine speed and load, which naturally results in a greater emission of exhaust gases emitted by the vehicle engine. This phenomenon may contribute to a greater exhaust emission intensity for individual exhaust gas components, even if the change of thermodynamic parameters in the combustion chamber would contribute to a reduction in the concentration of any exhaust gas component.

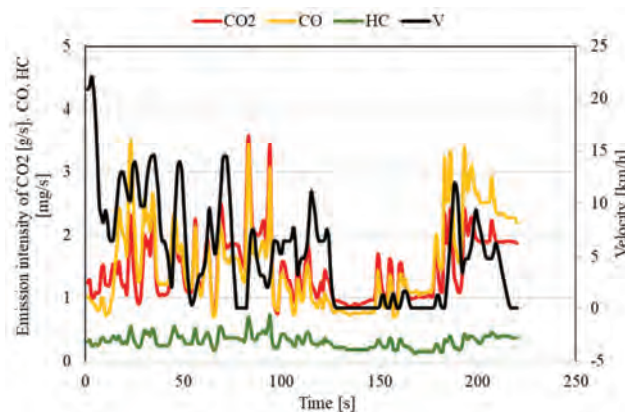


Fig. 6. Vehicle speed along with the CO₂, CO and HC emission intensity observed while driving on the ground floor

The CO₂ emissions from combustion-powered vehicles are closely related to their fuel consumption. Figure 7 shows the emission of carbon dioxide emitted in individual test drives. Generally, it can be assumed that when looking for a parking spot, CO₂ emissions increase with the increasing distance traveled necessary to park the vehicle. However, this relationship was not direct, and the CO₂ emission value was also influenced by the nature of the drive. In the ground floor zone, where traffic is greatest, the vehicle would often brake and then start moving again. Accelerating the vehicle, i.e. the sudden change in engine load, requires energy, which is obtained from the fuel. With smooth driving, fuel consumption, and, as a result, CO₂ emissions were much lower. The described conditions are most evident for the measurement defined as the descent. This is due to the nature of the drive, which includes the exit from the multi-storey car park, starting from the second floor. Thus, in this case, the vehicle is travelling down slopes from the top to the bottom levels of the car park, and thus the engine is operated at a lower load.

Spark ignition engines are characterized by an increased emission of carbon monoxide compared to compression ignition engines. This is due to the fact that the engine runs on rich mixtures at high loads. The highest emissions CO was characterized by the passage in the ground floor stage, reaching approximately 338 mg (Fig. 8). As mentioned, this zone is characterized by high vehicle traffic intensity and pedestrian movement. This forces constant speed changes that affect the engine load, and thus also the carbon monoxide emissions. The smallest emission of CO (approx. 94 mg) was emitted by the vehicle during the test defined as level 1, which is approximately three and a half times less than in the ground floor stage.

In addition to carbon dioxide and carbon monoxide, the research was supplemented by measuring the hydrocarbon emissions. During the test drives, the highest emission of these compounds was observed in the ground floor stage tests (almost 70 mg, Fig. 9). The smallest HC emission was measured during a run on level 1 (approx. 5.9 mg). During the level 2 and down slope driving, the vehicle emitted approx. 27 mg and 17.3 mg HC, respectively, which is still much lower than when travelling through the ground floor.

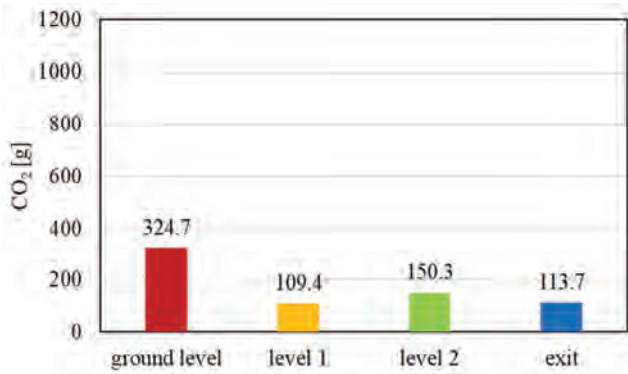


Fig. 7. Comparison of CO₂ emissions for each test drive stage

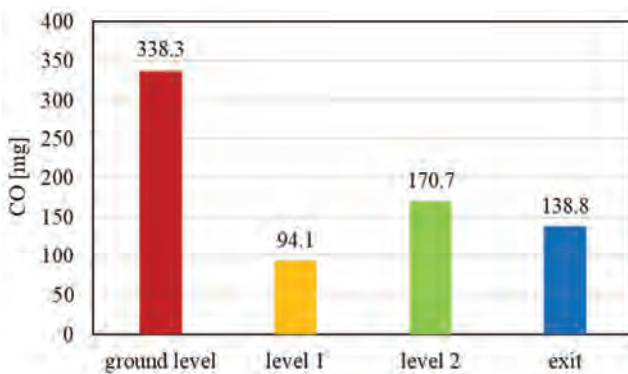


Fig. 8. Comparison of CO emissions for each test drive stage

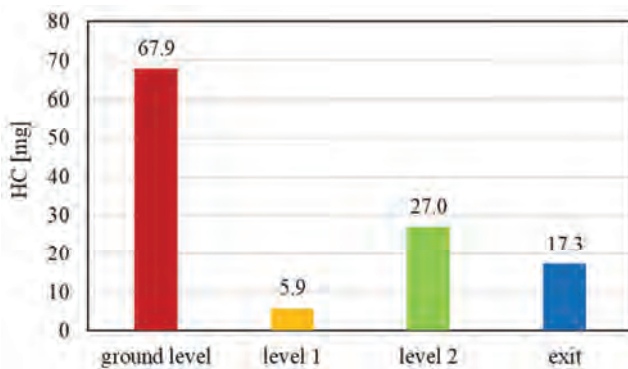


Fig. 9. Comparison of THC emissions for each test drive stage

4. Results analysis

In order to fully establish the impact of the parking spot selection method within a multi-storey car park, it is necessary to know the emissions both when entering and leaving the car park. As the conducted research is the Authors' initial approach to the subject of the environmental impact of vehicles using a multi-storey car park, the analyzes of the total emissions (entry and exit) were estimated using the recorded

emission results when leaving the second floor of the car park. For this purpose, the recorded exit from the parking lot has been divided into individual fragments (Fig. 10):

- I – moving from the parking spot to the exit to the lower level,
- II – moving down a level,
- III – moving between the exit ramps and leaving the car park,
- IV – moving back to the starting point.

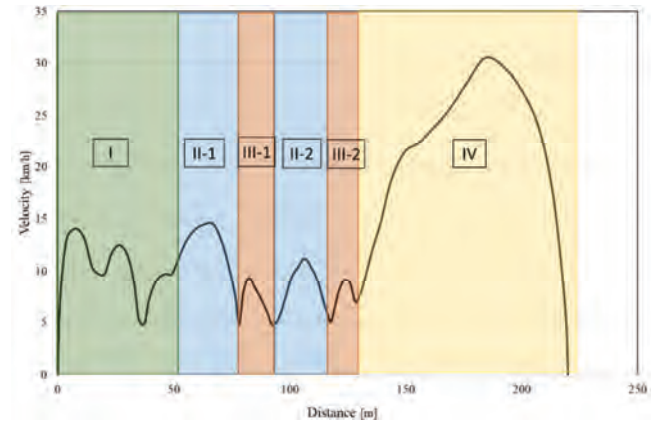


Fig. 10. The velocity in individual stages of leaving the second floor of the analyzed multi-storey car park

When estimating the total emission from the whole drive test within the analyzed car park for entry and exit points, a methodology was adopted where the emission values recorded during the entrance to the car park and the appropriate combination of phases including the exit from the car park were all summed up (Table 4).

Table. 4. The three parking scenarios

Scenario	Analyzed data
Ground floor parking	Moving through the ground level and exiting the car park (sections: I, III-2 and IV)
1st floor parking	Moving through level 1 level and exiting the car park (sections: I, II-1, III-2 and IV)
2nd floor parking	Moving through level 2 and exiting the car park

As a result of the analyzes in terms of the nature of the drive tests parameters (distance, time, mean travel speed) were shown in Fig. 11. When analyzing the nature of the entire drive through a multi-storey car park, it can be noticed that the greatest distance was traveled by a vehicle parked on the ground floor (482.5 m). This situation reflects the long-term search for a parking spot in a heavily crowded part of the parking lot - the time between entry and exit was 267 seconds while the test lasted, and the mean vehicle speed was 6.5 km/h. Parking on the second floor, which means parking in a theoretically more distant place, resulted in travelling a distance of 430 m. This means a reduction of the distance traveled by approx. 52 m (-10%). The travel time decreased by 44%, and the average travel speed was increased by approx. 60%. The shortest distance and the shortest time traveled were both observed for the vehicle when parking on the 1st floor.

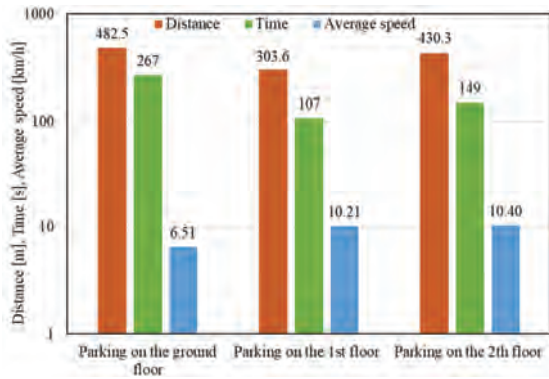


Fig. 11. The distance, time and average speed of the vehicle movement during different parking scenarios in a multi-storey car park

Exhaust emission values for the adopted scenarios of finding a parking spot a multi-storey car park, estimated in accordance with the methodology discussed, including both entry and exit to and from the car park, have been shown in Fig. 12. In the analyzed case, the least favorable, in terms of the total emission of harmful exhaust gases, was parking on the ground floor of a multi-storey car park. During this test drive, the vehicle emitted 405 g CO₂, approx. 436 mg CO and approx. 81 mg HC. Parking on the 1st level was found to be the most favorable in terms of total emissions. The emission from a vehicle parking on the 1st level were lower for each of the analyzed exhaust compounds: -50% CO₂, -53% CO and -75% HC comparing to parking on the ground floor. The emission of compounds when parking on the 2nd floor was greater than when parking on the 1st floor, but these values were still lower than when parking on the ground floor.

Similar relationships can be observed in the field of specific distance emissions (Fig. 13). Despite comparing the emission of compounds to the distance traveled by the test vehicle, parking in the crowded part of the parking lot – so parking on the ground floor was characterized by the highest exhaust emission values. In relation to the distance traveled, the lowest CO₂, CO and HC emission values have been observed when parking on the 1st level of the tested multi-storey car park (respectively 48%, 52%, 74% less than when parking on the ground floor) Proportional relations, as in the case of specific distance CO₂ emissions, was obtained in the case of the vehicle fuel consumption (Fig. 14).

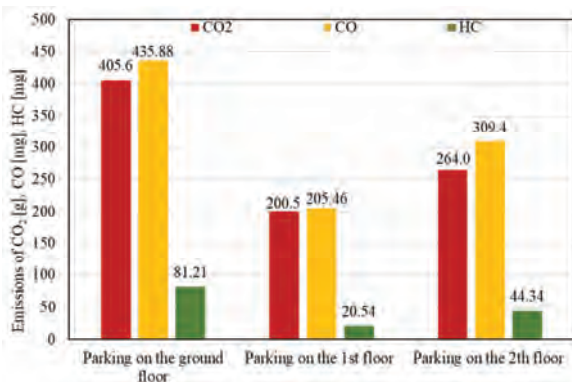


Fig. 12. The total emission of harmful exhaust components in different parking scenarios in a multi-storey car park

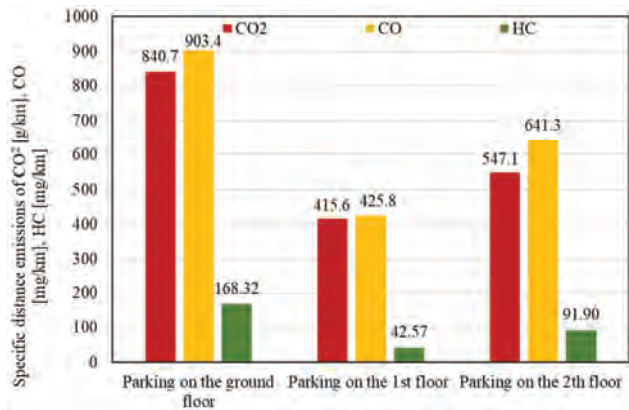


Fig. 13. Specific distance emissions of harmful substances during various parking scenarios in a multi-storey car park

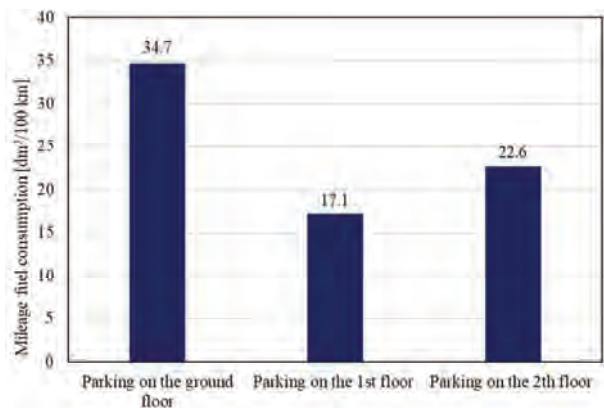


Fig. 14. The operational fuel consumption values during various parking scenarios in a multi-storey car park

5. Conclusions

The floor 1 drive stage was characterized by having the shortest distance travelled, while the vehicle covered the longest distance in the ground floor stage. Due to the volume of traffic, finding a parking spot on the ground floor was significantly more time-consuming, and the high level of congestion comes from the desire of people to park right after entering. However, this leads to an increase in the time needed to search for a free spot. This time can be significantly reduced by entering a higher level of the car park, which is not so often chosen by other drivers. According to the obtained results the optimal choice was floor 1, which was a compromise between congestion (less than on the ground floor) and the length of the access route (shorter than to floor 2). Due to the high volume of traffic, the lowest average speed was observed for the stage on the ground floor, and the highest for the exit drive. The fuel-consumption related CO₂ emissions were lowest for the drive at floor 1 and highest on the ground floor. Taking the operating costs and the emission of harmful substances as a criterion (depending, among others, on fuel consumption), the best choice was concluded to be entering the 1st floor to find a spot. Parking on the ground floor, on the other hand, was unfavorable, including due to the CO and HC emissions, which then reached the highest value.

The considerations were supplemented with an extended analysis of the test drives. After compiling the three scenarios of route stages within the parking lot, taking into ac-

count the entrance to and exit from the multi-storey car park next to a shopping mall, it can be concluded that looking for a parking spot on the ground level is the worst

choice taking into account all the considered criteria (distance, time, mean speed, specific distance emissions and fuel consumption).

Nomenclature

CO	carbon monoxide	NO _x	nitrogen oxides
CO ₂	carbon dioxide	OBD	on-board diagnostics
FID	flame ionization detector	PC	passenger car
GPS	global positioning system	PEMS	portable emission measurement dystem
NDIR	non-dispersive infrared	THC	total hydrocarbons
NDUV	non-dispersive ultraviolet	TWC	three way catalyst

Bibliography

- [1] Climate change consequences. European Commission. ec.europa.eu/clima/change/consequences_en (accessed on 15.07.2020).
- [2] Regulation (EC) No 715/2007 of the European Parliament and of the Council of 20 June 2007 on type approval of motor vehicles with respect to emissions from light passenger and commercial vehicles (Euro 5 and Euro 6) and on access to vehicle repair and maintenance information. <https://eur-lex.europa.eu/legal-content/EN/ALL/?uri=celex%3A32007R0715>
- [3] CO₂ emissions from cars: facts and figures. European Parliament. <https://www.europarl.europa.eu/news/en/headlines/priorities/climate-change/20190313STO31218/co2-emissions-from-cars-facts-and-figures-infographics> (accessed on 15.07.2020).
- [4] Passenger cars in the EU. Eurostat. Statistics Explained. ec.europa.eu/eurostat/statistics-explained/index.php?title=Passenger_cars_in_the_EU&stable=1%20#Highest_share_of_passenger_cars_over_20_years_old_in_Poland/ (accessed on 15.07.2020).
- [5] TomTom International. www.tomtom.com/en_gb/traffic-index/poznan-traffic/ (accessed on 15.07.2020).
- [6] STEINBERGA, I., KLEPERIS, J. Urban air pollution: input car parking places. *Urban Transport X*. 2004, **75**, <https://doi.org/10.2495/UT040831>
- [7] DEMIR, A. Innovation and entrepreneurship investigation of air quality in the underground and aboveground multi-storey car parks in terms of exhaust emissions. *Procedia – Social and Behavioral Sciences*. 2015, **195**, 2601-2611. <https://doi.org/10.1016/j.sbspro.2015.06.461>
- [8] MERKISZ, J., PIELECHA, J., FUĆ, P. et al. Assessment of vehicle emission indicators for diverse urban microinfrastructure. *Combustion Engines*. 2013, **154**(3), 787-793.
- [9] ELSONBATY, A.A., SHAMS, M. The smart parking management system. *International Journal of Computer Science & Information Technology*. 2020, **12**(4), 55-66. <https://doi.org/10.5121/ijcsit.2020.12405>
- [10] ALAM, M., MORONI, D., PIERI, G. et al. Real-time smart parking systems integration in distributed ITS for smart cities. *Journal of Advanced Transportation*. 2018, **2018**. <https://doi.org/10.1155/2018/1485652>
- [11] GUERRERO-IBÁÑEZ, J., ZEADALLY, S., CONTRERAS-CASTILLO, J. Sensor technologies for intelligent transportation systems. *Sensors*. 2018, **18**(4), 1212. <https://doi.org/10.3390/s18041212>

Maciej Andrzejewski, DEng. – Łukasiewicz Research Network – Rail Vehicle Institute "TABOR", Poland.
e-mail: maciej.andrzejewski@tabor.lukasiewicz.gov.pl



Aleksandra Woch, MEng. – Łukasiewicz Research Network – Rail Vehicle Institute "TABOR", Poland.
e-mail: aleksandra.woch@tabor.lukasiewicz.gov.pl



Mateusz Nowak, DEng. – Faculty of civil and Transport Engineering, Poznan University of Technology.
e-mail: mateusz.s.nowak@put.poznan.pl



Natalia Stefańska, MEng. – Łukasiewicz Research Network – Rail Vehicle Institute "TABOR", Poland.
e-mail: natalia.stefanska@tabor.lukasiewicz.gov.pl



The aircraft engines in the land vehicles

ARTICLE INFO

Received: 5 July 2021

Revised: 28 August 2021

Accepted: 30 August 2021

Available online: 1 September 2021

The examples of the applications of the aircraft engines to propulsion of the heavy armored land vehicles are presented in this paper. They provide the power necessary for high mobility of these land vehicles, which have a weight much greater than trucks. These engines were mass produced and thus were readily available. It was easier to repair damaged engines, too. Both spark-ignition and compression-ignition piston engines as well as turbocharged engines were used to propulsion of the armored vehicles. General solutions of the dual-purpose engines for the vehicles during the First and Second World War as well as the engines used nowadays are presented. Attention is also given to the specific solutions of these engine assemblies. Their basic technical and operational parameters are described. The implications of adapting aircraft engines to land vehicles were analyzed.

Key words: *aircraft engines, land vehicles, propulsion systems, dual application, dual use*

This is an open access article under the CC BY license (<http://creativecommons.org/licenses/by/4.0/>)

1. Introduction

The application of the heavy armored vehicles featuring a weight of approximately 30 tons on the battlefields of the First World War, necessitated the use of the adequately powerful engines for their propulsion. These engines had to provide the required speed of the vehicles and the ability to overcome the terrain destroyed by the warfare. Initially, it was assumed that the speed of tanks should be close to the speed of a movement of infantry. Therefore, the first tanks introduced developed a speed up to 6 km/h (e.g., British Mark I–IV tanks. For their propulsion one or two mass-produced vehicle engines were sufficient. It quickly became apparent that a fireteam of infantry moving through the damaged terrain could not keep up with the tanks, and the vehicles themselves were destroyed or captured by the enemies. Therefore, on the one hand the works on the armored infantry carriers (the first was the British Mark IX carrier) were commenced, and on the other hand more powerful engines were searched for. Such engines should provide an increased speed of tanks making it difficult to be targeted by a projectile, and to overcome the difficult terrain. For this purpose, the aircraft engines were considered, which were adapted for a propulsion of the tanks. The development of engines for aircraft and land vehicles proceeded in parallel [10]. However, the rapid development of weaponry and warfare necessitated a partial fusion of the development paths of these engines.

The purpose of this article is to present a solution to the problem of providing the necessary number of 300–500 hp engines to power tanks and other heavy land vehicles, which developed fast in the first half of the 20th century. This was necessary to achieve the expected mobility parameters of tanks. The basic comparative indicator of such mobility was the unit power of a tank as a ratio of power to vehicle weight (hp/t). For this purpose, some aircraft engines were adopted. Solutions of such aircraft engines and their assemblies are presented, and the results of such adaptations are evaluated.

During the description of the engines presented in the photographs and the specification of their structure and operational parameters, mainly the descriptions of the presented engines were used, as they were presented on the descriptions of the tanks and engines displayed in museums. These data may differ slightly from the data from other sources.

2. First tank engines

The first British tanks used during the First World War (Mark I–Mark IV) were powered by the 6-cylinder Daimler – Knight engines with a displacement of 13 dm³ and power of 76 kW (105 hp) at the speed of 1000 rpm (Fig. 1). The producer of these engines was an independent British company, The Daimler Company Limited, whose founder bought the rights to use the Daimler business name from Gottlieb Daimler and an ownership title to the Daimler-Motoren-Gesellschaft. This company acquired the rights to use the sleeve valve timing mechanism in its products from Charles Knight. When this design was perfected, it produced an engine that ran quietly because it did not have many of the moving parts of a valve train system (valves, springs, pushrods). Its combustion chamber was spherical in shape, which ensured a low heat loss.



Fig. 1. The Daimler – Knight engine in the Mark II tank (The Tank Museum at Bovington Camp in Dorset, photo by the author)

The engines from the Daimler factory caused a sensation and were mass produced by the company. These engines featured a wide power range and powered a variety of vehicles. Their popularity caused the company to discontinue the manufacturing of the overhead valve engines until the 1930s. The Daimler engines used in the first tanks were not aircraft engines, but sleeve valve timing technology also found its way into many piston aircraft engines with the inline or star cylinder positions, including the Napier high-performance engines with the H-type cylinder arrangements.

The quiet operation of the Daimler-Knight engines was their significant advantage when the engine was operated without a cover in the open interior of the tank. The crew was not exposed to the much higher noise levels that head valve engines would emit. The disadvantage of these engines constituted the unreliable lubrication systems, the unreliability of which increased as speed increased. This caused the frequent engine faults. In addition, a significant oil consumption resulted in a bluish exhaust gas color that showed the positions of the tanks powered by the engines.

The boost in engine power by increasing the combustion pressure and speed required the new engine solutions for the subsequent versions of the British tanks. This was due to the need to increase the speed of the next versions of the tanks, which weighed up to 40 tons during the First World War.

Tanks of the 38-ton Mark VIII version being the result of the British-American cooperation had a separate engine compartment with the engine in the rear part of the hull. Ricardo V-12 engines of 220 kW (300 HP) were used to drive the British version of the tank, while the American tanks were powered by the Liberty V-12 aircraft engines of 249 kW (338 hp) at 1400 rpm (Fig. 2) [11].



Fig. 2. The Liberty V-12 engine to power tanks (The Tank Museum at Bovington Camp in Dorset, photo by the author)

The Liberty V-12 engines were developed for the aviation [5]. They were designed so that to have a maximum power-to-weight ratio and should be easy to mass produce and service. The various versions of this engine were developed differing in the quantity and configuration of cylinders. They were 4- and 6-cylinder engines in the inline versions and from 8 up to 12 cylinders in the 'V' shape versions (prototype version even had the L-8-cylinders mounted in a straight line). Later engines did not exceed 6

cylinders in a straight line. The versions of the engines with the inverted cylinders, facing downwards, supercharged versions of the engines were also developed. The largest engine was the X-24 (24 cylinders in the 'X' layout), 12 of which were in two rows facing up and 12 cylinders facing down.

The Liberty engine was designed in a record short time of less than two months. It had single steel cylinders bolted to an aluminum crankcase. The cylinders were expanded at the top to allow for larger valve diameters (Fig. 3). The jackets of the liquid cooling system were welded to the cylinders. Individual camshafts for each row of valves were rotated by means of king shafts and bevel gears. Ignition distributors were mounted on the ends of the shafts. The design of the cylinders and camshaft drive was based on the Mercedes Benz D.III engine for the German aircraft, as well as the solutions of other aircraft engines.

The cylinders of the Liberty engine were forked at the angle of 45°. The V-12 twelve-cylinder engine had a capacity of 27 dm³, the ratio of stroke to piston diameter was of 1.4 (S/D = 178×127 mm), and its compression ratio was $\epsilon = 5.4$; compression ratio of the engine was lowered in the non-aircraft versions. In the tank version, the output of the Liberty engine was of 250 kW (340 hp) at 1400 rpm [11].

A major advantage of the Liberty engines constituted their modularity, that enabled to create the engines with the different numbers of cylinders and their configuration. The engine also had design flaws that were partially corrected, however vibration during engine operation was not completely eliminated. Its durability was not high.

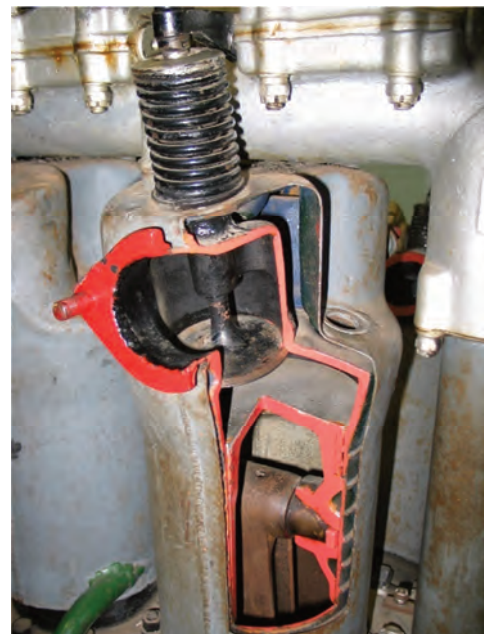


Fig. 3. Combustion chamber of the Liberty V-12 engine (The Tank Museum at Bovington Camp in Dorset, photo by the author)

3. The engines from the period of the Second World War

The rights to produce the Liberty V-12 engines were acquired by the British before the Second World War. They planned to use these engines to power the fast Cruiser MK III and MK IV tanks and their subsequent versions (Cru-

sader, Cavalier and Centaur). These engines developed 250 kW (340 hp) running at 1500 rpm. This was not sufficient to drive next generations of tanks featuring the increasing weight and to provide them with a sufficiently high ratio of power to vehicle weight. It was necessary to search for the more powerful engines. In the beginning, the power of Nuffield Liberty engines produced in Great Britain was increased. Despite obtaining 310 kW (410 hp), the assumed unit power of tanks of 20 hp/ton (15 kW/t) was not achieved. Therefore, it was decided to adapt the Rolls-Royce aircraft engines to power the tanks.

Initially, the use of the Rolls-Royce Kestrel engines was considered, but they did not provide the required unit power and larger engines were necessary. The Rolls-Royce Merlin met these requirements. In the aircraft version, these were engines in a V-12-cylinder configuration with supercharging by mechanically driven compressors (Fig. 4). These engines were commonly used to power the British fighter and bomber aircraft. Their adaptation to the tank propulsion was not difficult, although many significant changes had to be made. This primarily involved removing the air compressors and their transmission systems, building liquid cooling systems for the engines with air fans, making changes to the lubrication and fuel supply systems, and making the auxiliary engine units drive from the camshafts on each head. In the land version, the engines were fueled with low-octane gasoline instead of high-octane jet fuel.



Fig. 4. The Rolls-Royce Merlin engine with centrifugal compressor (Royal Museum of Army and Military History, Brussels, photos by the author)

The land version of the engines, known as the R-R Meteor, had a power output of 450 kW (600 hp) at 2500 rpm (Fig. 5) [6]. The piston stroke was equal to 150 mm, the cylinder diameter was of 140 mm, and the compression ratio depended on the version (from $\epsilon = 6:1$ to $\epsilon = 7:1$). The use of these engines to drive the 28-ton Cromwell tanks (A27T Cruiser Tank) provided the specific tank power at the required level of 21.4 hp/t (16 kW/t) and cruising speeds up to 64 km/h tanks and engines.

These engines powered many post-war British tanks, which were originally the upgraded versions of the Cromwell tank such as the Comet A34 (weight of 33 t) and the Challenger A30 (weight of 32 t). They were also used to propel the later tanks with much higher weight which resulted in reduction of their speed. For example, the Centurion tank had a weight of 52 ton and its maximum speed

was of 35 km/h, while the experimental Tortoise tank with a weight of 79 ton had a speed of only 20 km/h.

The Rolls-Royce Meteor M120 gasoline-injected engines were developed to power the 64-ton Conqueror (FV 214) heavy tanks. These engines developed 810 hp (640 kW) and provided the tank with a cruising speed of up to 35 km/h. A smaller version of this engine designated as the Rolls-Royce Meteorite was also developed with a V8 cylinder configuration and a displacement of approx. 18 dm³. They were used to power wheeled tractors, small ships, and stationary equipment. The power output of these engines was of 190 kW (260 hp) at 2300 rpm in the Mk. 204 version, and in the Mk. 202B version the engine developed 380 kW (520 hp) at 2700 rpm.

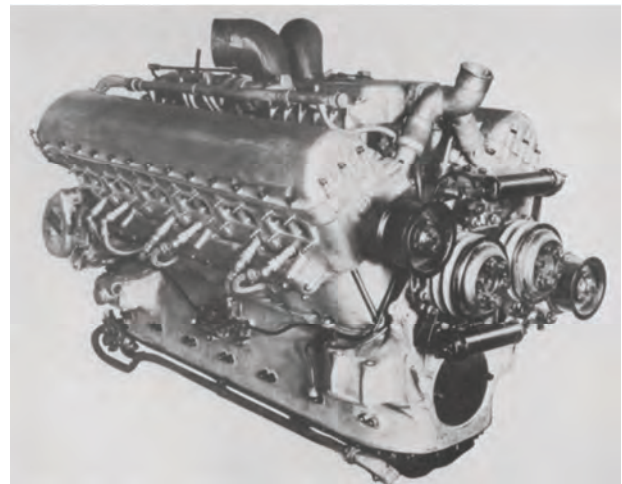


Fig. 5. The Rolls-Royce Meteor engine without any compressor [6]

The aircraft engines were commonly used to power the American light and medium tanks and many other tracked (floating) vehicles within a period of the Second World War. The Continental R-670 engines (factory designation W-670) were used to power the M1, M2 and M3 light tanks and the different varieties of the LVT (Landing Vehicles Tracked) tracked amphibious vehicles used in landing operations. They were 7-cylinder engines of about 180 kW (250 hp) at 2400 rpm, with a star cylinder arrangement of a capacity of circa 11 dm³ (piston stroke of 117.5 mm, cylinder diameter of 130.2 mm) and a weight of circa 200 kg [11]. The engines were air-cooled, which required a suitably large blower and covers directing the airflow to the cylinder ribs and head (Figure 6). They were fueled with low-octane gasoline via a carburetor. The fuel-injected versions of the engine with an increased compression ratio and a power up to 6% were also developed. Unlike the aircraft engines, these engines had the flywheels to help start the vehicle and the cooling air blowers.

Some of the M3 light tanks (M3-Diesel) were powered by the Guilberson T-1020-4 9-cylinder, star compression-ignition aircraft engines of circa 180 kW (250 hp) at 2200 rpm. These engines, with a displacement of 16.7 dm³ (piston stroke of 140 mm, cylinder diameter of 130 mm), had a compression ratio equal to $\epsilon = 15$, a weight of circa 300 kg and were air-cooled [5].

The larger armored vehicles required more powerful engines. The mass-produced Wright R-975 Whirlwind engines were used for this purpose. They were developed and produced by a division of the Curtiss–Wright, but most of these engines were built under a license by the Continental Motors Company. These engines were chosen initially to power the M2 tank, weighing approximately 18 tons, and later for the heavier M3 Lee and M4 Sherman tanks. They were also used to power the M7 self-propelled guns, tank destroyers and many other specialized vehicles built on the same chassis as the M3 and M4 tanks.

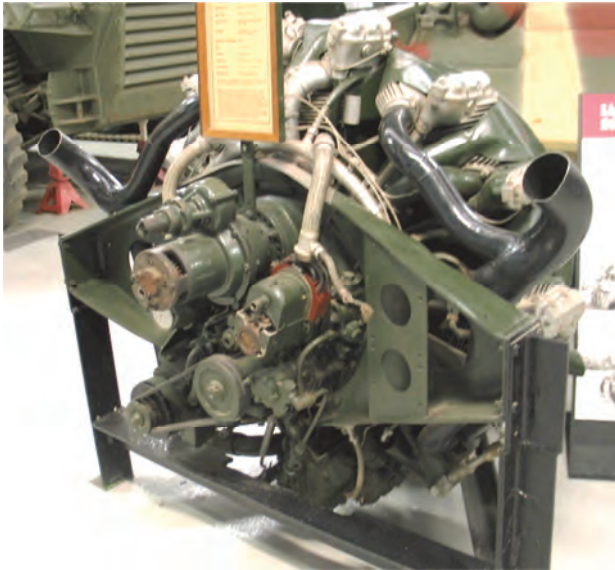


Fig. 6. The Continental W670-9A engine (The Tank Museum at Bovington Camp in Dorset, photo by the author)

The R-975 engines were 9-cylinder spark-ignited star engines (Fig. 7). They were air-cooled by a blower located on the torque take-off shaft. The engines had a displacement of circa 16 dm^3 (piston stroke of 140 mm and cylinder diameter of 127 mm) with a power rating of 220–340 kW (300–450 hp), depending on the engine version [11]. The increase in power of the subsequent versions of the engine was achieved through design changes in the engine head, increasing its compression ratio and the maximum speed and supercharging the air. After the war, the Continental developed this engine by increasing its starting power to about 390 kW (530 hp) at 2300 rpm.

The M4 Sherman tanks were powered by a variety of engines, including aircraft engines, featuring 266–330 kW (350–450 hp), which gave the tanks a unit power of 11–13.5 hp/t and provided a cruising speed of 35–48 km/h. A large number of the versions of the tanks and vehicles on their chassis, as well as engines for these vehicles, makes their exact specification difficult. Their parameters vary depending on the source and therefore approximate values are given. For the propulsion of the mass-market versions of the Sherman M4 and M4A1 tanks, the versions of the R-975 engine with 260–300 kW (350–400 hp) at 2400 rpm were used.

The final production version of the Sherman tank was the M4A6 tank. It was powered by a modified version of the Wright R-1820 Cyclone 9-cylinder aircraft gasoline

engine, adapted for self-ignition and diesel fuel supply by the Caterpillar Inc. The Caterpillar used the crankshaft, crankcase, cylinders, and supercharging system of the R-1820 gasoline engine for its project (Fig. 8). This new engine was designated the RD-1820. This supercharged engine had a weight of circa 0.8 t; displacement of circa 29.9 dm^3 ; piston stroke to cylinder diameter ratio $S/D = 1.12$ (stroke of 174.6 mm, diameter of 155.6 mm); compression ratio $\epsilon = 15.5$ and developed power of 330 kW (450 hp) at a speed of 2000 rpm. Maximum speed was limited by a speed controller. The M4A6 tank developed a maximum speed of close to 50 km/h (31 mph) and had good multi-fuel capability – it could run on both diesel fuel and low-octane gasoline.



Fig. 7. Wright R-975 engine (The Tank Museum at Bovington Camp in Dorset, photo by the author)



Fig. 8. Cross-section of the Cyclone Wright R-1820 engine (San Diego Air and Space Museum, photo by the author)

The Wright R-1820 G-200 gasoline engine with power increased to 660 kW (900 hp) at 2300 rpm was used to

power the experimental M6 heavy tank with a combat weight of 57.4 ton and a maximum speed of 35 km/h.

Another American aircraft engine used to power many types of tanks were the Ford GAA inline cylinder configuration engines (Fig. 9). These engines were used to power the M4A3 Sherman tanks and their upgraded chassis version, and later many other tanks, including the M26 Patton medium tank in the different 42 t variants (Ford GAF engine version).



Fig. 9. The Wright Ford GAA engine (The Tank Museum at Bovington Camp in Dorset, photo by the author)

The Ford GAA engines were originally designed as naturally aspirated V-12-cylinder aircraft engines with aluminum cylinder blocks, crankcases, and heads [7]. They were engines with the same piston-crank system dimensions and 60° cylinder row pitch as the RR-Merlin engines. They had two camshafts in the head and were liquid cooled. They did not find acceptance as aircraft engines. Since there was a shortage of engines to power the M4 Sherman tanks it was decided to produce these engines, but in a V-8-cylinder version. These engines had a power output of 373 kW (500 hp) at 2600 rpm, sufficient to drive the M4 tank. In this version the Ford GAA engine had a displacement of 18 dm³, compression ratio of $\epsilon = 7.5$; piston stroke of 15.2 cm, cylinder diameter of 13.7 cm and two carburetors, one for each row of cylinders [11]. The GAA version of the engine differed from the GAF version in the type of Stromberg carburetors.

After the war, the twelve-cylinder engines were revised in the Ford GAC version with power increased to 480 kW (650 hp) at a speed 2800 rpm. They were used to power the prototype T29 heavy tanks (weight of 64 t) and T32 tanks (weight of 54 t).

In the further versions of tanks produced in a large quantity, air-cooled engines in the V-12-cylinder configuration and with a displacement of 29.3 dm³ (1790 in.³) were developed. These were spark-ignition V-12 engines: Continental AV-1790 (tanks: M-46, M-47, and M-48) and self-ignition Continental AVDS-1790 (tanks M-60, Merkava, Centurion). In some versions of the engines turbocharging was used.

The T23 tank was one of the tanks powered by the Ford GAN aircraft engine. It was built as a replacement intended for the M4 Sherman tank. It had an electric transmission system. The Ford GAN engine drove an electric generator (Fig. 10). The generator powered two drive motors with reducers that drove the drive wheels of the tank (Fig. 11). This electrical connection between the engine and the wheels allowed the engine to maintain operation as close to the optimum conditions as possible. The tank with this drive system could change direction with any steering angle (steplless). The vehicle could be controlled from any place inside and outside the tank at a distance limited by the length of the cable. The chassis of the tank was adapted from the M4 Sherman tank.

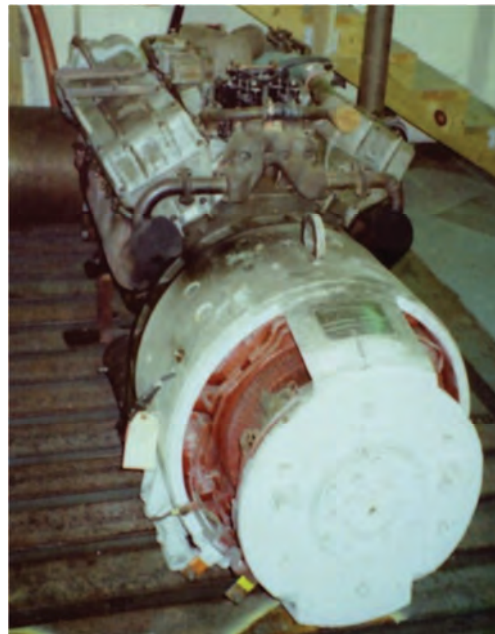


Fig. 10. The Ford GAA engine driving the alternator (photo by the author)

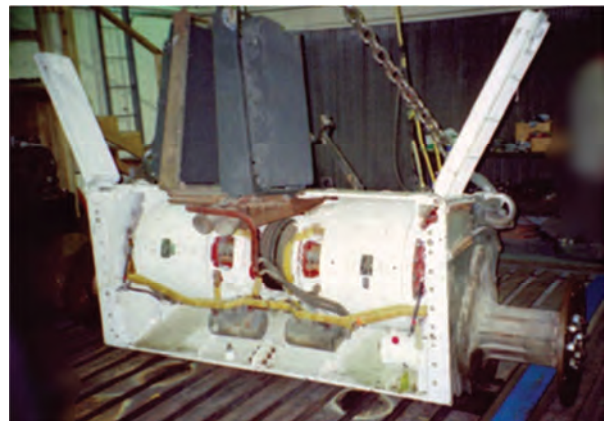


Fig. 11. The T-23 tank propulsion electric motors and reducers (photo by author)

Despite the good road and terrain properties of the tank equipped with electric and diesel propulsion, such a propulsion system was eventually abandoned. This was due to the necessity of providing well-trained and equipped operating facilities.

The history of the W-2 engines, which were developed as engines for driving land vehicles: tanks, self-propelled guns, and artillery tractors, was different. Like the aircraft engines, they had crankcases, cylinder blocks, pistons and heads made of aluminum alloys. They were self-ignition engines. Developed in the 1930s by a team with no experience in engine design. The work of this team was assisted by the experienced engine designers from other aircraft institutes, so they are in the structural terms like the aforementioned engines. One of the most important experts was A. D. Charomskij, in whose team the diesel aircraft engines ACh-30 and ACh-40 were developed based on the experimental engine AN-1 [5]. The W-2 engine had the same configuration of cylinders and similar design solutions to Charomskij's engines, but it had smaller piston and cylinder dimensions and thus a smaller displacement (Fig. 12).

The structure of the W-2 engines like the aircraft engines was also influenced by the development of the aircraft engine production in the USSR in the 1920s and 1930s. For this production, machine tools and tooling were purchased in the West and in the USA, as well as patents, technologies, and licenses for the aircraft engine production.



Fig. 12. The W-2 engine (Armored Weaponry Museum, Poznan, photo by the author)

The W-2 engines were first supplied with the fuel injection equipment produced by the German company Bosch (feed pumps, injection pumps and injectors). After the production of these units was developed locally, they were applied to the engines produced in the various production plants within the territory of the USSR.

The W-2 engines were of the V-type 12-cylinder engines with a 60°-cylinder row pitch angle, with a single connecting rod [1]. The basic version of the engine had a power output of 368 kW (500 hp) at a speed of 1800 rpm. Reduced- and increased-power versions of the engines were also developed. Upon the use of a mechanically driven centrifugal compressor from the AM-38 aircraft engine, the power of the W-2 (W-12SN) engine was increased to 625 kW (850 hp). The straight six-cylinder W-6 engines with a power of 180 kW (240 hp) were also developed [1].

The cylinder diameter of the W-2 engines was of 150 mm, and their piston stroke depended on the connecting rod. The piston stroke of the main connecting rods was of 180 mm and that of the connecting rods was of 186.7 mm. This resulted in a little variation in the compression ratios of the cylinder rows. The dry weight of the engine was of 750 kg. The cylinder heads and blocks were attached to the crankcase by the long tie bolts. The crankcase was split into the main bearing axis and the parts were bolted together (Fig. 13). Starting could be done with an electric starter or compressed air. The engine was produced under license in many countries.

There are mentions of a project to develop a version of the W-2A engine for a reconnaissance aircraft which would provide a significant increase in operational range. However, the aircraft turned out to be obsolete in comparison with other pre-war aircrafts, and furthermore, the refinement of the engine version to the requirements of its use in the aircraft would have been laborious. Therefore, this idea was abandoned.



Fig. 13. The W-2 engine, cross-section (Armored Weaponry Museum, Poznan, photo by the author)

4. Present engines

The only mass-produced post-war engine that was developed using aircraft engine assemblies was the AGT-1500 engine. This engine was chosen to power the US M1Abrams tank, introduced into service in 1976 [7]. These engines were selected during the project on the MBT-70 medium tank because of the choice between the AGT-1500 turboshaft engine and the AVCR-1360 variable compression ratio piston engine (these were the rebuilt Continental AVDS-1790 engines).

While designing the AGT-1500 engine, the AVCO Lycoming drew on its own experience in producing turboshaft engines for the helicopters and the PLT27 turbine engine solution. This was a 2000 hp (1470 kW) engine in which the low-pressure part consisted of a five-stage axial compressor connected and powered by a shaft to the low-pressure turbine [9].

The high compression part included a four-stage axial compressor and a single stage radial compressor connected by a shaft to a single stage turbine [8]. Both parts of the

engine operated independently, and their speed depends only on the aero- and thermodynamic relationships between the compressors and turbines. Behind the turbines driving the compressors were two stages of drive turbines and a planetary reducer. This is where a similarity between the two engines ends. The annular single combustion chamber of the PLT27 engine with a return flow was replaced in the AGT-1500 engines by a single tubular combustion chamber on the side of the engine and a helical exhaust flow channel to the diesel turbine blades (Fig. 14). A heat recuperator was placed in place of the annular combustion chamber, where air compressed to 1.3 MPa for an engine power of 1500 hp (1100 kW) was preheated with exhaust gas downstream of the drive turbines. The heat recuperation reduced the fuel consumption of this engine. The compressed air pressure depends on the engine power, and it is decreased to 0.254 MPa for idling ($N_e = 40$ hp, 30 kW) [2]. The various versions of the AGT-1500 engines were developed with the improved operating parameters and increased operating economy.

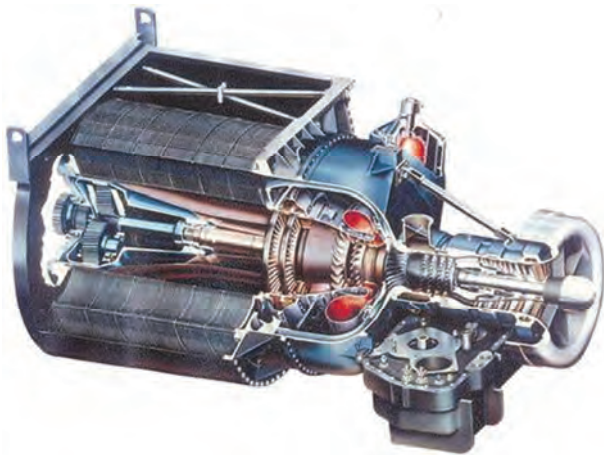


Fig. 14. The AGT-1500 engine (source: M1Abrams tank description, Internet)

5. Summary

The need for the 300–500 hp (220–370 kW) engines to power the heavy armored vehicles was addressed in the different ways by the countries participating in the Second World War. The Western Allies used the gasoline-powered aircraft engines with star and inline/straight line arrangements of the cylinders for this purpose. The Soviet Union used the diesel-powered engines in their tanks and heavy tractors, which were developed to power the land vehicles, but their solutions were the same as in the aircraft engines. Their opponents, the Germans produced the high-powered engines designed only to power the land vehicles. These were the spark-ignition engines that ran on gasoline with a high proportion of synthetic gasoline.

Considering the scale of applications of aircraft engines for tank propulsion, it is necessary to assess the consequences of the four most important decisions taken to application:

1. Gasoline-powered star aircraft engines for American light tanks M3/M5 Stuart and M4 Sherman
2. RR-Merlin (Meteor) and Ford GAA in-line petrol engines for British and American tanks

3. W-2 diesel engine for Soviet tanks

4. AGT-1500 turboshaft engine for US M1 Abrams tanks.

The mass use of the air-cooled aircraft radial engines to power tanks made it easy to produce large numbers of these engines at low cost. However, it was not advantageous in the practical terms and resulted in heavy tank losses. The drive shaft from the radial engine led under the tank turret increased its height and made it easier to hit with the projectiles. The exhaust system from the star engine was very elaborate inside the engine compartment. This facilitated the tank ignition upon its hitting by a shell, even if it did not penetrate the armor. The strong shock of a hit tank could easily unseal the fuel system and cause the fuel to leak and then ignite. The development of fire was favored by the intense, turbulent flow of cooling air in the engine compartment. It was estimated that 60–90% of the losses of tanks powered by star aircraft engines were as a consequence of their burning, and popular names for these tanks were "Ronson burner" (Allied term) or "Tommy Cooker" (German term) [3].

The more successful adaptations of aircraft engines to power tanks were the use V-60-engines (two banks of cylinder and one crankshaft, V-angle of 60°). RR-Meteor and Ford GAA engines developed for aircraft were used to power some British and American tanks. Despite being supplied with petrol, they were not as susceptible to fire as star engines. The RR-Meteor engine was developed, increased its power, and used to propulsion several British post-war tanks. Also, the Ford GAA engine was used in several tanks developed in production after the war, until the development of a tank-only engine (AV-1790) [7].

Diesel engines were less prone to fire. These were mainly Soviet Union engines based on the W-2 engine design. Compression-ignition engines were Japanese tank engines (e.g. Type 97 Chi-Ha with a Mitsubishi 125 kW engine, Type 1 Chi-He with a Mitsubishi 177 kW engine) and some American tank engines. Before the war, diesel engines were also used in Polish tanks (7TP tanks with PZInż. 235 engine). The use of such fuel resulted in the high requirements in respect of the fuel quality and cleanliness, as well as maintenance of these engines. However, more important was their greater resistance to fire.

Self-ignition of the mixture also has several other advantages. The diesel engines can also be fueled with aircraft kerosene and, under the special circumstances, even briefly with low-octane gasoline. The engines have no ignition system that can interfere with the communications equipment. More heat can be obtained from a comparable volume of diesel fuel compared to gasoline, making the engines more economical. The disadvantage of such a power system is a sensitivity of diesel fuel to low temperatures and the possibility of fuel filter blockage at such temperatures. This generally requires engine start-up heaters.

The tank engines originated from the aircraft engines were mostly made of aluminum alloys. These are less resistant to mechanical impact and temperature than cast iron. The use of lightweight materials reduced the weight of the engines, which undoubtedly made them easier to replace. During the warfare, this constituted an important advantage, as a rapid replacement of the entire assemblies is the prima-

ry means of recovering the damaged vehicles. A significant disadvantage of the "aluminum" engines is the lower rigidity of such cylinder blocks and crankcases, which can impair their durability under large and frequent changes in engine load. This is a typical load on land vehicle engines.

The W-2 engines with these properties and design solutions were a very successful design based on the forward-looking concept of an universal engine power about 500 hp (368 kW). In subsequent years they were upgraded to increase their power output. In the contemporary W-99 version with two turbochargers, 1200 hp (883 kW) was achieved [7]. The breakthrough idea was the transverse arrangement of this engine in the T-55 tank, which signifi-

cantly shortened its length and reduced the weight of the tank.

The turbine engines have better traction characteristics than the piston ones (multi-fuel, maximum turbine drive torque when starting and no torque discontinuity at the low speed). However, the operational and maintenance problems and the higher fuel consumption are greater in unsteady states. There is no indication that these engines will be developed to power heavy vehicles, including tanks. The improved LV-100 turbine engine was developed for this tank [4]. However, there is no indication of its implementation. Gas turbines could be used to drive electricity generators in hybrid drives if this is cost-effective.

Nomenclature

D cylinder diameter
 N_e engine power
 S piston stroke

V_s cylinder displacement
 ϵ compression ratio

Bibliography

- [1] BELOV, P. et al. Engines of Army Vehicles. *USSR Ministry of Defence Publishing House*. Moscow 1972 (Russian edition).
- [2] DODGE, L.G. et al. Fouling tests of AGT-1500 gas turbine fuel nozzle, interim report BFLRF No. 258, AD-A203 360. *Belvoir Fuels and Lubricants Research Facility (SwRI)*. San Antonio, Texas 78284, Sept. 1988.
- [3] FOX, J. The wrong truck: the inferiority of American tanks in WW II. *Southern Virginia University*, 10 May 2010.
- [4] FINN, D.P., The Abrams-Crusader Common Engine. *ARMOR*. March-April 2002.
- [5] GUNSTON, B. World Encyclopedia of Aero Engines, V Edition, *Sutton Publishing Limited*, Bill Gunston. 2006.
- [6] LLOYD, I., Rolls-Royce. The Merlin at War, *Palgrave Macmillan*. UK 1978.
<https://doi.org/10.1007/978-1-349-03908-1>
- [7] OGORKIEWICZ, R. Tanks: 100 Years of Evolution, *Bloomsbury Publishing PLC*. 2015.
- [8] POPOV, N.S. (ed.). Transport vehicles with gas turbine engines. *Mashinostroenie*. Leningrad 1987 (Russian edition).
- [9] RUBINS, P.L. et al. PLT 27 gas turbine engine exhaust emission and noise measurements. Avco Lycoming Division Report AD/A-001 728, *Stratford*. Connecticut 06497, September 1974.
- [10] WALENTYNOWICZ, J., History of heat engine development. *Publications of the Institute of Aviation*. Warsaw 2011 (Polish edition), ISBN 978-83-932592-4-3.
- [11] Descriptions of engines and tanks exhibited in museums.

Prof. Jerzy Walentynowicz, DSc. DEng. – Faculty of Mechanical Engineering, Military University of Technology, Warsaw.
 e-mail: jerzy.walentynowicz@wat.edu.pl



Cylinder liner wear as a function of selected physicochemical indicators of engine oil

ARTICLE INFO

Received: 13 July 2021
Revised: 31 August 2021
Accepted: 1 September 2021
Available online: 1 September 2021

The paper presents a new method of forecasting the durability of piston-rings-cylinder (PRC) liner assembly of the internal combustion engine on the basis of observed changes of physical and chemical properties of engine oil. Methods used so far for the durability evaluation of the PRC group required collecting information about the moments when the assembly reached its boundary state or used kinetic models of wear designed using accelerated research of real objects. In the proposed method, for the evaluation of durability of engine cylinders information gathered from engine oil is used. Course of changes of the proposed index of change intensity of kinematic viscosity at the temperature of 100°C – Cv100 allows for evaluation of the durability of PRC assembly of an IC engine. Obtained value was positively verified using forecasting method related to the technical criteria based on the assessment of the wear intensity.

Key words: engine durability, forecasting, operational research

This is an open access article under the CC BY license (<http://creativecommons.org/licenses/by/4.0/>)

1. Introduction

Designing of modern internal combustion engines is a challenge both in terms of their efficiency, production and operation ecology, as well as high durability. The last parameter, despite the bench and operational tests carried out by the manufacturer, is finally verified at the stage of use in natural operating conditions. Reliable information about the actual durability of the vehicle, including its engine, can only be obtained at this stage. On the one hand, this requires a long waiting time for the expected test results (sometimes several years), and on the other, proposing non-invasive methods of testing wear, so that the tribological processes in the observed kinematic nodes are not disturbed.

In case of an automotive vehicle, a component very important taking into account car's durability is a piston-rings-cylinder (PRC) assembly. Wear of this assembly directly influences reaching by the engine its borderline state (SG) [8]. Wear of the PRC group is mostly identified with the increase of the internal diameter of the cylinder liner. As the diameter increases, engine start becomes more difficult and engine delivers less power – these are technical criteria of SG. Moreover, engine consumes more fuel and lubricating oil. Increase in oil consumption, with severe regulations concerning exhaust emissions, results in the fact, that the engine (even fulfilling other criteria) can not be used any longer – these are economic and ecologic criteria of SG [7].

Considering possibilities of durability evaluation of the frictional couple (of the technical object), two methodical variants can be considered [5, 6, 14]:

1. An analysis of object's operation time (e.g. PRC assembly) till reaching boundary state. Having results of research for sufficiently high, homogenous population of objects, it is possible to estimate for any time moment t wear distribution taking into account average, maximum and minimum wear. A particular time of operation is the moment when the system reaches boundary wear, conditioning boundary state which corresponds to the durability of the object. Recording the particular moments of

reaching boundary state allows for establishing the average durability \bar{T} , minimum T_{min} and maximum T_{max} for the given population. This method (a' posteriori) in case of PRC assembly is difficult to realize. Such type of research allows for determination of numerical and functional characteristics (point and range) with given probability. This method is however costly and time consuming, and obtained results can be transferred on objects of similar class only with certain approximation. Fig. 1 presents the determination of object's durability using the method described above.

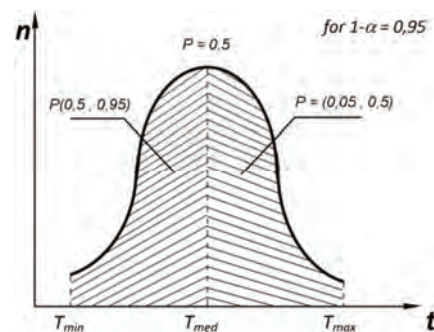


Fig. 1. Determination of durability using a' posteriori method

2. Second of methods allows for significant shortening of research time and creates possibility to forecast durability a' priori. In case of this method, research is done in a shorter time than object's service life. It includes an analysis of individual realizations of wear process and estimation of tendencies in the course of phenomena (theoretical models are obtained). Having information regarding boundary state, an assessment of object's durability can be done. The condition of correctness of the estimation is the calculation of tendencies of average wear and possible minimum and maximum values for the given confidence level. This theoretically-experimental methods of durability estimation belong to

the group of accelerated research, as – from the assumption – they do not require any tests till the object reaches its boundary state. Gathered information about the kinetics of changes of wear characteristics (models of wear kinetics) allow for forecasting durability on the basis of theoretical reliability models of the distribution of correct time of operation. The idea of such type of assessment is shown on Fig. 2a, 2b.

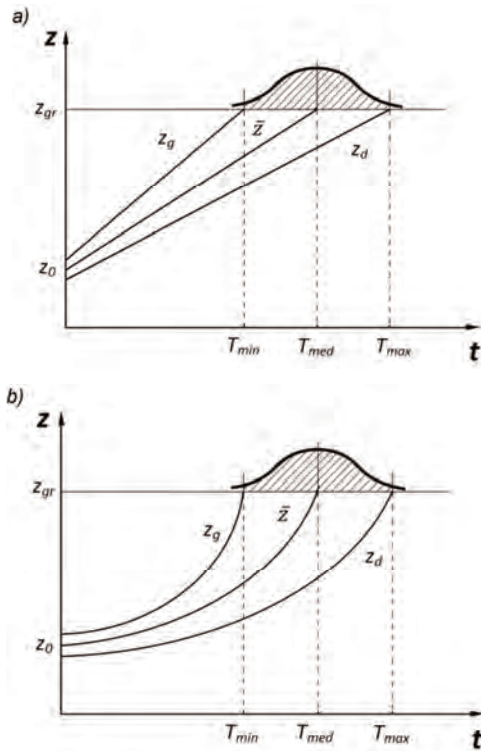


Fig. 2. Schematic presentation of durability assessment using a priori method

2. Essence of the method

As mentioned above, the reliability of the results of the wear tests of the engine's kinematic systems is related to the limitation of interference in the operated unit. Also, the measurement methods used should interfere with the tribological system as little as possible, or even not cause temporary changes in its environment, disrupting the functioning of the system.

For the evaluation of the durability of the PRC assembly, methods used so far require research till the object reaches its boundary state (methods a posteriori), or require intervention in the tribological system so as to determine object's regular service time, e.g. micro measurements, method of artificial bases, isotopic methods. A new method described below eliminates these disadvantages.

For the durability evaluation of cylinder liners information gathered from engine oil is used. Engine oil has important function forming with the engine a tribological system [7]. Changes in physical and chemical properties of oil result from the influence of the system and are strictly related to its technical condition, i.e. wear of cylinder liners.

The levels of specific physical and chemical properties of engine oil affect the quality and range of functions performed by the oil and, as such, they are a prerequisite for its

suitability for a particular type of engine. Among the parameters and physicochemical quantity levels outlined in subject standards and literature, the preference is given to the kinematic viscosity and dynamic viscosity (some of the basic properties of fluids). Kinematic viscosity is always stipulated in the quality requirements relating to lubricating oils. It can increase or decrease during operation. An increase in viscosity is generally connected with progressive oxidation processes at elevated temperature, and a decrease with the shear of oil. The assessment of oil viscosity allows the user to estimate the time between oil changes [2, 11–13].

Currently, it is possible to observe the phenomenon of extending the service life of the oil in the engine. This applies to both mileage and calendar time. This significantly reduces environmental pollution with used petroleum products, but the most important aspect should be to ensure the correct operation of the lubricated kinematic nodes in terms of the properties of the lubricant in the tribological system. You can meet with research carried out in this area.

According to the current state of knowledge, the quality of engine oil can be determined through a series of tests, which include laboratory evaluation of the physicochemical properties, as well as through assessing its particular properties which, however, entails lengthy and costly operational research. Knowledge and understanding of the characteristics of motor oils and developing effective methods of analysis enables the creation of systems of quality monitoring which may be conducted within the life cycle of the engine [13].

A number of studies have been conducted to scientifically measure the quality of engine oils. Inayatullah et al. [3] used the technique of acoustic emission to analyze engine oil viscosity. Karpovich et al. [4] attempted to develop a universal instrument to measure and control the quality of motor oils. Their evaluation of the quality and condition of engine oil was centered around viscosity as a key performance indicator. Agoston et al. [1], on the other hand, have focused in their research on thermal aging of engine oils. They have shown that oil evaporation and oil burning have the most significant impact on the process of aging, thus leading to the loss of its key properties, which inevitably affects the overall performance of the engine oil [13].

The method of durability evaluation of engine cylinders presented here, in general assumption is designed for the use by a wide group of users who do not have sufficient technical and diagnostic resources. Therefore oil exchange service can be used to gather information about:

- parameters of new oil,
- parameters of used oil,
- oil operation time in an engine.

On the basis of above data it is possible to determine value of index of change intensity of oil properties C_W (1):

$$C_W = \frac{W_p - W_k}{t_{ol}} \quad \text{for } t > 0 \quad (1)$$

where: W_p – value of the measured index of oil technical condition for the new oil, W_k – value of the measured index of oil technical condition for the used oil (at exchange), t_{ol} – oil operation time in the engine (till exchange), C_W – index of change intensity of oil properties.

This index brings averaged information about intensity of engine impact on the oil. It does not take into account periodic changes in the value of measured oil parameter, and reflects long term tendency in observed changes. Periodic changes of measured index can result from, among others, the fact of topping up oil as a effect of oil loss (leaks, combustion). Detailed analysis of index changes in such case would lead to erratic evaluation of diagnostic information. Long term observation of index of change intensity of oil properties and observed its changes allow to conclude, that the reason of these variations are wear processes occurring in the engine. Graphic interpretation of described phenomena is shown on Fig. 3.

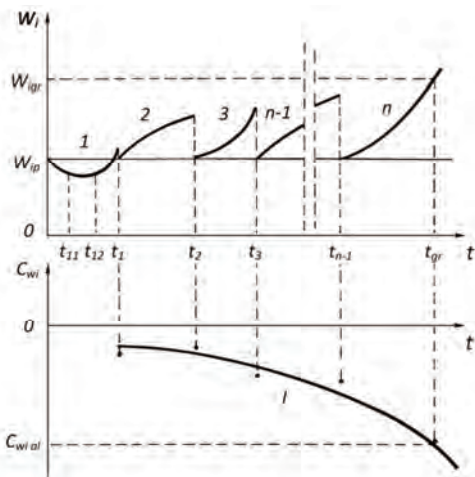


Fig. 3. Graphic interpretation of changes in the index of change intensity of oil properties: W_p – preliminary index value, $W_{k1}, W_{k2}, \dots, W_{kn}$ – end value of index of oil technical condition at the moment 1, 2, ..., n of oil change, t_1, t_2, \dots, t_n – moments of oil change in the engine, C_w – index of change intensity of oil properties

Curves 1, 2, 3, ..., n represent changes of observed index of oil technical condition W_{oi} in the time between oil changes $t_1, t_2, t_3, \dots, t_n$. Detailed analysis of momentary index values for the time points $t_{11}, t_{12}, t_{21}, t_{22}, \dots, t_{n1}$ and calculated on this basis momentary values of index of change intensity of oil properties C_{wch} do not carry any important diagnostic information in the sense of technical condition – engine wear. They result from the influence of momentary or short term inputs acting on the engine (increase of load, technical service) or directly on the engine oil (topping up new oil, outside impurities resulting from filter damage). However analysis of changes in the longer research period (between oil changes) permits to observe long term tendency of changes – curve I. Fig. 3 shows also marked position of index boundary value. It is a intersection of curve I with the value corresponding to the lower permissible value of index of change intensity of oil properties C_w . In this case, it is related to the reaching of the upper permissible value of observed index of oil condition W – value resulting from accepted criteria of boundary state. In situation, when value of the observed index of oil condition decreases ($W_{k1}, W_{k2}, \dots, W_{kn} < W_p$), reaching boundary state will result from crossing upper boundary value of index C_w , related to lower permissible value of the index of oil condition W .

Fig. 3 shows hypothetical realization (changes of values of oil properties index) related to the single object (engine) under operation. In reality, for every individual object from the investigated sample from the population obtained results are scattered. Therefore the dependence describing variability of the index of change intensity of oil properties can be only of stochastic value – correlative.

The dispersion area is limited by regression curves $C_{wi \max}$ and $C_{wi \min}$ corresponding to the upper and lower border of confidence interval. Specific values depend from the arbitrary assumption of confidence interval (for technical purposes 0.9; 0.95; 0.99) – Fig. 4.

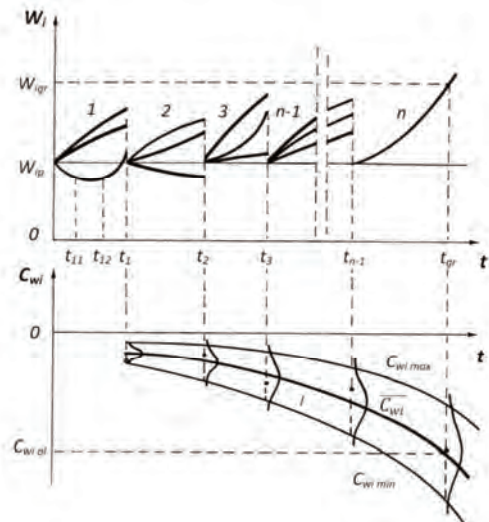


Fig. 4. Graphic interpretation of changes in the index of change intensity of oil properties for the population of objects: W_p – preliminary index value, $W_{k1}, W_{k2}, \dots, W_{kn}$ – end value of index of oil technical condition at the moment 1, 2, ..., n of oil change, t_1, t_2, \dots, t_n – moments of oil change in the engine, C_w – index of change intensity of oil properties

Changes in engine oil presented on Figs. 3 and 4 take place parallel to the wear of cylinder liners of the engine. Mathematical description of this phenomena is created by three curves reflecting expected value of changes \bar{z} (calculated on the basis of operational research), upper border of realization of the stochastic wear z_g and lower border of the wear course z_d . These three equations all together create statistic model of wear process of cylinder liners (Fig. 5).

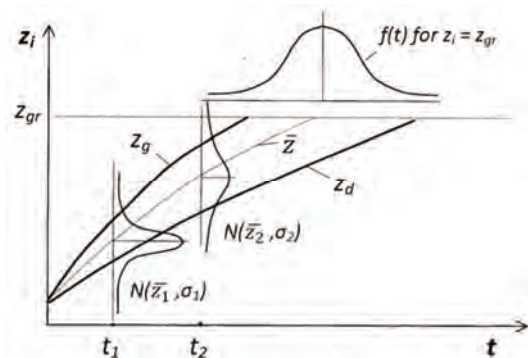


Fig. 5. Graphic interpretation of mathematical model of wear process of the cylinder liners

Such description of wear process permits – for any time moment t – to determine width of confidence interval on the confidence level β , where real realizations of the stochastic process are located. Choice of confidence interval is a matter of decision. Boundaries of the confidence interval for the results related to the time of observation t_1 can be written as follows:

$$z_1^g = \bar{z}_1 + q_\beta \cdot \sigma_1 \tag{2a}$$

$$z_1^d = \bar{z}_1 - q_\beta \cdot \sigma_1 \tag{2b}$$

where: q_β – proportionality coefficient.

Value of the coefficient q_β should be determined (in relation to the batch size of the results set) according to the rules of building the range estimators.

Making use of engine oil as a source of information for forecasting engine durability is possible only when it can be proved, that the kinetics of changes of chosen physical and chemical properties of the oil reflects wear changes taking place in the analyzed PRC assembly. Confirmation of such correlation can be done on the basis of comparable values of estimated durability of the cylinder liner with the use of “wear” as well as “oil” method. Operational research should be done, so as to determine course of curves I (Fig.4) and \bar{z} (Fig. 5).

3. Results of experiments

The proposed test method was verified on the basis of the results of measurements of the wear of cylinder liners of engines performed as part of supervised operation tests. The subject of the research was five compression-ignition engines with direct fuel injection, in-line cylinder arrangement, installed in medium-duty trucks. The amount of wear of individual cylinder liners was recorded for the mileage of 0–250 thousand km in intervals of approx. 50 thousand km. Technical maintenance was done according to the manufacturer’s instructions.

So as to determine course of the curve \bar{z} in used engines, periodically micro-measurements of cylinder liners was done, according to the standard recommendation of the branch norm [9]. Additionally during obligatory technical inspections united with oil change service, oil samples were taken from the engine and put under physical and chemical analysis. Basic physical, chemical and functional indexes of the used oil were determined.

On the basis of gathered information it was possible to obtain equations for the expected value and for the lower and upper boundaries of the wear process realization. Full mathematical description of the wear process of the cylinder liners for the period of operation $t > t_d$ (t_d – running-in) is shown by the set of equations (3):

$$\bar{z} = (0.000132) \cdot t + 43.961 \text{ [}\mu\text{m]} \tag{3a}$$

$$z_d = \min\{0.000105 \cdot t + 43.961 | 0.000132 \cdot t + 38.466\} \text{ [}\mu\text{m]} \tag{3b}$$

$$z_g = \max\{0.000159 \cdot t + 43.961 | 0.000132 \cdot t + 49.456\} \text{ [}\mu\text{m]} \tag{3c}$$

where: t – engine operation time (mileage) [km].

Similar analysis was made in case of research results obtained for the used oil. It was concluded – on the basis of theoretical analysis and statistical analysis of research results, that the best index for the evaluation of changes in oil properties is kinematic viscosity at the temperature of 100°C and corresponding index of change intensity of kinematic viscosity at 100°C– C_{v100} (equation (1)). Course of C_{v100} changes in a function of operation time is given by the dependence (4):

$$C_{v100} = (3.277) - (2.142) \cdot t^{(0.033)} \left[\frac{\text{mm}^2}{\text{s} \cdot \text{km}} \right] \tag{4}$$

where: t – engine operation time (mileage) [km].

Using equations (3) and (4) durability of PRC assembly for the engine under test was determined. In case of technical criterion, durability of the system results from reaching permissible value of cylinder liner wear. This value was accepted on the basis of work [11]. In case of “oil” criterion, boundary values of kinematic viscosity v_{100} were accepted using the norm BN-77/0535-46 [10]. Then boundary value of C_{v100gr} index was calculated, which was later used for the determination of cylinder liners durability on the basis of oil criterion. Results of calculations are presented in Table 1.

Table 1. Comparison of forecasts of cylinder liners durability of the 359M engines

Data source	Type of criterion	Limit state parameter		Durability $\times 10^3$ [km]		
		Parameter description	Limit value	T_{min}	T_{sr}	T_{max}
own	technical	cylinder liner wear \bar{z} at depths 20, 35, 50, 95 [mm] in the plane A–A and B–B	126 [μm]	516.0	621.5	781.3
own	oil	index of intensity of changes in kinematic viscosity of engine oil in temperature 100°C– C_{v100}	–0.066 $\left[\frac{\text{mm}^2}{\text{s} \cdot \text{km}} \right]$	–	630.2	–

4. Conclusions

Presented oil criterion takes into account possibilities of correct evaluation of mating of components in the PRC assembly with regard to the type of friction. One of conditions of fluid friction is, for instance, existence of appropriate crevice between mating components in relation to the viscosity of used lubricant. Increase of clearance between components of PRC assembly intensifies degradation processes taking place in engine oil, and thus, faster change of its viscosity. Proposed method of forecasting tribological durability using results of current (in kinetic sense) assessment of oil properties, gives results regarding average durability which are comparable with results determined according to the forecasting method related to the technical criterion. Values of forecasted durability average $621.5 \cdot 10^3$ km using technical criterion and $630.2 \cdot 10^3$ km for the oil criterion. So, basing on the information describing technical condition of the used lubricant it is possible, with no need of interference in the monitored PRC assembly, to deter-

mine durability of the cylinder liners (on the accepted confidence level). Moreover simple measurement methods

away from the investigated object are used, and with no need of taking the engine out of service.

Nomenclature

PRC piston-rings-cylinder

SG borderline state

Bibliography

- [1] AGOSTON, A., ÖTSCH, C., JAKOBY, B. Viscosity sensors for engine oil condition monitoring – Application and interpretation of results. *Sensors and Actuators A: Physical*. 2005, **121**(2), 327-332. <https://doi.org/10.1016/j.sna.2005.02.024>
- [2] GOMÓŁKA, I., AUGUSTYNOWICZ, A. Evaluation of applicability of dielectric constant in monitoring aging processes in engine oils. *Eksploatacja i Niezawodność – Maintenance and Reliability*. 2019, **21**(2), 177-185. <https://doi.org/10.17531/ein.2019.2.1>
- [3] INAYATULLAH, O., JAMALUDIN, N., ALI, A. et al. Application of acoustic emission technique to observe the engine oil's viscosity. *2nd International Conference on Instrumentation Control and Automation*. IEEE 2011, 344-348. <https://doi.org/10.1109/ICA.2011.6130184>
- [4] KARPOVICH, I.A., ODZHAYEV, V.B., AZARKO, I.I. et al. Universal device for motor-oil quality control. *11th International Conference Microwave and Telecommunication Technology. Conference Proceedings* (IEEE Cat. No01EX487). 2001, 673-674. <https://doi.org/10.1109/CRMICO.2001.961712>
- [5] KHANIYEV, T., BASKIR, M.B., GOKPINAR, F. et al. Statistical distributions and reliability functions with type-2 fuzzy parameters. *Eksploatacja i Niezawodność – Maintenance and Reliability*. 2019, **21** (2), 268-274. <https://doi.org/10.17531/ein.2019.2.11>
- [6] NADOLNY, K. Podstawy modelowania niezawodności materiałów eksploatacyjnych, Nadolny K. (red.), Seria: *Biblioteka Problemów Eksploatacji*, Wyd. ITeE, Radom 1999.
- [7] NIEWCZAS, A., RYMARZ, J., DĘBICKA, E. Stages of operating vehicles with respect to operational efficiency using city buses as an example. *Eksploatacja i Niezawodność – Maintenance and Reliability*. 2019, **21**(1), 21-27. <https://doi.org/10.17531/ein.2019.1.3>
- [8] NIEWCZAS, A. Trwałość zespołu tłok-pierścienie tłokowe-cylinder silnika spalinowego. *WNT*. Warszawa 1998.
- [9] Norma BN-79/1374-04. Silniki samochodowe. Badania stanowiskowe. Badania niezawodności.
- [10] Norma BN-77/0536-46. Ocena stopnia przepracowania olejów do silników z zapłonem samoczynnym.
- [11] URZĘDOWSKA, W., STĘPIEŃ, Z. Wybrane zagadnienia dotyczące zmian właściwości silnikowego oleju smarowego w eksploatacji. *Nafta-Gaz*. 2012, **12**(LX), 1102-1110.
- [12] WOLAK, A., JANOCHA, P. Zmiany właściwości użytkowych olejów silnikowych w warunkach eksploatacji - analizy FTIR. *Nowoczesne środki smarowe do specjalistycznych zastosowań w urządzeniach przemysłowych, transporcie i komunikacji*. Kraków: Instytut Nafty i Gazu – Państwowy Instytut Badawczy. 2015, **201**, 84-105.
- [13] WOLAK, A., ZAJĄC, G. The kinetics of changes in kinematic viscosity of engine oils under similar operating conditions. *Eksploatacja i Niezawodność – Maintenance and Reliability*. 2017, **19**(2), 260-267. <https://doi.org/10.17531/ein.2017.2.14>
- [14] YAN, S., MA, B., ZHENG, C. Health index extracting methodology for degradation modelling and prognosis of mechanical transmissions. *Eksploatacja i Niezawodność – Maintenance and Reliability*. 2019, **21**(1), 137-144. <http://dx.doi.org/10.17531/ein.2019.1.15>

Zbigniew Chmielewski, DEng. – Faculty of Mechanical Engineering, University of Technology and Humanities in Radom.
e-mail: zbigniew.chmielewski@uthrad.pl



Analysis of the operation of the hybrid drive system in the light of the proposed Euro 7 standard

ARTICLE INFO

Received: 15 July 2021
Revised: 30 July 2021
Accepted: 15 August 2021
Available online: 8 September 2021

The article presents the issues of energy recovery in the hybrid drive system of a vehicle. Road tests of a vehicle equipped with a hybrid powertrain were carried out in accordance with the recommendations of the RDE test. In these studies, measurements of braking energy recovery were carried out in urban, rural and motorway traffic conditions. The analysis of the obtained test results may constitute a premise for the creation of an appropriate strategy for the operation of the hybrid drive system in terms of meeting the requirements of the currently prepared Euro 7 standard.

Key words: *hybrid drive system, real driving emissions, Euro 7 standard, vehicle road tests*

This is an open access article under the CC BY license (<http://creativecommons.org/licenses/by/4.0/>)

1. Introduction

The activities of the European Commission in the field of new test procedures used to measure emissions of toxic exhaust gas components, in practice, may result in a complete suspension of the production of internal combustion engines intended for passenger cars. This applies especially to the preliminary assumptions for the Euro 7 standard, which is to apply from 2025. According to the new assumptions, the changes would concern both a drastic reduction of the permissible emission limits, but also the method of conducting measurements. For example, the proposal provided for the reduction of the CO₂ emission limit for combustion engines from the current value of 95 g/km to 30 g/km and the NO_x emission limit for nitrogen oxides from 60 mg/km to 30 mg/km. Moreover, it was planned to introduce changes to the RDE (Real Driving Emissions) test procedure, the test sections of which cover various traffic conditions in which the instantaneous emission value is subject to changes. For this reason, the so-called divergence factor, which determined the acceptable differences. According to the proposal, in the Euro 7 standard, the emission value of individual exhaust components could not exceed the established limits, regardless of the traffic conditions in the test, as well as regardless of the version of the vehicle's additional equipment, including e.g. when the vehicle is moving with a roof rack or a trailer. In addition, it was proposed to equip the vehicle with an emission monitoring system, and the time to meet these requirements was set at 15 years or 240 thousand kilometers.

As the automotive industry would not be able to meet these conditions, and would not be able to ensure an adequate supply of zero-emission vehicles, even by carrying out a deep modernization of the currently produced engines, the AGVES (Advisory Group on Vehicle Emission Standards) advisory group operating at the European Commission strongly recommended a relieved version of the initial bill of law. The legal regulations proposed in this recommendation, although they will constitute a further evolution of the currently applicable Euro 6d standard, are assessed as technically very demanding. One of the most important

changes is leaving the so-called difference factor used to calculate the emissions from a real road test. Thanks to this, the increased emission in a given section of the route will be able to be compensated by a reduced emission in another section of the test. This will allow not only to meet the requirements of the new Euro 7 standard, but also to further development of internal combustion piston engines, especially in hybrid drive systems with zero emissions when driving in electric mode or during energy recovery [1].

2. Characteristics of an internal combustion engine operation in a hybrid drive system

In a hybrid system, the internal combustion engine works with one or two electric machines. In addition to operating the vehicle with an internal combustion engine and supporting it with an electric motor, this system allows operation with an electric drive only [6].

The most important advantage of this system is the possibility of recovering some energy through an electric current generator, which is activated during braking and when the vehicle is moving by inertia. The recovered energy is stored in an energy accumulator which powers the propulsion electric motor. As a rule, these are electric accumulator batteries with a sufficiently high voltage level (usually nickel-metal-hydride NiMH or lithium-ion Li-Ion) [7-9].

In all types of standard vehicles, braking energy is usually irretrievably lost and converted into heat in the braking systems [11].

Internal combustion engines with spark ignition systems presently used in the hybrid drive, usually work in a cycle similar to the Atkinson cycle in which one can use a larger value of compression ratio than standard engines, which contributes to increased overall efficiency. In addition, the control system forces the engine to work in this area characteristics, which achieves the highest energy conversion efficiency and minimum emission of toxic fumes. Including avoiding engine operation with a high load, where nitrogen oxide emission is the highest [2, 3].

All the above-mentioned features of the hybrid powertrain, compared to standard systems, give a measurable

effects in the form of reduced fuel consumption and resulting lower carbon dioxide emissions, as well as reduced emission of toxic exhaust components.

Possible operating states of the hybrid drive system:

- hybrid drive (diesel-electric),
- combustion engine,
- electric drive,
- supporting the internal combustion engine with an electric motor,
- generator operation of the electric machine,
- braking with energy recovery,
- disengaging the drive system (start/stop system).

3. The effects of using a hybrid drive system

The effects of the hybrid drive system are already visible during the initial analysis carried out on the basis of a comparison of selected factory parameters of a vehicle equipped with this system with a vehicle equipped with a standard drive system. For this purpose, two Toyota Yaris models were compared, the first of which: the Yaris 1.5 Dynamic Force Multidrive S with a standard driveline and automatic transmission, and the second: the Yaris 1.5 Hybrid Dynamic Force e-CVT with a hybrid driveline and series stepless transmission.

According to the factory data, the performance of both vehicles is similar.

Table 1. Specifications of Yaris 1.5 Vehicle Dynamic Force Multidrive S and Yaris 1.5 Hybrid Dynamic Force E-CVT

	Yaris 1.5 Dynamic Force Multidrive S	Yaris 1.5 Hybrid Dynamic Force e-CVT
Acceleration time 0-100 km/h [s]	10.2	9.7
Top speed [km/h]	180	175
Fuel consumption according to the WLTP procedure [dm ³ /100 km]	5.3–5.7	3.8–4.3
Carbon dioxide CO ₂ emissions according to the WLTP procedure [g/km]	125–133	87–98
Curb weight [kg] min/max	1065/1145	1080/1190

The significantly more favourable parameters of the hybrid drive system result mainly from the possibility of recovering the braking energy and the vehicle moving without the combustion engine switched on in certain traffic conditions. Therefore, from the point of view of the proposed requirements of the new Euro 7 standard, the hybrid drive system, compared to other solutions, has the greatest development potential due to the significant share of emission-free operation [5].

4. Analysis of the operation of the hybrid drive system during road tests

In order to verify the factory data, road tests of the Toyota Yaris 1.5 Hybrid Dynamic Force e-CVT car in real road traffic conditions were carried out at the Department of Motor Vehicles at the Cracow University of Technology, according to the RDE test recommendations. The tests were carried out on 28-29 January 2021 in real road traffic condi-

tions in the area of the Krakow agglomeration during a road test consisting of the participation of the vehicle in urban traffic, in suburban traffic and on the motorway. Their main goal was to conduct an in-depth analysis of the operation of the hybrid drive system during various phases of the test. Besides, additional tests were performed consisting in the assessment of energy recovery during braking in various speed ranges of the vehicle.

Test parameters:

- Total test distance: S = 73.04 km, total test time: t = 96 min.
- City route: S = 17.27 km, t = 40 min.
- Suburban route (Rural): S = 35.6 km, t = 33 min.
- Motorway route: S = 35.6 km, t = 23 min.

Energy distribution in a hybrid drive system should be analysed in various components responsible for vehicle propulsion and energy recovery. The propulsion system of the Toyota Yaris 1.5 Hybrid Dynamic Force e-CVT can be assigned to the group of hybrid series-parallel systems. It is equipped with two electric machines marked with the symbols MG1 and MG2, a 3-cylinder spark ignition engine working according to the Atkinson cycle and a planetary continuously variable transmission [10]. The analysis of energy flow in the hybrid drive system of this vehicle was carried out on the basis of measurements of electric energy received and transmitted by the traction battery and both MG1 and MG2 electric machines. For the measurement of electrical energy and other parameters used in the existing sensors mounted in the vehicle and a dedicated diagnostic software allowing the registration of the selected parameters in real time with a frequency of 10 Hz. Moreover, on the basis of fuel consumption and its calorific value, calculations of the thermal energy processed in the internal combustion engine were performed. During carrying out this analysis, the individual energy streams in the collective diagrams are marked with rectangles of different colours. They mean in turn:

- red rectangle: electricity absorbed by the traction battery of the vehicle, which comes from both energy recovery and the operation of the internal combustion engine,
- red dashed rectangle: electric energy given by the traction battery to the vehicle drive and power supply to the internal installation of the vehicle,
- yellow rectangle: electricity generated by the MG1 electric machine,
- yellow dashed rectangle: electricity supplying the MG1 machine to start the internal combustion engine,
- green rectangle: energy recovered by the MG2 generator in the process of braking or moving the vehicle by inertia,
- green dashed rectangle: electricity supplying the MG2 machine while the vehicle is electrically powered (the energy comes from the MG1 machine and the traction battery),
- blue rectangle: thermal energy released in the combustion engine (due to its high value – it is given on the chart on a scale 10 times smaller than the other components).

Figures 1, 2 and 3 show the energy distribution in the hybrid drive system during the driving test in real road traffic conditions.

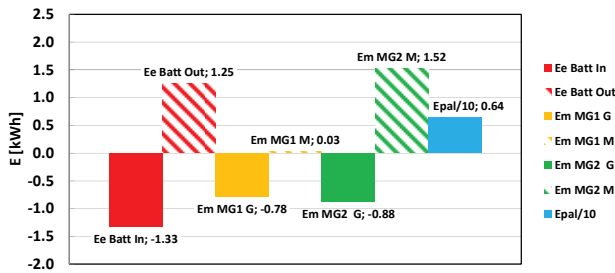


Fig. 1. Energy distribution in the hybrid drive system in the city part (City) of the RDE test (Toyota Yaris 1.5 Hybrid Dynamic Force e-CVT)

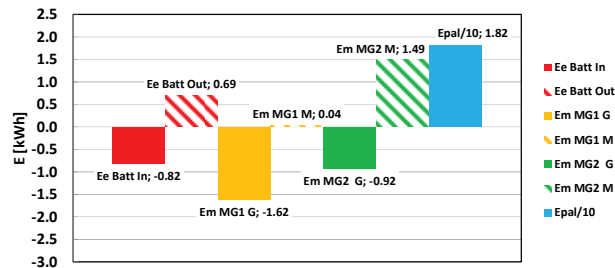


Fig. 2. Energy distribution in the hybrid drive system in the motorway part of the RDE test (Toyota Yaris 1.5 Hybrid Dynamic Force e-CVT)

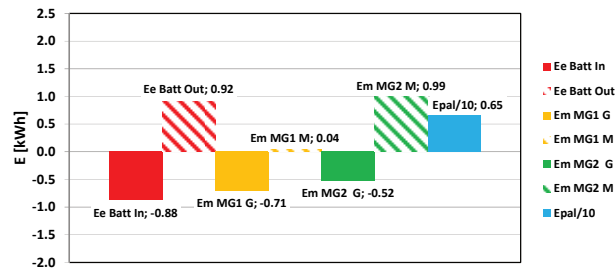


Fig. 3. Energy distribution in the hybrid drive system in the rural part of the RDE test (Toyota Yaris 1.5 Hybrid Dynamic Force e-CVT)

From the point of view of the analysis of the energy balance in the hybrid drive system, the green rectangle deserves attention, which indicates that 0.88 kWh of energy was recovered in the city cycle (City), 0.92 kWh in the motorway cycle, and 0.52 kWh in the extra-urban cycle. In total, in the entire RDE test on the 73.04 km route, 2.32 kWh of energy was recovered.

5. Analysis of the operation of the hybrid drive system during the braking test

During the tests, a brake test was also carried out from the initial speed of 53 km/h until the vehicle stopped (Fig. 4). This test was performed during the urban part of the test and had the characteristics of a typical stop for a vehicle in city traffic before the crossing of the streets with traffic lights. The distance from the beginning of the test, when the driver, seeing the red signal of the signaling device, took his foot off the accelerator pedal until the vehicle stopped, was approx. the 200 m braking process (Fig. 4). In the initial phase of the process, the reduction of the vehicle speed

was mainly caused by the load on the MG2 electric machine, which recovers braking energy. Only in the final phase of the vehicle stopping process, the main reason for the reduction in speed was the operation of the friction linings of the braking system. The energy recovered by the MG2 electric machine at each point of the braking process was also measured (Fig. 5). The reduction of energy recovery in the final phase of the braking process resulted from the lower possibility of generating electricity due to the low rotational speed and due to the operation of the friction brake.

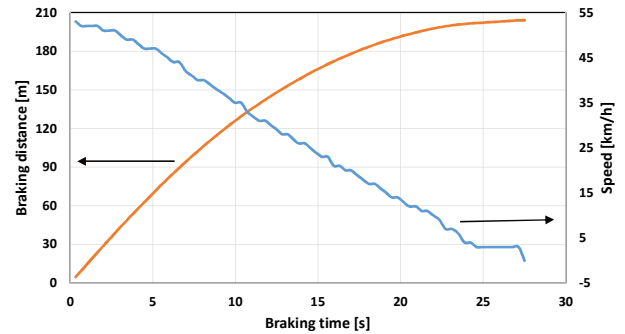


Fig. 4. The course of the braking process in the hybrid drive system

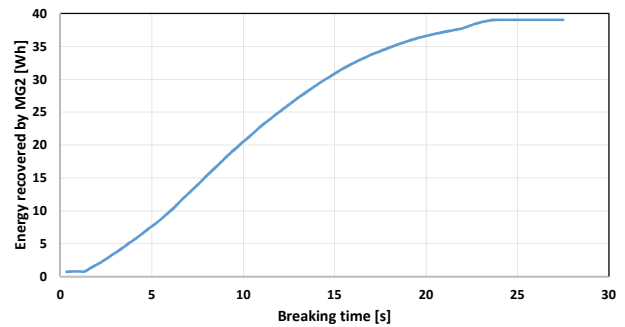


Fig. 5. The course of energy recovery in the braking process in a hybrid drive system

The total value of energy recovered in the test was approx. 39 Wh, while the energy supplied to the traction battery was approx. 37 Wh (Fig. 6). The difference, amounting to about 2 Wh, resulted from the losses related to energy transmission and the necessity to use it to power the vehicle accessories.

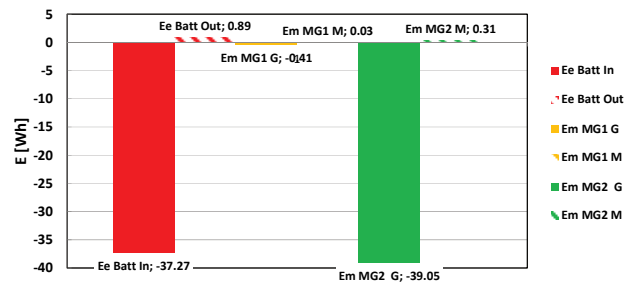


Fig. 6. Energy distribution in the hybrid drive system during braking

6. Conclusions

A characteristic feature of reciprocating heat engines is the high variability of the achieved efficiency of the engine

in its field of operation. The hybrid drive system allows the optimal use of the engine's operating area, where it achieves the greatest efficiency, while the shortage or excess of developed torque is compensated by the electric machine. Thanks to such a system, it is possible to significantly reduce fuel consumption by motor vehicles and reduce heat emission and the emission of toxic components to the environment.

The most important advantage of hybrid drive systems in motor vehicles is the recovery of braking energy, which is irretrievably lost in standard vehicles, causing the environment to be loaded with heat. An important feature of the cooperation of a heat engine with an electric machine is the possibility of mutual supplementation of energy demand in the vehicle drive system, implemented according to the adopted criteria of energy consumption optimization.

Contemporary compact cars powered only by electricity usually have a battery with an electric capacity of 40–60 kWh, which allows for a range of 400–500 km. BEVs that are powered solely by electricity are currently subject to a number of limitations in terms of range, refill time and the amount of energy that can be stored. Therefore, during the

transition period, a lot of attention should be paid to the development and optimization of hybrid drive systems.

In the context of the research, the energy recovery of approx. 2.3 kWh on a route with a length of approx. 70 km and variable road conditions in the hybrid drive system of the Toyota Yaris 1.5 Hybrid Dynamic Force e-CVT is significant and has a significant importance from the point of view of the rational use of energy in transport. This results in a significant reduction in fuel consumption in relation to a similar class of vehicles equipped with a conventional drive system. Preliminary studies of braking energy recovery, carried out in urban traffic, show a great potential for the development of a special control algorithm, allowing for the optimal selection of the strategy of cooperation between a piston heat engine and an electric machine, based on the criterion of energy savings in transport.

Such actions meet the legislative activity of the European Commission in the field of new emission limits and measurement procedures, especially with regard to the initial assumptions provided for the Euro 7 standard. In practice, it is currently the only possibility of further use of internal combustion engines to power passenger cars.

Nomenclature

RDE	Real Driving Emissions	Li-Ion	lithium-ion cell
AGVES	Advisory Group on Vehicle Emission Standards	e-CVT	Electronic Continuously Variable Transmission
NiMH	nickel metal hydride	BEV	Battery Electric Vehicle

Bibliography

- [1] Europejskie normy emisji z pojazdów – Euro 7 dla samochodów osobowych, dostawczych, ciężarowych i autobusów. https://ec.europa.eu/info/law/better-regulation/have-your-say/initiatives/12313-Europejskie-normy-emisji-z-pojazdow-Euro-7-dla-samochodow-osobowych-dostawczych-ciezarowych-i-autobusow_pl (accessed on 13.07.2021).
- [2] BRZEŻAŃSKI, M., JUDA, Z. (ed.). Napędy hybrydowe, ogniwa paliwowe i paliwa alternatywne. *Wydawnictwo Komunikacji i Łączności*. Warszawa 2010.
- [3] MERKISZ, J., PIELECHA, I. Układy mechaniczne napędu hybrydowego. *Wydawnictwo Politechniki Poznańskiej*, Poznań 2015.
- [4] Katalog – Nowa Toyota Yaris. <https://www.toyota.pl/new-cars/yaris/yaris-2020/ebrochure> (accessed on 10.08.2021).
- [5] Nowa Toyota Yaris. https://pdf.sites.toyota.pl/spec_yaris_MY21.pdf (accessed on 13.07.2021).
- [6] HU, X., JIANG, J., EGARDT, B. et al. Advanced power-source integration in hybrid electric vehicles: multicriteria optimization approach. *IEEE Transactions on Industrial Electronics*. 2015, **62**(12), 7847–7858. <https://doi.org/10.1109/TIE.2015.2463770>
- [7] HU, X., MOURA, S.J., MURGOVSKI, N. et al. Integrated optimization of battery sizing, charging, and power management in plugin hybrid electric vehicles. *IEEE Transactions on Control Systems Technology*. 2016, **24**(3), 1036–1043. <https://doi.org/10.1109/TCST.2015.2476799>
- [8] WEI, Z., XU, J., HALIM, D. HEV power management control strategy for urban driving. *Applied Energy*. 2017, **194**, 705–714. <https://doi.org/10.1016/j.apenergy.2016.10.023>
- [9] ZHU, L., YU, F.R., NING, B. et al. Optimal charging control for plug-in electric vehicles in smart microgrids fueled by renewable energy sources. *International Journal of Green Energy*. 2013, **10**(9), 924–943. <https://doi.org/10.1080/15435075.2012.727364>
- [10] SZALEK, A., PIELECHA, I. The influence of engine downsizing in hybrid powertrains on the energy flow indicators under actual traffic conditions. *Energies*. 2021, **14**, 2872. <https://doi.org/10.3390/en14102872>
- [11] PIELECHA, I., CIEŚLIK, W., SZALEK, A. Energy recovery potential through regenerative braking for a hybrid electric vehicle in a urban conditions. *IOP Conference Series: Earth and Environmental Science*. 2019, **214**, 012013. <https://doi.org/10.1088/1755-1315/214/1/012013>

Mateusz Szramowiat, MEng. – Faculty of Mechanical Engineering, Cracow University of Technology.
e-mail: mateusz.szramowiat@pk.edu.pl



Andrzej Szalek, DEng. – Advisor of the Board, Toyota Motor Poland Company Limited, Warsaw.
e-mail: andrzej.szalek@toyota.pl



SI engine fuel mixture type indicator and an assessment of its suitability of an economic driving style

ARTICLE INFO

Received: 15 July 2021
Revised: 8 August 2021
Accepted: 16 August 2021
Available online: 8 September 2021

The article presents the structure and a principle of operation of a simple indicator of the type of a fuel-air mixture supplying a spark-ignition engine with a direct fuel injection. The designed indicator was tested, as a result of which its correct operation was verified. By using information from the indicator, it was possible to assess its usefulness for assisting the driver in an economical driving style. Preliminary studies show that thanks to the use of the developed indicator, it is possible to save about 10% of fuel as a result of the correction of the economic driving style on the route selected for the purpose of this research paper. The target of this study was to confirm a noticeable reduction in fuel consumption when supplying the engine with a stratified mixture. In order to obtain more accurate data, the research should be extended to include a greater number of routes and its division into urban and non-urban areas.

Key words: *SI engine with direct fuel injection, stratified and homogeneous mixture, mixture type indicator, economical driving style, fuel consumption*

This is an open access article under the CC BY license (<http://creativecommons.org/licenses/by/4.0/>)

1. Introduction

SI engines are still used to drive passenger cars. Most of them are powered by direct fuel injection into the combustion chamber. This type of fuel injection allows the combustion of very lean fuel-air mixtures by their stratification in the combustion chamber. Burning lean mixtures makes better use of the fuel and thus reduce its consumption. A spark ignition engine can operate on a stratified mixture only within a limited range of speeds and loads [1, 2]. It also requires a specific thermal state of the engine and the exhaust system, including the catalytic reactor. For these reasons, it is the engine control unit that decides which mixture is supplied to the engine: stratified (economical) or homogeneous.

There was a question posed: could the driver of the car, having information about the type of a fuel mixture at the given moment, change the driving style to a more economical one? In order to answer this question, the plan was to build a simple indicator of the type of a fuel mixture supplying the SI engine with a direct fuel injection and to conduct tests in road conditions. The indicator was built and tests were conducted on the Mitsubishi Carisma GDI car.

The presented research paper on the construction of a mixture type indicator is an engineering diploma thesis at studies in the automotive field, the author and promoter of which are the authors of this paper.

2. Knowledge analysis

Spark ignition engines are powered by fuel-air mixtures of various compositions. The amount of fuel contained in the air-fuel mixture is determined by the air-fuel equivalence ratio λ . The composition of the air-fuel mixture affects the main parameters of the engine performance such as: power output, fuel consumption and the content of toxic components in the exhaust gasses. Until recently, SI engines were supplied with almost homogeneous air-fuel mixtures. Combustion of such mixtures in the SI engine

does not allow to use up all the fuel they contain. It is known that the higher the value of the coefficient ratio λ , the more fuel contained in the mixture will be burnt. At the same time, it is known that mixtures with the coefficient $\lambda > 1.4$ do not ignite from the spark. The solution that allows for the combustion of very lean mixtures is layering of the mixture in the combustion chamber. It consists in the formation of a rich mixture around the electrodes of the spark plug and progressively poorer in the areas further away from the spark plug as far as the air itself at the walls of the combustion chamber. Such a load may have an average composition defined by the factor λ above the value considered to be a flammable mixture (ignitable by an ignition spark). Mitsubishi was the first make in the world to use GDI (Gasoline Direct Injection) engines in the mass produced Carisma model, which burn stratified mixtures. Their combustion allows to reduce fuel consumption in the range of lower engine speeds and engine power. This translates into a reduction in fuel consumption when driving the car, mainly at a constant speed, up to approx. 100 km/h.

A driver who wishes to use an economical driving style should try to drive primarily on stratified mixtures [5, 6]. Unfortunately, the manufacturer did not install any indicator informing the driver about the type of mixture the engine is supplied with. Three types of mixtures can be distinguished in the power supply of the Mitsubishi Carisma GDI engine:

- homogeneous air-fuel mixture (uneconomical),
- stratified air-fuel mixture (economical),
- air only (during the so-called engine braking).

In SI engines with direct gasoline injection, a homogeneous mixture is created by injecting fuel into the combustion chamber at the beginning of the fill stroke. As a result of the air turbulence, it evaporates and mixes with air during the filling and compression strokes. A stratified mixture occurs when fuel is injected into the combustion chamber at the end of the compression stroke, just before ignition. The

position of the injector in the cylinder head is such as to direct the jet of injected fuel towards the electrodes of the spark plug. Fuel injection just before ignition prevents it from evaporating and mixing with the entire volume of air in the combustion chamber. In this way, the charge in the combustion chamber is stratified, i.e. correspondingly rich in the vicinity of the spark plug electrodes and progressively poorer in the areas closer to the walls of the combustion chamber. The average value of the factor λ of a stratified charge in this way is outside the flammability range.

The formation of a stratified mixture and its combustion in the engine depends on many factors. Rotational speed, load, thermal condition and more have an influence on the type of the mixture that is generated and burned. This is determined by the engine control unit [3, 4].

It is known that many of the processes supervised by the ECU are optimized. The authors of this research paper did not find reliable information whether the method of selecting the type of mixture was optimized in terms of low fuel consumption. This issue became the reason for taking up the topic.

3. Construction of the air-fuel mixture type indicator

3.1. Design assumptions for the indicator of the type of a combustion mixture

By analyzing the method of creating fuel mixtures supplying the SI engine by direct fuel injection into the combustion chamber, it is possible to link the fuel injection phase with the type of a fuel-air mixture. Early (at the beginning of the filling stroke) fuel injection creates a homogeneous mixture (Fig. 1a). Late fuel injection (at the end of the compression stroke, just before ignition) creates a layered mixture (Fig. 1b).

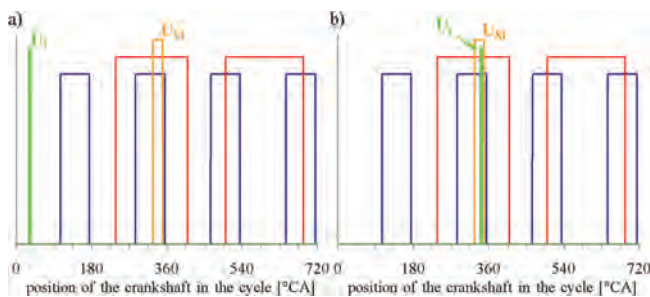


Fig. 1. Waveforms in the direct fuel injection system, when the mixture is formed: a) homogeneous, b) stratified

The navy blue waveforms show impulses from the crankshaft position sensor, while the red ones show the pulses from the camshaft position sensor. Based on these, it was possible to scale the first axis of the angular position of the crankshaft for the first cylinder. The duty cycle begins when the piston is at TDC before its fill stroke and the crankshaft is assigned an angle of 0°CA . Completion of the duty cycle occurs when the piston reaches TDC after the exhaust stroke and the crankshaft is assigned an angle of 720°CA .

In order to determine the fuel injection phase (i.e. early, late), it is necessary to check whether the injection pulse U_i occurs simultaneously with the ignition pulse U_{SI} . In Figure 1a, the pulses occur at different times, determining the

formation of a homogeneous mixture. In Figure 1b, the pulses occur at the same time, defining the formation of a stratified mixture. In this situation question should be posed whether at each point of the engine operation the mutual position of the injection pulse relative to the ignition pulse is as unambiguous as in Fig. 1. The following cases may raise doubts:

- high, close to maximum rotational speed and long injection time (Fig. 2a),
- low engine speed or idle running and short injection time (Fig. 2b).

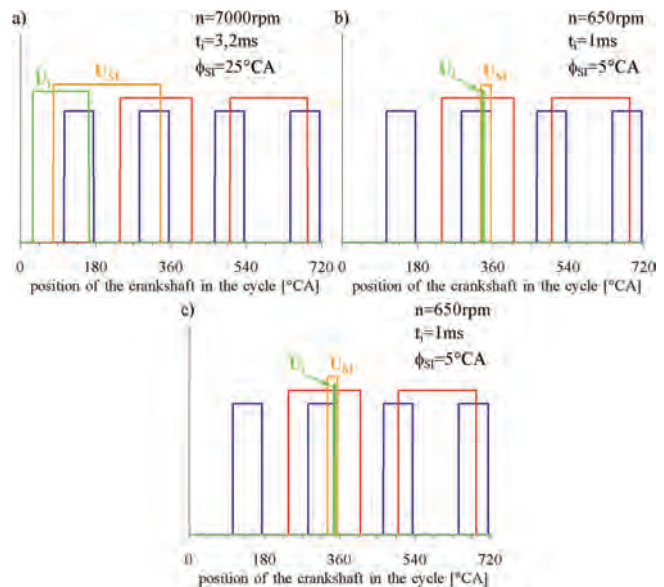


Fig. 2. Waveforms in situations giving rise to doubts as to the unambiguity of the assessment of the fuel-air mixture type

If the simultaneous occurrence of injection and ignition pulses is treated as a state indicating the formation of a stratified mixture, the waveforms in Fig. 2a misrepresent the formation of a stratified mixture. It is obvious that at high revs the engine is powered by a homogeneous mixture. Thus, the coexistence of signals is not always true information about the type of a mixture being created. A better method of determining the type of the mixture turned out to be checking the occurrence of the ignition pulse at the moment of the rising slope of the injection pulse. In this case, the signals shown in Fig. 2a correctly determine the formation of a homogeneous mixture. Figures 2b and 2c show two cases of the mutual position of the U_i and U_{SI} pulses, specific for the formation of a stratified mixture. Determining a type of a mixture by examining the ignition signal at the moment of the rising slope of the injection pulse will give an erroneous result for the signals shown in Fig. 2b. The question arises whether the engine controller, when supplying the engine with a stratified mixture, generates an injection impulse early enough for its rising slope to occur before the appearance of the ignition impulse. The literature [8] presents experimental studies of the Mitsubishi Carisma GDI engine control unit.

They show that the case of the mutual position of the ignition and injection pulses shown in Fig. 2b does not occur when the ECU controls the operation of the engine.

For low engine speeds and low engine loads, the injection start angle is approximately 320°CA . Ignition advance angle of approx. 25°CA , therefore an ignition pulse that is always 6.1 ms starts earlier than the injection pulse.

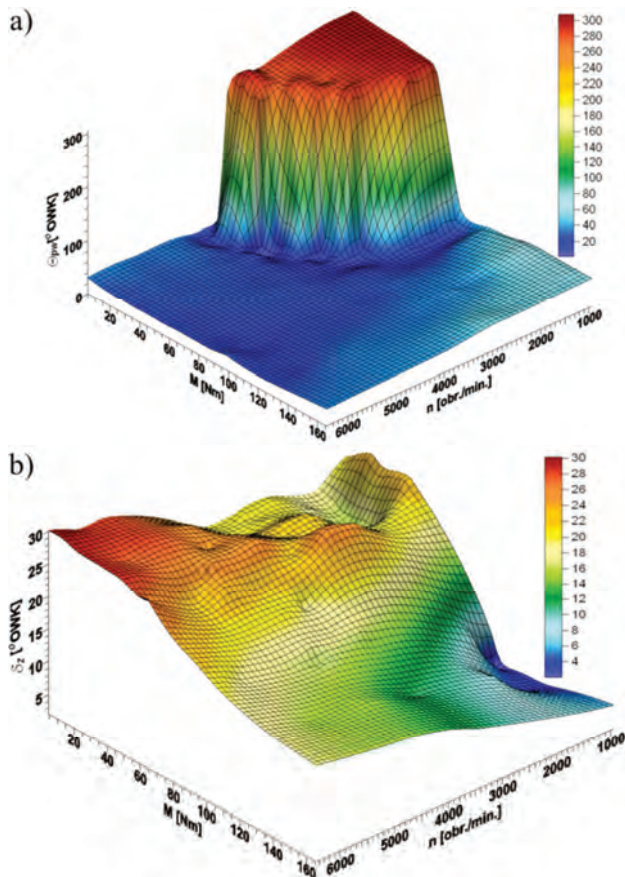


Fig. 3. Maps of: injection start angle (a) and ignition advance angle (b) for Mitsubishi Carisma GDI engine [8]

To sum up, on the basis of the mutual position of the injection and ignition pulses, it is possible to unequivocally determine the type of the formed fuel-air mixture. For this purpose, the occurrence of the ignition pulse during the rising slope of the injection pulse should be tested. The occurrence of the ignition pulse is confirmed by the formation of a stratified mixture, and its absence of a homogeneous mixture.

There is another condition in the SI engine management system in which the fuel is not injected. This is the case of engine braking. No injection pulse is generated. In subsequent cycles, the type of mixture will not be determined in the manner described above. In order to signal this state as well, it is necessary to test the occurrence of the injection pulse in each cycle in which the ignition pulse occurs. The ignition pulse is generated by the engine control unit in each cycle, regardless of the presence of an injection pulse. For both the homogeneous mixture and the stratified mixture, the fuel injection takes place before the ignition occurs (Fig. 1). Therefore, the falling slope of the ignition pulse is the moment when the occurrence of the injection pulse in the current work cycle should be checked. It is therefore necessary to remember the injection pulse at least until ignition. A way to do this is to generate an auxiliary signal

that remembers the injection I_{ip} at least for the remembering time t_{ipm} from the occurrence of U_i until the moment of ignition at the lowest rotational speed. (Fig. 4). Figures 4a and 4b show the injection signal that was remembered in the event of loss of the injection signal after the formation of a homogeneous mixture. Figures 4c and 4d show the injection signal that was remembered in the event of loss of the injection signal after the formation of a stratified mixture. The method described above will allow for a detection of the no injection after no more than t_{ipm} .

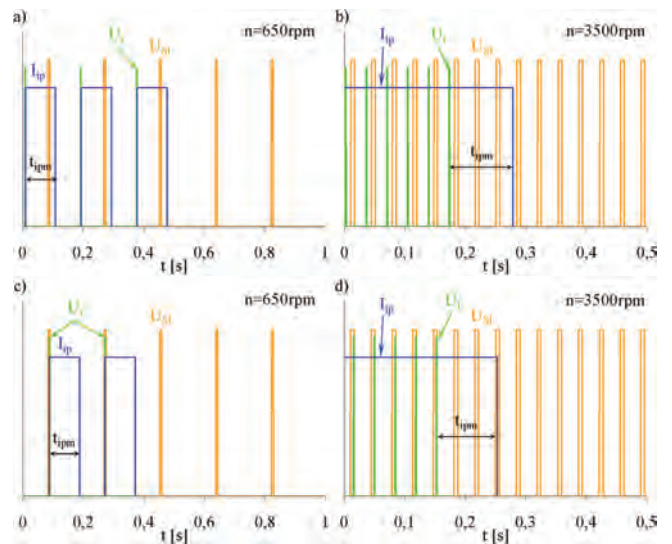


Fig. 4. Auxiliary injection signal at low (a) and high (b) engine rotational speed

The injection pulse elongation time should be equal to the time of two strokes at the minimum rotational speed $n = 600 \text{ rpm}$, i.e. $t_{ipm} = 0.1 \text{ s}$. At higher rotational speeds, the U_{ip} signals generated for individual injection pulses will overlap creating one pulse ending at t_p from the time of the last injection pulse [7].

3.2. Construction of the mixture type indicator

The device is to inform the driver about one of the three types of fuel-air mixtures with which the engine combustion chambers are filled. For this purpose a three-colour (RGB) LED was used. It was assumed that the colour:

- green will indicate a stratified mixture – as the most economical one,
- red will indicate a homogeneous mixture – as less economical,
- blue will indicate no fuel injection.

In the design assumptions, injection and ignition signals were selected to evaluate the type of a mixture supplying the SI engine with a direct gasoline injection. It was assumed that these are two-state signals in a simple form. The presented method of analyzing the type of mixture can be based on simple elements of digital electronics, e.g. flip-flops. Due to the place of use of the indicator, TTL technology was selected as more appropriate for use in automotive technology. Elements made in this technology are more resistant to interference and damage (mainly electrostatic).

In the next step, the diagram of the Mitsubishi Carisma GDI engine control system was analyzed in order to obtain

the required signals for the indicator being built. The injection signal for the first cylinder is available on pin no. 1 of the engine ECU, and the ignition signal on pin no. 3. These signals were assessed for compliance with the TTL technique. It turned out that they do not comply with the TTL standard (Fig 5).

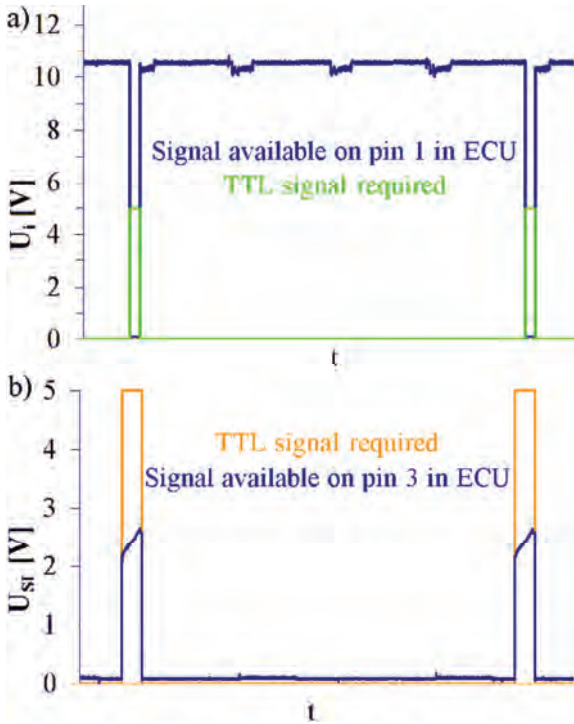


Fig. 5. Injection and ignition signals available in the GDI engine of a Mitsubishi Carisma

Thus, the constructed indicator requires a system that adjusts the signals available in the engine control system to the TTL standard.

The electronic system was designed and built, the block diagram of which can be seen in Fig. 6 [7].

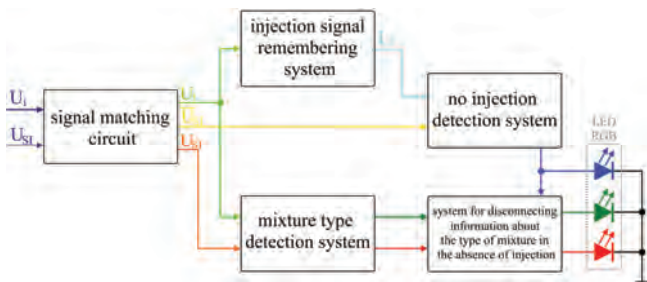


Fig. 6. Block diagram of the indicator of the type of a combustion mixture used to supply an SI engine with direct fuel injection

The electronic circuit has the form of a double-sided printed circuit board placed in the housing. It is connected to the car installation through an eight-pin connector (Fig. 7a). A three-colour LED diode informing the driver about the type of a mixture is mounted in the dashboard of the vehicle (Fig. 7b).



Fig. 7. Electronic circuit of the indicator and the location of its components

3.3. Verification of the mixture type indicator electronic systems

The developed and constructed mixture type indicator was tested to verify its operation. The research consisted in the analysis of simultaneously registered signals:

- fuel injection U_i and ignition U_{sr} for the first cylinder,
- injection memory I_{ip} ,
- controlling a three-colour LED.

The signal registration was made with a PC equipped with a GAGE A/C converter card. Due to the short injection times (< 1 ms), the sampling time was set to $20 \mu s$. The trial time was set to 10 s. During this time, the driver operated the accelerator pedal in such a way that the indicator changed the indication of the type of mixture several times (to change the colour of the LED diode). The results of one of the concluded tests are shown in Fig. 8.

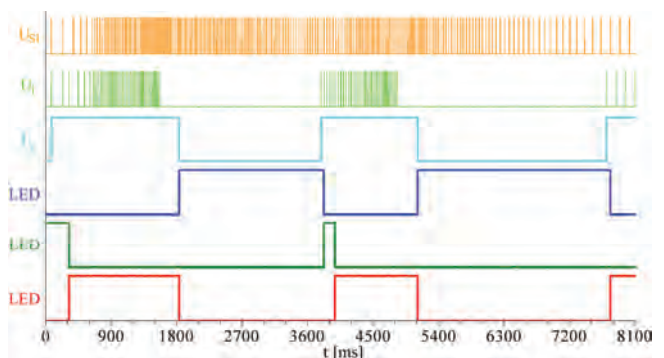


Fig. 8. Test results for the indicator of the type of a mixture

All signals in the figure above are two-state waveforms. Their colours are directly related to the signals in the block diagram (Fig. 6). Ignition signal U_{sr} shows the ignition pulses where high state means the current flow through the primary winding of the ignition coil. Injection signal U_i shows injection pulses, where the high state means the current flow through the injector winding. High state of the

injection memory signal I_{ip} shows information about the injection occurrence over the time t_{ipm} . Time t_{ipn} is selected in such a way that the information about the injection occurrence is remembered until the moment of ignition in the next cycle of work at the lowest possible rotational speed of the engine. If a blue LED signal is high, it is emitting blue light. If a green LED signal is high, it is emitting green light. If a red LED signal is high, it is emitting blue light.

The assessment of the correctness of the operation of the mixture type indicator was based on the analysis of the recorded waveforms of the above-mentioned signals. For this purpose, Fig. 9 shows the signals from Fig. 8 for the characteristic periods in which the indication changes appear.

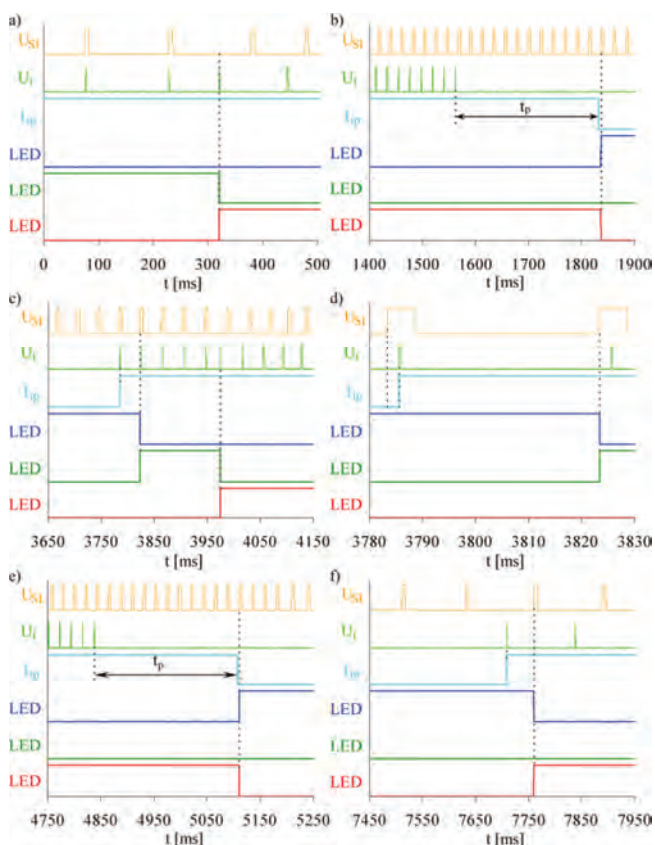


Fig. 9. The results of the test of the indicator of the type of mixture at the characteristic periods

Figure 9a presents the signals recorded within 500 ms from the start of the measurement. In the two first cycles, the fuel injection signal occurs simultaneously with the ignition signal, which indicates that the engine is supplied with a stratified mixture. During this time, the LED diode emits green light. In the third cycle, the fuel injection signal does not occur simultaneously with the ignition signal, which indicates that the engine is supplied with a homogeneous mixture. At the moment of the rising slope of the injection pulse, the colour of the light emitted by the LED diode changes to red. Figure 9b shows the disappearance of injection pulses. This state causes that after time t_{ipm} , signal I_{ip} changes to low. The closest rising slope of the ignition signal turns the LED diode to blue. Figure 9c shows the reappearance of injection pulses. The first one is remem-

bered by changing the I_{ip} signal into high. After this moment, the first ignition impulse will switch off the blue colour of the LED diode with the use of the rising slope. At the same time, the colour indicating the type of a mixture will be turned on. The mutual position of the ignition and injection pulses (the type of a mixture) is verified at every rising slope of the injection signal. Figure 9d explains why only during the second cycle after the injection there is a shut down of the blue colour of the indicator diode. Time on Figs 9b and 9e is equal to the duration of several cycles. This causes the indicator to show no delayed injection. It does not matter much for a driver, as it is about 1/4 second. On the other hand, it allows the indicator to work properly at a very low rotational speed, e.g. 500 rpm. The waveforms shown in Fig. 9, similarly to Fig. 9c, show the change of indication after the disappearance of injection pulses. Figure 9f shows the reappearance of injection pulses and the change of indication. This time, resuming a fuel injection creates a homogeneous mixture.

It can be concluded that the indicator correctly indicates the type of a fuel mixture that is being supplied to the engine of the car. The indication is carried out by the colour of the LED diode. The indicator reacts to a change in the type of a mixture created in less than one engine operation cycle, with the exception of no injection indication. The no fuel injection indication appears approximately 1/4 seconds after the last fuel injection. The time is short enough for the indicator to work correctly.

4. The assessment of the usefulness of the mixture type indicator for an economical driving style

4.1. Research methodology

The method of planned and conducted research results from the concept of using the fuel mixture indicator in maintaining an economic driving style. The indicator as a device is to help the driver to cover the longest possible section of the route while supplying the engine with a stratified mixture. The indicator diode seen by the driver is to help him to operate the accelerator pedal in such a way that he can cover the longest distance in an economical way. The indicator is not intended to put pressure on a driver, but to help him or her to learn the economical driving style that makes it possible to burn very poor mixtures.

The base of the test method for this research paper is the comparison of fuel consumption for the mapped route driven with and without the indicator. For the research to be reliable, the following criteria were adopted:

- the route should be as long as possible (e.g. several dozen kilometers),
- the route should be completed in similar road conditions (e.g. at the same time of day, at a similar average speed),
- the route should be completed in similar weather conditions (e.g. dry road surface, no strong wind, similar temperature),
- the car should be driven by the same driver,
- the driver should be able to use the indications of the indicator so as to complete the largest possible part of the route on the indication corresponding to the stratified mixture,
- the route should be completed several times.

4.2. Plan and the course of research

In order to meet the criteria resulting from the research methodology, a car was used for everyday commuting. This enabled the reduction of the costs and time for conducting research. A route with a length of approximately 84 km has been adopted, consisting of two parts: commuting to work for approx. 48 kilometers and returning approx. 37 km. The map of the route is shown in Fig. 10.

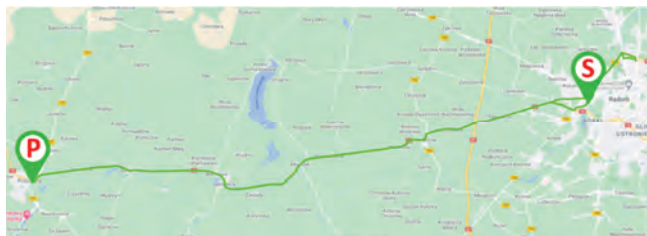


Fig. 10. The map with a marked daily route

The route passes through the urban and non-urban areas. A speed limit of 70 km/h applies over a long distance. The first 10 km of the first route is located within the city limits of Radom. The remaining 37 km are the route to Przysucha on the national road No. 12. The second part of the route is the return to Radom by the national road No. 12, which is the same one. The first part of the route was driven in the morning between 7¹⁵ and 8³⁰ (Fig. 11). The second part of the route was driven in the afternoon between 16⁰⁵ and 17¹⁵ (Fig. 12).

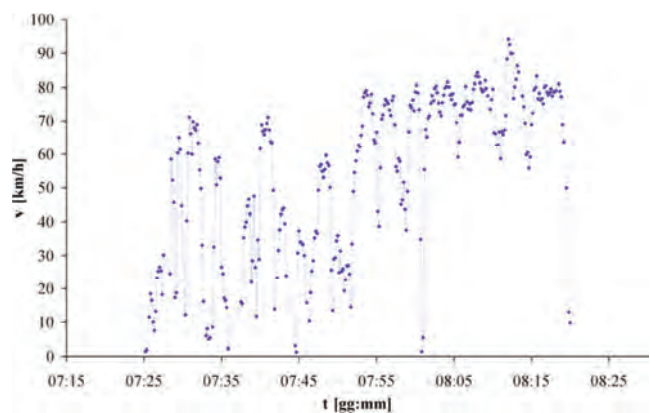


Fig. 11. Speed and time of day during the exemplary run of the first part of the route

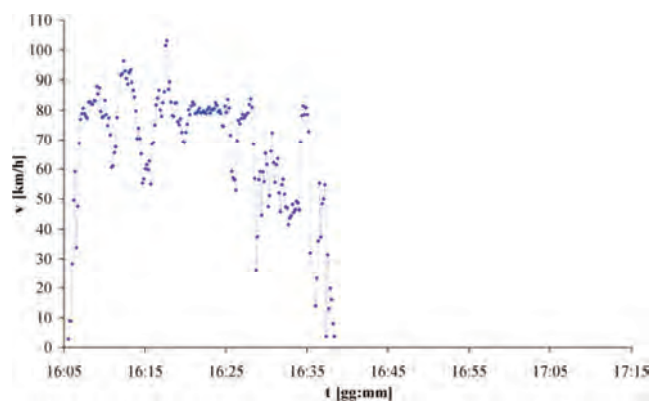


Fig. 12. Speed and time of day during the exemplary run of the second part of the route

The research was conducted in March and April 2021. Ten runs of the route were analyzed with the use of the indicator and five without the use of the indicator (the driver did not see the indication). Only those runs, which took place in similar weather conditions, were selected. Dry road surface, similar temperature (approx. 10 degrees Celsius) and no strong wind qualified the run for the analysis. In order to assess the repeatability of the driving cycles, vehicle speeds were presented and compared as a function of the road (Fig. 13). Fuel consumption was measured during each trip of the route (Table 2).

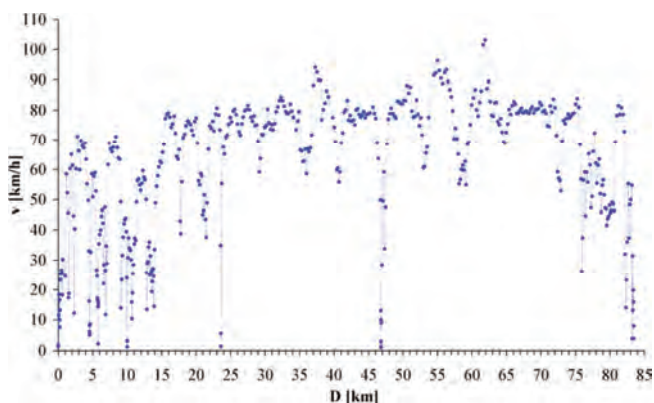


Fig. 13. Speed of travel at individual stages of the route during the exemplary run

During all the runs, the indications of the indicator were recorded every half a second. Examples of indications during the run in which the driver did not use the indicator (the indicator was covered) are shown in Fig. 14a. Figure 14b shows an example of an indication during which the driver uses the indicator.

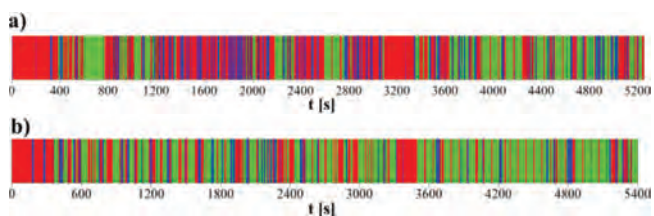


Fig. 14. Registration of the indicator operating during the run: a) in which the driver does not use the indications, b) in which the driver uses the indications

4.3. Analysis of research results

Figure 14a shows the recording of an indicator that is invisible to the driver during the work. The run lasted 5250 seconds. Figure 14b shows the recording of an indicator that is visible to the driver during the work. The run lasted 5400 seconds. Visually, it can be assessed that the use of the indicator significantly increased the driving time on a stratified mixture, i.e. economical one (green colour). Table 1 presents numerically the times for the runs shown in Fig. 14 with the division into the first and second part of the route.

Table 1. Route times for the cases shown in Fig. 14, divided into the first and the second part of the route and with the percentage share of each indication

	Travel time for the first part of the route			Travel time for the second part of the route			Time of travel of the entire route		
	Total	With an indication		Total	With an indication		Total	With an indication	
	[s]	[s]	[%]	[s]	[s]	[%]	[s]	[s]	[%]
Without the help of the indicator	3100	907.5	29.3	2150	1069	49.7	5250	1976.5	37.6
		1725.5	55.7		824	38.3		2549.5	48.6
		467	15.1		257	12		724	13.8
With the help of an indicator	3300	1753.5	53.1	2100	1441	68.6	5400	3194.5	59.2
		1234	37.4		500.5	23.8		1734.5	32.1
		312.5	9.5		158.5	7.5		471	8.7

The numerical and percentage values presented in the table clearly confirm that the driver using the fuel-air mixture type indicator was able to drive a much larger part of the route on the stratified mixture. Measurements of fuel consumption (Table 2) confirm that the operation of the engine in a stratified mixture is more economical.

Table 2. Fuel consumption for individual trips of the route

Trip number	Use of the indicator	Fuel consumption	
	[yes/no]	[dm ³]	[dm ³ /100 km]
1.	yes	5.27	6.27
2.	no	5.8	6.90
3.	yes	5.26	6.26
4.	no	5.9	7.02
5.	yes	5.33	6.35
6.	no	5.87	6.99
7.	yes	5.24	6.24
8.	no	5.85	6.96
9.	yes	5.25	6.25
10.	no	5.88	7.00

Nomenclature

A/C	analog to digital converter
D	distance
ECU	electronic control unit
GDI	gasoline direct injection
I _{ip}	injection pulse indicator
n	engine speed
RGB	red green blue
SI	spark ignition
U _i	injection control signal

The average value of fuel consumption for trips using the indicator was 6.27 dm³/100 km, while for trips without using the indicator 6.98 dm³/100 km. Thus, the fuel economy resulting from the economical driving style allowed by the use of the fuel mixture indicator is 10.07%.

5. Summary

The article presents a simple electronic mixture type indicator. It detects what mixture the engine with direct fuel injection is supplied with. For operation, it uses signals generated by the engine control unit. As a result of the research, it was confirmed that the information generated by the indicator helps the driver to drive more economically. The savings in fuel consumption in relation to driving without the indicator are approx. 10%. They result from deliberate and confirmed by indication driving on a stratified mixture. Driving a longer distance with the engine supplied with a stratified mixture (more economical) requires the driver to drive in a proper style. The indicator's usefulness is evidenced by the driving recording shown in Fig. 14a in the range from 1200 to 2000 seconds, where the driver, trying to maintain a constant speed, was driving on a homogeneous mixture with short-term fuel cut-offs. Slow acceleration to the target speed is also inappropriate from the point of view of driving economy. It takes place while supplying with a homogeneous (uneconomical) mixture for a long time. From time to time (about 1 minute), the ECU changes the type of mixture from stratified to homogeneous. This change takes approximately 10 seconds. During this time, the driver should not change the position of the accelerator pedal or increase the speed and then restore the position of the accelerator pedal until the indicator shows a stratified mixture.

The developed electronic indicator and the conducted research allowed to clearly and positively verify its usefulness in an economical driving style.

U _{SI}	ignition control signal
TDC	top dead centre
TTL	transistor-transistor logic
t _i	injection time
t _{ipm}	injection pulse memorization time
v	car speed
λ	air-fuel equivalence ratio

Bibliography

- [1] LAKE, T., SAPSFORD, S., STOKES, J. et al. Simulation and development experience of a stratified charge gasoline direct injection engine. *SAE Technical Paper* 962014. 1996. <https://doi.org/10.4271/962014>
- [2] PIELECHA, I. Diagnostics of stratified charge combustion under the conditions of multiple gasoline direct injection. *Journal of Thermal Analysis and Calorimetry*. 2014, **118**, 217-225. <https://doi.org/10.1007/s10973-014-3956-3>
- [3] TSAI, W.-C., ZHAN, T.-S. An experimental characterization for injection quantity of a high-pressure injector in GDI engines. *Journal of Low Power Electronics and Applications*. 2018, **8**(36). <https://doi.org/10.3390/jlpea8040036>
- [4] DURONIO, F., DE VITA, A., ALLOCCA, L. et al. Gasoline direct injection engines – a review of latest technologies and trends. Part 1: Spray breakup process. *Fuel*. 2020, **265**, 116948. <https://doi.org/10.1016/j.fuel.2019.116948>

- [5] DURONIO, F., DE VITA, A., MONTANARO, A. et al. Gasoline direct injection engines – a review of latest technologies and trends. Part 2. *Fuel*. 2020, **265**, 116947, <https://doi.org/10.1016/j.fuel.2019.116947>
- [6] LOIS, D., WANG, Y., BOGGIO-MARZET, A. et al. Multivariate analysis of fuel consumption related to eco-driving: Interaction of driving patterns and external factors. *Transportation Research Part D: Transport and Environment*. 2019, **72**, 232-242. <https://doi.org/10.1016/j.trd.2019.05.001>
- [7] ŻAK, M. Development of the fuel mixture indicator for the GDI engine of the Mitsubishi Carisma. *Doctoral thesis*. Kazimierz Pulaski University of Technology and Humanities in Radom, Faculty of Mechanical Engineering. Radom 2021.
- [8] WOŁCZYŃSKI, Z. Identification of properties of GDI engine and its control system. *Combustion Engines*. 2011, **146**(3), PTNSS-2011-SC-116.

Zbigniew Wołczyński, DEng. – Faculty of Mechanical Engineering, Kazimierz Pulaski University of Technology and Humanities in Radom.
e-mail: z.wolczynski@uthrad.pl



Mikołaj Żak, Eng. – Faculty of Mechanical Engineering, Kazimierz Pulaski University of Technology and Humanities in Radom.
e-mail: mikunio107@gmail.com



Team durability test of a 1.3 MW locomotive diesel engine with prototype piston rings

ARTICLE INFO

Objective of this work was to realize a test of durability of railway engine EMD645 with power about 1300 kW. Within the framework of this test were investigated a prototyped piston's rings with diamond embankment. Piston rings are made of chromium layer with including of diamond powders technology with a porous chromium coating, where in pores is deposited on said diamond powder with a grain size about 1 micron. The work will be carried out of an analysis of collaboration piston-piston rings-cylinder unit in internal combustion engine and an analysis of the use of hard materials (diamond powder) in friction pairs. During work of this unit we can observe wear of piston rings, precisely – of coating which is deposited on ring to prolong service life. After testing of the locomotive engine EMD645 on the basis of the collected results are developed conclusions of the wearing intensity on piston ring and relating them to the requirements for coatings. The work aims to show the possibilities and benefits of the application of new protective coatings on structural elements of the internal combustion engine in order to reduce their wearing, which is consistent with the observed trend of technology development.

Received: 15 July 2021

Revised: 5 August 2021

Accepted: 10 August 2021

Available online: 12 September 2021

Key words: *combustion engine, durability test, piston ring, diamond powder, multilayer*

This is an open access article under the CC BY license (<http://creativecommons.org/licenses/by/4.0/>)

1. Introduction

This paper describes part of a larger program to reduce wear the set working parts (piston, piston ring and bearing surface). The project is implemented through the development of new designs of piston rings with anti-wear coating that contains synthetic diamond in the form of loose embedded in a coating of chromium (PRS). The main purpose of coating is to reduce ring wear while maintaining or reducing wear cylinder sleeve. Application for said part of the research is EMD 645 engine. The engine used in this study was manufactured by the Electro-Motive Division of General Motors Corporation (EMD). This engine is available in both naturally aspirated and turbocharged configurations, and in V-8, V-12, V-16, and V-20 configurations [1]. It is popular for locomotive applications in North America, as well as in marine, industrial and power generation applications. For this program, the EMD 12-645-E engine was chosen because it is commonly found in switcher and road-switcher locomotive applications in North America, in power ranges from 750 kW to 1,500 kW. Roughly 3,000 of these switcher locomotives are in operation in North America. Figure 1 shows an EMD GP38-2 road-switcher locomotive, which is equipped with an engine like the one tested in this program. Specifications for the EMD 12-645-E engine are given in Table 1. The EMD 645-E engine is a uniflow-scavenged, two-stroke, direct-injected diesel. Figure 2 shows a power assembly from the EMD 645-E engine. Figure 2 shows that the power assembly has four compression rings on the piston crown and two oil control rings at the piston skirt. Prior to testing, the model engine was rebuilt, and equipped with a set of commercially available power assemblies, and broken in for 85 hours of operation.



Fig. 1. EMD GP38-2 road-switcher locomotive



Fig. 2. EMD 645-E power assembly [2]

Table 1. EMD 12-645-E engine specifications [2]

Cylinders	V-12
Bore	230 mm
Stroke	254 mm
Displacement/cylinder	10.6 dm ³
Compression ratio	16:1
Power	1,100 kW
BMEP	5.9 bar @ 900 rpm
BSFC@ rated power	254 g/kWh
Air charging	Gear driven roots – blower
Fuel injection	Cam driven unit – injectors
Crankcase ventilation	Crankcase fumes are returned into the blower
Engine condition	About 100 hours break-in upon complete engine overhaul
Emission certification	EPA Tier 0 – switcher Cycle 2

2. Finite-element simulation

Finite element as such is a simple geometric shape – flat or spatial, for which are set out special points called nodes, and certain functions of interpolation, called functions shape. The nodes are located at the vertices of the finite element may also be placed against its sides, this is called the higher order components [4, 5]. If the nodes are only the vertices of the finite element is called a linear component or element of the first row. The Government of the element is always equal to the rank shape function, while the number of functions in a single component shape corresponds to the number of its nodes [3, 8]. All finite elements and nodes must be numbered, usually seeks to ensure that the numbering will guarantee a minimum bandwidth of non-zero coefficients matrix of equations [4, 8]. FEM concept assumes that any quantity, for example, stress or strain described by a continuous function, approximated discrete model. Discrete model is composed of a set of continuous functions defined in a finite number of subdivisions called elements, to which divided the region [4, 8].

Individual continuous functions of the subdivisions is determined by the value of the primary functions of a finite number of points called nodes. To obtain a discrete model should therefore:

- distinguish a finite number of nodes,
- nodes to determine physical quantities, subject to approximation – such as stress or displacement,
- divide the area in question on a finite number of elements,
- approximate size of the physical elements using polynomial approximation, for example, ranks, or strings [4].

Now that the finite element method is used widely, there are many types and kinds of finite elements. In order to determine the type of finite element makes the following basic criteria characterizing featured item [6]:

- dimension of the element: one-dimensional – 1D, two-dimensional – 2D, three-dimensional – 3D,
- geometric shape,
- the degree and type of shape function adopted,
- number of nodes in the element,
- constraints imposed on the item [5].

Due to the size of finite elements can be divided into one-dimensional, two-dimensional and three-dimensional, exemplary diagrams of data elements are presented below [8]. Of the three-dimensional elements, which describe the three-dimensional space, we can distinguish volume elements such as TETRA, PENTA, HEXA, and elements axially – symmetrical. Due to the geometrical shape can distinguish the following finite elements [2, 8].

In some cases, the mapping area of the curved lines use elements with curved contours – isoparametric elements. For ease of description of the geometry of the curved elements is transformed to the geometry of the core. We can distinguish 3 classes of curved elements:

- isoparametric,
- superparametric,
- subparametric [8].

By constraints imposed on the finite element meant to receive the possibility of movements in different directions points that belong to this element. The element arises field strains and stresses. In the space generally occurs 6 degrees of freedom, while the number of degrees of freedom of the finite element is presented below [4, 5, 8]:

- rod elements 2D and 3D {ux, uy, uz},
- Beam Elements 2D and 3D {ux, uy, uz, ax, ay, az},
- membrane elements {ux, uy},
- disc elements {ux, uy, az},
- plate elements {u, ax, ay} or {u, ax, ay, axy},
- coating elements {ux, uy, uz, ax, ay, az},
- volume elements {ux, uy, uz}.

During the execution of the strength calculations band of piston rings were carried out in order to calculate the state of stress in the piston rings whose method of implementation and the scope can be reduced to:

1. Develop calculation module piston rings (Fig. 3).
2. Carry out calculations for the three engines of the Rings: EMD 645, I0470, according S359 of Computing Module Piston Rings.

Developed and implemented Piston Rings Calculation Module is compatible with the idea of numerical computational methods is to say: functionally consists in carrying out a calculation of the desire to achieve the exact solution (the nearest is real) by conducting and receiving intermediate solutions (the next). Shown in Fig. 3, a block diagram of a computing unit piston ring contains the names of the functionality of each of the stages in the quest to achieve the final effect, which is to define the geometry and material of piston rings. Presented a block diagram of a computing unit piston rings (Fig. 4) has a sub-module implemented in the rump.

„Load calculation in the model assembly TPC combustion engines using the MES”. Said sub-module is marked in red and will be described in the task of work.

Spreadsheet – Data input at this stage, collected all available data measurement in the piston ring grooves and measurements of the diameters of cylinders, as well as data on the materials from which the consortium member FPT "Prima" SA can make piston rings. Then made estimates based on empirical formulas and pre-defined geometry and material of piston rings. The preprocessor – construction geometry at this stage been set in the previous step geome-

try of the rings. The construction geometry was carried out in the preprocessor to the program Ansys CFD, construction geometry was based on coordinates of points then combined their curves, which were spread on surfaces which were then sealed in volume and given boundary condition "solid".

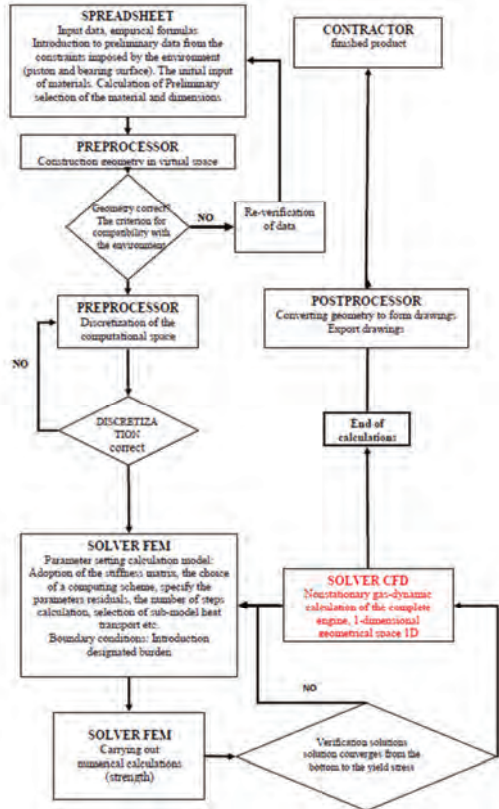


Fig. 3. A block diagram of the computing unit of piston rings

Geometric correct – at this stage was inspected by checking whether the geometry of the virtual rings are located in annular grooves of the pistons. Preprocessor – Discretization computing space, at this stage in the software Ansys CFD made discretization or the distribution of geometry into a finite number of elements, choosing cubic higher-order elements (Fig. 4).



Fig. 4. The discreet form a ring geometry of an exemplary EMD 645E - mesh FEM

Discretization correct – at this stage was made to verify the quality of discrete area of scanning all the elements of the criterion: volume differences, differences in diagonals, differences in lengths of the sides. SOLVER FEM – Abaqus, at this stage, carried out all the necessary steps to

build a numerical model of the above/in the system; adoption of stiffness matrix, the choice of a computing scheme, specify the parameters of convergence, the number of steps calculation, selection of sub-model heat transport etc. One of the most important things was the introduction of boundary conditions through proper task force vector. Verification solution – at this stage completed the task of receiving the first targets as a result of stress in the rings under two conditions of load: compression (Fig. 5) and stretching (Fig. 6) for each of the rings. After the analysis for each of the rings to give the results. In Fig. 5 and Fig. 6 have been included distribution of stresses and displacements for the individual rings.

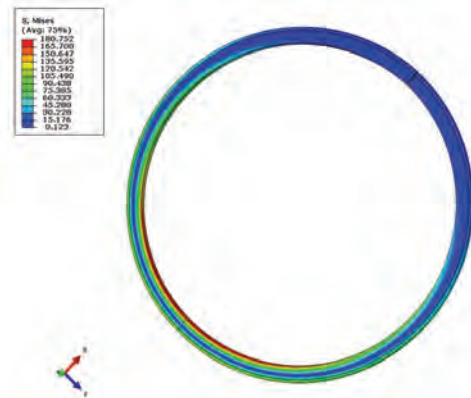


Fig. 5. View of the state of stress in the compression ring engine EMD645

The state in which the rings are shown in the figures $k = 1.2$ for the material. Noticeable is the accuracy of the highest stresses experienced during assembly ("expansion" of the ring) are found in the most remote from the slot assembly, a similar tendency appears in the case of compression to close the lock.

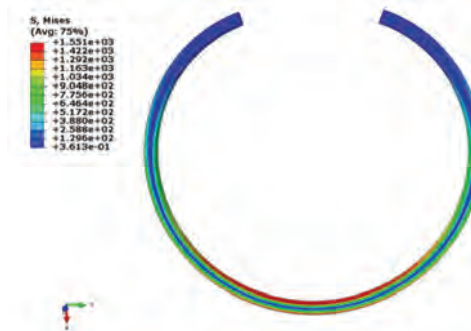


Fig. 6. View of the state of stress in the tension ring exemplary engine EMD 645E

3. Team durability test

The next subject of the research work was to test the durability of internal combustion engine with self-ignition, also equipped with steel piston rings made in the technology of diamond coating of the first groove. The purpose was to check the quantity of piston rings wearing with the diamond-derivative coating on the external surface [7, 9–12]. The scope of work included the geometric measurements and a description of the cylinders surfaces with whom they cooperated.

After the geometric measurements was made an installation of engine components in the engine EMD 645-E, which was mounted on a test bench in the engine laboratory in the Southwest Research Institute in San Antonio, USA. The next step was the operation of the locomotive engine Pacific 3450 Union in the ongoing 85 hours endurance test at maximum, the value of 550 rev/min and a rated power of 650 kW. After completion of the test the rings were measured geometrically again to determine the value of the wear.

The guiding idea of this endurance test unit is intensifying extremely variable loads. The transition from the traffic with a maximum torque of traffic without load at maximum speed has intensified engine load, contributing to a measurable value of wearing, despite the relatively short duration of the test.

This coating is a multilayer porous chromium coating applied galvanically where in the pores after the reversed polarity of the process is deposited synthetic diamond dust. Coating constituted in that process is characterized by good tribological properties, while ensuring a high hardness. In the case of boundary friction and contact with surface asperities, in the similar technology hard alumina particle was deposited and getting to the top of cylinder imbalances caused the intensive use, of a considerable abrasive wear in high temperature conditions. Elaborated coating is devoid of this defect. Diamond as the hardest known mineral ensures a significant increase hardness of the coating in total. At the same time in the case of boundary friction caused by the contact of surface roughness's between the ring and the cylinder is accompanying increase in temperature causes the transition of diamond into graphite. This occurs even at 973 K and higher. Thanks to this phenomenon this hardest known mineral becomes a kind of grease. The coating consists of twenty-two layers.

4. Measurement of the rings before and after the test

The tests were designed for two-stroke diesel locomotive diesel engine type EMD 645 with a cylinder diameter of 9.065 inch (230.2 mm). Each of the cylinders of the engine is equal to the stroke volume of 10.35 liters. The power of the engine varies between 0.6 MW for the six-cylinder unit (10 engine weight 10,000 kg) supplied by the Roots compressor, to 3.1 MW unit twenty-cylinder (19 engine weight 500 kg) powered by turbocharger. The tests were powered by turbocharged engine EMD 645E3 (V12) with a capacity of 1200 kW and a torque of 12,000 Nm. Displacement volume is 124.2 liters. We found a place where the motor was installed on the chassis dynamometer. It is a Southwest Research Institute in San Antonio, USA. The tested engine EMD 645 is a typical power unit used in the US market to drive diesel locomotive. The result of the implementation of the sample was measurable wear on the radial thickness and axial height of rings and cylinders and pistons wear (Table 3, 4). The measurements were made in accordance with the diagram in Fig. 7.

The average wearing value of the radial thickness, and therefore the wearing of the chrome coating ring with PCD is equal to: 13 μm. The average wearing value of the radial thickness of the rings is equal to a standard: 19 μm. With a measurement accuracy equal to 1 μm differences between

the wearing of new rings and standard rings are very important.

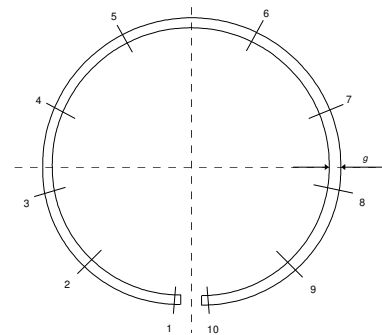


Fig. 7. Measurement diagram of the piston ring

Table 3. Value of the axial height wearing of the rings after the test

Ring	Value of the axial height wearing of the rings after the test [μm]									
	1	2	3	4	5	6	7	8	9	10
1b	-5	9	4	5	4	7	7	4	7	9
2	14	3	10	0	9	11	13	17	9	10
3b	12	1	1	4	1	8	8	6	1	8
4	0	0	-5	1	2	7	2	4	3	8
5b	3	3	0	4	6	2	7	0	3	0
6	0	4	7	1	-2	14	4	2	3	5
7	-2	-3	-1	1	11	17	10	-7	-5	-3
8b	-2	2	3	4	6	3	15	20	11	7
9	1	1	0	-6	-6	-1	5	0	-1	-5
10b	2	16	-2	8	9	-3	18	0	0	3
11	-7	3	-2	-8	1	1	-1	5	5	8
12b	0	4	0	0	6	4	2	-1	5	5

Table 4. Value of the radial thickness wearing of the rings after the test

Ring	Value of the radial thickness wearing of the rings after the test [μm]									
	1	2	3	4	5	6	7	8	9	10
1b	13	11	14	13	8	8	10	12	17	4
2	18	9	73	10	13	8	11	13	12	20
3b	13	11	10	10	11	12	9	7	6	12
4	24	18	24	26	27	23	22	28	18	21
5b	33	13	14	17	15	12	9	12	11	11
6	11	12	11	25	27	10	8	13	23	24
7	27	27	26	30	19	19	18	24	17	22
8b	19	16	15	13	15	14	17	15	14	14
9	8	9	14	18	22	12	13	19	15	10
10b	15	15	16	18	14	11	11	13	14	12
11	13	10	20	24	14	12	14	18	16	19
12b	15	13	13	18	14	12	14	17	12	10

Diamond – derivative coatings are mainly characterized by a lower friction coefficient and a much greater resistance to wear in comparison to rings that are covered by the common superhard coatings. Without a doubt, the application of such coatings will have an impact not only to extend the life of system piston-ring-cylinder, but also will reduce fuel consumption even under the most strenuous conditions of work of the unit.

5. Measurements of emissions of exhaust components

During the tests, the emissions of exhaust components were also measured. Measurements were made before the start of the test in the zero state and after its completion. The values of sulfur dioxide (SO₂) emissions, particulate

matter emissions, carbon monoxide (CO), hydrocarbons (HC) and nitrogen oxides (NO_x) were measured. These values are summarized in Table 5 as emissions per 1 liter of consumed fuel. As the load during the group durability test was constant, the values of the content of the said toxic components in the exhaust gases were measured many times and converted in relation to the amount of fuel consumed in the test, creating the emission values. An exception is the value of sulfur dioxide emissions, which is the result of the consumption of lubricating oil when using sulfur-free fuel. In this case, the results are given in ppm.

Table 5. Emission value of the toxic exhaust components of an EMD 645 engine before and after the team endurance test

Chemical compound measured	Emission before test	Emission after test
Sulfur dioxide, SO ₂ , ppm	0.15	0.18
Particulate matter, g/dm ³	2.16	2.15
Carbon monoxide, CO, g/dm ³	9.46	9.85
Hydrocarbons, HC, g/dm ³	4.32	4.55
Nitrogen oxide, NO _x , g/dm ³	81.02	90.5

The emission values were referenced to the amount of fuel consumed in order to be a benchmark for the emission limit of individual compounds, which in the US (target market of the FPT Prima S.A. project consortium) is usually given in grams per gallon of fuel consumed. In summary, it can be stated that the tested emissions are within the standards applicable to the EMD645 engine in the USA.

Throughout the test, many engine performance indicators were discreetly measured. The measurement was performed every 3 seconds of the subject operation during the 85 hours of the team endurance test. As a result, a very rich research material was obtained. The engine is running around its maximum torque value. Due to the fact that the measurement of engine performance indicators was performed, every 3 seconds, it is a large database consisting of 102,000 records collected in the so-called running; here is an example screen with Run055. The analysis of all the collected material allowed for the drawing of a number of utilitarian conclusions.

6. Summary and conclusion

In conclusion obtained maxima strain ring, which comes to maximum stress. On this basis it was concluded that the rings meet designed in terms of strength required Formed during both compression and installation pistons [8].

Studies show that with % increasing of the carbon in the coating composition and decreasing of the hydrogen

amount is related to improved strength and wear resistance at the time of no lubricating function of the lubricant. The use of diamond – derivative coatings is a new direction in the development of technology for internal combustion engines.

Replacement of worn parts of the piston-ring-cylinder set would decrease considerably their properties and their improvement has a definite dimension, so the use of such modern shells prolonging the life could change a lot on what evidence may be carried out research and very promising results. These the hardest coatings available on the market today are increasingly used, mainly in the automotive and electronic equipment. The properties of these coatings and getting their increased popularity also contribute to the decrease in costs associated with their production, and the problem of their insufficient thickness will likely be solved with the most modern methods of hardfacing on components.

Solution to the given research problem is based on the results of these studies of 85-hour endurance test. They allow you to acquire new knowledge and skills in the manufacture of coatings PCD, in particular the constitution layers of diamond coating with a specific weight percentage composition. Positive test results realized in Southwest Research Institute in San Antonio in the US pose a real chance to increase the quantities of produced rings with diamond coating for large combustion engines powering locomotives and small inland waterway vessels in the US and in the future perhaps for small internal combustion engines for use in vehicles like a cars, thus extending their life.

Diamond – derivative coatings can be applied to elements working in high-speed diesel engines and because of the opportunity to work at very high temperatures [14]. They also exhibit good adhesion to the substrate steel and cast iron, and less stress their own, so they seem to be a breakthrough in the use of materials with excellent tribological properties. A complete set of advantages of applying diamond – derivative coatings contains very high hardness (70 GPa), high value electrical resistance, relatively low weight, and most importantly, low coefficient of friction and excellent wear resistance.

Acknowledgements

This work was supported by the National Research Centre of Poland.

Bibliography

- [1] REIF, K., DIETSCHKE, K.H. *Automotive Handbook*. Robert Bosch GmbH. Karlsruhe 2014.
- [2] FROELUND, K., FRITZ, S., SMITH, B. Ranking lubricating oil consumption of different power assemblies on an EMD16-645-E locomotive diesel engine. *CIMAC Congress* 2004, Kyoto.
- [3] CORCIONE, F.E., VAGLIECO, B.M., CONSALES, S. et al. Temporal and spatial evolution of radical species in the experimental and numerical characterization of diesel auto-ignition. *Proceedings of the Fifth International Symposium on Diagnostics and Modeling of Combustion in Internal Combustion Engines* (COMODIA 2001), 2001, 355-363. <https://www.jsme.or.jp/esd/COMODIA-Pros/Html/005.html>
- [4] RUSIŃSKI, E., CZMOCHOWSKI, J., SMOLNICKI, T. Zaawansowana metoda elementów skończonych w konstrukcjach nośnych. *Wydawnictwo: Oficyna Wydawnicza Politechniki Wrocławskiej*. Wrocław 2000.
- [5] RUSIŃSKI, E. *Zasady projektowania konstrukcji nośnych pojazdów samochodowych*, *Oficyna Wydawnicza Politechniki Wrocławskiej*. Wrocław 2002.

- [6] <https://www.mimuw.edu.pl/~lmarcin/lab/nrrr/wyklad.pdf> (update 12.07.2021)
- [7] BESSLER, W.G., SCHULZ, C., LEE, T. et al. Laser-induced fluorescence detection of nitric oxide in high-pressure flames with A-X (0,1) excitation. *Proceedings of the Western States Section of the Combustion Institute*. Spring Meeting, 145-156, Oakland 2001.
- [8] BUCKMASTER, J., CLAVIN, P., LINAN, A. et al. Combustion theory and modelling. *Proceedings of the Combustion Institute*. 2005, **30**(1), 1-19. <https://doi.org/10.1016/j.proci.2004.08.280>
- [9] POULON-QUINTIN, A., FAURE, C., TEULE-GAY, L. et al. microstructure coating influence for optimized diamond deposition. *Material Science Forum*. 2012, **706-709**, 2898-2903. <https://doi.org/10.4028/www.scientific.net/MSF.706-709.2898>
- [10] ALDWELL, B., TRIMBLE, D., YIN, S. et al. Enabling diamond deposition with cold spray through the coated particle method. *Material Science Forum*. 2017, **879**, 1194-1199. <https://doi.org/10.4028/www.scientific.net/MSF.879.1194>
- [11] OZOMAKI, E.T., LAMBERT, C.S., BELANGERO, W.D. et al. Biocompatibility of titanium based implants with diamond-like carbon coatings produced by plasma immersion ion implantation and deposition. *Key Engineering Materials*. 2017, **361-363**, 677-680. <https://doi.org/10.4028/www.scientific.net/KEM.361-363.677>
- [12] MOULIN, D., RAYMOND, O., CHEVRIER, P. et al. CVD diamond coatings for machining. *Material Science Forum*. 2006, **526**, 55-60. <https://doi.org/10.4028/www.scientific.net/MSF.526.55>
- [13] MELLOR, B.D. Surface coatings for protection against wear. *Woodhead Publishing*. CRC Press 2006. <https://doi.org/10.1533/9781845691561.1>

Prof. Andrzej Kaźmierczak, DSc., DEng. – Faculty of Mechanical Engineering, Wrocław University of Science and Technology.
e-mail: andrzej.kazmierczak@pwr.edu.pl



Marcin Tkaczyk, DEng. – Faculty of Mechanical Engineering, Wrocław University of Science and Technology.
e-mail: marcin.tkaczyk@pwr.edu.pl



Analysis of operating parameters of the aircraft piston engine in real operating conditions

ARTICLE INFO

The article presents the results of analysis of operational parameters of piston engine CA 912 ULT which is a propulsion system of ultralight gyroplane Tercel produced by Aviation Artur Trendak. Research was conducted under normal operating conditions of the autogyro and data was collected from 20 independent tests including a total of 28 flight hours, divided into training flights and competition flights. Engine speed, manifold air pressure and temperature, fuel pressure, injection time, and head temperature were recorded at 9 Hz during each flight. Collective results were presented to show the statistical analyses of the individual parameters by determining the mean values, standard deviations and histograms of the distribution of these parameters. Histograms of operating points defined by both engine speed and manifold air pressure were also determined. Analyses of the engine dynamics as a distribution of the rate of change of the engine rotational speed were also carried out. It was shown that the engine operating points are concentrated mainly in the range of idle and power above 50% of nominal power. The most frequent range is 70-80% of nominal power. It was also shown that the dynamics of engine work in real operating conditions is small. It was also shown that the way of use significantly influences the distribution of operating points. During training flights, an increase in the number of take-offs and landings causes an increase in the amount of engine work at take-off and nominal power and at idle.

Received: 6 August 2021

Revised: 26 August 2021

Accepted: 1 September 2021

Available online: 13 September 2021

Key words: *piston engine, engine parameters, statistic, normal operating conditions*

This is an open access article under the CC BY license (<http://creativecommons.org/licenses/by/4.0/>)

1. Introduction

Aviation is a rapidly developing sector, where the latest solutions are being introduced and modern technologies used [13]. Modern materials make it possible to reduce the aircraft empty weight, electronic systems improve flight safety, and introduction of electric and hybrid drives reduces the negative environmental impact [3]. However, the development of electric propulsion systems is still in its early stages, and most aircraft use internal combustion engines for propulsion [6, 17].

In order to meet the increasingly demanding requirements of both minimising engine weight and efficiency, engine components are being modified and their overall design optimised. This includes the shape of components as well as materials and manufacturing technologies.

One of the fastest growing branches of aviation is ultralight aviation, i.e. small, maximum two-seat aircraft with take-off mass not exceeding 600 kg [8, 14]. They are characterized by a short take-off and landing runway, possibility of using grass airfields, simplicity of operation and maintenance as well as simplified procedure for approval for production and use. Piston engines are most often used as propulsion systems. They are characterized by simplicity of construction, low inertia, low failure rate and low weight [11].

The development of ultralight aircraft propulsion systems is mainly aimed at increasing the power-to-weight ratio. The aim is to minimize the size and reduce the weight of engine components, while maintaining adequate power. Another solution is to increase power while maintaining or slightly increasing the weight of the engine. A common solution is therefore the turbocharging systems [10]. It

allows to obtain higher power at similar weight. However it leads to increase of the mechanical and thermal load of the engine. This requires increased attention in operation and maintenance.

A fundamental aspect of aviation is safety. During operation, the pilot is obliged to constantly observe selected parameters of the propulsion unit and the whole aircraft. This allows early detection of damage or malfunction and appropriate action for safe further operation. For this purpose, on the aircraft are built appropriate sensors and instruments presenting the important parameters [12, 20].

The development of electronic systems has led to the replacement of analog instruments by electronic systems. This allows not only a better presentation of parameters but also their recording. This makes it possible to collect this information during normal operation and analyze it after the flight. These data can be used for example for optimization of propulsion units construction.

The availability of data allows to perform numerous studies on the distribution of engine performance under normal operating conditions. The authors of paper [1] show that the conditions of real operation significantly differ from the conditions of tests conducted as part of vehicle type approval. They showed that the differences between emissions in the test and in reality are significantly greater. It is also confirmed by the research conducted by [9, 21, 23]. With the authors of the paper [9, 23] focusing primarily on identifying differences in emissions between these conditions, the authors of the paper show as focusing on analyzing the causes of these differences [21]. They show that the difference lies primarily in dynamic conditions.

This is also demonstrated by the authors of the work [4, 22] highlighting the significant contribution of dynamic states under normal vehicle operating conditions. They show that dynamic conditions occupy from 20% to 50% [22] of engine operating conditions in motor vehicles.

As demonstrated by the authors of paper, dynamic conditions significantly affect the propagation of the flame front [18] and thus the results of the combustion process [5]. It is therefore important to test engines under these conditions [14].

For aircraft engines or engines operating in hybrid assemblies, the contribution of dynamic conditions is much smaller [24]. As it was shown by the authors, it ranges from 5 to 20% of the engine operating time [25]. The difference also includes the average conditions of steady state engine operation. In the case of motor vehicles, the average conditions correspond to about 20-30% of the nominal power [2], while in the case of engines, they are much higher [25]. However, detailed analyses of the distribution of aircraft engine operating points under real operating conditions are lacking.

This paper presents an analysis of performance of modified Rotax – CA 912 ULT engine, used to propel the Tercel autogyro in real operating conditions.

2. Methodology and research object

2.1. Research object

The research was carried out on a Tercel autogyro with registration number SP-XXLX, produced by Aviation Artur Trendak company. It is a two-seat ultralight aircraft, designed for recreational, training, sport and demonstration purposes in ground visibility conditions. The Tercel autogyro is shown in Fig. 1. Table 1 presents basic technical data of the tested autogyro.



Fig. 1. Tercel autogyro produced by Aviation Artur Trendak

The Tercel is powered by a CA 912 ULT engine, which is a modification of the Rotax 912 engine most commonly used in ultralight aviation. The power supply system was rebuilt: two constant vacuum carburetors were replaced by multi-point port injection system. In addition, the engine was equipped with a turbocharger with an exhaust gas pressure control valve, allowing the maximum charge pressure to be limited. The technical data of the CA 912 ULT engine

are shown in Table 2. Figure 2 shows the engine performance characteristics [26].

Table. 1 Technical data of Tercel autogyro [26]

Dimensions		
Rotor Diameter	8.60	m
Rotor Disc Area	60.82	m ²
Rotor blade chord	0.20	m
Overall length (without rotor)	5.04	m
Hull width	2.35	m
Cabin width	2.20	m
Cabin width	1.36	m
Overall height	2.35	m
Wheel diameter	2.87	m
Weight		
Maximum take-off weight	560	kg
Empty weight	295	kg
Payload weight	265	kg
Propulsion System		
Engine gear ratio	1:2.43	
Propeller diameter	1.72	m
Propeller	KASPAR Aero 2/3 LT	
Fuel tank capacity	120	l

Table. 2 Technical data of CA 912 ULT engine [26]

Parameter	Value
Cylinder no.	4 – boxer
Displacement	1211 cm ³
Cylinder diameter	79.5 mm
Piston stroke	61 mm
Compression ratio	9.0:1
Engine gear ratio	2.43:1
Fuelling system	Indirect, multipoint injection system Auris by Auto&Aero technologies
Turbocharging	Turbocharger with an exhaust gas pressure control valve

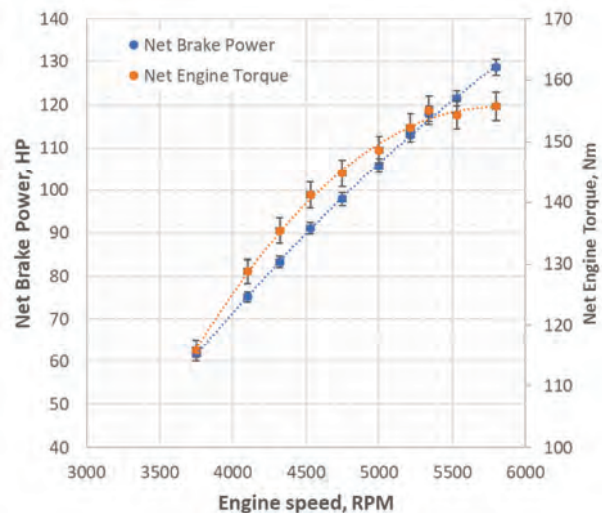


Fig. 2. Performance characteristics of the engine [26]

2.2. Scope of research

The aim of the study was to analyze the statistical distributions of the basic parameters of the aircraft engine operation in real operating conditions. The data acquisition system Flight Data Recorder FDR K.01 developed by Auto&Aero Technologies Sp. z o.o. was used to carry out the tests. It collects the information sent from the avionics

system and the fuel injection system via RS485 communication (Fig. 3).



Fig. 3. Flight Data Recorder used in the research

The tests were conducted from 11.06.2021 to 22.06.2021. There were 20 independent tests (flights) divided into two types of tasks: training flights (Flying School) and flights during the competition (Sport Competitions). Training flights included mainly full Airfield traffic pattern with full landing or touch-and-go. The time to complete one Airfield traffic pattern was about 20 minutes and the time for a single recording ranged from 30 to 60 minutes. There were 14 flights with a total duration of 15 hours and 20 minutes during which a total of 37 take-offs and landings were made. Flights during the competition (Microlight Championships of Poland) included mostly distance flights lasting from 45 to 120 minutes. They included a total of 6 flights with a total duration of 12 hours and 45 minutes involving 6 takeoffs and landings. During the flights, the following parameters, among others, were recorded at 9 Hz:

- Air speed, km/h;
- Altitude, m. asl;
- Climb rate, m/s;
- Rotor speed, rpm;
- Crankshaft speed, rpm,
- Intake manifold pressure, kPa,
- intake manifold air temperature, °C,
- fuel pressure, kPa,
- oil pressure, kPa;
- oil temperature, °C.
- 2 × head temperature, °C.
- 2 × exhaust temperature, °C.

2.3. Methodology

This article presents the results of statistical analysis of selected parameters obtained from all flights. The analysis included the engine operating point determined by two basic parameters: engine speed and manifold air pressure. To determine the dynamics of changes in operating conditions, the rates of changes of engine speed and manifold air pressure were determined. They were determined as the slope of the straight line approximated from consecutive 9 measurement samples. Data were grouped into two blocks:

data from training flights (Flying School) and data from flights during the competition (Sport Competitions).

For each block of data statistical analyses were performed including determination of distributions of analyzed parameters. Results were presented as histograms. Additionally, analysis of two-dimensional distribution as a function of engine speed and manifold air pressure was performed.

3. Analysis of results

3.1. Analysis of engine operating conditions

Figure 4 shows the distribution of engine operating point rates during training flights (Flying School). The operating points are defined by engine speed and manifold air pressure. Two groups of operating points can be seen: the idle range ($n = 1500\text{--}2000$ rpm and $\text{MAP} = 20\text{--}40$ kPa) and the heavy engine load ($n = 4500\text{--}6000$ rpm and $\text{MAP} = 80\text{--}150$ kPa). The highest frequent engine operating points occur at idle for 1500–2000 rpm and intake manifold pressure 30–40 kPa and their rate is 14.2%. In the case of higher engine loads, the highest frequency is 13.8% and occurs at 4500–5000 rpm and $\text{MAP} = 110\text{--}120$ kPa, which corresponds to about 80% of the nominal engine power. There is also a significant occurrence of the engine starting power ($n = 5500\text{--}6000$ rpm and $\text{MAP} = 140\text{--}150$ kPa) amounting to 4.5% in the studied flights. This power is used during take-offs. A large part of engine work is also at nominal power ($n = 5000\text{--}5500$ rpm and $\text{MAP} = 120\text{--}140$ kPa) – it is about 11.3%. It corresponds to the climb after take-off. A very small proportion of intermediate conditions is also evident.

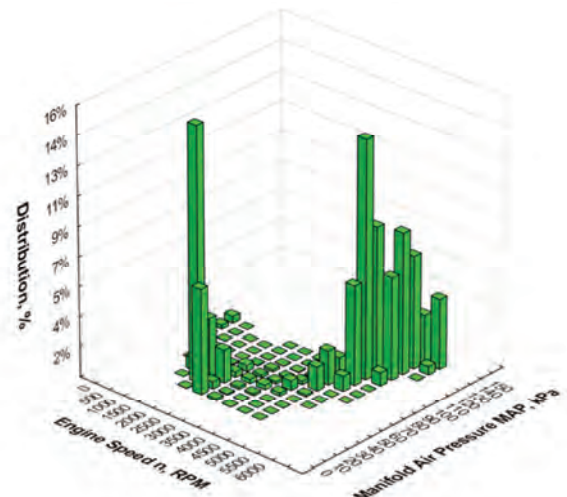


Fig. 4. Distribution of engine operating points during training flights

Figure 5 shows the analysis of engine operating points distribution for the flights during the sport competition. It can be seen that most of the time the engine was running at $n = 4500\text{--}5000$ rpm and $\text{MAP} = 110\text{--}120$ kPa. The engine worked at this point as much as 54.3% of the total engine operating time. The second most frequent point was the same rpm and lower MAP pressure = 100–120 kPa. The engine ran 26.2% at this point. Engine idling ($n = 1500\text{--}2000$ rpm and $\text{MAP} = 30\text{--}40$ kPa) was only 5.4% and at takeoff power 1.8%. Compared to the distribution for the

training flights (Fig. 4), a significant concentration of operating points is evident, as well as measuring the idle and takeoff power section specific to the landing and takeoff stages.

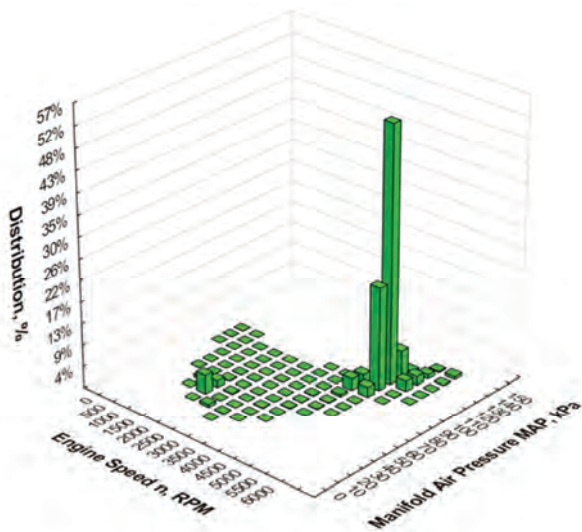


Fig. 5. Distribution of engine operating points during the sport competition

To further analyze the engine speed distribution, the analysis was performed with reduced intervals to 100 rpm (Figs 6 and 7). For the training flights, the highest frequency of occurrence was a speed around 1800 rpm corresponding to engine idle. The engine operated at this speed 12.9% of the total engine run time. The second most common speed range is around 4800 rpm. The 4700–4800 rpm range is 8.4% and the 4800–4900 rpm range is 8.1%. These ranges correspond to a cruising power of about 75% of the nominal power of the engine. The next range is the rated power at 5300–5400 rpm and 5400–5500 rpm occurring at 6.9% and 6.2% respectively. The speed range 2000–2500 rpm, corresponding to the engine warm-up process, is also a significant part of the engine work and occupies a total of 9%. This is due to short single flights, for which the warm-up time is a significant part.

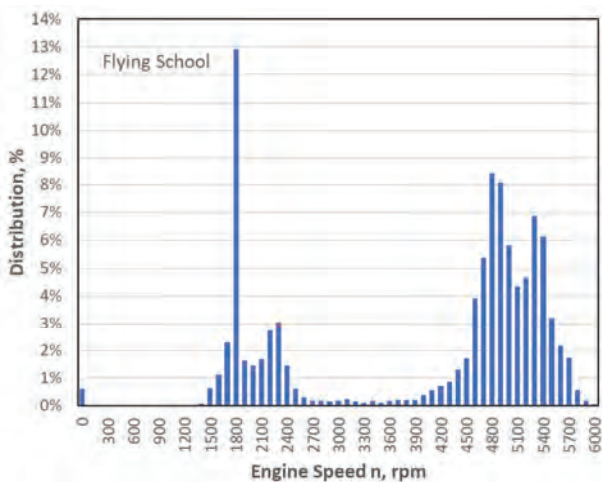


Fig. 6. Distribution of engine speed during training flights

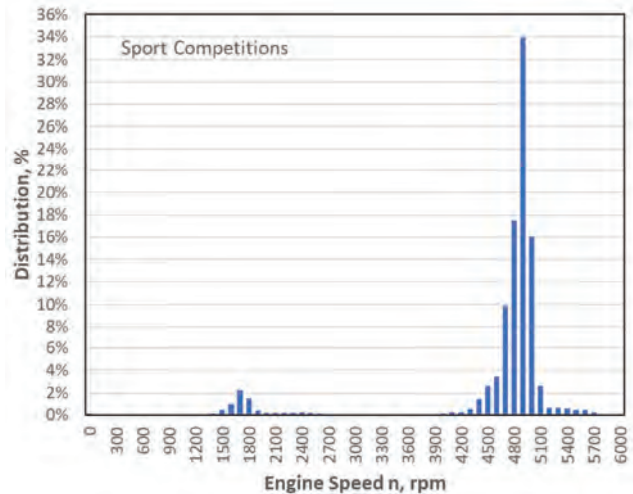


Fig. 7. Distribution of engine speed during the sport competition

For the sport competition flights (Fig. 7), the spread of engine speed occurrences is much smaller. Most of the time the engine was running in the 4700–4800 rpm range: 34%. This is the point corresponding to 75% of nominal power being the optimum flight speed for this model of autogyro. Due to the small number of take-offs and landings and the engine warm-up process, the speed ranges corresponding to these states occur much less frequently. Idle is only 4%, warm-up is 1.5% and take-off power is 1.4%.

Similar distributions are seen when the manifold air pressure is analyzed (Figs 8 and 9). For training flights (Fig. 8), the most common pressure is the 35–40 kPa range corresponding to engine idle. This occurs for 14.5% of the engine operating time. The pressure ranges from 100 to 120 kPa occur with a similar frequency of about 6–8%.

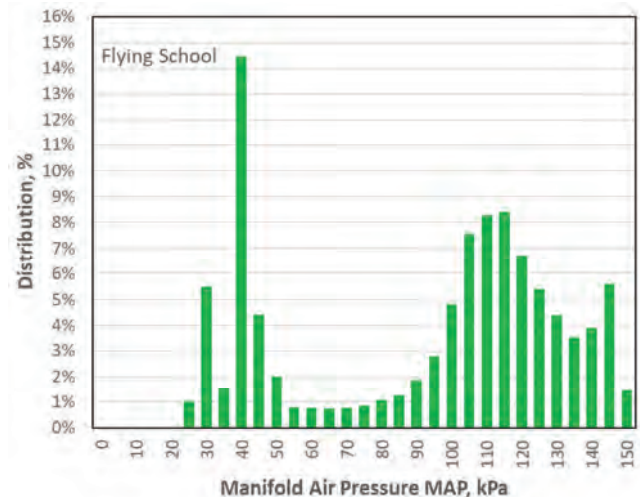


Fig. 8. Distribution of manifold air pressure during training flights

This range (100–120 kPa), on the other hand, dominates for flights during the sport competition. It occupies more than 50% of the engine operating time, with the range around 115–120 kPa being the most represented (27.9%). As with the previous analyses, a much smaller share of idle and take-off power is evident here as well.

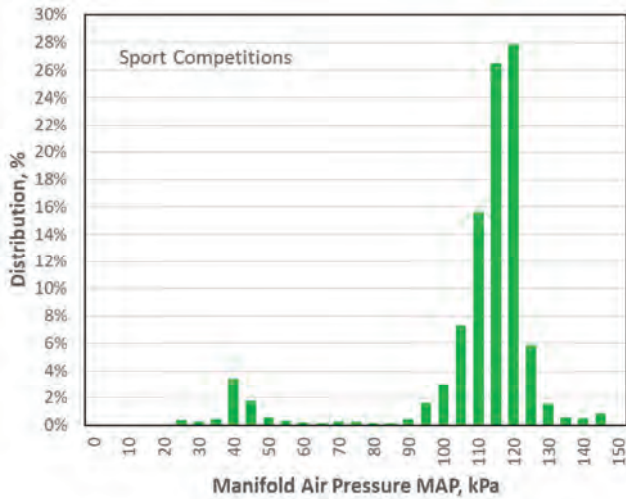


Fig. 9. Distribution of manifold air pressure during the sport competition

Another analysis included the rate of change of engine speed (Figs 10 and 11). For training flights (Fig. 10), more than 90% of the operating time is stable conditions in which the rate of change of engine speed does not exceed ± 50 rpm/s. For competition flights (Fig. 11), 95% of the engine operating time is within this range. For training flights, I stick out 1.8% of the values of decreases over 200 rpm/s and about 1.7% of increases above 200 rpm/s. These values are due to the landing (taking off the throttle before landing) and takeoff (rapid addition of throttle) stages.

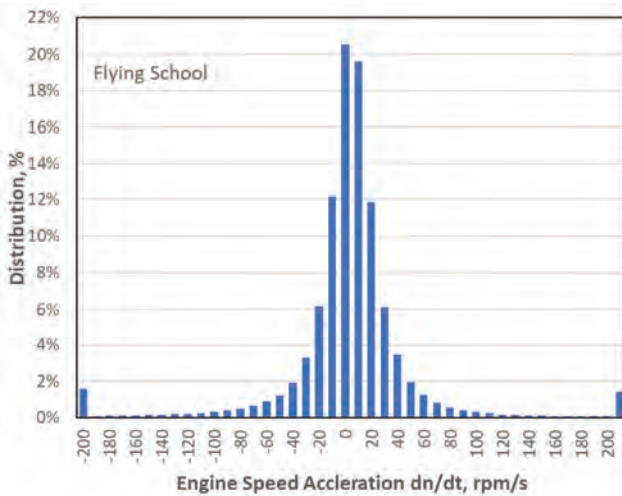


Fig. 10. Distribution of the rate of change of engine speed during training flights

For sport competition flights, these values occur much less frequently (Fig. 11). This is due to both fewer takeoffs and landings and a different, smoother control by the experienced pilot.

The stability of engine operating conditions is even more apparent when the rate of change of manifold air pressure is analyzed (Figs 12 and 13). For both groups of flights, the pressure practically does not change faster than ± 2 kPa/s.

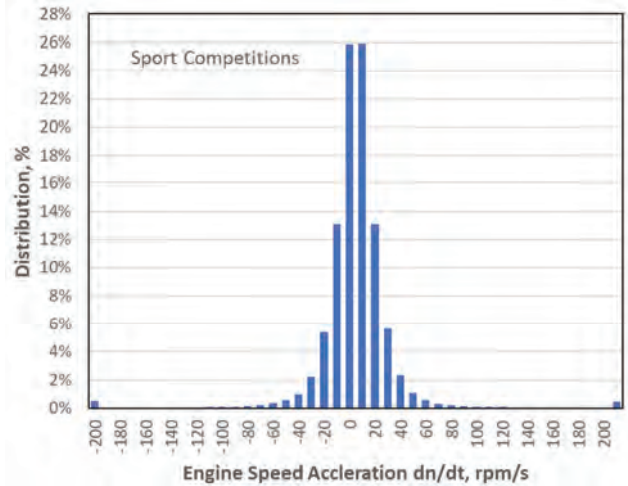


Fig. 11. Distribution of the rate of change of engine speed during the sport competition

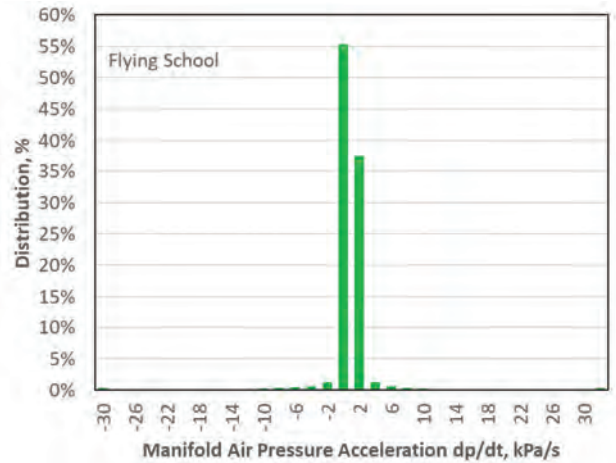


Fig. 12. Distribution of the rate of change of manifold air pressure during training flights

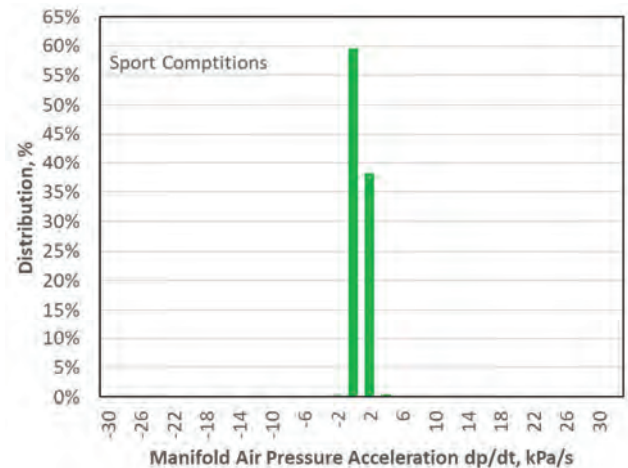


Fig. 13. Distribution of the rate of change of manifold air pressure during the sport competition

4. Conclusions

The following conclusions can be concluded from the study:

- 1) The aircraft engine is operated at predominantly steady state conditions. The speed does not vary more than ± 50

- rpm/s for 90% of the training flight time and 95% of the competition flight time. The difference in the rate of change of engine speed with different groups of flights shows that the transient conditions occur mainly during takeoff and landing.
- 2) Aircraft engines operate at average high loads. During the flights, the most common operating condition was an engine load of 70–80% of nominal power. For sport competition flights, this range covered more than 50% of the total engine operating time. The second most frequent operating condition of the engine is idling. Especially in the case of training flights, where it occupied 14% of the engine operating time. Small engine loads (below 50%) practically did not occur during the research. Their share in the total engine operating time is marginal.
- 3) Takeoffs and landings strongly influence the engine operating point distribution. During takeoff and climb immediately after takeoff, the engine operates at takeoff power or nominal power while during landing it idles. This is due to the way windlasses are controlled, where the engine is switched to idle during descent to landing. In summary, the operation of an aircraft engine mainly consists of stable operation under heavy load.

Acknowledgments

This work was supported by the EU under the project No. PMA.01.02.00-14-9542/17, "Research and development on the design of a hybrid rotor drive at AVIATION ARTUR TRENDAK". within the framework of the European Regional Development Fund from the Regional Operational Program of Mazowieckie Voivodeship 2014-2020.

Bibliography

- [1] ANDRYCH-ZALEWSKA, M., CHŁOPEK, Z., MERKISZ, J. et al. Evaluation of the test drive cycle conditions impact on exhaust emissions from an internal combustion engine. *Combustion Engines*. 2018, **175**(4), 3-9. <https://doi.org/10.19206/ce-2018-401>
- [2] ANDRYCH-ZALEWSKA, M., CHŁOPEK, Z., MERKISZ, J. et al. Static internal combustion engine operating states in vehicle driving tests. *Combustion Engines*. 2019, **177**(2), 50-54. <https://doi.org/10.19206/ce-2019-209>
- [3] BAKHOLDIN, D., BIRYUKOV, V., TOLSTOBROVA, L. Determining parameters of electric power unit for light aircraft. Advances in Engineering Research (AER). *International Conference "Actual Issues of Mechanical Engineering" AIME*. 2018, **157**, 65-69. <https://doi.org/10.2991/aime-18.2018.13>
- [4] BERA, P. Torque characteristic of SI engine in dynamic operating states. *Combustion Engines*. 2017, **171**(4), 175-180. <https://doi.org/10.19206/ce-2017-429>
- [5] BIENIEK, A., BROL, S., MAMALA, J. The system for estimation parameters of internal combustion engine in the road test. *Journal of KONES*. 2011, **18**(2), 279-286.
- [6] CHŁOPEK, Z. Some remarks on engine testing in dynamic states. *Combustion Engines*. 2010, **143**(4), 60-71. <https://doi.org/10.19206/CE-117131>
- [7] CHŁOPEK, Z., BIEDRZYCKI, J., LASOCKI, J. et al. Assessment of the impact of dynamic states of an internal combustion engine on its operational properties. *Eksploatacja i Niezawodność*. 2014, **17**(1), 35-41. <https://doi.org/10.17531/ein.2015.1.5>
- [8] CZARNIGOWSKI, J., WENDEKER, M., JAKLINSKI, P. et al. Model of injection system for SI radial aircraft engine. *SAE Technical Paper 2007-01-1903*. 2007. <https://doi.org/10.4271/2007-01-1903>
- [9] GAO, Y., CHECKEL, M.D. Emission factors analysis for multiple vehicles using an on-board, in-use emissions measurement system. *SAE Technical Paper 2007-01-1327*. 2007. <https://doi.org/10.4271/2007-01-1327>
- [10] GRABOWSKI, Ł., KARPIŃSKI, P., & RUDZIK, D. Study on operating load of the compression ignition engine. *Combustion Engines*. 2017, **168**(1), 168-171. <https://doi.org/10.19206/ce-2017-127>
- [11] JAKLIŃSKI, P., WENDEKER, M., CZARNIGOWSKI, J. et al. The comparison of the operating parameters in an aircraft radial piston engine fuelled by 100LL and ES95 gasoline. *Combustion Engines*. 2009, **136**(1), 52-59. <https://doi.org/10.19206/CE-117220>
- [12] KIERNICKI, Z. Simulation method of operating parameters assessment used for engine comparative analysis. *Combustion Engines*. 2008, **132**(1), 73-78. <https://doi.org/10.19206/CE-117290>
- [13] KUŹNIAR, M. Energy comparative analysis of power units for use in light aircraft. *Autobusy – Technika, Eksploatacja, Systemy Transportowe*. 2019, **20**(1-2), 88-92. <https://doi.org/10.24136/atest.2019.013>
- [14] MAL'TSEVSLDI, V.V., GDANSKII, N.I. Simulation of the dynamics of drives under their real operating conditions. *Chemical and Petroleum Engineering*. 1997, **33**, 269-271. <https://doi.org/10.1007/BF02418471>
- [15] MARKOWSKI, J. Correction of the model for assessing the emission of harmful exhaust emissions from the engine of a small aircraft during the flight. *Transportation Research Procedia*. 2018, **35**, 230-239. <https://doi.org/10.1016/j.trpro.2018.12.025>
- [16] MARKOWSKI, J., PIELECHA, J. Emission tests of the AI-14RA aircraft engine under real operating conditions of PZL-104 'Wilga' plane. *Combustion Engines*. 2009, **138**(3), 64-70. <https://doi.org/10.19206/CE-117180>
- [17] SITNIK, L. Statistic of fuel consumption in test and in natural operation of vehicles. *Combustion Engines*. 2017, **171**(4), 239-244. <https://doi.org/10.19206/CE-2017-440>
- [18] SURESHKUMAR, J., VENKITACHALAM, G., MALLIKARJUNA, J.M. et al. Study on effect of engine operating parameters on flame characteristics. *SAE Technical Paper 2015-01-0749*. 2015. <https://doi.org/10.4271/2015-01-0749>
- [19] ERDMAŃSKI, M., SZYMANIEC, K. Performance characteristic of C-130E Hercules aircraft engine under variable work conditions. *Combustion Engines*. 2010, **142**(3), 41-47. <https://doi.org/10.19206/CE-117134>
- [20] WYSOCKI, O., KROPIWNICKI, J., CZYŻEWICZ, J. Analysis of the possibility of determining the general characteristics using the operational data of a vehicle engine. *Combustion Engines*. 2017, **171**(4), 33-38. <https://doi.org/10.19206/CE-2017-406>
- [21] RAHMAN, S.M.A., FATTAH, I.M.R., ONG, H.C. et al. State-of-the-art of establishing test procedures for real driving gaseous emissions from light- and heavy-duty vehicles. *Energies*. 2021, **14**, 4195. <https://doi.org/10.3390/en14144195>
- [22] SONG, J., CHA, J. Analysis of driving dynamics considering driving resistances in on-road driving. *Energies*. 2021, **14**, 3408. <https://doi.org/10.3390/en14123408>
- [23] ANDRYCH-ZALEWSKA, M., CHŁOPEK, Z., MERKISZ, J. et al. Investigations of exhaust emissions from a combus-

- tion engine under simulated actual operating conditions in real driving emissions test. *Energies*. 2021, **14**, 935. <https://doi.org/10.3390/en14040935>
- [24] BAI, M., YANG, W., SONG, D. et al. Research on energy management of hybrid unmanned aerial vehicles to improve energy-saving and emission reduction performance. *International Journal of Environmental Research and Public Health*. 2020, **17**, 2917. <https://doi.org/10.3390/ijerph17082917>
- [25] YUHIMENKO, V., BAIMEL, D., SITBON, M. et al. Hybrid internal combustion engine based auxiliary power unit. *Micromachines*. 2020, **11**, 438. <https://doi.org/10.3390/mi11040438>
- [26] AVIATION ARTUR TRENDAK “Tercel Carbon RSTi Aircraft Maintenance Manual” Tercel-C-AMM-001-EN Edition 1, 28 Oct. 2020.

Jacek Czarnigowski, DSc., DEng. – Faculty of Mechanical Engineering, Lublin University of Technology.
e-mail: j.czarnigowski@pollub.pl



Krzysztof Skiba, MEng. – Faculty of Mechanical Engineering, Lublin University of Technology.
e-mail: k.skiba@pollub.pl



Karol Ścisłowski, MEng. – Faculty of Mechanical Engineering, Lublin University of Technology.
e-mail: k.scislowski@pollub.pl



Daniel Rekas, MEng. – Faculty of Mechanical Engineering, Lublin University of Technology.
e-mail: d.rekas@pollub.pl



Michał Trendak, MEng. – Aviation Artur Trendak.
e-mail: michal@trendak.eu



The emission of harmful compounds from the marine diesel engine fueled by a blend of n-butanol and marine fuel

ARTICLE INFO

Received: 14 July 2021
 Revised: 6 August 2021
 Accepted: 8 September 2021
 Available online: 13 September 2021

The use of renewable fuels may be an action leading to the reduction of pollutant emissions. This group includes biobutanol as a product of biomass fermentation. Some of its physicochemical properties, including the ability to mix with hydrocarbon fuels, make it suitable for use as a fuel component for marine diesel engines. The article presents the results of research on the concentration of exhaust gas components of a Sulzer 6AL20/24 diesel engine powered by a mixture of n-butane and diesel oil. The emission intensity were calculated for the tested components: carbon monoxide, carbon dioxide and nitrogen oxides. The emission intensity surface graphs were created based on the calculated data. The tests were carried out using different concentrations of the mixture of n-butanol and marine fuel.

Key words: *emission, marine diesel engine, n-butanol, marine fuel blend*

This is an open access article under the CC BY license (<http://creativecommons.org/licenses/by/4.0/>)

1. Introduction

It is estimated that almost 70% of global emissions of harmful compounds from maritime transport fall within 400 km from land, and have a significant impact on air quality in the coastal zone [1]. The increase in the traffic of commercial ships going to ports, not only the largest but also medium and small ones, causes a significant deterioration of air quality in coastal areas, and thus affects human health and the ecosystem. In recent virtual meeting, the International Maritime Organization (IMO) working group agreed on a set of draft guidelines to support mandatory measures to reduce the emissions of all ships [2]. The MEPC Marine Environment Protection Committee (MEPC 76) has adopted amendments to Annex VI to the International Convention for the Prevention of Pollution from Ships (MARPOL), which will require ships to reduce greenhouse gas emissions (GHG). These changes combine technical and operational approaches to improve the energy efficiency of ships, in line with the targets set in the IMO's initial 2018 GHG reduction strategy, and are important building blocks for future GHG reduction measures. The new measures will require all ships to calculate the Efficiency Existing Ship Index (EEXI) of existing ships in line with technical measures to improve their energy efficiency and establish an annual operational carbon intensity indicator (CII) and assess CII. The intensity of carbon dioxide emissions links greenhouse gas emissions with the transport work of ships. The changes apply to ships of 5000 gross tonnage and above (ships already subject to the ship fuel consumption data collecting system requirement). These ships are required to define the required annual operational carbon dioxide intensity (CII). Ships will receive an assessment of their energy efficiency (A, B, C, D, E – where A is the best), which will be included in their mandatory Administration Compliance Statement. Administrations, port authorities and other stakeholders, as appropriate, are also encouraged to provide incentives to A or B rated ships. The key decision was the establishment of reduction factors for the CII.

With 2019 as the base year for the reference lines, the reduction factor defines the mid-point of the C-rating band for each year. The CII reduction rates were set to increase by 1 percentage point (pp) per year for 2020–2022, followed by 2 pp per year for 2023–2026. The rates for 2027–2030 will be decided as part of the review to be concluded by 1 January 2026. The reduction factors are as follows [3].

Table 1. Reduction factors [3]

Year	Reduction from 2019 reference
2023	5%
2024	7%
2025	9%
2026	11%
2027–2030	To be decided

The ban will cover the use and carriage for use as fuel of oils with a density at 15°C higher than 900 kg/m³ or a kinematic viscosity at 50°C higher than 180 mm²/s. Ships involved in ship safety or in search and rescue, and ships involved in oil spill preparation and response would be exempted. Ships that meet certain design standards with regard to the protection of fuel tanks will have to comply with the requirements on or after 1 July 2029 [2].

Firstly efforts are made to develop more and more perfect technologies to reduce pollutant emissions. Secondly new energy sources are sought, including fuels from renewable sources. This group includes biobutanol as a product of biomass fermentation [4], [5].

The authors of the paper [6] examined the effects made by using various n-butanol–diesel fuel blends on the combustion history, engine performance and exhaust emissions of a turbocharged four-stroke, four-cylinder, CRDI 1154HP (85 kW) diesel engine. At first, load characteristics were taken when running an engine with normal diesel fuel (DF) to have 'baseline' parameters at the two ranges of speed of 1800 and 2500 rpm. Analysis of the changes occurred in the ignition delay, combustion history, the cycle-to-cycle varia-

tion, engine efficiency, smoke, and exhaust emissions nitrogen oxides (NO_x), carbon monoxide (CO) obtained with purposely designed fuel blends was performed on comparative bases with the corresponding values measured with 'baseline' diesel fuel to reveal the potential developing trends.

In reference [7], the authors presented bio-butanol as a renewable, environmentally friendly, and economical alternative fuel that, like many other alternative fuels such as methanol, ethanol, and natural gas, is also considered to be one of the most advantageous fuels to replacement for conventional petroleum fuels (such as gasoline or diesel fuel). Bio-butanol fuel has recently been used as an alternative fuel to conventional fuels for IC engines (gasoline or diesel engines) to meet some environmental and economic considerations. Compared with conventional fuels (gasoline and diesel fuels), bio-butanol has many advantages, so it has the potential to reduce vehicle emissions, thereby improving the atmospheric environment, reducing energy demand pressure, and significantly decreasing the car's dependence on non-renewable resource.

The research works are underway with the use of fuel blends in combustion engines and includes research on engine design also. In the paper [8], dynamic flow rates of a common rail injector using diesel fuel and different biofuels were determined. As biofuels, fatty acid methyl esters originating from canola, poultry, cattle and used cooking oil were tested. The tested fuels exhibited different physical properties e.g. density and viscosity.

In reference [9], the authors presented an experimental investigation of the relationship between the pulse width of a gasoline engine port fuel injector and the quantity of the fuel injected when butanol is used as a fuel. Two isomers of butanol, n-butanol and isobutanol, are considered as potential candidates for renewable, locally produced fuels capable of serving as a drop-in replacement fuel for gasoline, as an alternative to ethanol which poses material compatibility and other drawbacks.

2. Research object

The tests were carried out on the laboratory stand of the Cegielski-Sulzer 6AL20/24 marine diesel engine located in the Laboratory of Operating Marine Power Plants of the Mechanical and Electrical Faculty of the Naval Academy in Gdynia. The laboratory stand is presented in Fig. 1 and the technical data are shown in Table 2.



Fig. 1. The marine diesel engine laboratory stand

The Testo 350 Maritime portable exhaust gas analyzer was used to measure the concentrations of harmful compounds in the laboratory stand. The analyzer is designed to measure gas concentrations:

- oxygen (O_2),
- carbon monoxides (CO),
- carbon dioxide (CO_2),
- nitrogen oxides (NO_x),
- sulfur dioxide (SO).

The device can be used as a stand-alone measuring system or part of the system. The tested marine diesel fuel (MDF) is a sulfur-free fuel, therefore sulfur oxide were not included in the conducted research.

Table 2. Marine diesel engine Sulzer type 6AL20/24

Specification	
Piston arrangement	Inline
Cylinder diameter	200 mm
Piston stroke	240 mm
Displacement volume	1 cyl. – 7.54 dm ³
Nominal power	420 kW
Starter	pressure compressed air – 3 MPa
Number of cylinders	6
Number of valves per cylinder	4

According to the theory of experiment planning, one of the most important task is to determine the set of quantities characterizing the research object in terms of the investigation problem. Based on analysis, a qualitative simulation model of the object was developed. The following simplifications were adopted in the planned experiment:

A set of constant values, due to their invariable influence on the output values, are not considered;

The set of disturbing quantities are ignored due to the research conducted in similar environmental conditions;

The set of input quantities x are limited to the following: torque – T , engine speed – n , butnol concentration in the fuel – C_{but} ;

The set of output quantities are limited to: concentration of carbon monoxide in the exhaust manifold (C_{CO}), concentration of nitrogen oxides in the exhaust manifold (C_{NO_x}), concentration of carbon dioxide in the exhaust manifold (C_{CO_2}), oxygen concentration in the exhaust gas (C_{O_2}).

Based on the theory of the working process and curves of characteristics, it can be assumed that the diesel engine is a non-linear object due to the exhaust gas emission. The nonlinear nature of the object, described by a function in the form of a nonlinear polynomial, is best reflected by plans with at least three input values. It is assumed that at least in model three output values are taking into account to calculate the linear and quadratic effects for them and the interactions between them. These plans were developed by Draper and Box-Behnken, compiled by Connor and Zelen [10], relatively simple 3^{**} (k-p) three-valued fractional designs and their variation – fractional designs for two- and three-valued quantities. The analysis of the poliselection plans shows that in the assumed experiment it is possible to apply a complete 3^{**} (3-0) three-valued poliselection plan consisting of 1 block and 27 measurement points, which meets the requirements in terms of its feasibility and with

acceptable efficiency. Adopting one measuring block in the layout of the plan is associated with the adopted assumption that the tests are carried out under almost unchanged environmental conditions. This assumption excludes the need to eliminate the impact of changes in test conditions as quantities corresponding to higher-order coefficients. Their impact is considered to be negligible, and there is no need to statistically assess the significance of this impact [10].

The complete three-valued plan was selected for the experiment, consisting of 1 block and 27 measuring points (Table 3). The selection of one measuring block was associated with the assumption that the tests were carried out under almost unchanged environmental conditions.

Table 3. The configurations of parameters and concentration applied in the experiment

The config. number	The engine speed n [rpm]	The water break torque T [kN·m]	The conc. of n-butanol C _{but} [%]
1	600	0.98	0
2	600	0.98	15
3	600	0.98	30
4	600	2.81	0
5	600	2.81	15
6	600	2.81	30
7	600	4.65	0
8	600	4.65	15
9	600	4.65	30
10	675	0.98	0
11	675	0.98	15
12	675	0.98	30
13	675	2.81	0
14	675	2.81	15
15	675	2.81	30
16	675	4.65	0
17	675	4.65	15
18	675	4.65	30
19	750	0.98	0
20	750	0.98	15
21	750	0.98	30
22	750	2.81	0
23	750	2.81	15
24	750	2.81	30
25	750	4.65	0
26	750	4.65	15
27	750	4.65	30

Calculations of the emission intensity were carried out on the basis of the obtained measurement data in the experiment. They were used to prepare maps of the emission intensity of harmful compounds during the combustion of n-butanol fuel blend. The emission intensity of individual harmful compounds calculated on the basis of equation:

$$e_j = u \cdot c_j \cdot \dot{m}_{ex} \quad (1)$$

where: \dot{m}_{ex} – exhaust mass flow rate, c_j – concentration of the exhaust component, u – the coefficient depending on the exhaust component.

3. Results and discussion

Figure 2 presents a comparison of mass fuel consumption of the engine fed with marine diesel engine and blend n-butanol fuels. One can notice that the fuel consumption are similar for all tested points. In the case of measuring points with lower values engine load, fuel consumption is lower for blended fuel. In the measuring points with higher values of load, the fuel consumption values are slightly higher in relation to the marine diesel fuel (MDF).

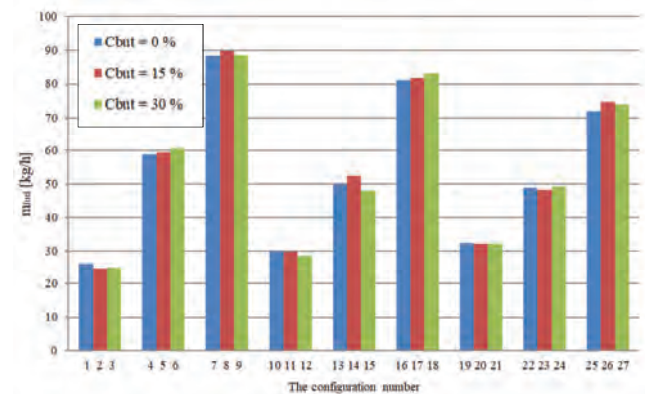


Fig. 2. Comparison of the fuel consumption for the engine fed with blend n-butanol fuel and MDF

Figure 3 shows a comparison of the overall efficiency for engine fed by tested fuels. There is a significant increase in the efficiency values in case of using the n-butanol mixture. It is connected with the oxygen and additional carbon and hydrogen atoms in the fuel chemical compounds. Due to the measuring device used in the experiment, it was not possible to measure the hydrocarbons in the exhaust gas.

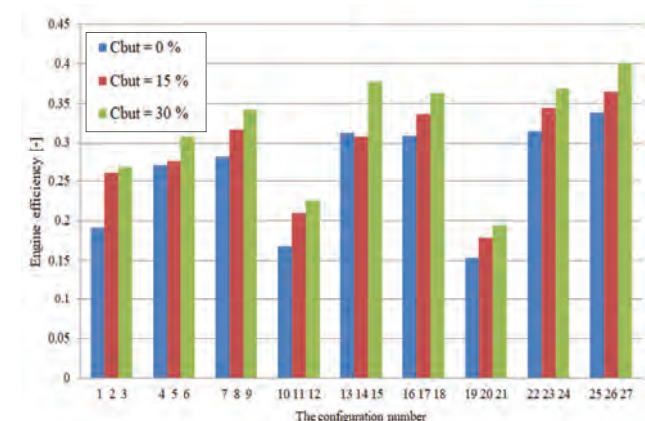


Fig. 3. Comparison of the engine efficiency for the engine fed with blend n-butanol fuel and MDF

Figure 4 presents a comparison the specific NO_x emission for tested fuels. In general, the blend n-butanol fuels have higher values of specific NO_x emission compare to marine diesel fuels and the tested C_{but} = 15% n-butanol fuel has the highest values in conducted tests.

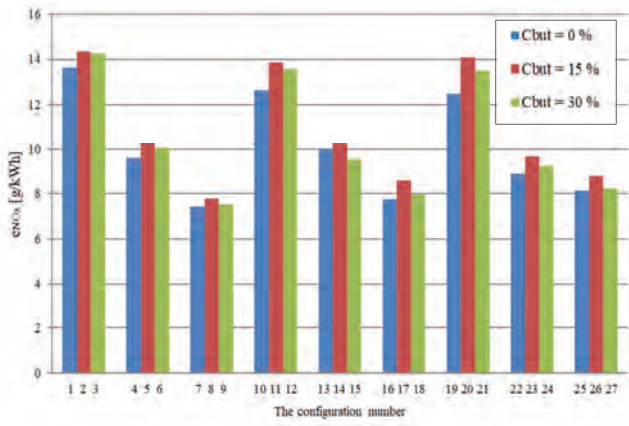


Fig. 4. Comparison of the specific NO_x emission for the engine fed with blend n-butanol fuel and MDF

Figure 5 presents a comparison the specific CO emission for the engine fed with tested fuels. Most of the conducted tests show a reduction in the specific emission value in relation to MDF. This demonstrates the improvement of the combustion conditions of blended fuels.

Figure 6 presents a comparison the specific CO₂ emission for the engine fed with tested fuels. The values of the specific emission are comparable. However, more accurate calculations show a slight decrease in value relative to the MDF. This is more evident with lower values of rotational speeds and lower values of engine load. The exception are configuration points 25, 26 and 27 in which a reduction a value of specific emission was recorded to blend n-butanol fuel.

Figures 7–9 show the surface graph of emission intensity exhaust components: carbon monoxide, carbon dioxide and nitrogen oxides for the tested rotational engine speed (600, 675, 750 rpm). The graphs were created to illustrate the changes in the intensity of the emission of harmful compounds depending on the n-butanol concentration and the engine load. The matrixes are based on data obtained on

the basis of research carried out at the previously mentioned points of the experiment.

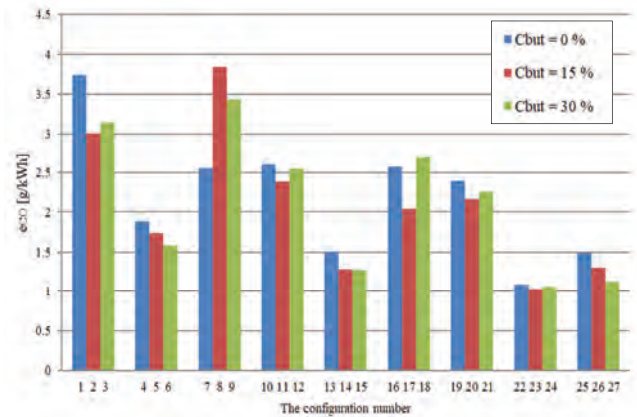


Fig. 5. Comparison of the specific CO emission for the engine fed with blend n-butanol fuel and MDF

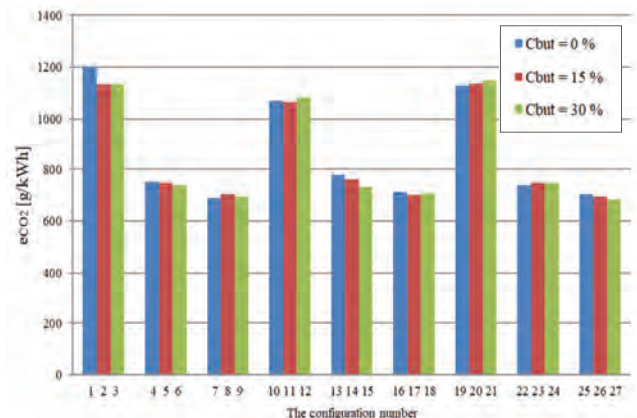
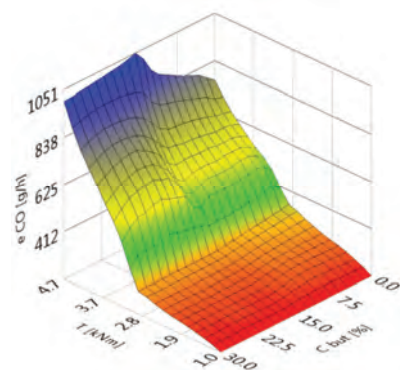
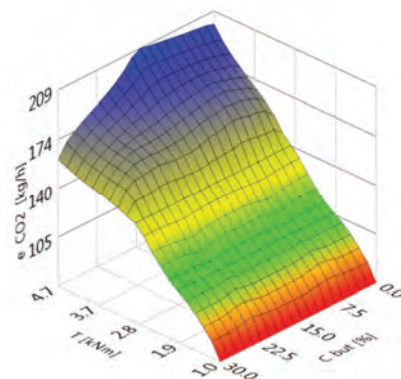


Fig. 6. Comparison of the specific CO₂ emission for the engine fed with blended n-butanol fuel and MDF

a)



b)



c)

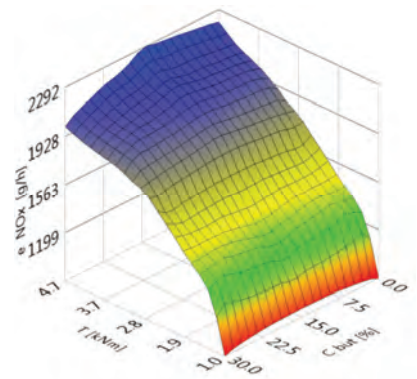


Fig. 7. The surface of emission intensity: a) carbon monoxide, b) carbon dioxide, c) nitrogen oxides at rotation speed $n = 600$ rpm

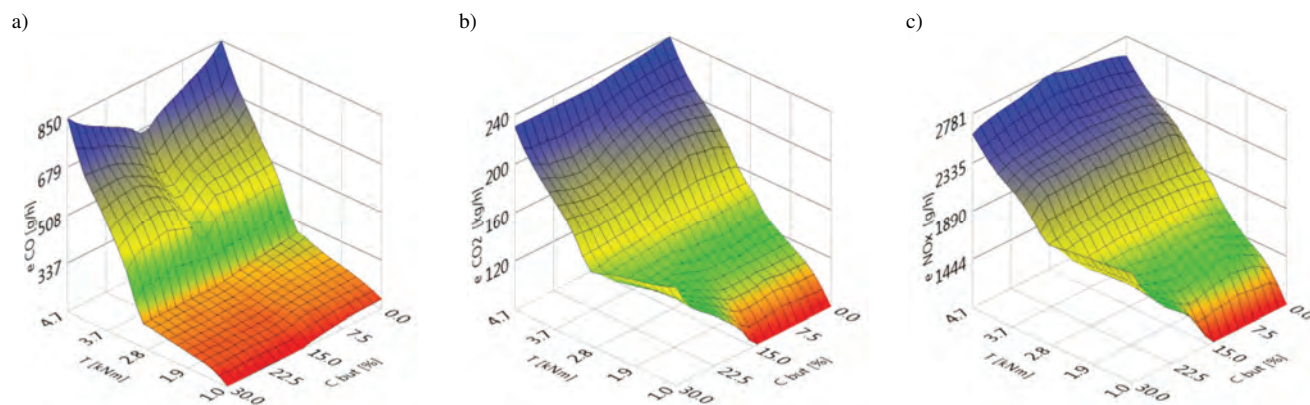


Fig. 8. The surface of emission intensity: a) carbon monoxide, b) carbon dioxide, c) nitrogen oxides at rotation speed $n = 675$ rpm

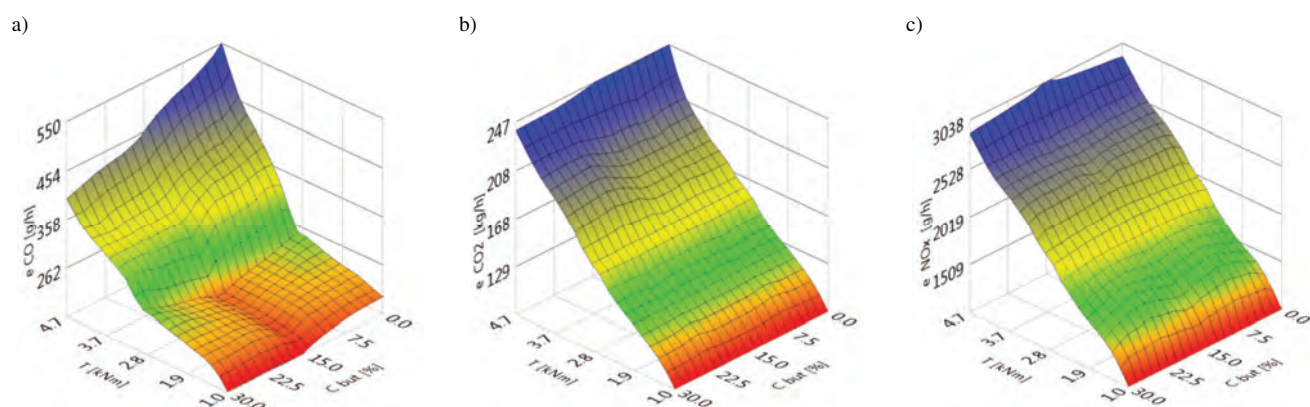


Fig. 9. The surface of emission intensity: a) carbon monoxide, b) carbon dioxide, c) nitrogen oxides at rotation speed $n = 750$ rpm

4. Summary

Research results are satisfactory and will be continued. This is particularly evident in the designated overall engine efficiencies, which have significantly increased. The content of molecular oxygen improved the combustion process in relation to marine diesel fuel. The next tests stages will be supplemented with hydrocarbon concentrations and will cover the remaining area of the load field of the marine diesel engine. The research will focus on issues directly

related to the optimal selection of the n-butanol fuel blend. It is planned to conduct optimization process aimed at minimization of emissions harmful compounds from the marine diesel engine relative to then-butanol concentration used in the fuel blend. Based on the emission results it can be concluded, that the blend fuel represents a good fuel alternative for marine fuel in minimalizing greenhouse gases and therefore it should be taken into consideration in the future of marine transport.

Nomenclature

CO	carbon oxide	MDF	marine diesel fuel
CO ₂	carbon dioxide	NO _x	nitrogen oxides
GHG	greenhouse gas		

Bibliography

- [1] SEA SHIPPING EMISSIONS 2018: Netherlands Continental Shelf, 12 Mile Zone and Port Areas Sea Shipping Emissions 2018: Netherlands Continental Shelf, *12 Mile Zone and Port Areas Final Report*, 2020.
- [2] Marine Environment Protection Committee (MEPC 76), 10 to 17 June 2021 (remote session), (n.d.). <https://www.imo.org/en/MediaCentre/MeetingSummaries/Pages/MEPC76meetingsummary.aspx> (accessed on 5.07.2021).
- [3] IMO update: Marine Environment Protection Committee – MEPC 76, (n.d.). <https://www.dnv.com/news/imo-update-marine-environment-protection-committee-mepc-76-203128> (accessed on 5.07.2021).
- [4] SCHIEL-BENGELSDORF, B., MONTOYA, J.S., LINDER S. et al. Butanol fermentation. *Environmental Technology*. **34**(13-14), 1691-1710, 2013. <https://doi.org/10.1080/09593330.2013.827746>
- [5] JANG, Y.S., MALAVIYA, A., CHO, C. et al. Butanol production from renewable biomass by clostridia. *Biore-source Technology*. 2012, **123**, 653-663. <https://doi.org/10.1016/j.biortech.2012.07.104>
- [6] LABECKAS, G., SLAVINSKAS, S., RUDNICKI, J. et al. The effect of oxygenated diesel-n-butanol fuel blends on

- combustion, performance, and exhaust emissions of a turbo-charged CRDI diesel engine. *Polish Maritime Research*. 2018, **25**, 108-120.
<https://doi.org/10.2478/pomr-2018-0013>
- [7] ZHEN, X., WANG, Y., LIU, D. Bio-butanol as a new generation of clean alternative fuel for SI (spark ignition) and CI (compression ignition) engines. *Renewable Energy*. 2020, **147**(1), 2494-2521.
<https://doi.org/10.1016/j.renene.2019.10.119>
- [8] RYBAK, A., HUNICZ, J., KRZACZEK, P. et al. Effect of different biofuels on common rail injector flow rate. *Combustion Engines*. 2017, **171**(4), 39-43.
<https://doi.org/10.19206/CE-2017-407>
- [9] FENKL, M., PECHOUT, M., VOJTISEK, M. N-butanol and isobutanol as alternatives to gasoline: Comparison of port fuel injector characteristics. *EPJ Web of Conferences*. 2016, **114**.
<https://doi.org/10.1051/EPJCONF/201611402021>
- [10] STATSOFT, Statistica – data analysis software system, ver. 6, Tulsa, USA. 2001.

Artur Bogdanowicz, DEng. – Faculty of Mechanical and Electrical Engineering, Polish Naval Academy.
e-mail: a.bogdanowicz@amw.gdynia.pl



Prof. Ryszard Zadrąg, DSc., DEng. – Faculty of Mechanical and Electrical Engineering, Polish Naval Academy.
e-mail: r.zadrag@amw.gdynia.pl



Prof. Tomasz Kniaziewicz, DSc., DEng. – Faculty of Mechanical and Electrical Engineering, Polish Naval Academy.
e-mail: t.kniaziewicz@amw.gdynia.pl



Hybrid drivetrain systems 48 V in rally cars

ARTICLE INFO

Received: 3 August 2021
Revised: 23 August 2021
Accepted: 1 September 2021
Available online: 8 September 2021

This article deals with the issue of using a 48 V hybrid drive system in rallying. Conclusions regarding the selection of elements of the above-mentioned system for further research were presented. An analysis and calculations of the energy recoverable from regenerative braking using the BISG on a given section of the rally were carried out. Conclusions were also drawn regarding further work that will be carried out to successfully implement the above-mentioned systems for rally cars.

Key words: hybrid drivetrain, mHEV, 48 V, regenerative braking, car rallies

This is an open access article under the CC BY license (<http://creativecommons.org/licenses/by/4.0/>)

1. Introduction

The popularity of 48 V hybrid drivetrain systems is systematically increasing in modern cars. This is not without reason, given the very ambitious legal targets to reduce the emissions of CO₂ and other pollutants, their use is increasingly justified. Fuel consumption can be reduced by up to 20% compared to a car without this system [1–3]. The components of 48 V technologies are diverse and are constantly evolving, which allows them to implement the above-mentioned tasks in various ways. These are, for example a Belt Integrated Starter Generator (BISG), Crankshaft Integrated Starter Generator (CISG), which can both drive the internal combustion engine (ICE) and recover part of the braking energy, or electrically driven compressors (eBooster® [4]) supporting the work of the ICE turbocharger. An important advantage of the 48 V technologies is a very favorable relation between the costs of their implementation and the results obtained, compared to drive systems with a higher supply voltage or purely electric cars. Attention should be paid to the fact that 48 V is a safe voltage, which is not without significance when it comes to handling or using cars equipped with this technology.

In rallying, the competition takes place with the use of cars, the vast majority of which are to a lesser or greater extent based on mass-produced cars. For this reason, they are related to the current technological trends of the automotive sector. The consequence of this relationship are the activities of the International Automobile Federation (FIA), which realizes the strategy of implementing hybrid and electric propulsion systems for cars taking part in rallies. The first representation of this direction from the next 2022 season will be the Rally1 group [5]. These cars will be equipped with a 100 kW rear-axle mounted electric motor and a 3.9 kWh battery. The first presented Rally1 car was the Ford Puma Rally1, built by M-Sport, so the official Ford Motor Company rally team [6]. At the same time, it is planned to hybridize lower groups of rally cars. Therefore, consequently, subsequent groups, i.e. Rally2, Rally3 and Rally4, are also to be equipped with alternative drive systems. Due to the limited level of car modifications and much more cost-oriented thinking in these groups compared

to Rally1 cars, they cannot be equipped with the same hybrid system. It must meet such conditions as: a significantly reduced level of costs, the possibility of retrofitting existing rally cars, ensuring operational safety with relatively easy to implement procedures.

The current work is based on discussions between the FIA and car manufacturers interested in participating in rallies. M-Sport takes part in the above-mentioned discussions and conducts internal research of possible solutions in their rally cars. One of the most important findings so far is the supply voltage of these hybrid systems, i.e. it was defined at 48 V. The final cost limit and the selection of components in the 48 V technologies still remain to be determined. Aspects such as the development of the system operation strategy are also important issues and, consequently, the determination of the battery capacity. In motorsport, it is also necessary to pay attention to the increase in weight of the car, as it directly affects the decrease in the performance. At the present stage of works, it is assumed that the applied system will increase the car's performance and reduce the emission of harmful substances. Following functions of the 48 V components are discussed:

- Recovery of braking energy,
- ICE support in transient states by means of an electric motor or electrically driven compressor.

2. Hybrid drivetrains 48 V

The possibilities offered by the 48 V technology include partial recovery of previously irretrievably lost braking energy, or ICE support, especially in transient states. Although the approach differs, the goal is one – to implement a technology that will reduce fuel consumption and improve ICE performance at a reasonable cost level.

48 V hybrid drivetrain systems are implemented in many different forms. Possible variants of integration of these systems with the car are presented in Fig. 1. It shows four currently known combinations of connecting the electric motor with the car propulsion system [1]:

- P0 – to the internal combustion engine through the accessories belt,
- P1 – to the internal combustion engine through the crankshaft,

- P2 – to the gear input (disconnection from the combustion engine possible),
- P3 – to the gear output through gears (disconnection from the combustion engine possible),
- P4 – to the rear axle drive system (no connection to the internal combustion engine).

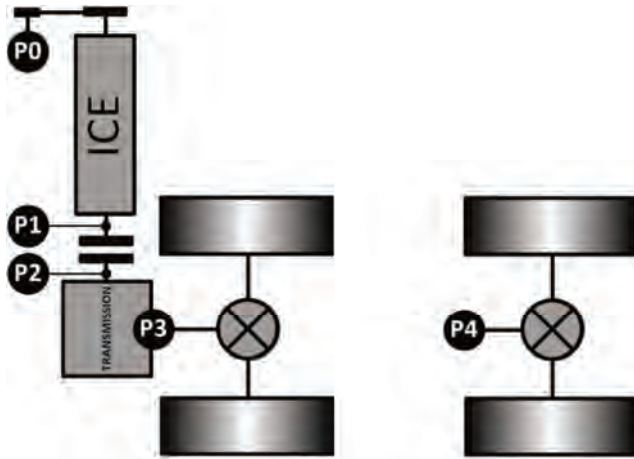


Fig. 1. Possible variants of the 48 V hybrid drivetrains in the car

The P0 configuration, the main element of which is BISG, was adopted as the first choice for a broader analysis.

2.1. BISG

The choice of the P0 configuration is not accidental. An important argument when implementing 48 V technologies is, above all, the ease of its integration with both new and existing rally cars. When choosing BISG, it is not necessary to redesign the driveline and all the integration work will focus on the ICE accessory drive. It should be added that in the case of configurations other than P0, the problem would be to find parts from series production that are universal enough to be able to integrate them without significant interference with other car systems. Another advantage of BISG is their relatively good availability on the market, which is the reason for their more and more frequent use in mass-produced cars. It should be noted here that both the FIA and other manufacturers participating in the discussions about hybrid rally cars prefer to use as many parts from series production as possible. To sum up, the lack of flexibility with possible integration with the car, higher costs and currently low popularity of configurations other than P0 in mass-production mean that they will not be analyzed at the moment. This is aimed at reducing implementation costs by using existing components, as well as increasing R&D and marketing potential by using serial parts under extreme rally conditions. In the Rally1 car, a dedicated hybrid system in the P3 configuration was used, however, in this group, the cost of building the car and its operation is at a much higher level. BISG can perform the following functions [1]: engine starting, generating electricity, supporting the ICE in various situations, and as a result, it also allows extending the operation of start-stop systems through the so-called sailing [3]. BISG with a power of up to 13 kW of maximum motor power and up to 7 kW of

continuous motor power is assumed to use and such systems are now available on the market [2].

2.2. Electrically driven compressor

To further increase the benefit of a 48 V installation, an electrically driven compressor is contemplated. One such solution is eBooster® [4]. Its operation is based on a complementary action in relation to the ICE turbocharger, thanks to which in states of high demand for torque, it significantly reduces the ICE response time. In addition, it was confirmed in tests that eBooster® improves acceleration time by about 18% compared to the car without it and by 3% compared to the version with BSIG while consuming less than half of the electricity [4]. Rally cars use internal combustion engines with relatively small displacements, i.e. between 998 cm³ and 1620 cm³. It is required by the FIA regulations, which at the same time reflect the current trends of the automotive sector. With the assumption of obtaining high output parameters of these engines, it is necessary to use turbochargers with high efficiency. This causes a delay in the operation of the turbocharger, especially at low and medium ICE speeds. To prevent this, the Anti Lag System (ALS) is used, which ensure a quick response of the turbocharger in transient states, but also increase fuel consumption and can increase the engine operating temperature and reduce the durability of the turbocharger. An electrically driven compressor can potentially replace the ALS system and thus its disadvantages will be eliminated. Taking into account the above benefits, the ease of integration with the car and the complementary operation of the above-mentioned system with a 48 V system, its use will be further analyzed for use in a rally car.

2.3. Diagram of the analyzed 48 V hybrid system

The configuration of the 48 V hybrid drive system intended for further analysis for use in the Rally2, Rally3 and Rally4 rally cars is shown in Fig. 2. Similar solutions have already been tested with good results for use in production cars [4, 7]. This system consists of the following 48 V powered components:

- BISG,
- Electrically driven compressor.

Additionally, components of the 48 V system (not shown in the diagram) are:

- 48 V battery,
- DC-DC converter.

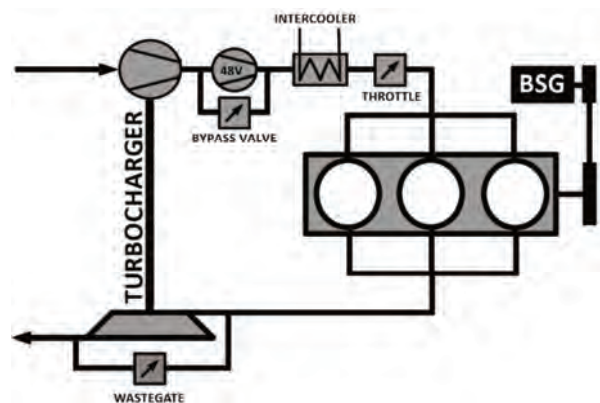


Fig. 2. Diagram of the analyzed 48 V hybrid system

3. Characteristics of the car

The Ford Fiesta ST Rally3 is a rally car that is being analyzed for the use of 48 V hybrid drivetrain. The car is presented in Fig. 3.



Fig. 3. M-Sport Poland Ford Fiesta ST Rally3

It is a rally car designed and manufactured by the M-Sport Poland company. Table 1. presents the basic technical data of the above-mentioned car.

Table 1. Basic technical data of the Ford Fiesta ST Rally3

Parameter	Unit	Value
Weight of the car	kg	1210
Engine type	–	turbocharged, petrol
Number of cylinders	–	3
Displacement	cm ³	1496
Maximum power	kW	158 (FIA 30 mm restrictor)
Maximum torque	Nm	400
Drivetrain	–	constant four wheel drive
Transmission	–	five speed sequential gearbox

5. Analysis of the car rally section in terms of energy that can be recovered by BISG

A rally consists of both Special Stages (SS), which, as defined by the FIA, are timed speed test on roads closed to the public for the rally and Road Sections, which are the parts of an itinerary which are not used for SS [8]. From the point of view of the analyzes carried out, the most important are the SS, because there the actual sports competition takes place and the system analyzed will be used.

The first stage of further work was to calculate the energy that can be obtained by regenerative braking using BISG, analyzing for this purpose a section of the FIA ERC (FIA European Rally Championship). The rally section was analyzed, as it is assumed that between sections it will be possible to charge the 48 V battery of the hybrid system. This stage of the analysis is very important as further decisions regarding the capacity of the 48 V battery or the operating strategy of the systems depend on it. The rally section schedule is shown in Table 2.

Taking into account the above, the analysis of the possibility of energy obtained from regenerative braking on the SS was carried out. The calculation of the braking power

and energy was performed using the data on the instantaneous value of pressures in the front and rear brake circuits stored in the car's data logging system. A rally with a gravel surface with high average speeds was selected to verify the worst case, i.e. with the lowest possible braking energy of the car.

Table 2. Rally section characteristic

Length of	Unit	Value
SS1	km	18
SS2	km	17
SS3	km	29

The calculations were performed by determining the pressure force of the pistons in the brake calipers, knowing their surface based on the measured value of the instantaneous pressure in the front and rear brake circuits. Then, the circumferential force on the active circumference of the brake discs was calculated taking into account the coefficient of sliding friction in the disc brake. The last step to calculate the total braking force F_B was to calculate the braking force on the dynamic radius of the tire, taking into account the active radius of the brake disc and the dynamic radius of the tire. The pressure in the brake circuits was measured with a constant sampling frequency, which allowed to record the instantaneous value of pressure every $\Delta t = 0.1$ s. For the road in the analyzed case, for the section where braking occurred, the braking work W_B was determined according to the relationship (1) (taking into account that $\Delta x \rightarrow 0$):

$$W_B = \int_0^1 F_B dx \quad (1)$$

The braking power was determined subsequently as below in (2) (taking into account that $\Delta t \rightarrow 0$):

$$\Delta P_B = \frac{\Delta W_B}{\Delta t} \quad (2)$$

where in (1) and (2): Δx – road increment, W_B – work of braking force, Δt – time increment, ΔP_B – instantaneous braking power.

The work W_B performed during braking is treated as the energy E_B needed to brake the car, which theoretically can be used for the BISG drive. The Figures 4–6 shows the braking power and vehicle speed from SS1, then on the next SS2 and SS3.

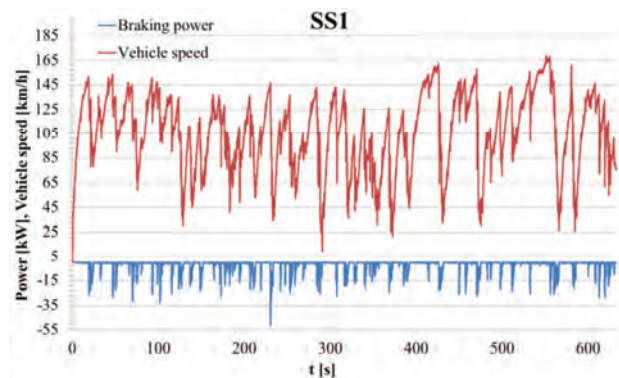


Fig. 4. Braking energy and vehicle speed during SS1

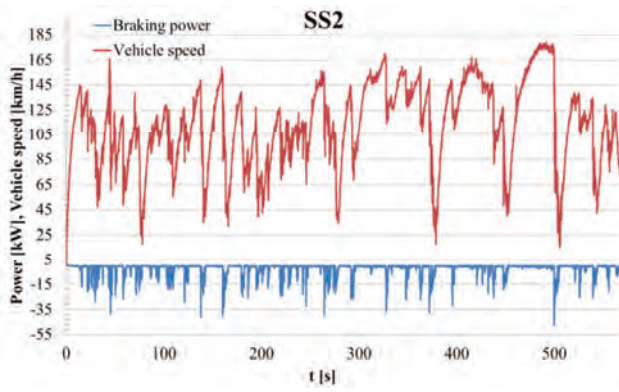


Fig. 5. Braking energy and vehicle speed during SS2

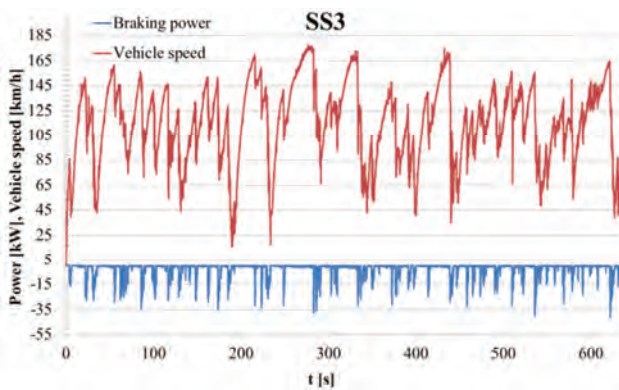


Fig. 6. Braking energy and vehicle speed during SS3

The maximum values of the braking power for each SS are presented in the Table 3.

Table 3. Maximum braking power in SS1, SS2 and SS3

Maximum braking power in	Unit	Value
SS1	kW	52
SS2	kW	48
SS3	kW	41

It can be assumed that when using BSIG, in which the maximum power of generating electricity is up to a maximum of 14 kW and in continuous mode up to 10 kW, the recovered energy will be much lower, because the calculated values of the maximum values of the braking power significantly exceed them. Another significant limitation when analyzing the ability to regenerate braking energy is the design of the 48 V battery itself and the maximum electric current that can be charged by the BISG. As it was researched the currents within the 48 V MHEV (Mild Hybrid Electric Vehicle) battery are significantly higher than in the BEV (Battery Electric Vehicle) with voltage usually around 400 V [9]. These high currents in the 48 V applications are serious challenge in terms of battery design.

Using data form the same SS, the braking energy was calculated, which is theoretically available for the application of regeneration braking, driving the BISG and thus charging the 48 V battery. The results are presented in Figs 7–9 for each of analyzed SS.

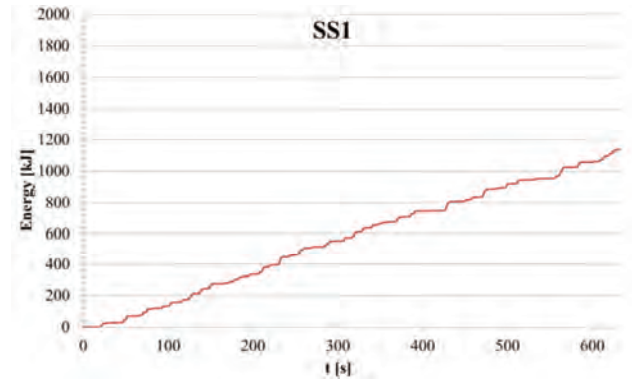


Fig. 7. Braking energy in SS1

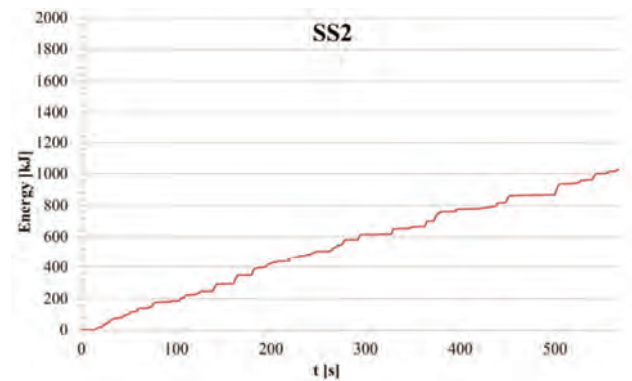


Fig. 8. Braking energy in SS2

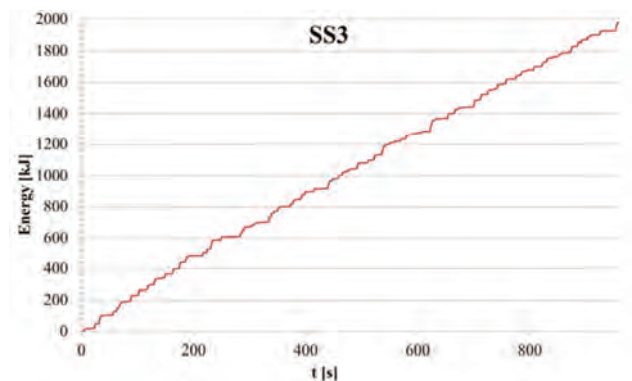


Fig. 9. Braking energy in SS3

In the above figures of the braking energy, only cases where the driver's foot was off the accelerator pedal were taken into account, i.e. at these moments the BISG system could perform regenerative braking.

Note that these are theoretical values as the following was not considered in this analysis:

- the resistance in the drive train while driving the BISG,
- the maximum possible power generated by BISG,
- the maximum electric current that the BISG can charge the battery with.

When analyzing the curves of these graphs, it can be noticed that there is a constant and continuous increase in energy generated as a result of braking. At the same time, it is good phenomenon considering the possibility of using regenerative braking in the rally, which can be a significant part of the energy possible for use in the 48 V hybrid drive system.

An attempt to answer what part of the determined theoretical braking energy is possible to recover was made on the basis of the previously conducted researches [2]. On their basis, it can be concluded that about 62% of the braking energy is recoverable and about 36% of this energy was recovered during these tests using BISG with parameters similar to the assumed ones. The conclusion from this is that a total of 1493 kJ would be recovered when driving the analyzed SS. This amount of energy would allow the BISG to be powered for 115 seconds in maximum power mode and 213 seconds in continuous power mode. Comparing this to the times obtained from all stages, the driver would be able to use the additional power generated by the BISG as shown in the Table 4.

Table 4. SS time percentage at which BISG or eBooster® can be used

Parameter	Unit	Value
BISG maximum power 13 kW	%	5.3
BISG continuous power 7 kW	%	9.8
eBooster® maximum power 5 kW	%	13

It should be noted here that the maximum power of BISG support, i.e. 13 kW, can only be generated for 5 seconds [2], so finally the percentage of the BISG support that can be used will fall between the two values listed in the Table. By analyzing the possibilities of using the recovered energy for eBooster®, the maximum power is 5 kW, its use would be possible for 295 s, and consequently the percentage of the eBooster® support in relation to the all SS distance is presented in the Table 4.

This discussion does not take into account the SOC (State of Charge) of the battery, showing only the potential for using the energy from regenerative braking. It can be concluded that the above-mentioned results, assuming the use of a 48 V battery with a capacity properly matched to the characteristics of rallies, along with the possibility of charging them between sections, will be much better. Moreover in order to achieve even better parameters of the analyzed system possibility of use supercapacitors should be recognize to reduce peak battery current and handle with the high power during acceleration and capture more regenerative braking energy than with the battery itself [10].

6. Operation modes and equal competition

The use of a 48 V hybrid drivetrain system combined with regenerative braking creates completely new challenges in rallies as to the way they are used. The FIA is currently discussing this on the Rally1 group. Looking at FIA series such as Formula 1, WEC and Formula E, it can be concluded that planning kinetic energy recovery and its subsequent use during a race is an increasingly large part of the racing strategy. As an example of the importance of energy planning in motorsports where regenerative braking is used, the Formula E principle is that cars enter the race with 70% of the battery charge and the missing 30% must be recovered by regenerative braking during the race [11].

In the case of the 48 V hybrid drive system in the Rally2, Rally3, Rally4 groups, it is important to understand the following issues:

- a method of aligning systems coming from different manufacturers,
- regenerative braking mode or modes,
- BISG ICE support mode or modes,
- the operating strategy of an electrically powered compressor.

It should be assumed that each of the manufacturers involved in the creation of Rally2, Rally3, Rally4 cars with a 48 V hybrid drivetrain system will want to use components from their series-produced car models. For this reason, BISG, DC-DC converters and potentially electrically driven compressors will vary from one rally car to another. Taking this into account, the most advantageous element of the system, in order to equalize parameters between systems, is to develop a battery with specific, identical parameters for all. Determining battery parameters such as maximum voltage, capacity, charging/discharging powers (these parameters should be determined in relation to the capabilities of the BISG with the lowest power) will potentially allow limiting and, as a result, equalizing performance between systems from different manufacturers. Standardized battery parameters between different systems would create a real limitation in the use of BISG.

Regenerative braking modes must strive for maximum energy recovery, but also take into account the different conditions of the car's grip on the road and the driver's preferences. A more sophisticated brake-by-wire system can be used, where the braking signal given by the driver will then be processed and as a result will automatically decide whether to use traditional or regenerative braking and to what extent. When the brake-by-wire solution turns out to be too complicated and thus expensive, it is also possible to adopt a strategy that regenerative braking takes place with a constant predefined intensity and the braking force needed by the driver above it is obtained by activating traditional braking. In this case, it is necessary to define the number of predefined strategies and their intensity levels in order to cover as many variants of the car's grip on the road as possible.

The ICE assist mode of the BISG depends primarily on the decision to use an electrically driven compressor in the system. If used, then according to the research carried out and the logic of the ALS system, which must operate along the entire length of the SS, the electrically driven compressor would have priority in operation over the BISG. In other studies it was proved that the influence of an electrically driven compressor on the improvement of ICE characteristics in transients is more favorable than BISG, and this with lower energy consumption. In the event that the electrically driven compressor would not be finally applied, then the support of the ICE by the BISG would take on a much greater role. In such a case, it is necessary to define the method of turning on this support and define the limits of its use (e.g. the limit of energy during a single activation). The aim is that the use of this support should be evenly distributed over the entire length of the SS as far as possible.

The electrically driven compressor, intended to replace the current ALS system, would have to operate along the entire length of the SS, in line with the ICE's transient

needs. The 48 V hybrid drive system must be configured so that it is possible to use an electrically driven compressor on all SS in the section between battery charges.

7. Conclusions for further work

The next steps to draw conclusions for discussion with the FIA regarding the implementation of 48 V hybrid propulsion systems should be to analyze the different operating strategies of the BISG and the electrically driven compressor and simulate the energy consumption by them in sections of different rallies. The pool of rallies analyzed should be as large as possible so that the conclusions drawn are consistent with the actual use of the system. Then, having the specified electric energy consumption and energy re-

coverable during regenerative braking, the parameters of a battery that meets the assumptions regarding the capacity and charging/discharging power should be determined. Then it will be possible to create a prototype of the system and start testing in conditions similar to real ones, which will allow validating numerical simulations as well as checking the durability of components in the extreme rally use.

Acknowledgements

This work was supported by the M-Sport Poland sp. z o.o. and was partially supported by the statutory research of Institute of Thermal Technology Silesian University of Technology.

Nomenclature

ALS	turbocharger anti lag system	SOC	state of charge
BEV	battery electric vehicle	SS	special stage
BISG	belt integrated starter generator	Δx	road increment, [m]
CISG	crankshaft integrated starter generator	W_B	work of braking force, [kJ]
ERC	European Rally Championship	Δt	time increment, [s]
FIA	International Automobile Federation	ΔP_B	instantaneous braking power, [kW]
ICE	internal combustion engine		
MHEV	mild hybrid electric vehicle		

Bibliography

- [1] PELS, T., DAVYDOV, V., ELLINGER, R. et al. 48V – where to place the e-machine? Liebl J. (eds) Der Antrieb von morgen 2017. Proceedings. *Springer Vieweg*. Wiesbaden 2017. https://doi.org/10.1007/978-3-658-19224-2_3
- [2] HAKVOORT, H., OLBRICH, T. Series application of a 48-V hybrid drive. *Motortechnische Zeitschrift MTZ Worldwide*. 2017, **78**, 26-31. <https://doi.org/10.1007/s38313-017-0089-7>
- [3] HELBING, C., BENNEWITZ, K., MANN, A. The 48-V mild hybrid drive system of the Volkswagen Golf 8. *Motortechnische Zeitschrift MTZ Worldwide*. 2020, **81**, 18-25. <https://doi.org/10.1007/s38313-019-0164-3>
- [4] GRILL, M., KELLER, P., MOHON, S. et al. Development of a 48V P0 demonstration vehicle with eBooster® air charging. *18. Internationales Stuttgarter Symposium*. 2018, 551-566. https://doi.org/10.1007/978-3-658-21194-3_43
- [5] FIA World Rally Championship Hybrid Programme Update. FIA 2021. <https://www.fia.com/news/fia-world-rally-championship-hybrid-programme-update> (accessed on 12.07.2021).
- [6] PUMA RALLY1 Press News. Ford Media Center 2021. <https://media.ford.com/content/fordmedia/feu/en/news/2021/0/08/ford-and-m-sport-reveal-new-puma-rally1-wrc-prototype--electrify.html> (accessed on 08.07.2021).
- [7] GRIEFNOW, P., XIA, F., ANDERT, J. et al. Real-time modeling of a 48V P0 mild hybrid vehicle with electric compressor for model predictive control. *SAE Technical Paper* 2019-01-0350. 2019. <https://doi.org/10.4271/2019-01-0350>
- [8] 2021 FIA Regional Rally Sporting Regulations. FIA 2021. https://www.fia.com/sites/default/files/2021_rrsr_fr-en_2021-07-12.pdf (accessed on 12.07.2021).
- [9] BANK, T., KLAMOR, S., SAUER, D.U. Lithium-ion cell requirements in a real-world 48V system and implications for an extensive aging analysis. *Journal of Energy Storage*. 2020, **30**, 101465. <https://doi.org/10.1016/j.est.2020.101465>
- [10] SREEDHAR, S.B., SIEGEL, J., CHOI, S. Topology comparison for 48V battery-supercapacitor hybrid energy storage system. *IFAC-PapersOnLine*. 2017, **50**, 4733-4738. <https://doi.org/10.1016/j.ifacol.2017.08.864>
- [11] CAMPBELL-BRENNAN, J. System addicts. *Racecar Engineering*. 2021, **31**, 58-63.

Bartłomiej Urbański, MSc. – Institute of Thermal Technology, Silesian University of Technology.
e-mail: bartlomiej.urbanski@polsl.pl



Grzegorz Przybyła, DSc., DEng. – Institute of Thermal Technology, Silesian University of Technology.
e-mail: grzegorz.przybyla@polsl.pl



Comparative analysis of the emissions of carbon dioxide and toxic substances emitted by vehicles with ICE compared to the equivalent emissions of BEV

ARTICLE INFO

Received: 14 July 2021
 Revised: 28 August 2021
 Accepted: 30 August 2021
 Available online: 9 September 2021

In the article were compared the vehicles (by pairing) the vehicles on the basis of selected criteria considering vehicles': weight, length, wheel width, maximum output and acceleration time. The article was carried out by analysing the available source materials and specific energy mix based on coal. The emission of air pollutants (exhaustive) was estimated using the mathematical calculation. In order to carry out the analysis, the data provided by the manufacturers of the considered cars were used, concerning fuel consumption by the cars equipped with the internal combustion engines or electricity consumption in the case of cars with equipped with electric motors. The air pollutants that were taken into consideration: carbon monoxide, nitrogen oxides, sulphur dioxide, carbon dioxide, and total particulate matter. Apart from the exhaustive emissions, the total particular matter emissions from the tyre and brake wear and road abrasion is also included. The pollutant emission was estimated on the basis of emission factors using the average mileage characterizing for driving in European conditions.

Key words: *air pollutant, vehicle, electric vehicle, ICE vehicle, BEV*

This is an open access article under the CC BY license (<http://creativecommons.org/licenses/by/4.0/>)

1. Introduction

The assumptions of the European Green Deal and the pursuit of climate neutrality influence the development of BEV [3, 8–10].

However we can describe electric means of transport as 'ecological', the actual emissions generated by the electric vehicles are associated with the fuel structure occurring in particular country. Then we can say '100% ecological' or 'climate friendly' about vehicles that are powered mainly from renewable energy sources.

According to the last submission of the national air pollutants' emission inventory [5, 6, 12], Polish energy mix (structure of the fuel combusted) in the public power generation sector consists of 81% solid fuels, mainly hard coal and lignite. Considering the energy mix, the air emissions from electric vehicles in Poland can be qualified as translation of coal emissions to the road transport sector.

That means the ecological properties of electric vehicles are associated mainly to the national energy mixes in energy production sectors. There are very limited number of scientific publications taking into account comparison between the air pollutants' emissions associated with the BEV, and with ICE vehicles in terms of the energy mix used for electricity production [2, 3]. This fact gives an opportunity for investigating the 'ecological side effects' associated with the BEV, and generated as a result of applying of the national energy mix based on the fossil fuels.

2. Methodology

The article compares the emission of harmful substances caused by cars which are equipped with: internal combustion engines, and electric motors. Basing on the sets of parameters that affect fuel consumption and, consequently, the emission of harmful substances (descri-

bed in three criteria, as below), there are compiled together a pairs of cars (fuel powered vs. electric).

Classification criteria [12]:

1. The ratio of the maximum power output [kW] to the car's own weight in kilograms. Its aim is to select cars with the most similar engine performance. When the criterion is used for cars with internal combustion engines, it is also named 'balance weight ratio'. The reason for this is the higher (approximately a constant multiple) curb weight of a car with an electric motor compared to its internal combustion counterpart, resulting from the design of the drive. Therefore, in order to obtain a reliable result, this disproportion had to be levelled. Criterion No. 1 has been expressed by the formula (1):

$$Q_1 = \frac{P}{m \times q} \quad (1)$$

where: P – maximum power output [kW], m – curb weight of the car [kg], q – balance weight ratio for cars with internal combustion engines = 1.215.

2. Using this criterion it is possible to select cars with the most similar geometrical dimensions, i.e. the length and height of the car. The mentioned parameters also affect the ability to overcome air resistance of a similar value (translating into fuel consumption). The values of which result from a similar maximum power of the engines of the compared cars. Criterion No. 2 has been expressed by the formula (2):

$$Q_2 = \frac{l \times h}{P} \quad (2)$$

where: P – maximum power output [kW], l – length of the car [m], h – length and height of the car [m].

3. The purpose of this criterion is to select cars of the similar rolling resistance and hence of the similar

energy consumption and emissions. Rolling resistance depends on the tire width and the maximum engine power, as well as the acceleration time. Criterion No. 3 has been expressed by the formula (3):

$$Q_3 = \frac{P}{w_o \times t} \quad (3)$$

where: P – maximum power output [kW], w_o – tire width [mm], t – acceleration time (0–100) km/h [s].

The assumptions for comparing cars with each other were:

- matching a car with an internal combustion engine to a car with an electric engine according to the enumerated criteria,
- finding the results of the criteria in the tolerance field of ± 0.01 in relation to each other,
- fulfilment of all criteria.

The comparative criteria were selected so that the compared cars were as similar as possible to each other in terms of technical parameters following the design purpose of their use, geometric parameters that affect fuel/electricity consumption, as well as the work performed by engines during operation, which translates into the similar consumption of supplied energy.

In order to obtain meaningful results, both cars (electric vs. fuel powered) of different brands were compared with each other, selecting cars with internal combustion engines from specific ranges of engine displacement i.e. (800–1400) cm^3 , (1401–2000) cm^3 and above 2000 cm^3 (Fig. 1) and cars of the same brand (Fig. 2).

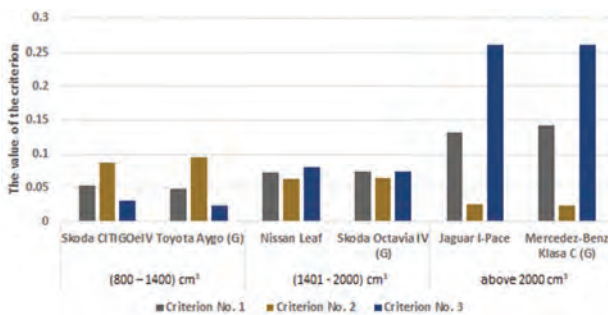


Fig. 1. Summary of the criteria for the selection of cars for testing in terms of engine displacement. G – gasoline, D – diesel

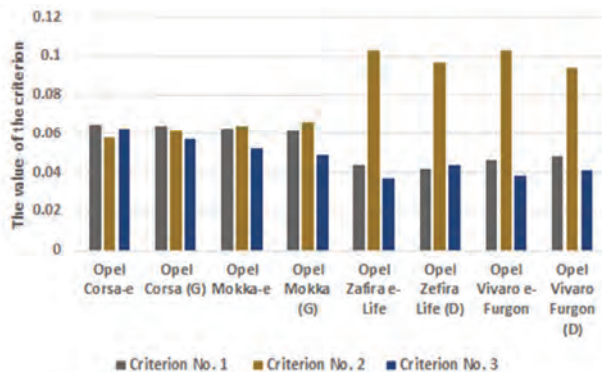


Fig. 2. Summary of criteria for selecting vehicles for testing because of the brand of vehicle. G – gasoline, D – diesel

In order to calculate the emissions from the selected ICE vs BEV pairs, the authors calculated the emission of individual harmful substances from combustion processes from a source appropriate for the type of engine for the averaged mileage per year for Polish conditions (including cold start parameter) [4] in a mixed driving cycle.

The emission of CO , NO_x and PM from cars with an internal combustion engine was determined based on the formula (4) [7]:

$$E_{i,j} = M_{i,k} \times EF_{i,j,k} \quad (4)$$

where: E_i – emission of pollutant i [g], $EF_{i,j,k}$ – emission factor of pollutant i for vehicle category j and technology k (type of fuel and engine displacement) [g/veh-km], $M_{i,k}$ – distance driven by vehicle of category j and technology k [km].

The emission of CO_2 from cars with an internal combustion engine was determined based on the formula (5) [1]:

$$E_{\text{CO}_2} = EF_{i,j,m} \times FC_{j,m} \quad (5)$$

where: E_i – emission of pollutant i [g], $FC_{j,m}$ – fuel consumption of vehicle category j using fuel m over the distance driven by vehicle [g], $EF_{i,j,k}$ – fuel consumption-specific emission factor of pollutant i for vehicle category j and fuel m [g/kg].

The emission of SO_2 from cars with an internal combustion engine was determined based on the formula (6) [7]:

$$E_{\text{SO}_2} = 2 \times k_s \times FC_m \quad (6)$$

where: E_{SO_2} – emissions of SO_2 per fuel m [g], k_s – weight related sulphur content in fuel of type m [g/g_{fuel}], FC_m – fuel consumption of fuel m [g]

The emission of harmful substances from BEV was determined on the basis of the formula (7) [7]:

$$E_i = N \times EF_i \times M \quad (7)$$

where: E_i – emission of pollutant i [g], N – consumption of the electric energy [Wh], EF_i – emission factor of pollutant i for electricity produced by installations for combustion of fuels [g/Wh], M – distance driven by vehicle [km].

For the calculations the following data were used:

- fuel and electricity consumption over a distance (catalogue data),
- emission factors for harmful substances for cars with internal combustion engines [1, 7],
- TSP emission factors from the tyre and brake wear and road abrasion [7],
- emission factors of harmful substances by fuel combustion installations [6],
- weight and calorific value of gasoline and diesel oil (catalogue data).

3. Results

The described methodology allowed for the selection of cars and carrying out the research using the computational method. The results concerning the emission of pollutants are presented in the Figs 3–6.

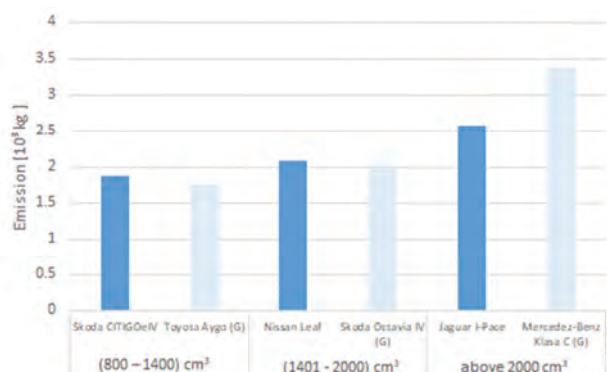


Fig. 3. Comparison of CO₂ emissions for the selection of cars for testing in terms of engine displacement. BEV – navy blue, ICE – light blue, G – gasoline

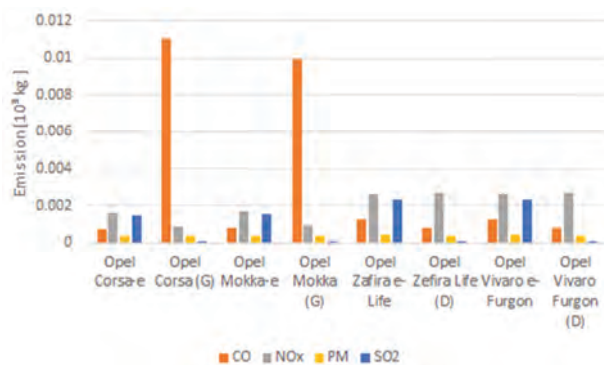


Fig. 6. Comparison of emissions of CO, NO_x, PM and SO₂ selecting vehicles for testing because of the brand of vehicle. G – gasoline, D – diesel

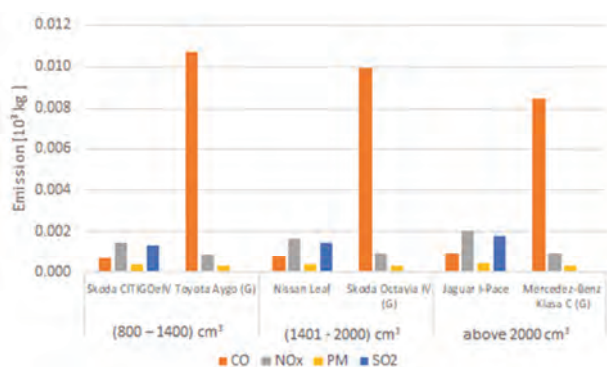


Fig. 4. Comparison of emissions of CO, NO_x, PM and SO₂ for the selection of cars for testing in terms of engine displacement. G - gasoline

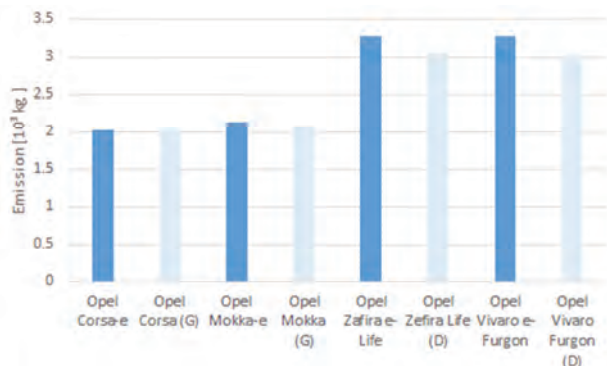


Fig. 5. Comparison of CO₂ emissions of selecting vehicles for testing because of the brand of vehicle. BEV – navy blue, ICE – light blue, G – gasoline, D – diesel

4. Conclusions

The calculations, as well as the information collected in this article, show that the emissions of carbon dioxide and harmful substances from cars with electric engines and cars with internal combustion engines mainly depend on factors such as:

- type of internal combustion engine (spark-ignition or compression-ignition),
- displacement of the internal combustion engine,
- energy mix.

After conducting a comparative analysis, it can be concluded that in Polish conditions, introducing cars with electric engines into circulation at the expense of withdrawing cars with internal combustion engines is not unequivocally positive.

This is evidenced by the results obtained which show that the CO₂ emission from BEV is higher than for cars with combustion engines except for the engines of engine displacement above 2000 cm³ (Figs 3 and 5). In the case of CO emissions, it is clear that for ICEs powered by gasoline, the emissions are higher than for BEVs, but for ICEs powered by diesel, the emissions are lower than for BEVs. For the remaining pollutants, the emissions from ICE are lower than for BEV.

Summing up, the results of the research and the presented analysis of sources show that for the current energy mix in Poland, increasing the number of cars with an electric engine while reducing the number of cars with internal combustion engines will not have a better impact on the natural environment and human health, because the content of CO, NO_x, SO₂ will increase in the air. In the case of CO₂ emissions, it will slightly decrease.

The comparative analysis conducted in this paper can be a reference point for further research on electromobility in the context of the energy mix or electricity and power supply. The aim of the research may be to determine the legitimacy or directions of development of electromobility in terms of its impact on the natural environment and economic aspect. It is also possible to expand the included methodology of comparative analysis to include cars powered by other types of fuels, such as natural gas or biofuels.

Nomenclature

BEV battery electric vehicle
 CO carbon monoxide
 CO₂ carbon dioxide
 ICE internal combustion engine

NO_x nitrogen oxides
 PM particulate matter
 SO₂ sulphur dioxide

Bibliography

- [1] DAVIES WALDRON, C., HARNISCH, J., LUCON, O. et al. Mobile combustion. *2006 IPCC Guidelines for National Greenhouse Gas Inventories*. EGGLESTON, H.S., BUENDIA, L., MIWA, K., NGARA, T. et al. (eds), 2006. <https://www.ipcc-nggip.iges.or.jp/public/2006gl/index.html>
- [2] FERNÁNDEZ, R.A. A more realistic approach to electric vehicle contribution to greenhouse gas emissions in the city. *Journal of Cleaner Production*. 2018, **172**, 949-959. <https://doi.org/10.1016/j.jclepro.2017.10.158>
- [3] HOEKSTRA, A. The underestimated potential of battery electric vehicles to reduce emissions. *Joule*. 2019, **3**(6), 1412-1414. <https://doi.org/10.1016/j.joule.2019.06.002>
- [4] MENES, M. Studies results concerning passenger cars' average annual mileages in Poland in 2014. *Przegląd komunikacyjny*. 2015, **5**, 6-10. http://www.przegląd.komunikacyjny.pwr.wroc.pl/05_2015/PK_05_15.pdf (in Polish with English abstract).
- [5] MINISTRY OF CLIMATE AND ENVIRONMENT. Poland's National inventory report 2020 Greenhouse gas inventory for 1988-2018 Submission under the United Nations Framework Convention on Climate Change and the Kyoto Protocol. 2021. <https://unfccc.int/documents/274762>
- [6] MINISTRY OF CLIMATE AND ENVIRONMENT. Poland's Informative Inventory Report. Submission under the UNECE CLRTAP and NEC Directive. 2021. https://cdr.eionet.europa.eu/pl/eu/nec_revised/iir/envyei5sq/
- [7] NTZIACHRISTOS, L., SAMARAS Z. Road transport. EMEP/EEA air pollutant emission inventory guidebook 2019. 2019, **13**. <https://doi.org/10.2800/293657>
- [8] RANGARAJU, S., DE VROEY, L., MESSAGIE, M. et al. Impacts of electricity mix, charging profile, and driving behavior on the emissions performance of battery electric vehicles: A Belgian case study. *Applied Energy*. 2015, **148**, 496-505. <https://doi.org/10.1016/j.apenergy.2015.01.121>
- [9] REGULATION OF THE EUROPEAN PARLIAMENT and of the COUNCIL on establishing the framework for achieving climate neutrality and amending Regulation (EU) 2018/1999 (European Climate Law). <https://eur-lex.europa.eu/legal-content/EN/TXT/PDF/?uri=CELEX:52020PC0563&from=EN>
- [10] THE EUROPEAN GREEN DEAL. 2019. Communication from the Commission to the European Parliament, the Council, the European Economic and Social Committee and the Committee of the Regions. <https://eur-lex.europa.eu/legal-content/EN/TXT/PDF/?uri=CELEX:52012DC0673&from=EN>
- [11] WIATRAC, M. Analiza porównawcza emisji dwutlenku węgla i substancji toksycznych emitowanych przez samochody z silnikami spalinowymi w porównaniu do równoważnej emisji z samochodów z silnikami elektrycznymi. Graduate thesis. *Warsaw University of Technology*. 2021 (in Polish with English abstract).
- [12] Wskaźniki emisyjności CO₂, SO₂, NO_x, CO i pyłu całkowitego dla energii elektrycznej, na podstawie informacji zawartych w Krajowej bazie o emisjach gazów cieplarnianych i innych substancji za 2019 rok. *Instytut Ochrony Środowiska Państwowy Instytut Badawczy*. Warsaw 2020.

Piotr Laskowski, DEng. – Faculty of Automotive and Construction Machinery Engineering, Warsaw University of Technology.
e-mail: piotr.laskowski@pw.edu.pl



Damian Zasina, DEng. – Faculty of Building Services, Warsaw University of Technology.
e-mail: damian.zasina@pw.edu.pl



Magdalena Zimakowska-Laskowska, DEng. – Institute of Environmental Protection – National Research Institute.
e-mail: magdalena.zimakowska-laskowska@kobize.pl



Marcin Wiatrak, Eng. – Faculty of Automotive and Construction Machinery Engineering, Warsaw University of Technology.
e-mail: marcin.wiatrak1995@gmail.com

Examples of the use of the embedded systems for the long-term collection of slowly-changing parameters in the traction of a car

ARTICLE INFO

Received: 15 July 2021
Revised: 6 September 2021
Accepted: 8 September 2021
Available online: 15 September 2021

The article presents how embedded systems can be used to collect data in the long-term traction of a car. It is assumed that the long period is the time of a travelled distance, e.g. a few thousands of kilometres, or a time, e.g. a month. Such data can be used to optimize the control systems and to diagnose unusual faults in mechatronic systems. The research paper presents how, with the use of very cheap devices, it is possible to collect data that quite often could not be collected even with the use of very expensive measuring devices. The possibility of simple analysis of signals in real time was also pointed out.

Key words: *embedded system, collecting and archiving data, software, signal matching systems, real-time analysis*

This is an open access article under the CC BY license (<http://creativecommons.org/licenses/by/4.0/>)

1. Introduction

A large number of vehicles with internal combustion engines requires constant efforts from manufacturers to develop as eco-friendly a car as it is possible to protect the human environment. The legislator dictates the standards for the toxicity of exhaust fumes from car engines. Scientists and car manufacturers try to meet the requirements set out in the standards. It is becoming more and more difficult. The concept of "eco-driving" has been in use for some time. It can be understood as applying a driving style by drivers that reduces fuel consumption and thus the emission of toxic substances, especially CO₂ [1–3]. There have been many scientific publications on this issue [4]. Many of them present the parameters of the traction of the car and the behaviour of the driver. These are data collected from on-board diagnostic systems or directly from sensors and actuators thanks to the use of a variety of measuring devices. On-board diagnostic systems provide a number of parameters that determine their operation. They can be read with a diagnostic tester in the real-time data reading mode [4]. However, many testers do not provide an option to save read data. There are specialized devices available on the market that can record selected real-time data of mechatronic systems through a diagnostic connector. Unfortunately, the cost and limitations of such recorders are an obstacle to obtain the necessary data. The second method of collecting information in traction is the registration of specific signals directly from sensors and actuators (e.g., fuel injectors). Various mobile and stationary recorders are used for this purpose. Often applied and very universal, they are compatible with computers (e.g., a laptop). Their goal is to sample selected signals with an appropriate frequency and save the values in disk sets. This method has both advantages and disadvantages. The biggest advantage is the possibility to configure the measuring device in a very simple way and a number of options available for the user in this respect. There are also downsides, the first of which is the cost of the device, ranging from several to even tens of thousands of zloty. The second disadvantage is the inability to analyse the measured signals in real time, and the

ability to only save their values. Due to that, the data obtained by this method are formed in files of a very large volume, whereas the useful information contained is often-times relatively small. There are also restrictions as far as the recording time is concerned due to the amount of memory samples installed in the measuring device.

The analyses of the behaviour of drivers and the work of mechatronic systems carried out as a part of the "eco-driving" often require collecting data over long periods of time (e.g., several days or several months). These are slowly-changing data (e.g., vehicle speed, accelerator pedal position, temperature, etc.) Thus, their measurement and recording can take place at a low frequency (e.g., every 0.5 seconds). High accuracy is not required for many of these signals (e.g., it is enough to measure the vehicle speed with an accuracy of 1 km/h).

In analyses related to eco-driving, accurate and fast-changing data may also be needed (e.g., duration of all fuel injections with accuracy of 1 μs). Collecting them in the form of an injection signal recording at a frequency that provides the required accuracy over long distances will result in the creation of large data sets. For this reason, it will be impossible to implement, even for many professional measurement systems.

As a result, there is a problem of collecting various data from mechatronic systems in a long-distance traction.

The aim of this article is to present embedded systems as recorders of slowly-changing parameters (e.g., vehicle speed) that occur in mechatronic systems of cars over long periods of time.

Such measurements are especially useful in various analyses of mechatronic systems of cars related to the "eco-driving" and wherever the observation in a long period of time is necessary (e.g., a month).

The proposal to use embedded systems to collect slowly-changing data in the car traction is justified primarily by the low price of the devices and the ability to analyse signals in real time. In some cases, the real-time data analysis allows you to significantly reduce the amount of data collected without losing useful information. The method of the

analysis is precisely defined by the researchers in the form of a program implemented by a microcontroller. The idea of using embedded systems to collect data in traction arose from the need to collect data and, at the same time, the lack of financial resources to purchase a professional measurement system. Therefore, it is directed to young researchers of automotive issues as well as students of automotive faculties. However, it should be remembered that it has limitations related to the computing power of the microcontrollers used as well as the quality of the A/D converter.

Being able to register and then analyse the results can certainly support the work related to increasing the reliability and optimization of the car's mechatronic systems.

The use of an embedded system as a simple and at the same time specialized computer gives the opportunity to not only collect, but also to analyse data in real time and then save the results. However, in order for a simple and very cheap computer to simultaneously perform a specialized measurement task, it must be properly programmed. Such a program has to be written by a user who knows what information he or she wants to collect and how to do it [5]. Therefore, programming skills are required, which in the case of an engineer (e.g., of mechatronics) is an easy ability to obtain. Many engineers know the basics of microcontroller programming due to their faculty, most often in the form of C++ language [6, 7].

The article presents some examples of measuring signals and parameters in a car with the use of an embedded system.

2. Embedded systems

Embedded systems as simple computers equipped with software have been developed in recent years for various microprocessors. The most famous are as follows: Arduino, Raspberry Pi, Nucleo, etc. Due to the price, hardware availability, and dissemination in the academic and student environment, Arduino was chosen to present as an exemplary measuring device. The microcontroller used in Arduino is the least effective among the above-mentioned platforms. Nevertheless, it is able to carry out some of the measuring tasks with sufficient accuracy and quality. For more demanding measuring tasks, other embedded systems can be used that are more advanced and more expensive than Arduino.

The literature presents a lot of different applications of specialized computers with embedded software. Embedded systems are primarily used to control various processes and devices. The use of embedded systems for recording slowly-changing parameters in running cars was not found. Hence the proposal for such an application of a simple and cheap computer in automotive research.

2.1. ARDUINO boards as simple computers

There are several types of embedded systems for the ARDUINO development platform. The most common ones are the following: Arduino Uno, Arduino Nano, Arduino Mega (Fig. 1).

All of the above-mentioned boards are made of a microcontroller, a quartz resonator, a USB-RS232 converter, a supply voltage stabilizer, a RESET button, signalling diodes, and sockets: USB and power (the latter is not pre-

sent in the nano board). They are in the form of a printed circuit board with led out digital and analogue ports.

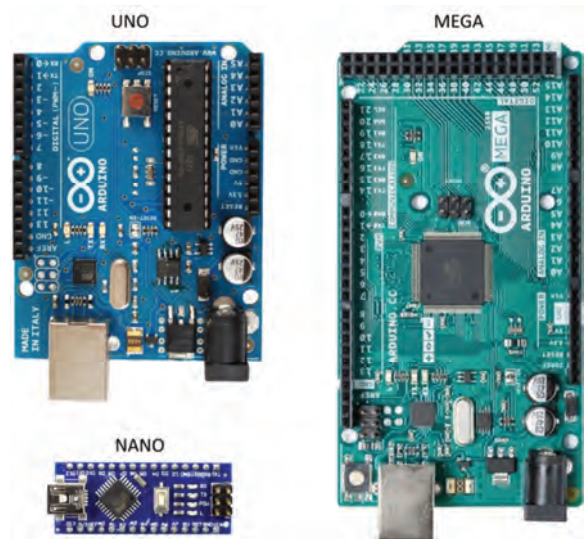


Fig. 1. Examples of Arduino computers (boards)

Arduino Nano and Arduino Uno boards have the ATmega328P microcontroller. It is equipped with three types of memory, such as:

Flash (32kB) – dedicated to the program code,

SRAM (2kB) – as operational memory,

EEPROM (1 kB) – as a non-volatile memory for storing results.

The first 2 kB of flash memory is occupied by the factory-installed software used to start the computer and load the user's software, the boot loader. It acts as such a micro-operating system. The ATmega328P microcontroller is also equipped with one 10-bit analogue-to-digital converter. It enables the measurement of voltage values on analogue inputs in the range from 0 to a given reference value (5 V maximum). Digital ports operate in the so-called 5 V logic. Thus, signals with other voltages require adjustment [6].

2.2. Simple signal matching systems

For the correct identification of binary signals, it is required that their voltage is within the range from 0 to 5 V. Many signals in the mechatronic systems of cars change in this range. There are also binary signals, the amplitude of which reaches approximately 14V (Fig. 2).

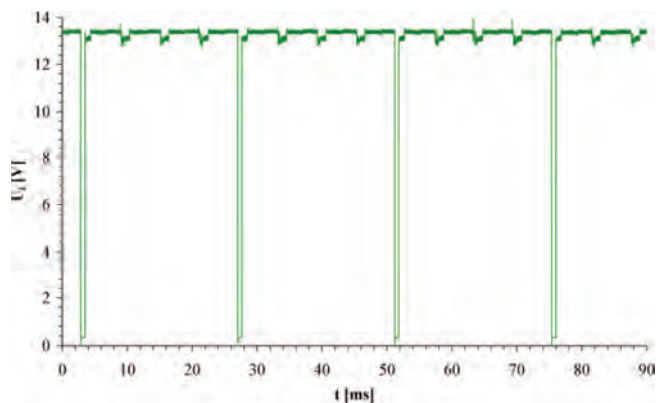


Fig. 2. An example of a binary signal with an amplitude exceeding 5 V

There are also signals similar to square waveforms, but they are not square (Fig. 3). They carry information about the moment of their occurrence and duration, while their amplitude carries no information. Before introducing the microcontroller to the digital port, it is necessary to shape and adjust their amplitude.

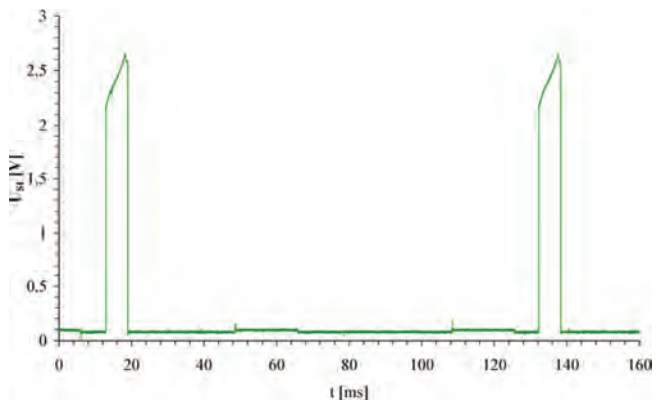


Fig. 3. An example of a signal similar to a square one

Some sensors in mechatronic systems generate analogue signals in which the information is contained in the frequency. An example may be the signal from the inductive speed sensor of the car wheel in the ABS system (Fig. 4).

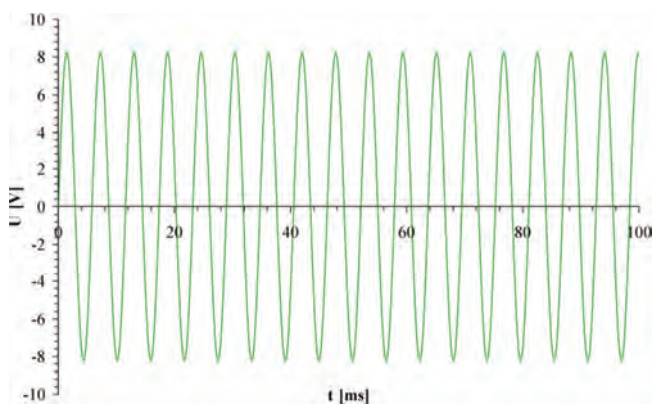


Fig. 4. An example of an analogue signal that carries information only through frequency

Such a signal also changes amplitude with speed. However, its amplitude is not dependent on speed alone. Therefore, transforming it into a square signal will not cause the loss of the carried information, but it will enable the introduction to the digital input of the microcontroller.

The signals shown in Figs 2, 3, and 4 can be converted into square (binary) signals using very simple electronic circuits shown in Fig. 5.

The circuits shown in Fig. 5 are powered by 5 V, which makes their signal output with a voltage of up to 5 V. Each of them requires the selection of resistive elements to the input voltage range. To convert the signals shown in Figs 2 and 3, it is enough to use the circuit shown in Fig. 5a to obtain a square wave signal with an amplitude of 5 V (Fig. 6). However, when transformed, it will be inverted. In order to restore it to its original form in phase, a double transformation should be applied (Fig. 7).

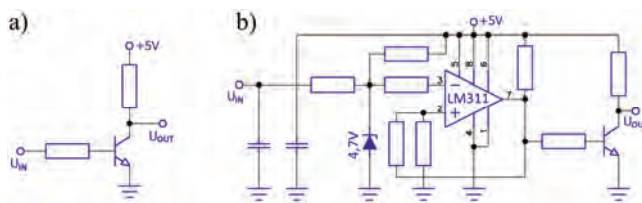


Fig. 5. Examples of two systems of matching the signals in the mechatronic systems of the car to the binary form: a) single-stage inverting voltage amplifier, b) voltage comparator with a hysteresis loop

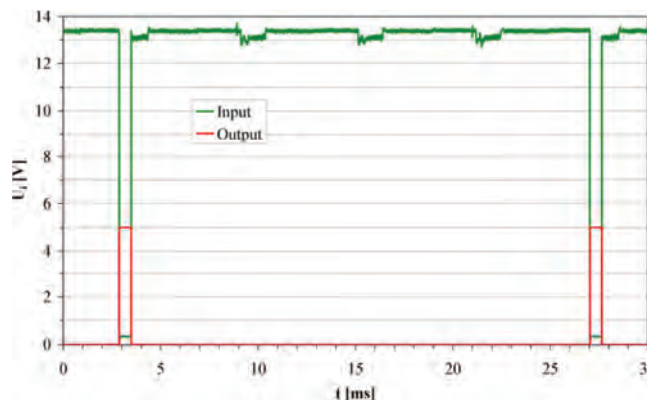


Fig. 6. Signal conversion to a rectangular form with 5 V amplitude limitation and phase reversal

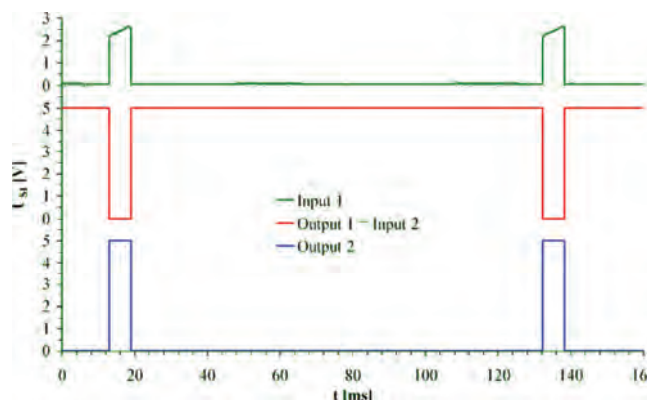


Fig. 7. Double conversion of the signal to a rectangular form with amplitude adjustment up to 5 V

In order to convert an analogue signal (Fig. 4) into a binary one, it is necessary to compare it to the set level. As a result of a disturbance when passing the set threshold, an alternating high and low state can be generated at the output. Therefore, the circuit (Fig. 5b) uses a hysteresis loop in the comparator input that sets the reference level. This causes a certain switching of the comparator output when the signal passes a given threshold. The result of the transformation of the signal from Fig. 4 is shown in Fig. 8.

The presented signal matching systems are characterized by high simplicity and low cost of implementation. At the same time, they enable signal measurements with the use of the embedded system. These are just examples for the presented signals. In a similar manner, other equally simple systems can be designed and implemented for specific needs.

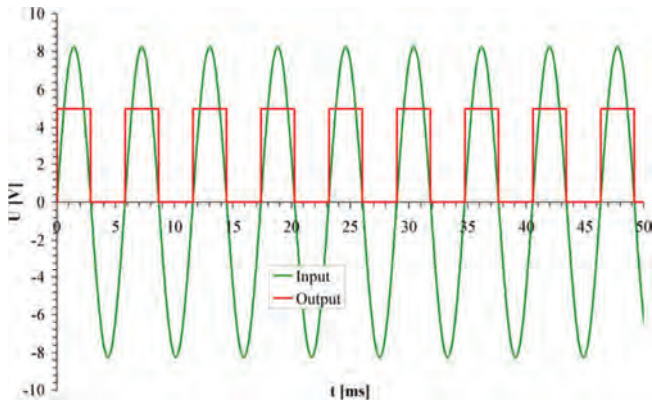


Fig. 8. Conversion of an analogue signal carrying information through frequency into a binary signal with an amplitude of 5 V

3. Measurement system based on an embedded system for the Arduino platform

Embedded systems for the Arduino platform are popular "Arduino boards". These are tiny computers that perform simple tasks. These simple tasks, dictated by the program code, can be a measurement action. The microcontroller is responsible for performing at a high speed many simple actions. Noticing a high or low state on a digital port takes place in less than 1 microsecond. Reading the time of the internal clock also takes a very short period. Such simple actions allow us to measure the duration of binary pulses and count their number. The microcontroller also performs simple arithmetic operations. Unfortunately, these take a longer time. It can also measure analogue voltage signals. It has 8 analogue inputs on which the voltages are measured with the use of one ten-bit analogue-to-digital converter with a maximum sampling rate of 10 kS/s. Though this frequency is not high, the recording of slowly-changing signals is definitely possible and accurate. The measurement resolution at the maximum reference voltage of 5 V is approximately 1.25 mV.



Fig. 9. Measuring systems of slowly-changing parameters were installed in a Mitsubishi Carisma GDI car

In addition to performing measurement actions, the measuring device has to collect measurement results as well. This embedded system has internal memory, yet it is

very small. Therefore, it must use an external non-volatile memory, to which it will transfer the measurement results from time to time. Such external non-volatile memory can be an SD card. The Arduino development platform has libraries to support the SD card and the SPI interface used for the communication process with the SD card. The use of memory in the form of an SD card for measurement data is a very cheap solution, ensuring a very large capacity and easy transfer of measurement data.

The exemplary measuring system presented in this article was made of an "Arduino nano board" and a microSD memory card reader (Fig. 9). The reader is fitted with a 32 GB card formatted for the FAT32 file system with a 16 kB allocation unit.

3.1. Examples of tasks, measurement programs, and their results

The tests of the measuring system were carried out on a Mitsubishi Carisma GDI car. All measured signals were binary in 5 V logic. Some of them were transformed using the matching circuit shown in Fig. 5a. Figure 9 shows two measurement systems. This allows different measurements to be made at the same time. The first system, with a horizontally mounted memory card reader, performs the measurement of:

- the state of three binary signals in 5 V logic that control a three-colour LED diode (the indication of the type of the fuel-air mixture supplying the GDI engine) every 0.5 s.
- the road and speed of the car over time by registering the number that is the sum of pulses from the vehicle speed sensor,
- the engine rotational speed by registering the number that is the sum of pulses from the crankshaft position sensor,
- the average injection time in half-second periods by recording the number that is the sum of the duration of the fuel injection pulses and the number of injections that makes up the sum of the duration times.

The results of the above-mentioned parameters were recorded every 0.5 s. The code of the program that measures the above-mentioned parameters to present its simplicity is presented below. It is related to the hardware capabilities of the microcontroller. Only commands to read ports, compare, sum, and save data are used. No multiplication or division commands were used. Operations on integers were used only. Program code:

```
#include <SPI.h>
#include <SD.h>
File plik;
uint16_t czas[20];
uint32_t droga[20];
uint32_t SCWK[20];
byte pomiar[20];
uint32_t tw[20];
uint8_t lw[20];
uint32_t tw1=0;
uint32_t tp;
uint8_t lw1;
uint32_t S=0;
uint32_t CAS=0;
byte i=0;
byte j1=0;
```

```

byte j2;
byte j3=0;
byte j4;
byte j5=0;
byte j6;
void setup() {
  SD.begin(10);
  pinMode(7, INPUT);
  pinMode(6, INPUT_PULLUP);
  pinMode(5, INPUT_PULLUP);
  pinMode(4, INPUT);
  pinMode(3, INPUT);
  pinMode(2, INPUT);
  plik = SD.open("pomiar.txt", FILE_WRITE);
}
void loop() {
  j2=digitalRead(5);
  if(j2<j1){S++;}
  j1=j2;
  j4=digitalRead(6);
  if(j4<j3){CAS++;}
  j3=j4;
  j6=digitalRead(7);
  if(j6>j5){tp=micros();}
  if(j5>j6){
    tw1=tw1+micros()-tp;
    lw1++;}
  j5=j6;
  if(millis() % 500 == 0){
    czas[i]=millis()/500;
    pomiar[i]=digitalRead(2);
    pomiar[i]=pomiar[i]+digitalRead(3)*2;
    pomiar[i]=pomiar[i]+digitalRead(4)*4;
    droga[i]=S;
    SCWK[i]=CAS;
    tw[i]=tw1;
    lw[i]=lw1;
    tw1=0;
    lw1=0;
    i++;
    delay(1);
  }
  if(i == 20){
    for(BYTE j=0;j<20;j++){
      plik.print(czas[j]*0.5,1);
      for(byte k=0;k<2;k++){
        plik.print(char(9));
        plik.print(bitRead(pomiar[j],k));
      }
      plik.print(char(9));
      plik.print(bitRead(pomiar[j],2));
      plik.print(char(9));
      plik.print(droga[j]);
      plik.print(char(9));
      plik.print(SCWK[j]);
      plik.print(char(9));
      plik.print(tw[j]);
      plik.print(char(9));
      plik.println(lw[j]);
    }
    plik.flush();
    i=0;
  }
}

```

The operation of the measuring system was verified over a distance of 456 km, i.e. On the route from Radom to Gdańsk. The registration results are shown with the use of images in Figs 10, 11, 12. Each waveform shows 42,700 measured values.

High state of a signal in a given colour causes the LED to light in the same colour (green colour indicates that the engine is supplied with a stratified mixture, red colour indicates a homogeneous mixture, and blue colour – no fuel injection, i.e., engine braking).

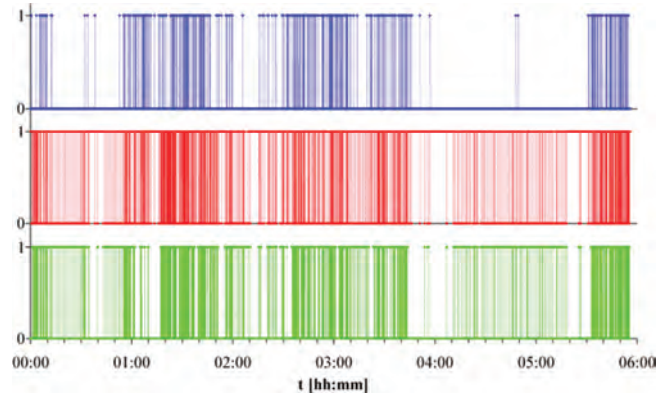


Fig. 10. Three-colour led colour led control signals, (the indication of the type of the fuel-air mixture)

Only one of the three signals is high at a given time. The registration of the results allows us to assess the state of the system at a given moment and allows us to conduct the analysis of its operation. They can also be used in the statistical analysis, e.g., to determine the percentage share of the supply of the engine with a stratified mixture.

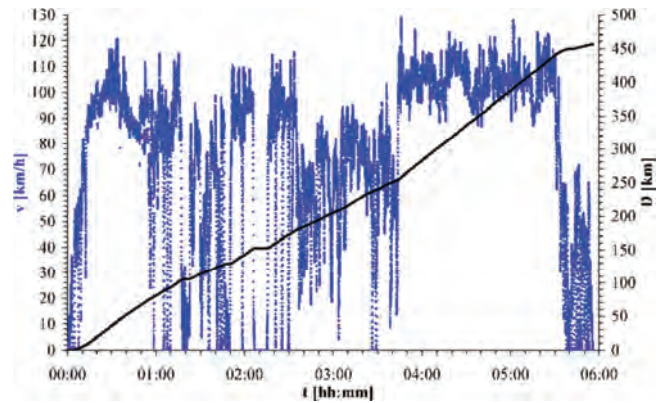


Fig. 11. The waveform of the route and vehicle speed while driving

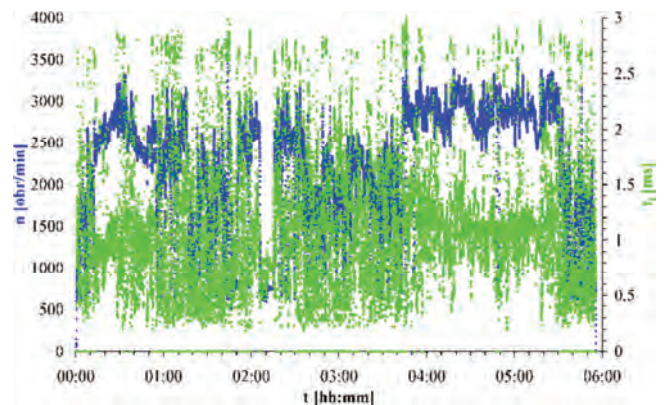


Fig. 12. The waveform of the changes in the rotational speed of the engine and the average injection time in half-second periods

The graph in Fig. 12 shows, inter alia, average injection times in half-second measurement periods. Due to the occurrence of many injections in one measuring period, it is impossible to record the duration of each of them. In addition, there is a different number of injections in each measurement period depending on the rotational speed of the

engine. An attempt was made to record the duration of each fuel injection. The second measuring system was applied (with a vertically installed memory card reader in Fig. 9). This measuring system is designed to measure and record the duration of each injection. During the appearance of the rising slope, the current time is recorded. Immediately after the appearance of the falling slope, the duration of the injection pulse is determined and stored. The code of the program which measures the times of all fuel injections is very simple and looks as follows:

```
#include <SPI.h>
#include <SD.h>
File plik;
byte i=0;
uint32_t t[32];
uint32_t tw[32];
uint32_t tp;
byte j1=0;
byte j2;
void setup(){
  SD.begin(10);
  pinMode(7, INPUT);
  plik = SD.open("tw.txt", FILE_WRITE);
}
void loop() {
  j2=digitalRead(7);
  if(j2>j1){tp=micros();}
  if(j1>j2){
    tw[i]=micros()-tp;
    t[i]=millis();
    i++;
  }
  j1=j2;
  if(i==32){
    for(byte j=0; j<32; j++){
      plik.print(t[j]);
      plik.print(char(9));
      plik.println(tw[j]);
    }
    plik.flush();
    i=0;
  }
}
```

The results of measurements of selected injections on the route of 456 km are presented with the use of a pictorial diagram (Fig. 13). The graph shows 376 thousand fuel injections. The injection time measurement results can be converted into injected fuel doses. These can be analysed in a number of ways.

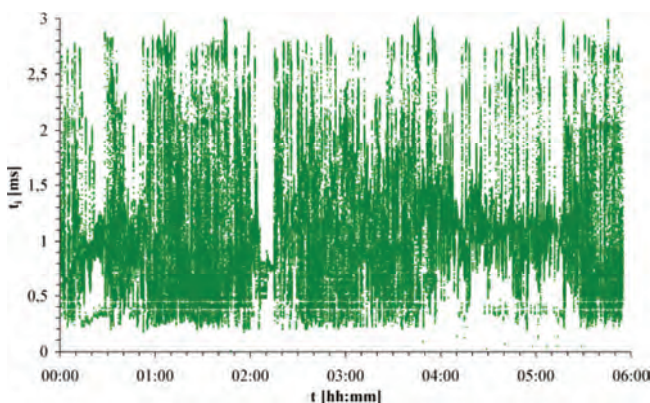


Fig. 13. Times of fuel injections measured on the distance of 456 km

3.2. Verification of a measuring device constructed on the basis of an embedded system

The presented proposals of measuring devices for collecting slowly-changing data were verified. The verification consisted in the comparison of the measurement results obtained with the presented device and a professional measurement system. The first of the two presented measuring systems counts pulses from two sensors and records their numbers every 0.5 s. The second of the presented systems measures the duration of injection pulses and records each of them with an accuracy of 1 μ s. It is connected with the necessity to detect signal slopes, as well as calculate and save the injection pulse duration to a file on the SD card. There is; therefore, a risk that slopes will be noticed with different delay, which will result in incorrect time measurements.

In order to verify the accuracy of the proposed measuring device, a comparative test was conducted. The same signal (of fuel injection for cylinder 1) was introduced on the input of the tested system and on the input of the professional measuring system. The professional measuring system consisted of a PC with an A/D converter card of GAGE manufacturer, Octopus ComuScope 8380 series [9]. The computer measuring system was configured so it records the signal every 1 μ s. The recording time was 50 s, which result from the sampling frequency and the amount of memory of the measurement card. The measurement results were synchronized in such a way that both measurement lines were initialized first, and then the engine was started. Therefore, the analysis of the measurement results was started with the first generated and recorded injection pulse. During the test, the position of the accelerator pedal was changed multiple times, so as to generate pulses with duration times from the entire work range. During the test, the computer measuring system recorded 575 injection pulses. Their times were determined based on the recorded injection signal course and adopted as real values. Then the errors were determined: absolute and relative of the duration measurement for all 575 injections:

$$\Delta t_w = t_{wA} - t_{wp} \quad (1)$$

where: Δt_w – the absolute error of the injection time measurement, t_{wA} – the injection time measured with a device based on the Arduino platform, t_{wp} – the injection time measured with a professional measuring system,

$$\delta t_w = \frac{|\Delta t_w|}{t_{wp}} \cdot 100\% \quad (2)$$

where: δt_w – the relative error of the injection time measurement.

The values of the errors were presented in the form of diagrams.

During the verification of the measuring device, the injection times were changed in the range from approximately 200 μ s to 3350 μ s.

The analysis of the injection time measurement errors presented in Fig. 14 and 15 provides us with the chance to positively assess the measuring device constructed on the basis of a simple computer for the Arduino platform. The measurement of the duration of the vast majority of injec-

tions differs by $\pm 2 \mu\text{s}$ from the real value. What is more, the absolute error of the duration of the vast majority of injections is lower than 1%.

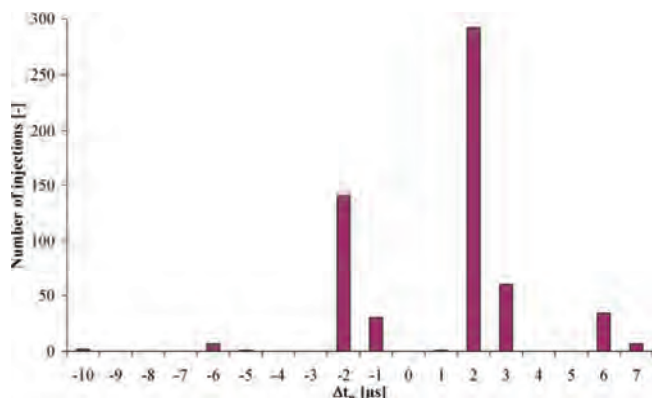


Fig. 14. Diagram of discrepancy (absolute error) of injection time obtained during verification

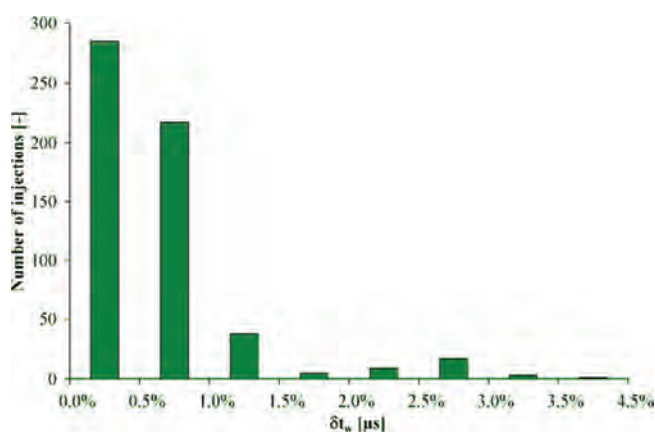


Fig. 15. Diagram of the relative error of injection time obtained during verification

4. Summary and conclusion

The use of embedded systems, i.e., simple computers based on microcontrollers allows for the measurement of various parameters of the signals present in the mechatronic systems of vehicles. Such systems have certain limitations related to the amount of operating memory and the speed of operation. Nevertheless, they provide us with the opportunity to apply quite complex measurements over a very long period of time, e.g., a six-hour measurement of fuel injection duration takes up 5.1 MB of memory on a 32 GB memory card. The only difficulty related to the use of embedded systems for long-term measurements of slowly-changing parameters is the need to write a program and possibly build simple signal matching circuits. However, it can be concluded that these are not tasks beyond the capabilities of every engineer. It is evidenced by the following:

- very low complexity of signal matching circuits, as presented in this research paper,
- simple program code as evidenced by the two examples of the presented programs.

The paper mainly presents the possibility of using embedded systems for the long-term data collection in mechatronic systems of cars. Presented registration results should be treated only as an example of the possibilities offered by this type of microprocessor system. In particular, emphasis should be put on the very low price compared to the potential measurement possibilities. The proposal to use embedded systems to collect slowly-changing data is addressed primarily to young researchers who do not have professional measuring equipment and students of automotive faculties. Another advantage of the presented measuring system is the possibility to permanently install it in the car and collect the necessary data in everyday use of the car. This will reduce the cost of the conducted research and result in the data collection during typical operation of the vehicle.

The accuracy that can be obtained in the more difficult task of measuring the timing of successive fuel injections is satisfactory.

Bibliography

- [1] LOIS, D., WANG, Y., BOGGIO-MARZET, A. et al. Multivariate analysis of fuel consumption related to eco-driving: Interaction of driving patterns and external factors. *Transportation Research Part D: Transport and Environment*. 2019, **72**, 232-242. <https://doi.org/10.1016/j.trd.2019.05.001>
- [2] HUERTAS, J.I., DÍAZ, J., GIRALDO, M. et al. Eco-driving by replicating best driving practices. *International Journal of Sustainable Transportation*. 2018, **12**, 107-116. <https://doi.org/10.1080/15568318.2017.1334107>
- [3] PUCHALSKI, A., KOMORSKA, I. Driving style analysis and driver classification using OBD data of a hybrid electric vehicle. *Transport Problems*. 2020, **15**(4), 83-94. <https://doi.org/10.21307/tp-2020-050>
- [4] FAFOUTELLIS, P., MANTOUKA, E.G., VLAHOGIANNI, E.I. Eco-driving and its impacts on fuel efficiency: An overview of technologies and data-driven methods. *Sustainability*. 2021, **13**(1), 226. <https://doi.org/10.3390/su13010226>
- [5] RIBBENS, W.B. Understanding automotive electronics: an engineering perspective. *Butterworth-Heinemann an imprint of Elsevier*. 2017, Paperback ISBN: 9780128104347, eBook ISBN: 9780128104354.
- [6] MCROBERTS, M. Beginning Arduino. *Apress* 2011.
- [7] CICOLANI, J. Beginning Robotics with Raspberry Pi and Arduino. *Apress* 2018.
- [8] ISERMANN, R. Mechatronic systems – Innovative products with embedded control. *Control Engineering Partice*. 2008, **16**(1), 14-29. <https://doi.org/10.1016/j.conengprac.2007.03.010>
- [9] Gage. Egmont Instruments. http://www.egmont.com.pl/gage/techn/dso_PCI.html

Zbigniew Wołczyński, DEng. – Faculty of Mechanical Engineering, Kazimierz Pulaski University of Technology and Humanities in Radom.
e-mail: z.wolczynski@uthrad.pl





INSTYTUT TECHNICZNY WOJSK LOTNICZYCH

ul. Księcia Bolesława 6, 01-494 Warszawa, skr. poczt. 96

tel.: 261 851 300; faks: 261 851 313

www.itwl.pl

e-mail: poczta@itwl.pl

SYSTEM DIAGNOSTYKI TRIBOLOGICZNEJ



System Diagnostyki Tribologicznej (SDT), opracowany w Instytucie Technicznym Wojsk Lotniczych, przeznaczony jest do wspierania eksploatacji obiektów technicznych.

Na podstawie wyników badań próbek oleju pobranych z układów tribologicznych prowadzi się ocenę i prognozowanie stanu technicznego obiektów technicznych (statki powietrzne, pojazdy mechaniczne, statki wodne, maszyny robocze i inne).



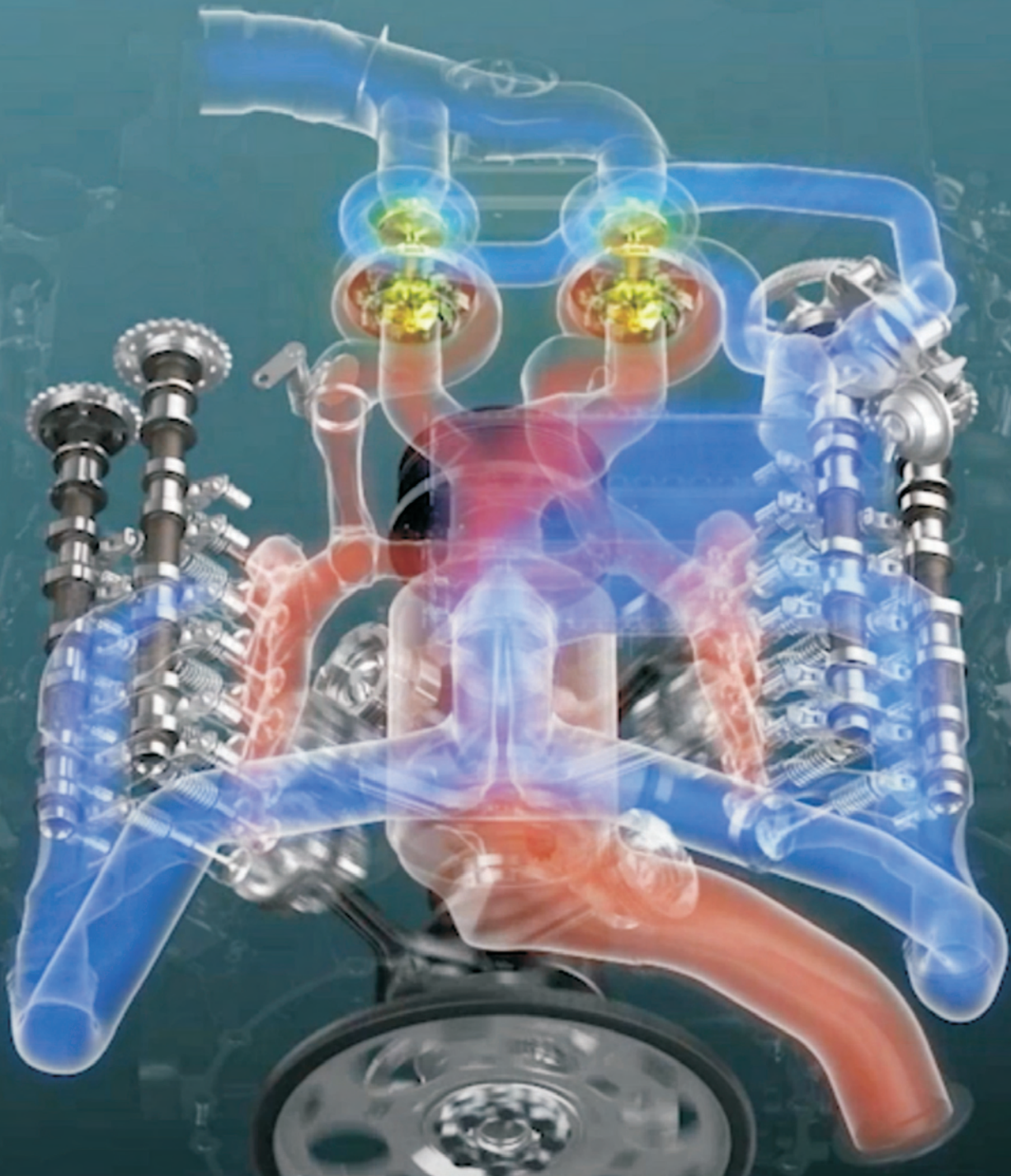
AB 138



9/MON/2017



INSTYTUT TECHNICZNY WOJSK LOTNICZYCH
ZAKŁAD SILNIKÓW LOTNICZYCH
Akredytowane laboratorium:
Laboratorium Diagnostyki Systemów Tribologicznych



Publisher:

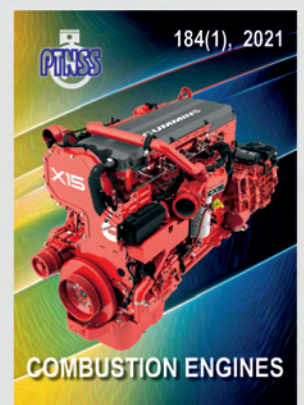
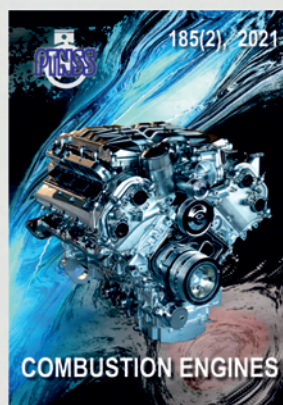
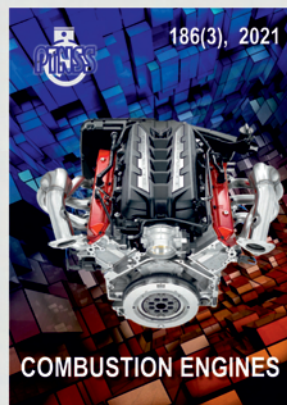
**Polish
Scientific
Society
of Combustion
Engines**



**ISSN: 2300-9896
eISSN: 2658-1442**

Combustion Engines

Polskie Towarzystwo Naukowe Silników Spalinowych



www.combustion-engines.eu